An Implantable Microsystem for Autonomous Intraocular Pressure Monitoring

by

Razi-ul Muhammad Haque

A dissertation submitted in partial fulfillment
of the requirements for the degree of
Doctor of Philosophy
(Electrical Engineering)
in The University of Michigan
2011

Doctoral Committee:

Professor Kensall D. Wise, Chair
Professor Paul R. Lichter
Professor Khalil Najafi
Professor Dennis M. Sylvester
Professor Eusik Yoon

© Razi-ul Muhammad Haque
2011

All Rights Reserved

To my parents, teachers, and mentors for their guidance.

ACKNOWLEDGMENTS

So many people have helped me over the years on this great journey that it would be difficult to list and express my appreciation to all of them. This work would not have been possible without luck and the involvement of several people. First, Prof. Wise, my advisor and mentor during my graduate studies, has been an inspiration and role model for me. If it were not for his support and participation in my work, I know I would not have achieved good quality research that I am proud of. His support and encouragement when I started this project has been unwavering, even when I proposed a highly-complex microsystem that pushed the boundaries of research in at least three different areas. I firmly believe that without Prof. Wise, this work would not have been possible.

My committee members, Profs. Paul Lichter, Khalil Najafi, and Dennis Sylvester, and Eusik Yoon have all had a strong impact on my work as well. Prof. Paul Lichter has taken so much time out of his schedule as Chair of the Kellogg Eye Center to have discussions with me and respond to email inquires. Prof. Najafi introduced me to MEMS during my undergrad coursework. Prof. Sylvester and Prof. Blaauw have together worked with me developing specialized circuitry for the intraocular project. They both are highly motivated, pushing the boundaries of implanted electronics so I am excited to see their continued progress. Finally, Prof. Yoon has been most helpful and supportive with his discussions during our special Biothrust meetings, combining bio-related projects in WIMS.

My work would have not been possible without the support and friendship of so many people. In particular, my closest friends since I was young, Syed Mohiuddin and Omar Razzacki have been there for me whenever I needed them and their support is greatly appreciated. My extended family is also special to me, helping to make life more enjoyable. And finally, I must thank my classmates here at the University of Michigan, from my undergrad years up through my graduate years. Specifically, my group members, Angelique, Johnson, Gayatri Perlin, Jianbai Wang, Joe Potkay, Kyusuk Baek, Helena Chan, Pamela Bhatti, Ying Yao, and Yang Li all had a profound influence on me, setting high standards for achievements in this group. Ning Gulari and Katharine Beach are two amazing process engineers who helped me get started in the cleanroom with their expert advice and help. My coworkers and colleagues across undergraduate Electrical Engineering, Computer Engineering, Chemical Engineering and other users of the Lurie Nanofabrication Facility have been great sources of information and help when needed. There are far too many people who have been of great service and have my highest regard to list here, but I am sure you all know who you are.

Financial support was provided by the National Science Foundation through the Engineering Research Center for Wireless Integrated MicroSystems (WIMS). Additional funding was provided by a gift from Ms. Polly Anderson. Without these contributions, I would not have been able to spend as much time in the cleanroom as I did.

Finally, I would like to thank my parents for the many sacrifices they have made for their children while we were growing up in an effort to ensure that we had the best education possible. My family has been supportive of my work and encouraging me when I needed it so this thesis is undoubtedly a product of their efforts.

TABLE OF CONTENTS

DEDICATION ii

ACKNOWLEDGMENTS iii

LIST OF FIGURES ix

LIST OF TABLES xvii

ABSTRACT xviii

CHAPTER 1. INTRODUCTION 1
- 1.1. MOTIVATION 2
  - 1.1.1. Background 3
  - 1.1.2. Conventional Measurement Methods 4
  - 1.1.3. Atmospheric Pressure 4
  - 1.1.4. Intraocular Pressure Variations 5
  - 1.1.5. Measurement Challenges 6
- 1.2. PAST WORK 7
  - 1.2.1. Contact Lens Devices 8
  - 1.2.2. Replacement Intraocular Lens Devices 9
  - 1.2.3. Passive Intraocular Monitoring Devices 9
  - 1.2.4. Low-Power RF Monitoring Devices 10
  - 1.2.5. Ideal Intraocular Pressure Monitoring 11
- 1.3. THE MICHIGAN INTRAOCULAR MICROSYSTEM DESIGN 12
  - 1.3.1. The Pressure Sensor Module 15
  - 1.3.2. The Microbattery Module 16
  - 1.3.3. The Antenna Module 17
  - 1.3.4. The Application Specific Integrated Circuit (ASIC) 18
- 1.4. SUMMARY 19

CHAPTER 2. SYSTEM DESIGN AND PACKAGING 20
- 2.1. VERTICAL STACKING 21
  - 2.1.1. Femtosecond laser drilling 23
  - 2.1.2. Mechanical drilling 25
- 2.2. GLASS-IN-SILICON REFLOW 26
  - 2.2.1. Process Flow 28
  - 2.2.2. Feedthrough Resistance 30
  - 2.2.3. Cavity Formation 31
  - 2.2.4. Metal Feedthroughs 32
  - 2.2.5. Anodic Bonding 35
  - 2.2.6. Related Work 36
- 2.3. PROCESS CHALLENGES 36
  - 2.3.1. Inadequate Filling 36

2.3.2. Surface Adhesion....39
2.3.3. Gettering....40
2.3.4. Design Rules....41
2.3.5. Wafer Stress....42
2.4. GLASS-IN-SILICON ADVANTAGES....43
2.4.1. Die Release....43
2.4.2. Material Properties....43
2.4.3. Feedthrough Hermeticity....44
2.4.4. Electrical Isolation....44
2.5. PACKAGING....46
2.5.1. Sealing....48
2.5.2. Safety....49
2.6. SURGICAL IMPLANTATION....51
2.6.1. Location....51
2.6.2. Orientation....51
2.6.3. Haptics....52
2.6.4. Initial Experiments....54
2.7. SUMMARY....55
CHAPTER 3. PRESSURE SENSOR MODULE....57
3.1. DESIGN....57
3.1.1. Specifications....58
3.1.2. Transduction Method....59
3.1.3. Touch-mode versus Gap-mode....60
3.1.4. Sensitivity....62
3.1.5. Interconnect....63
3.1.6. Intrinsic Stress....65
3.1.7. Yield Strength....66
3.1.8. Deflection....66
3.2. SURFACE INTERACTIONS....68
3.2.1. Background....68
3.2.2. Adhesion Sources....69
3.2.3. Solutions....70
3.3. SIMULATION....71
3.3.1. Yield Strength....72
3.3.2. Intrinsic Stress....74
3.3.3. Capacitance....75
3.4. FABRICATION....78
3.4.1. Layout....78
3.4.2. Process Flow....80
3.4.3. Results....82
3.5. TESTING....84
3.5.1. Touch-Mode....84
3.5.2. Hysteretic Effect....85
3.5.3. Resolution....89
3.5.4. Discussion....89
3.6. SUMMARY....91

CHAPTER 4. POWER MODULE 93
4.1. PREVIOUS MICROBATTERY WORK 93
4.2. DESIGN 95
4.2.1. Layout 96
4.2.2. Electrochemistry 97
4.2.3. Electrochemical Reactions 101
4.2.4. Electrolyte Loading 101
4.3. MATERIALS 102
4.3.1. Zinc 102
4.3.2. Silver Oxide 103
4.3.3. Electrolyte 106
4.3.4. Other Materials 107
4.3.5. Challenges 107
4.4. FABRICATION 108
4.5. TESTING 109
4.5.1. Silver Oxide Analysis 109
4.5.2. Experimental Setup 111
4.5.3. Benchtop Testing Results 113
4.6. ALTERNATIVE POWER SOURCES 116
4.6.1. Cymbet Microbattery 116
4.6.2. Ultra-capacitors 117
4.7. ENERGY SCAVENGING 118
4.7.1. Electromagnetic 118
4.7.2. Solar power 119
4.7.3. Power Generation from Pressure Variation 128
4.8. SUMMARY 133
CHAPTER 5. INTRAOCULAR CIRCUIT DESIGN 135
5.1. CONTROLLER 136
5.2. POWER OPTIMIZATIONS 138
5.3. OPTICAL TRIGGER 142
5.4. CAPACITANCE-TO-FREQUENCY CONVERSION 147
5.5. PULSE GENERATOR 151
5.6. SYSTEM LAYOUT 154
5.7. TEST RESULTS 155
5.7.1. Power Consumption 158
5.8. PHOENIX PROCESSOR 161
5.9. IDEAL ASIC 161
5.10. SUMMARY 162
CHAPTER 6. WIRELESS MODULE 164
6.1. CONVENTIONAL IMPLANTABLE WIRELESS TECHNIQUES 165
6.1.1. Near-Field Systems 166
6.1.2. Far-Field Systems 169
6.1.3. Dual-Link Systems 169
6.1.4. Non-Conventional Approaches 170
6.2. ULTRAWIDEBAND (UWB) SYSTEMS 170
6.2.1. Circuits for UWB Communications 172

6.2.2. Antenna Co-Design 172
6.3. Wireless Link Analysis 173
6.3.1. Power Transfer Efficiency 174
6.4. Electromagnetics 178
6.4.1. Electromagnetic Properties 178
6.4.2. Electromagnetic Fields in Living Tissue 179
6.4.3. The Dielectric Effect 180
6.4.4. Reflections 182
6.5. UWB Antenna Design 183
6.5.1. Specifications 184
6.5.2. Material Properties 186
6.5.3. Archimedean Spiral 190
6.5.4. Equiangular Spiral 190
6.5.5. Simulation Results 191
6.5.6. Fabrication 193
6.5.7. Antenna Testing 195
6.6. Summary 196
CHAPTER 7. CONCLUSIONS AND SUGGESTIONS FOR FUTURE WORK 197
7.1. Thesis Contributions 198
7.2. Suggestions for Future Research 199
BIBLIOGRAPHY 202

LIST OF FIGURES

Figure 1.1. Fluid production and flow within the eye [11]. 3

Figure 1.2. Cross-section of human eye [11]. 6

Figure 1.3. The SENSIMED Triggerfish uses a contact lens to measure intraocular pressure [22]. The external power patch is not shown. 8

Figure 1.4. The Fraunhofer intraocular microsystem, consisting of a replacement intraocular lens containing a pressure sensor and associated circuitry. The device is externally powered using an inductive link with coils embedded in the eyeglasses [25]..9

Figure 1.5. An implanted parylene pressure sensor utilizing passive components in the eye of a rabbit [24]. 10

Figure 1.6. The Purdue implantable microsystem proposed for measuring intraocular pressure [26]. 11

Figure 1.7. Illustration of the implantable microsystem, with an external wireless wand placed against the closed eyelid of the patient during data transfer. 14

Figure 1.8. A cross-section of the proposed intraocular microsystem. The outer Parylene encapsulation layer is not shown. 15

Figure 1.9. The pressure sensor module with embedded cavity and vertical interconnects. 16

Figure 1.10. The battery module with deep cavity for ASIC and vertical interconnects for power and pass-through to pressure sensor module. 17

Figure 1.11. The antenna module with metal vertical interconnects. 18

Figure 2.1. Vertically-stacked compact microsystem enabled by vertical interconnects..21

Figure 2.2. Optical photograph of a 100 µm diameter hole in 100 µm thick glass drilled using femtosecond laser ablation in 1 minute. 24

Figure 2.3. SEM image of the laser-drilled hole in glass photographed in Figure 2.2......25

Figure 2.4. Photograph of a completed 250 µm thick 100 mm diameter silicon-in-glass wafer. 27

Figure 2.5. Magnified photo of glass-in-silicon wafer showing square posts in the corner of each glass die. The 1 mm x 1 mm die contains 50 µm posts while the largest 4 mm x 4 mm die contain 250 µm posts. 27

Figure 2.6. Process flow for glass-in-silicon, including double-sided metallization. 29

Figure 2.7. Borofloat viscosity versus temperature [34]. 30

Figure 2.8. Wafer for testing feedthrough resistance. 31
Figure 2.9. Cross-section illustration of test devices in Figure 2.8 showing the expected electrical path with probes. 31
Figure 2.10. Glass-in-silicon process flow modified for cavity formation. 32
Figure 2.11. Glass-in-silicon process flow modified for electroplating metal feedthroughs. 33
Figure 2.12. SEM image after silicon feedthrough etching (removal) in XeF2. 34
Figure 2.13. Bottom of the via showing gold after a short electroplating experiment, resulting in no voids. 34
Figure 2.14. Apparatus for anodic bonding with a glass-in-silicon wafer. 35
Figure 2.15. Photograph demonstrating incomplete corner filling, before planarization..37
Figure 2.16. Glass-in-silicon wafer showing inadequate filling, after planarization but before polishing 37
Figure 2.17. Silicon-glass interface side-profile; glass is lighter colored, silicon is dark. 38
Figure 2.18. Top view of square silicon post showing buildup with high carbon-content39
Figure 2.19. Planarized and polished silicon-in-glass wafer with embedded titanium. The ‘cracks’ are not in the glass but titanium and due to the intrinsic stress of deposited titanium. 41
Figure 2.20. (Top) Wafer bow before planarization; (bottom) flat and thinned wafer after planarization 42
Figure 2.21. SEM image of Cr/Au pad over a cylindrical vertical 50 µm diameter silicon feedthrough. 44
Figure 2.22. Photograph of a packaged and diced resonator sealed with a glass-in-silicon wafer. Silicon feedthroughs are embedded within the glass [40]. 45
Figure 2.23. Plot of multiple temperature sweeps indicating hermeticity. The change in quality factor of the resonator for each successive sweep is within ±9% [40]......46
Figure 2.24. Cross-section schematic of the full microsystem. 47
Figure 2.25. Isometric view of the IC cavity in the microbattery module; antenna connections not shown. 47
Figure 2.26. Reverse isometric illustration of the sensor; antenna connections not shown. 47
Figure 2.27. Photograph of a mockup of an intraocular microsystem with a custom ASIC (Chapter 5). 48
Figure 2.28. Side-profile of human eye [43]; red box indicates proposed implant location 52
Figure 2.29. Illustration of the physical dimensions of the integrated intraocular pressure sensor. 52

Figure 2.30. Several haptic designs, some fabricated and currently undergoing testing (top) and others for future implantation studies (bottom). 53

Figure 2.31. Cross-section illustration of implanted device demonstrating how the iris folds over the haptics of the implanted device. 54

Figure 2.32. A blank device with haptics is lowered near the surface of a human cadaver eye. Note the cloudiness of the cornea, making it difficult to see within the eye. 54

Figure 2.33. Glass substrate with haptics implanted into the surface of the iris, after cornea has been removed..55

Figure 3.1. (Top) Gap-sensitive diaphragm cross-section; (Bottom) Area-sensitive diaphragm cross-section. 61

Figure 3.2. Cross-section profile view of diaphragm at two different pressures: (Top) low pressure environment with diaphragm in contact with bottom substrate; (Bottom) high pressure environment. 62

Figure 3.3. (Left) Normal area-sensitive electrode shown in blue rectangle with green oval depicting diaphragm contact area; (Right) Modified area-sensitive electrode, reducing base capacitance. 63

Figure 3.4. (Left) Short circuit path through vertical interconnects embedded in the glass-in-silicon wafer, placed between bond tool and silicon wafer. (Right) Thick aluminum metal layer, in blue, prevents short. 65

Figure 3.5. Stress plot over increasing pressure along x-dimension of short side of diaphragm. 73

Figure 3.6. Stress across bottom surface of the diaphragm. The dark blue regions indicate zero or low stress, evident in the corners. Maximum stress (red) occurs on the short side of the diaphragm. 73

Figure 3.7. Total deflection for an applied pressure of 900 mmHg for a cut-plane along the center of the diaphragm (y-coordinate = 825 μm)...74

Figure 3.8. 3D plot of diaphragm deflection. 74

Figure 3.9. Stress of diaphragm without intrinsic stress included in the material properties. Note the increased maximum stress as compared to Figure 3.5..........75

Figure 3.10. Comparison plot showing deflection of diaphragm with zero intrinsic stress and with 40 MPa intrinsic stress at the same applied pressure, resulting in reduced contact area. 75

Figure 3.11. Simulated capacitance for a range of pressures without intrinsic stress. 77

Figure 3.12. Effect of intrinsic stress on capacitance. The touch-down point, or the pressure at which touch-mode begins, shifts to much higher pressures. 77

Figure 3.13. Layout of one pressure sensor...78

Figure 3.14. Selected layers shown in the layout of Figure 3.13 79

Figure 3.15. Full wafer layout 79

Figure 3.16. Pressure sensor process flow. Fabrication steps and masks outlined in Table 3.3. 81

Figure 3.17. Four pressure sensors fabricated with the silicon-in-glass process. Two sensors in the center show the deflected diaphragm and two sensors on the left and right show the backside of the sensor. 83

Figure 3.18. SEM image showing the side profile of the pressure sensor. 83

Figure 3.19. Magnified side-view profile of the embedded glass haptics. 84

Figure 3.20. Pressure sweep for a single pressure sensor. The three distinct modes of operation are present: (I) large-gap, (II) gap-sensitive, (III) area-sensitive 85

Figure 3.21. Pressure sweep plot magnified around ambient pressure point clearly showing hysteresis. 86

Figure 3.22. Plot of capacitance difference between successively measured data during an increasing pressure sweep minus decreasing pressure sweep. 86

Figure 3.23. Pressure sweep plot as measured by Mini-Convectron. 87

Figure 3.24. Plot of voltage difference between increasing pressure and decreasing pressure sweeps in the test chamber, measured with Mini-Convectron. 88

Figure 3.25. Difference between sequential steps of pressure change. 89

Figure 3.26. SEM image used for measuring diaphragm thickness by comparing thin silicon doping with thick silicon doping regions, such as the rim of the sensor. ..90

Figure 3.27. Olympus scanning confocal laser for touch-mode pressure sensor 91

Figure 4.1. Proposed process flow for the microbattery with vertical interconnect and fill ports. 96

Figure 4.2. Top view of the microbattery with vertical interconnects and electrolyte fill ports. 98

Figure 4.3. Typical battery discharge curves for the same mass and discharge rate [77] .99

Figure 4.4. Typical battery discharge curves for same-sized batteries (11.6 mm diameter x 5.4 mm) [78] 99

Figure 4.5. Energy density map for small batteries [76]. 100

Figure 4.6. Au-Zn phase diagram [92] 108

Figure 4.7. Fabricated microbattery test run. The two gold pads provide connection to the electrodes. 108

Figure 4.8. XPS analysis of as-deposited reactively sputtered silver oxide. 110

Figure 4.9. Binding energy of 3d orbital of Ag of as-deposited reactively sputtered silver oxide. 110

Figure 4.10. Auger peaks after annealing; (a) is no annealing, (f) is above 400° C [93] 111

Figure 4.11. Test setup configuration for flooded-cell experiments 112

Figure 4.12. Plot of silver-zinc battery voltage with a fixed 1 kΩ load. 113
Figure 4.13. Flooded-cell test showing flat power supply of almost 100 nW................114
Figure 4.14. Flooded-cell test with 100 Ω and voltage fluctuations due to the current draw. 114
Figure 4.15. A solar cell constructed of three diode-connected NPN transistors in series. 121
Figure 4.16. Cross-section of three photodiodes (vertical NPNs) connected in series. The orange region is the n-well, with the brown regions identifying the p-well located within the n-well. 122
Figure 4.17. Circuit model of diodes in the triple-stack solar cell structure. Blue diodes are the desired photodiodes while red photodiodes are parasitic. NPN parasitic transistors are also formed between closely-spaced deep n-well regions. 123
Figure 4.18. Layout of modified NPN transistor, occupying about 24 μm x 24 μm. 124
Figure 4.19. Mapping of layers as used in the solar cell of Figure 4.18 and Figure 4.20. 124
Figure 4.20. Layout of a 9 x 9 solar cell array, consisting of 27 total solar cells in parallel. The array measures 222 μm x 225 μm. 125
Figure 4.21. Plot of simulated voltages generated through the solar cell stack at different photocurrents. Note that all currents plateau and the lower the photocurrent, the slower to buildup the voltage. 126
Figure 4.22. Output of full solar cell array showing both short circuit current and open circuit voltage. 126
Figure 4.23. I-V characteristic of full photodiode array. 127
Figure 4.24. An electrostatic energy generation circuit demonstrating function at each stage of an energy generating cycle. 130
Figure 4.25. Electrostatic energy harvesting circuitry. 131
Figure 4.26. Plot of the output voltage over a period of 15 minutes. The electrostatic generator charges from 0 V to 0.7 V. The total energy stored is 245 nJ. 132
Figure 5.1. Overall block diagram of fabricated integrated circuit. 137
Figure 5.2. Power sub-circuit showing how the internal voltage supply is maintained during non-idle modes. When ENABLE goes high, the circuit charges Cstorage slowly to Vdd. Cstorage allows the local circuitry on Vinternal to dissipate current quickly. 139
Figure 5.3. Plot of current draw through the pulse generator circuit for both idle and non-idle states. The two peaks during the non-idle state indicate a pulse transmission. 140
Figure 5.4. Plot of current draw through the pulse generator circuit for both idle and non-idle states, but with power gating as described in this section. 141

Figure 5.5. Plot of current draw when ENABLE signal is high and all blocks are powered. 141
Figure 5.6. Plot of current draw when the ENABLE signal is low and most blocks are powered off....142
Figure 5.7. Optical trigger block diagram – an optical light source generates a photocurrent in the photo-diode, triggering the Schmitt trigger after passing through a high-pass filter....143
Figure 5.8. Cross-section of the photodiode, showing a parasitic photodiode. This diode does not function since the n-well and substrate are held at the same potential. 144
Figure 5.9. Circuit implementation of the optical trigger, showing the high-pass filter and Schmitt trigger....144
Figure 5.10. Photodiode and high-pass filter AC response as used in the optical trigger, showing a bandpass filter effect effectively passing signals between 32 kHz and 845 MHz....146
Figure 5.11. Simulation plot of optical trigger circuit showing operation with different optical pulse fre-quencies. Only signals above 100 kHz effectively generated a digital pulse. 146
Figure 5.12. Layout of the optical trigger circuit, showing that the majority of the 110 µm x 53 µm dimen-sions are reserved for the passive components (prior to the 40 µm marker). Active circuitry appears lower-left of center while the photodiode appears on the left side and appears as an orange square....147
Figure 5.13. Circuit diagram of the ring oscillator with dedicated ENABLE and LOAD inputs used to turn off the oscillator during idle mode and for checking various capacitive loads. 148
Figure 5.14. Layout of the ring oscillator, showing 12 transistors in a total area of 13 µm x 26 µm....149
Figure 5.15. Simulated ring oscillator frequency output with varying load capacitances. 150
Figure 5.16. Ring oscillator output over various process corners with 1 pF (less than 2 ms), 2.5 pF (2 ms to 4 ms), and 5 pF (greater than 4 ms) load capacitances. 150
Figure 5.17. Schematic of the pulse generator. The input pulse is buffered, split, and buffered again before driving two different halves of the differential antenna...152
Figure 5.18. Various waveforms at the output of the driver stage for different load capacitances. Note the variety in pulse shapes....153
Figure 5.19. Layout of the pulse generator. The bulk of this block consists of the internal capacitor - only the lower-left corner is active circuitry with the rest of the area dedicated to MOS and MIM capacitance. 153
Figure 5.20. The overall circuit layout, measuring 258 µm x 158 µm. The top-right corner contains the optical trigger, the top-left corner is the built-in reference capacitor

array, and the left-side is mostly digital logic for the counters and ring oscillator while the bottom-right is the pulse generator and its internal storage capacitor. 154

Figure 5.21. Die-level photograph of the 1.4 mm x 0.9 mm test chip. Only the center area is active; in future versions, unused die area will be dedicated to a solar array. . 154

Figure 5.22. Ring oscillator startup (top), entering State 1 after optical trigger (bottom). 156

Figure 5.23. Ring oscillator power-down on receipt of an optical trigger signal. 156

Figure 5.24. Ring oscillator switching between two different capacitive loads, from a larger capacitance (State 2) to a smaller capacitance (State 1), after optical triggering. 156

Figure 5.25. Plot of capacitance-to-frequency conversion using a test bench setup. Zero pF represents open-circuit connection; this is result of just parasitic capacitance applied at the input node. 157

Figure 5.26. Estimated capacitance-to-frequency conversion using two on-chip references of 1 pF and 5 pF. 158

Figure 5.27. Data showing four different ASIC chips tested at various power supply voltages. 160

Figure 6.1. FCC emission mask for ultrawideband devices [143] 171

Figure 6.2. Transfer efficiency in near-field and far-field; note far-field cut-off (Friis transmission validity) 175

Figure 6.3. Near-field power transfer efficiency for various internal coil radii and fixed range of 10 mm 176

Figure 6.4. Simplifying reflection between multiple layers of medium with different electromagnetic properties 183

Figure 6.5. Permittivity of saline 188

Figure 6.6. Loss tangent of saline 188

Figure 6.7. Permittivity of the cornea 189

Figure 6.8. Loss tangent of the cornea 189

Figure 6.9. Screenshot of an Archimedean antenna in HFSS on thin glass substrate with copper feedthroughs. 192

Figure 6.10. Screenshot from an HFSS simulation showing two identical antennas placed 10 mm apart used to determine transmission parameters (s12). 192

Figure 6.11. S11 reflection parameters for the Archimedean antenna in saline with variations in geometric parameters such as line width. 193

Figure 6.12. Transducer power gain between two Archimedean antennas in saline with variations in geo-metric parameters such as line width. 193

Figure 6.13. Layout of four different antennas on a glass substrate. The red metal lines provide a redistribution layer allowing the ASIC to connect to the antenna with vertical interconnects. 194

Figure 6.14. Process flow for the antenna module. 195

LIST OF TABLES

Table 1.1. Overview of various intraocular pressure sensing systems. 8

Table 2.1. Glass-in-silicon process overview with defined masks. 28

Table 2.2. Differences between silicon and borosilicate glass. 44

Table 3.1. Material properties as used in simulation [47] 72

Table 3.2. Simulation results for specific height, width, and thickness 74

Table 3.3. Pressure sensor process flow overview. 81

Table 4.1. A sampling of published microbatteries. 95

Table 5.1. Table of capacitance-to-frequency conversion for same supply voltage used in Figure 5.25. 158

Table 5.2. Current consumption of the ASIC during various states while at a supply voltage of 800 mV. For comparison, the simulated current draw from the local storage capacitor is included. 159

Table 6.1. Substrate material properties at a temperature of 300 K. 187

ABSTRACT

An Implantable Microsystem for Autonomous Intraocular Pressure Monitoring

by

Razi-ul Muhammad Haque

Chair: Kensall D. Wise

Glaucoma, a leading cause of blindness worldwide, is a disease in which the pressure within the eye is too high for the eye to tolerate and must be reduced in order to slow or prevent damage to the optic nerve. Conventional methods for monitoring eye pressure are normally only used in the physician's office and rely on indirect measurement methods, leading to inaccuracies. Furthermore, intraocular pressure can vary throughout the day and also depends on activity. An autonomous implantable microsystem capable of monitoring intraocular pressure with minimal patient intervention would provide useful information to the clinician in the management of glaucoma.

This dissertation studies the feasibility of an integrated microsystem for autonomously measuring intraocular pressure. Small size ensures minimal impact on the patient, preventing the device from entering the field of view and simplifying implantation. Integrated haptics aid surgical implantation and minimize trauma while allowing the implant to be removed if needed. A touch-mode capacitive pressure sensor, fabricated using the dissolved wafer process, transduces intraocular pressure into capacitance with a linear response and a sensitivity of 26 fF/mmHg. A new fabrication technique has been developed to embed vertical interconnects within a glass package

containing the pressure sensor, a microbattery, readout circuitry, and an antenna. This enables the vertical stacking of these components and very efficient use of limited volume. The 1.5 mm x 2 mm x 0.5 mm transparent parylene-coated glass package enables solar cells to be placed on the circuit chip for power generation, trickle charging an on-board microbattery formed using standard cleanroom materials and a non-toxic electrolyte. Flooded-cell tests verified the electrochemistry and achieved a current capacity of 8 $\mu Ah/mm^2$. A simple integrated readout circuit consuming 35 pW in the idle mode implemented a finite-state machine and used an optical wakeup trigger to further reduce power. The microsystem has also been demonstrated with a microprocessor to autonomously gather and store data, reading it out on demand. Finally, a pulse-based ultrawideband wireless transmission technique is proposed using non-resonant antennas. The all-digital transmitter is expected to consume much less power than conventional encoded wireless transmitters and eliminates complex circuitry.

CHAPTER 1

INTRODUCTION

Glaucoma is the second leading cause of blindness in the world today, affecting an estimated 60 million people worldwide, and is expected to grow to almost 80 million by the year 2020 [1]. Approximately 120,000 people out of the estimated 3 million Americans with glaucoma are now blind from the disease [2]. Glaucoma damages the optic nerve and cannot be reversed. The disease can be detected by visually inspecting the optic nerve during an eye exam and by administering a visual field test. Currently, reducing intraocular pressure (IOP) is the only proven method for treating glaucoma [3]. Normal intraocular pressure is considered to be within the range of 10 to 21 mmHg [4]; however, while elevated intraocular pressure is a risk factor for glaucoma, patients with normal intraocular pressures may also develop this disease.

During a typical eye exam, a non-invasive procedure called tonometry is used to measure intraocular pressure [5]. In this method, the deflection of the cornea due to a known amount of applied force (e.g., a puff of air) is used to infer the intraocular pressure. This indirect method assumes an average thickness, rigidity, and curvature of the cornea even though these parameters vary among patients.

There are several methods of treating glaucoma, and all are linked to reducing intraocular pressure [4]. Eye drops either reduce intraocular fluid (aqueous humor) production or improve its drainage [4]. More invasive treatments such as laser surgery or incisional procedures of various types can increase outflow and are viable options when medication is not sufficient [6].

The autonomous implantable intraocular microsystem presented in this thesis addresses several challenges with current solutions, introducing a continuous monitoring paradigm that works without patient intervention and during normal patient activity. This chapter begins with an overview of glaucoma, linking it to the physiology of the eye. Various intraocular pressure measurement techniques and their shortcomings are

presented, followed by a discussion of the ideal wireless intraocular pressure monitoring microsystem and its various components. The rest of this thesis explores in detail the requisite modules necessary to construct this microsystem.

1.1. Motivation

Blindness due to glaucoma can be prevented in most cases with early identification and managed appropriately. The most common forms of glaucoma produce no symptoms in their early stages and can only be detected during an eye exam. It is important to note that patients with normal intraocular pressures may also develop glaucoma so it is critical for all patients to obtain an accurate assessment of the optic disc. One of the earliest indications of glaucoma is the loss of peripheral vision as the disease progresses. Without appropriate treatment and follow-up to monitor intraocular pressure and evaluate the optic disc and visual field, glaucoma can result in major visual loss, ultimately leading to blindness. The cause of glaucoma is unknown, however underlying diseases such as diabetes increases the likelihood of its occurrence. The work here focuses on providing a tool to aid clinicians in monitoring intraocular pressure during the treatment of glaucoma. The device can also be used as a means for research investigating models of glaucoma.

The inability to track intraocular pressure levels over long periods of time [7], [8] and during various activities [9] has proved challenging for ophthalmologists. Additionally, the effects of secondary factors such as blood pressure and ambient pressure conditions have not been fully understood [10]. Unfortunately, none of these parameters are measureable within the controlled environment and limited duration of a typical visit to an ophthalmologist's office [2]. Furthermore, Goldmann applanation, the primary method of tonometry, has been criticized as an inaccurate measure of eye pressure. Its resolution sometimes exceeds 1 mmHg, the result of several sources of mathematical error and patient-to-patient variability [5]. Still other more error-prone methods such as through-eyelid measurements for patient in-home monitoring provide even less accurate data.

An implantable continuous-monitoring solution would address these shortcomings. The accuracy of the pressure data would improve because the

measurement is direct and from within the eye. Regardless of activity or the time of day, pressure readings would be automatically recorded, without the intervention of the patient or clinician. Information on patient compliance and drug efficacy are two additional outcomes useful for physicians treating patients with glaucoma. In the future, the data generated by patients undergoing continuous pressure monitoring could also help to evaluate new treatments, provide a better understanding of the disease and how it progresses, and possibly identify additional risk factors for developing glaucoma.

1.1.1. Background

Intraocular pressure is currently the only known controllable factor contributing to glaucoma. The cause of increased intraocular pressure is unknown, but the mechanics of how pressure is controlled within the eye is better understood. Fluid, called aqueous humor, is constantly produced behind the iris by the ciliary body to provide nourishment for the structures in the anterior portion of the eye. A corresponding drainage mechanism is also present in the eye, called the trabecular meshwork, to eliminate waste. Figure 1.1 provides an overview of fluid production in the eye.

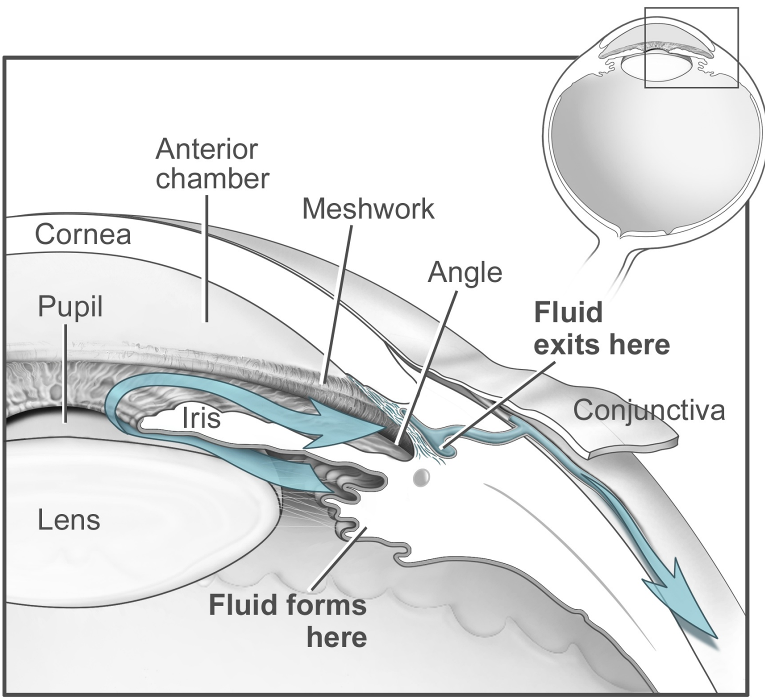

Figure 1.1. Fluid production and flow within the eye [11].

Elevated pressure within the eye can be caused by overproduction of fluid, a blockage at the drain, or a combination of both. Medication and surgical treatments target both the production of the fluid as well as improving drainage. Every visit to the eye doctor typically includes an intraocular pressure measurement to ensure that the intraocular pressure is within a safe range for that particular patient. Furthermore, as part of a complete eye examination, the physician will also look at the optic disc through a special lens, looking for signs of optic nerve damage. Even though intraocular pressure may not be elevated, the optic nerve may show signs of glaucomatous damage. The physician also evaluates the visual field to determine whether damage has occurred. If so, treatment is initiated to reduce the intraocular pressure.

1.1.2. Conventional Measurement Methods

In addition to Goldmann applanation tonometry, there are several other indirect methods for measuring intraocular pressure, such as non-contact tonometry and indentation tonometry. Goldmann applanation tonometry operates on the principle of applying a force to flatten a fixed area of the cornea. Non-contact tonometry generates a puff of air with increasing pressure until the cornea flattens, while indentation tonometry uses a plunger to push in on the cornea. All of these methods assume an average corneal rigidity because this is a parameter that is impossible to measure in live patients [2]. Corneal thickness can be measured using ultrasound and has been used to further analyze errors in conventional tonometry [11]. For patients who have already undergone corneal surgery, an intraocular device may be the only way to accurately measure intraocular pressure [13]. A newer technique called dynamic contour tonometry avoids flattening the cornea and instead attempts to match the curvature of the cornea. This method relies on an average corneal curvature instead of thickness, but this also varies among patients.

1.1.3. Atmospheric Pressure

An important issue for measuring intraocular pressure is understanding how atmospheric pressure affects the eye and whether or not the body compensates for such changes. Typically, tonometric methods do not take into account the atmospheric pressure when calculating intraocular pressure. However, since the eye is

incompressible, when the external atmospheric pressure drops, the force exerted by the fluid in the eye increases because the balance between the atmosphere and the internal fluids of the eye has been disrupted. Several studies have shown that intraocular pressure does in fact change with sudden changes in atmospheric pressure. Over time, the eye compensates and the intraocular pressure returns to the expected normal values. In cases where the body is in a pressurized environment, such as in undersea diving, intraocular pressure is reported to have decreased slightly [10]. Similarly, in cases where the body is at high altitude, such as in mountain climbing, intraocular pressure increases [15]. Interestingly, a dynamic corneal thickness variation was also reported [15], indicating a physical change in the eye that may result in additional error for the techniques that assume an average corneal thickness. Other effects in the eye due to changes in altitude, such as reduced availability of oxygen, may also have an impact on the physiology of the eye, affecting the intraocular pressure. Indirect measurement techniques will suffer inaccuracies for this reason, whereas a direct continuous measurement will track pressure changes as the atmospheric pressure changes.

1.1.4. Intraocular Pressure Variations

Changes in blood pressure have also been directly linked to intraocular pressure [16], [17]. Studies during exercise, which can affect blood pressure, have also been carried out [9]. Furthermore, it has been demonstrated that peak intraocular pressure may not occur during the hours of a typical workday [8]. This is significant because it suggests that intraocular pressure is not at its highest point during a typical office visit and therefore would not be observed by the physician. Even non-physiological effects, such as “white-coat syndrome”, when a patient’s blood pressure rises inadvertently in clinics and hospitals, may also have an impact on the measured intraocular pressure [3].

Another source of measurement error is the inherent pulsatile flow from the beating heart, which can lead to 1 mmHg variations in intraocular pressure in the resting state [18]. Importantly, it is also believed that the ocular pulse amplitude may play a role in glaucoma as well [19]. A measurement device that can actively record pressure variations over a period of seconds, sampling at a rate quick enough to capture the pulse amplitude, may provide useful new diagnostic data for ophthalmologists.

1.1.5. Measurement Challenges

The eye is a small and delicate fluid-filled organ, limiting practical implant locations, dimensions, and potential form factors. A labeled cross-section of the human eye appears in Figure 1.2. Of note is the retina, the light-sensitive tissue, and the iris, a muscle that controls the amount of light that enters the eye. Light passes through the cornea, iris, and lens where it is focused on the retina, forming an image.

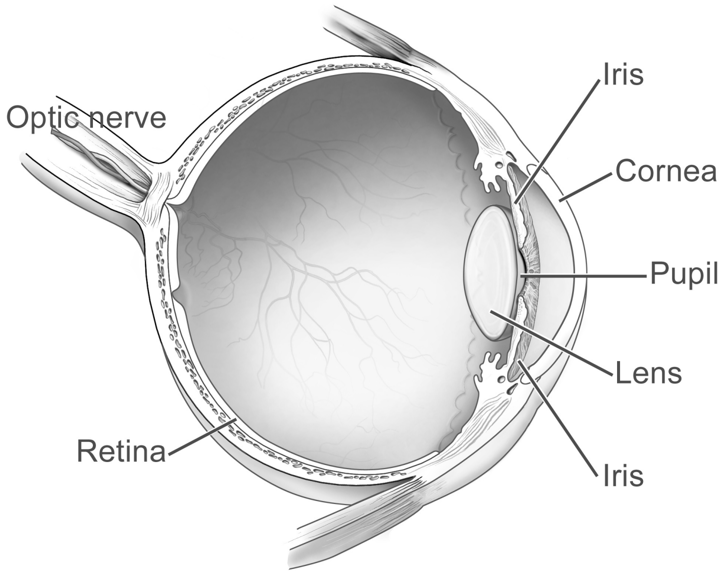

Figure 1.2. Cross-section of human eye [11].

The surface of the iris is a suitable implant site due to its relatively easy accessibility, short wireless communication distance, and access to ambient light for solar energy harvesting. The iris, the colored region of the eye, is an elastic sphincter muscle controlling the amount of light that passes to the back of the eye via the pupil. Two challenges are to avoid obstructing the field of view, even when the eye is fully dilated (such as in a dark environment), and to maintain a safe distance from the cornea. If the endothelial cells of the cornea are damaged from contact with an implant, they can react negatively, causing swelling of the cornea and loss of vision [14]. Other implant locations have been used before, but for the majority of ophthalmologic implants, such as certain intraocular lenses, the iris has been used successfully for many years.

1.2. PAST WORK

In 1967, an intraocular pressure sensor based on an inductive wireless technique was designed and fabricated [20]. Since then, various types of intraocular pressure monitoring devices have been developed. Very few have been commercialized, most likely due to the inability to remove, or explant, the devices [2]. Recently, several commercial entities and research groups have proposed solutions addressing the problem of continuous intraocular pressure recording.

Table 1.1 provides a brief overview of a select few of these approaches. The implant location varies, with both the Caltech and the Michigan (this work) intraocular implants targeting the iris. The majority of the devices provide continuous-type measurements, defined as a microsystem that can record intraocular pressure without patient intervention over an extended period of time. This requires a solution for powering the device, either by an external means or with an internal power source. The Purdue work and the Michigan device have an on-board power supply, the former in the form of a capacitor array and the latter with an on-board microbattery. Programmability allows for adjusting the functionality of the system after implantation, perhaps increasing the monitoring interval, manipulating the stored data, or adjusting the calibration of the sensor. The physical dimensions and shape of reported implants vary considerably, ranging from a 3 mm x 30 mm device built on a flexible substrate by Purdue to the minimally-invasive 2 mm x 1.5 mm device targeted in the Michigan work. However, only two devices are designed to be removable: the Triggerfish, which is non-invasive, and the Michigan implant, which while removable, would require a surgical explantation procedure. Finally, the last category for comparison is whether the measurement capability of the system is direct or indirect. All the invasive devices measure intraocular pressure directly because they are in direct contact with the aqueous humor, whereas the Triggerfish provides only an indirect measurement and relies on approximated physiological parameters that are presumed to stay constant over the monitoring period, e.g., corneal rigidity or thickness.

	SENSIMED [21]	Fraunhofer [22]	Caltech [24]	Purdue [26]	Michigan
Location	Non-invasive	Intraocular Lens	Iris	Anterior Chamber	Iris
Interval	24-hr Continuous	Awake	Patient-Initiated	Continuous	Continuous
Power Source	External (inductive)	External (inductive)	External (resonator)	Internal/External (RF)	Internal/External (optical/RF)
Programmable	No	Yes	No	No	Yes
Dimensions	14 mm diameter	2.6 mm x 2.6 mm	4 mm diameter	3 mm x 30 mm	2 mm x 1.2 mm
Removable	Yes	No	No	No	Yes
Measurement	Indirect	Direct	Direct	Direct	Direct

Table 1.1. Overview of various intraocular pressure sensing systems.

1.2.1. Contact Lens Devices

SENSIMED, a company located in Switzerland, has commercialized a non-invasive intraocular pressure measurement system called the Triggerfish. The product, currently unavailable for use in the United States, is based on contact lenses with embedded strain gauges [21]. Over a period of 24 hours, the contact lens records intraocular pressure by monitoring the change in the circumference of the cornea every 5 minutes. An external patch that must be worn during the entire monitoring period surrounds the eye and provides a power source.

The major benefits of this system are the lack of any required patient intervention for measurements and the non-invasive nature of the device. Potential drawbacks include artifacts due to mechanical motion, blinking, and variations in the corneal radius of curvature [3]. Furthermore, the Triggerfish contact lens is a single-use device and can only be used for a maximum of 24 hours. Figure 1.3 shows the contact lens in use but without the external patch to provide power, which is required for it to function.

Figure 1.3. The SENSIMED Triggerfish uses a contact lens to measure intraocular pressure [22]. The external power patch is not shown.

1.2.2. Replacement Intraocular Lens Devices

Intraocular pressure sensors coupling externally-supplied power over an inductive link have been developed at the Fraunhofer Institute [23], [25]. Data is transferred using the power transfer link by modulating the load on the external circuit. The dual-use coil is incorporated into a pair of eyeglasses as an inductive coil.

The drawback of this solution is that the power source must be applied at all times in order for the system to function. This approach also does not capture data during sleep. Another important challenge is that the internal device is implanted as part of a lens implant surgical procedure. For patients with healthy lenses, this is a major disadvantage but for those undergoing cataract surgery where the lens is replaced, this type of device may be a viable option. Figure 1.4 shows a cross-section of this system, including the coil used for communication and power embedded within the frame of eyeglasses, which must be worn at all times while pressure data is being collected.

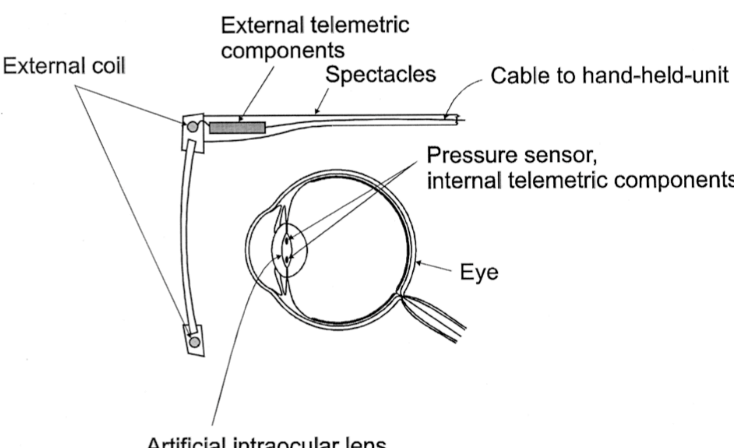

Figure 1.4. The Fraunhofer intraocular microsystem, consisting of a replacement intraocular lens containing a pressure sensor and associated circuitry. The device is externally powered using an inductive link with coils embedded in the eyeglasses [25].

1.2.3. Passive Intraocular Monitoring Devices

Much of the most recent work in intraocular pressure sensing microsystems is based on passive components. In these devices, eliminating the implanted integrated circuit reduces overall dimensions, simplifies production, and reduces costs. These implants implement a simple inductor-capacitor circuit, which resonates at a specific frequency. Either the capacitor or inductor changes its value in response to changes in

intraocular pressure, causing a shift in the resonant frequency and phase, detectable by an external antenna. The most recent work, from Caltech, is a parylene-based microsystem that utilizes such a mechanism [24]. The sensor is implanted in a minimally-invasive procedure by folding the sensor, inserting it into the eye, and then piercing the iris with a hook that serves as an anchor. The sensor then unfurls inside the eye. The size of this device is approximately 4 mm in diameter when unfurled, potentially entering the visual field when the pupil is fully dilated. Another major drawback here is the possible damage to the iris during implantation and the potential challenges associated with device removal if it becomes necessary. Figure 1.5 shows an implanted sensor in the eye of a rabbit. Due to the much smaller size of the coil as compared to the Fraunhofer design, the readout range is limited and requires the external coil to be placed within a few millimeters of the surface of the eye.

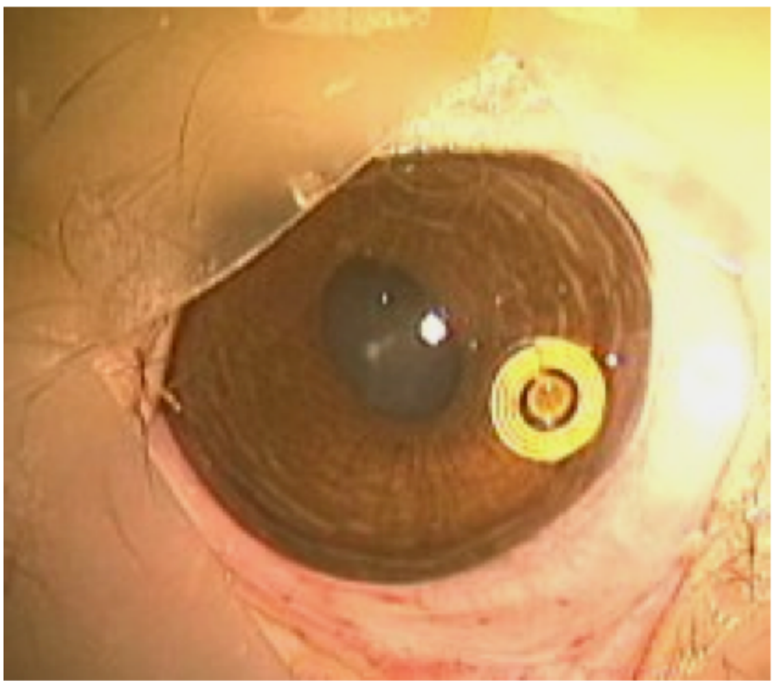

Figure 1.5. An implanted parylene pressure sensor utilizing passive components in the eye of a rabbit [24].

1.2.4. Low-Power RF Monitoring Devices

The most recent work was published by a research group at Purdue in 2010 and proposes a departure from the previous systems on several fronts [26]. First, and probably most interesting, is that the device harvests energy from an applied external radio frequency (RF) wave. To accomplish this, a 27 mm-long antenna is used, operating

at a frequency of 2.4 GHz. The advantages cited in the paper for using RF versus lower-frequency inductive solutions are the increased range and the decreased sensitivity to orientation between the receiver and transmitter. As shown in Figure 1.6, a commercial MEMS pressure sensor is placed alongside a custom ASIC with on-chip low-power FeRAM memory. This memory is also non-volatile, meaning that if power is completely lost, the contents of the memory are still preserved. Power is supplied via a 24 μF on-board capacitor array and is recharged through the externally applied 2.4 GHz carrier signal. It is expected to last for an entire 24-hour time period before requiring a recharge. The entire system is fabricated on a Liquid Crystal Polymer (LCP) substrate that provides flexibility and biocompatibility. The most critical drawback with this microsystem is the long antenna that may affect the field of view. The published work has also not proposed a detailed surgical technique for implantation within the eye and securing the antenna. Furthermore, the complete solution for the packaged microsystem is not clearly defined, although it may be assumed that an additional LCP coating will be necessary to protect the electronics.

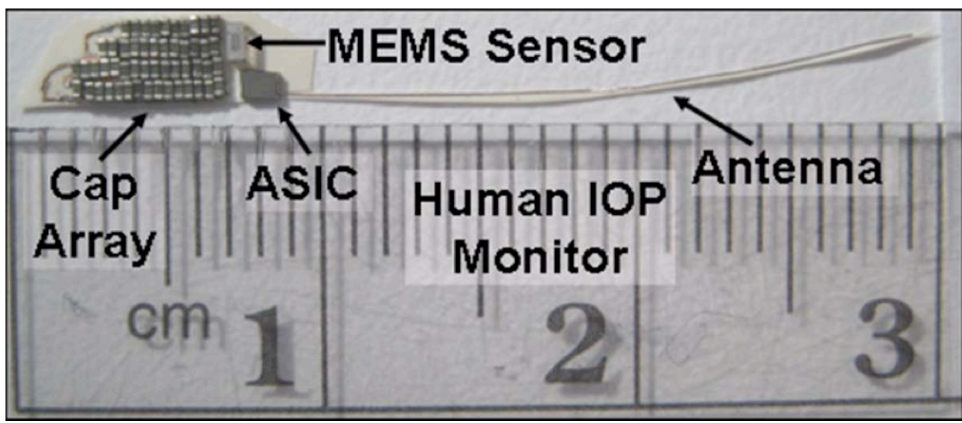

Figure 1.6. The Purdue implantable microsystem proposed for measuring intraocular pressure [26].

1.2.5. Ideal Intraocular Pressure Monitoring

The above discussion of previously published work has attempted to provide an overview of the current trends in intraocular pressure monitoring devices. In general, the shortcomings of these devices have prevented their practical use as accurate intraocular implants requiring little to no patient interaction. Primarily, the dimensions of these devices introduce surgical challenges that may increase patient discomfort and

complications from the implantation procedure. Secondly, the ability to remove the device should such a need arise is paramount to patient safety and must not result in irreversible damage. A concern for all of these devices is the implant package by which the device itself is protected from the corrosive environment within the body. Only the contact lens approach, which is non-invasive, avoids these issues, but it introduces concerns about accuracy and repeatability by relying on physiological parameters that indirectly yield intraocular pressure.

The ideal implantable intraocular pressure sensor, much of which has been addressed in this thesis, proposes solutions to the shortcomings of the reviewed techniques. Minimally-invasive surgery simplifies the surgical procedure and requires no sutures, allowing rapid recovery and reducing patient discomfort; all dimensions are therefore limited to 2 mm or less. The microsystem is packaged using hermetic seals to avoid device failure and provide excellent biocompatibility. A modular approach to constructing the microsystem aids fabrication and assembly, resulting in a practical device at reduced cost. The package maximizes the available volume by vertically-stacking the components. Circuitry and an on-board power source (e.g., a microbattery) are protected by the package; vertical feedthroughs provide electrical connections to the sensor and antenna. A method of energy scavenging, such as from solar power, could effectively extend the battery lifetime, resulting in a virtually infinite and energy autonomous implant. The on-board power source allows the microsystem to autonomously record pressure data and store it in memory, without patient intervention. A simple, external reader would gather the daily pressure readings on demand.

Specific details of the microsystem described here appear in the following sections and approximate the ideal intraocular implant. The primary purpose of this thesis is to demonstrate the feasibility of developing such a microsystem.

1.3. The Michigan Intraocular Microsystem Design

The work presented here focuses on an implantable microsystem designed to measure pressure continuously from within the eye. This approach circumvents potential errors in measuring pressure that affect indirect measurement techniques. Furthermore, the implantation procedure is designed to be relatively simple and quick, requiring a

single incision of at most 2 mm. Such an incision is classified as minimally-invasive because it eliminates the need for sutures, reducing recovery time and potential complications. Explantation, should it be necessary, is similarly simple and is made possible by the sutureless approach. In order to realize such a microsystem, there are two necessary requirements. The first is to miniaturize the device to achieve a highly integrated compact microsystem, and the second is to reduce power consumption as much as possible.

Miniaturization is an important focus for physiological and wireless communication, and power consumption is the driving force behind the design choices for each of the microsystem's modules. The antenna size typically determines the maximum device dimensions and determines the expected operating frequency. Dimensions also constrain the size of the various components that must be included in the microsystem, such as the accompanying pressure sensor, integrated circuit, and power source. The microsystem described here attempts to make the best tradeoffs in terms of power consumption and size while adhering to the performance requirements of the targeted application. It consists of a capacitive pressure sensor, an embedded integrated circuit for data acquisition and storage, a microbattery, an energy scavenging source, and a wireless interface including a driver circuit and antenna.

The intraocular system will record data at approximately 15-minute intervals, providing essentially continuous data due to the slowly-changing nature of intraocular pressure. In order to extract data from the implant, the patient is required to use an external reader in the form of a wand, placed on the surface of the closed eyelid. When initiated by the patient, data is transferred from the implant to the wand. The internal memory of the implant should allow the recording of intraocular pressure over the course of at least 24 hours. For example, just before bedtime, the patient can simply place the external wand on the closed eyelid to initiate data transfer, which will occur in a fraction of a second. From there, the data can be transferred to a computer or sent directly to the physician via a wireless data connection similar to that cell phones use. A typical pressure range for intraocular pressure is assumed to be 10 to 30 mmHg relative to atmospheric pressure.

In order to compensate for atmospheric pressure changes and to attain a true relative pressure measurement, an external atmospheric pressure sensor, incorporated into the wand, is necessary. This sensor will record atmospheric pressure data at the same time intervals as those used by the implantable microsystem. For the most accurate data, the external wand should be carried with the patient, especially during events such as during a flight. Figure 1.7 illustrates the wand with integrated ambient pressure sensor and implantable microsystem.

A power source is shown, indicating the portability of the wand. Of note is the flexible and soft substrate encasing the antenna and making direct contact with the eyelid. This simplifies patient use and reduces the amount of power required to transmit data to the external wand.

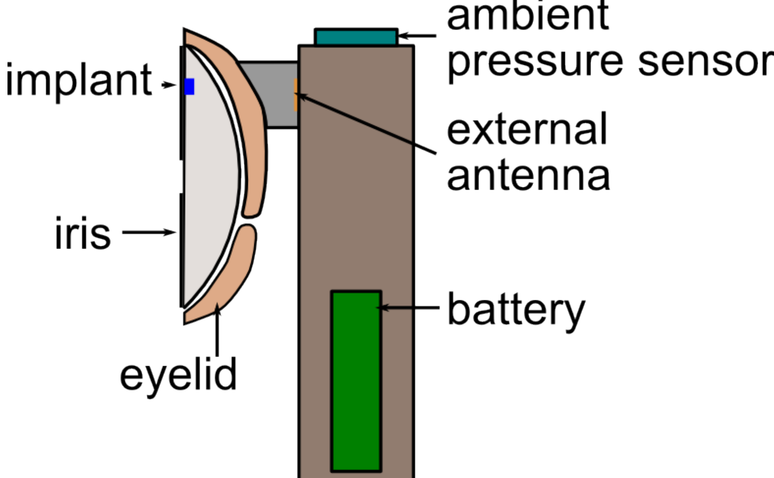

Figure 1.7. Illustration of the implantable microsystem, with an external wireless wand placed against the closed eyelid of the patient during data transfer.

The microsystem must be biocompatible, preventing any damage to the eye while simultaneously protecting the sensitive internal electronics from the corrosive intraocular environment. To that end, substrate materials and sealing components are of primary concern. Furthermore, the device must be held to the restrictions of governmental organizations (i.e., the Food and Drug Administration) to ensure safety during use.

Figure 1.8 shows the cross-section of the entire proposed microsystem. Three modules are vertically stacked: the pressure sensor, the battery with embedded Application Specific Integrated Circuit (ASIC), and the antenna. Vertical interconnects and cavities are incorporated within the glass substrates of the sensor and the antenna to

provide electrical connections to the ASIC. This modular structure allows testing at each step of the assembly process. Gold-gold pads provide electrical connections between the components while a biocompatible ultraviolet-curable adhesive holds the microsystem together. The following subsections describe each of the modules in further detail.

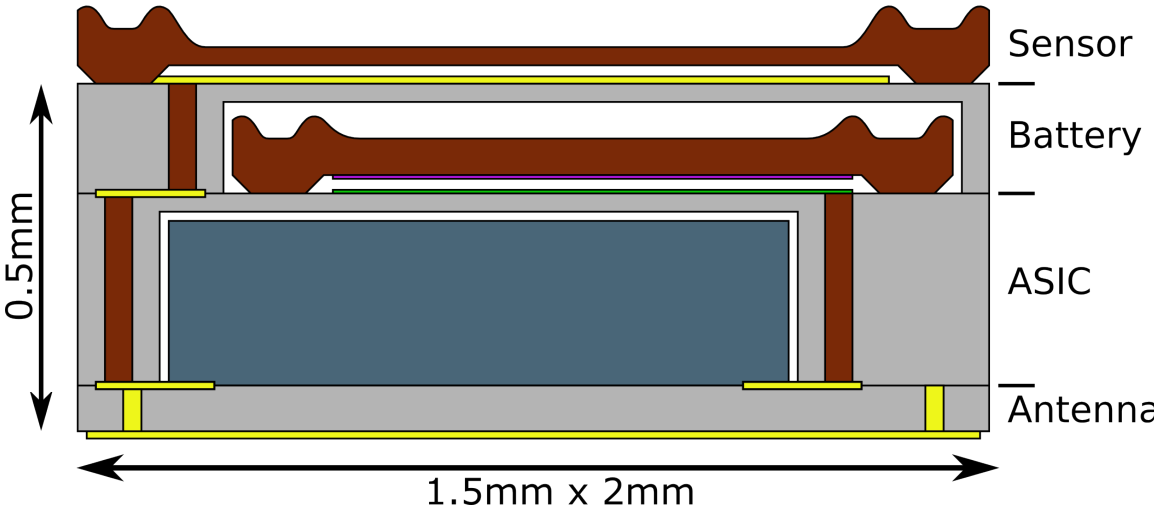

Figure 1.8. A cross-section of the proposed intraocular microsystem. The outer Parylene encapsulation layer is not shown.

1.3.1. The Pressure Sensor Module

The pressure sensor provides the means by which the implantable microsytem can determine intraocular pressure. Thus, it is important that it be designed for the specific application and environment within the eye. The design used here is based on decades-long work in the field of MEMS pressure sensors. The sensor consists of a thin silicon membrane that flexes with changes in applied pressure. Boron-doping is used to define the thickness of this diaphragm by providing an etch-stop during fabrication and to serve as an electrode. The sensor is a variable capacitor; as the silicon diaphragm flexes, the capacitance between the silicon diaphragm and a separate metal electrode on the glass changes. A glass substrate is used because it can provide an excellent hermetic seal when anodically bonded to the silicon. This is essential for capacitive pressure sensors because the gap between the two plates must be kept at vacuum and free of moisture for the life of the sensor. Figure 1.9 shows a cross-section of the pressure sensor with embedded cavity and vertical interconnects.

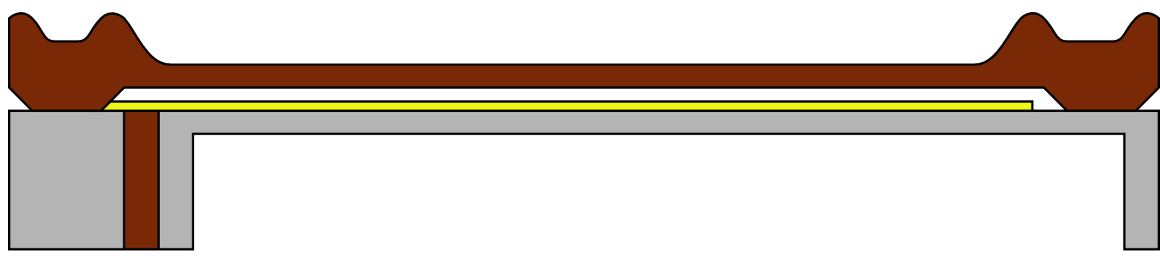

Figure 1.9. The pressure sensor module with embedded cavity and vertical interconnects.

A new fabrication method has been developed for this microsystem, called the glass-in-silicon reflow process. This process was used to form an absolute pressure sensor with embedded vertical interconnects that are protected from the environment of the eye. Only the outside of the package and the external surface of the sensor come into contact with the intraocular environment. Previous pressure sensors have primarily used lateral interconnects with wires passing through the pressure seal. This increases fabrication complexity and may also be a source of potential leaks.

The glass substrate on which the sensor is bonded also incorporates glass projections, or haptics, to provide a method of fixing the microsystem to the iris. This technique avoids sutures, simplifying the surgical procedure but also allowing the device to be easily explanted if the need arises.

1.3.2. The Microbattery Module

The microbattery is fabricated using a process similar to that of the pressure sensor with the addition of multiple metal depositions for the electrode materials. This module also includes the main cavity within which the application specific integrated circuit (ASIC) is placed. Vertical pass-through interconnects provide connections between the pressure sensor and the ASIC. A cross-section of this module appears in Figure 1.10 with the ASIC removed.

The ability to deposit the battery electrode materials in a standard cleanroom environment has been explored as a part of this work. A silver-zinc chemistry provides high instantaneous power, good charge capacity, and rechargeability. One interesting feature of this particular microbattery is the use of non-toxic saline for its electrolyte, avoiding the more corrosive and toxic substances typically used. The battery electrolyte introduces a new packaging challenge, limiting the maximum temperature the

microsystem can handle during fabrication to below 100 °C; above this temperature, the electrolyte will boil and increase pressure, which may cause the battery to burst.

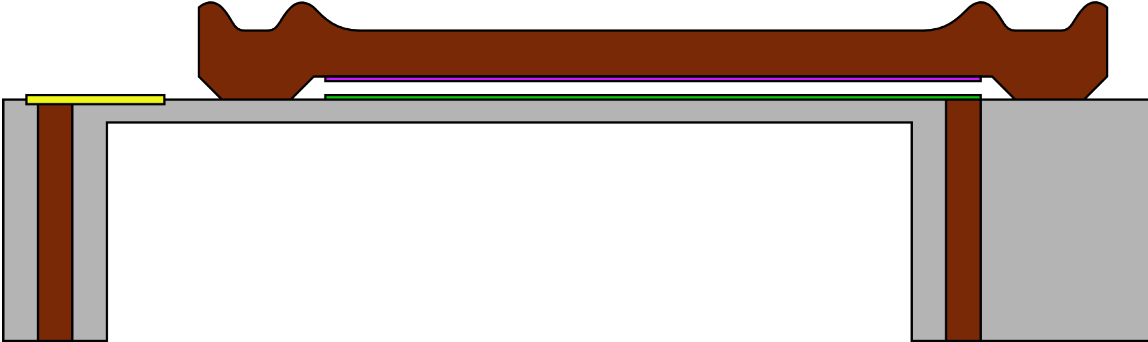

Figure 1.10. The battery module with deep cavity for ASIC and vertical interconnects for power and pass-through to pressure sensor module.

A commercial microbattery based on a solid-state lithium chemistry has also been used in a collaborative work. This avoids a liquid electrolyte, increasing the working temperature. This custom microbattery, manufactured by Cymbet, can also be placed within the cavity along with the ASIC. Other charge-storage approaches can also be used, such as the capacitor arrays used in the Purdue work for short-term energy storage with low energy density and super capacitors providing high-instantaneous charge and discharge rates with high energy density similar to batteries.

Along with a local power source, energy-harvesting solutions have also been explored to continuously trickle charge the microbattery. Solar power is an attractive choice here due to the use of an optically-transparent glass package. This implant is in an ideal location to capture ambient light whenever the patient is awake and the eyes are open.

1.3.3. The Antenna Module

The wireless interface is of critical concern since it is typically the primary power consumer of the entire microsystem. In order to optimize wireless functionality, many issues, some contradictory, must be taken into account. The frequency-dependent electrical properties of tissue limit the functionality and efficiency of the antenna as frequency is increased. Conversely, as the frequency increases, then antenna size can be

reduced. A tradeoff must therefore be made to balance the gains of reducing antenna size with the reduced efficiency of the wireless link as the operating frequency increases.

In order to help alleviate the power consumption challenges, an atypical wireless communication approach has been taken to minimize both idle-mode power and transmit power. A dedicated wakeup receiver circuit is avoided by using an optical trigger. The associated LED light source would be implemented in the external wand alongside the external receiver coil. The on-chip transmitter circuitry is all-digital and consumes power only when driving the antenna. This approach to wireless data transmission utilizes a pulse-based technique and falls within the category of ultra-wideband impulse technology, a relatively new name for an old approach based on non-resonant wireless techniques.

The antenna is fabricated incorporating electroplated metal (copper or gold) as the electrical conduit for its higher conductivity compared to highly-doped silicon. This is necessary due to the high-frequency operation of the radio frequency circuit used to drive the antenna. As the transmitted electrical signal increases in frequency, the resistance of the interconnect becomes more and more critical. Vertical interconnects are again incorporated in the glass substrate using a modified glass-in-silicon reflow process. Metal patterns on the backside provide lateral interconnects for the ASIC, as shown in the antenna cross-section in Figure 1.11.

Figure 1.11. The antenna module with metal vertical interconnects.

1.3.4. The Application Specific Integrated Circuit (ASIC)

The integrated circuit consists of readout circuitry designed to operate with the pressure sensor and contains a simple finite state machine to initiate sensor readout for data transmission via an integrated pulse generator. This chip consumes very little power during idle states. When repeatedly optically triggered, the device switches from the idle state to a reference capacitor, then to the sensor, and finally to a second reference capacitor before returning to the idle state. Embedded solar cells exposed to ambient light throughout the day can provide power for recharging the embedded microbattery.

The physical dimensions of the circuit cavity with the microbattery module shown in Figure 1.10 are 1.2 mm x 700 µm x 250 µm.

In addition to the custom ASIC designed in this work, a second, fully-integrated microprocessor was developed under the guidance of Professors David Blaauw and Dennis Sylvester. The two-chip Phoenix processor provides an integrated antenna along with all the necessary circuitry for wireless RF communication. Solar energy harvesting is also used to provide energy autonomous functionality. The Phoenix processor includes a memory to store successive pressure readings and can also provide subsequent processing of the data, including computation, compression, and/or trend analysis.

These two intraocular ASICs demonstrate a functionality that ranges from simple, on-demand readout to the more complex, autonomous data-acquisition, storage, and on-demand readout possible in programmable microsystems. Ultimately, the preferred ASIC will provide the programmable functionality of the Phoenix processor with the optical scavenging and triggering with the simplicity and reduced cost of a single-chip solution.

1.4. Summary

This chapter introduced glaucoma and the concept and ramifications of intraocular pressure in glaucoma diagnosis and management. Previous work in this area was summarized, along with the shortcomings and challenges of designing an implant small enough to fit within the eye. An ideal intraocular microsystem was described, followed by a description of the Michigan intraocular microsystem developed in this thesis. The following chapters describe the modules that make up this intraocular microsystem. Chapter 2 describes system design and packaging concepts that are particular to this challenging application, including the description of a new glass-in-silicon reflow fabrication process and the resulting microsystem assembly. Chapter 3 describes the design, fabrication and testing of a touch-mode capacitive pressure sensor. Chapter 4 discusses power storage and generation solutions. Chapter 5 discusses the ASIC implemented in this work and describes the circuit components in detail. Chapter 6 reviews wireless communication and the antenna module design. Finally, Chapter 7 concludes the work thus far by presenting the thesis contributions and anticipated future work.

CHAPTER 2

SYSTEM DESIGN AND PACKAGING

The intraocular microsystem makes use of a new fabrication technique in order to meet the aggressive size constraints presented by this application. The new process enables more compact packaging, arranging the components of the microsystem vertically and foregoing conventional lateral interconnects between sealed modules. Vertical interconnects reduce the required surface area and increase the useable volume. Furthermore, they improve reproducibility and device reliability since lateral interconnects introduce fabrication complexities, potential failure by way of crack propagation, and more challenging sealing.

The packaging of the intraocular system was driven by vertically stacking independently fabricated modules, all using a similar process flow. The environment within the body would be damaging to any exposed electronics so some method of ensuring the circuitry is protected is necessary. This is accomplished by placing the custom integrated circuit within a glass cavity. Sensing elements, in contrast to the electronics, must be placed in contact with the body in order to directly measure the local environment. The vertical interconnects permit passing signals from the externally mounted sensor to the internally protected circuitry. Figure 2.1 shows a cross-section of the microsystem, utilizing vertical interconnect and the stacking of modules.

This chapter begins by describing conventional techniques for fabricating holes in glass. The holes would later be filled with electroplated metal to form the vertical interconnects. Since initial experimental studies of hole formation proved less than useful and alternatives were either time-consuming or inaccurate, a new process technique was developed: the glass-in-silicon reflow process. This process is a simple, bulk-mode technique based on glass reflow and is applied to all the modules, with slight variations, described here. The overall package is then described in detail, including assembly techniques. Finally, a description of the planned surgical method, location and

process is included, aided by the glass-in-silicon process and its ability to form arbitrary edge shapes.

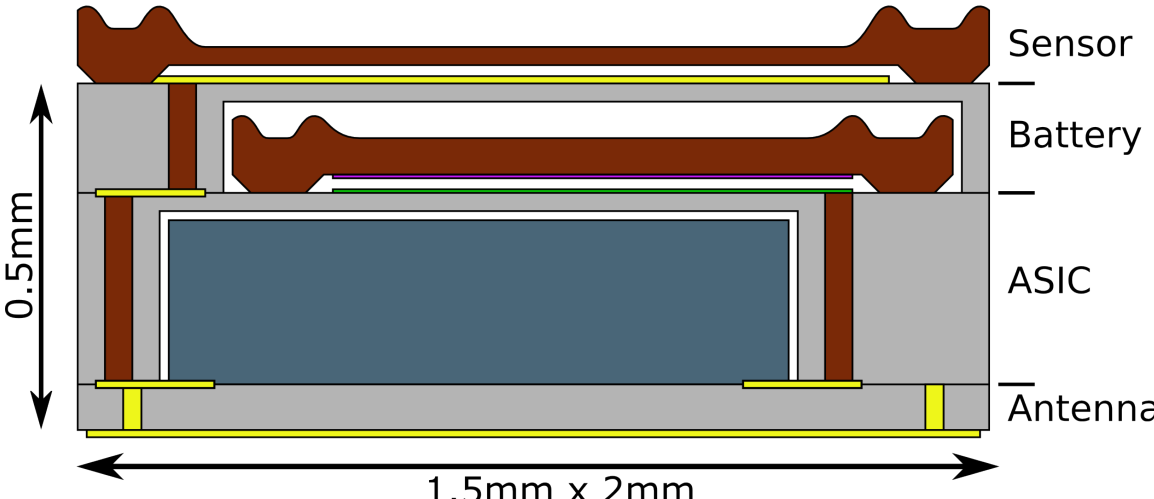

Figure 2.1. Vertically-stacked compact microsystem enabled by vertical interconnects.

2.1. Vertical Stacking

Implantable microsystems are physically constrained in dimension and by biocompatibility concerns. As dimensions are reduced, less scarring and tissue inflammation occurs, but challenges such as tissue reaction, biofouling, and post-surgical patient complications are all important concerns. Possibly no other application is affected by dimensional limits more than intraocular implants because of the limited available space and delicate nature of the eye. The vertically-stacked approach used here allows for the most optimal use of space, but brings challenges along with it, such as the need for vertical interconnect.

Vertical stacking also allows for a modular approach in engineering the structure. Several components are necessary for the fully functioning microsystem, including the sensor and the readout circuitry. By ensuring that each module is designed to provide vertical and lateral interconnects, the entire microsystem can be built by simply stacking the necessary modules together. Furthermore, the microsystem can be assembled using known good components by testing partially-assembled modules at each step during assembly. These are benefits that enhance the practical aspect of a modular, vertically stacked microsystem.

Glass and silicon are two preferred substrates for implantable microsystems. Each material has different advantages and disadvantages, almost complementary to each other. Glass is non-conductive and transparent to most wavelengths. Silicon can be made very conductive with the addition of dopants and is opaque in the visible regime. Fabrication processes for glass are still under development, with hydrofluoric acid the most common etchant, while vertical anisotropic glass etching is very challenging and expensive. Silicon, on the other hand, has been studied for decades with tools and process techniques that have improved greatly over time, increasing yield and reducing costs. Typical silicon etchants like XeF_2 (an isotropic gas-based etchant) or ethylene-diamene pyrocatecol (an anisotropic etchant) are virtually ineffective for etching glass. The biocompatibilities of both silicon and glass are good, with glass the more commonly used material. Glass has been chosen as the substrate for this work based on its optical transparency, dielectric properties, and known biocompatibility. Furthermore, the fabrication of the pressure sensor utilizes a highly-reliable technique called silicon-glass anodic bonding to provide a hermetic, vacuum-sealed cavity for the sensor, which is critical in order to ensure functionality of the sensor over long periods of time.

Forming holes in glass with high spatial resolution and repeatability at a relatively low-cost remains challenging. Several techniques exist currently, including sandblasting, ultrasonic drilling [28], electrochemical etching [29], laser drilling [30], reactive ion etching (RIE)/plasma etching [31], and mechanical drilling. All of these techniques are limited in at least one of four ways: 1) serial operation, 2) low spatial resolution, 3) large minimum feature size, and 4) excessive substrate damage. With respect to the first restriction, standard processing occurs at the wafer level and benefits from batch processing. Laser drilling is a serial process and can only drill holes one at a time without custom optics. Mechanical and electrochemical drilling are usually also single step processes, requiring alignment for every step or a dedicated jig. In terms of position and sizing, all of the aforementioned processes except laser drilling appear to be limited commercially to hole sizes above 250 μm diameter. Finally, mechanical, laser, ultrasonic and sand blasting can all damage the surface of the glass by generating microcracks or by redeposition of the removed material; precautions must be taken to reduce these effects, adding further complexity.

A process that is built on well-known silicon processing is reactive-ion etching (RIE) of glass; however, the etch rates are quite low at approximately a few microns per minute [32]. Much higher power is required to achieve practical etch rates but preclude the use of standard photoresist masks. RIE etching of glass using harder masking materials such as silicon have been studied [33]. This technique is possible, and dedicated etch tools have been developed, but requires long etch times, especially for borosilicate glasses such as Pyrex. Borosilicate glasses are often preferred because their coefficients of thermal expansion are similar to that of silicon.

2.1.1. Femtosecond laser drilling

Of all the options, laser drilling of glass initially appeared to be most appropriate for the requirements of this microsystem. If the vertical interconnect is much larger than 250 μm, then an appreciable volume of the substrate is consumed in simply providing electrical connections. Only laser drilling offers very small machined dimensions. In order to test this, a femtosecond laser was chosen as the energy source. A Ti:Sapphire laser, manufactured by Clark-MXR, was used to drill through 100 μm of glass. The test setup optically splits the source beam, halving power before it is routed to the target mounted on an optical table. Multiple interchangeable lenses and mirrors were used to route the laser, resulting in an elliptical beam shape. By swapping different lenses, different radii can be achieved, as defined in Equation (2.1), where r is the radius of the focused beam, λ is the wavelength of the laser (780 nm), f is the focal length, and D is the unfocused diameter.

$$r = 1.22 \frac{f}{D} \lambda \tag{2.1}$$

A 350 mm lens that yielded a 48 μm radius beam and a 200 mm lens yielding a 27 μm radius beam were tested. The pulse rate of the laser was fixed at 1 kHz, resulting in a maximum power of 780 mW (for the 350 mm lens) to 820 mW depending on the lens used. The fluence E, or energy per area, is calculated as in Equation (2.2), where P is the optical power, f_{rate} is the pulse rate, and r is the radius calculated from Equation (2.1). For comparison, silicon dioxide requires 16 mJ/cm^2 whereas silicon requires 0.3 mJ/cm^2 minimum energy for ablation.

$$E = \frac{2P}{f_{rate} 4\pi r^2} \quad (2.2)$$

Figure 2.2 shows a successfully drilled hole after 1 minute of applied laser power. Several experiments using longer times were also tested, but all resulted in very poor holes in terms of shape and smoothness. Optimizing the laser as well as improved focusing would most likely reduce the drilling time and might improve the shape of the hole.

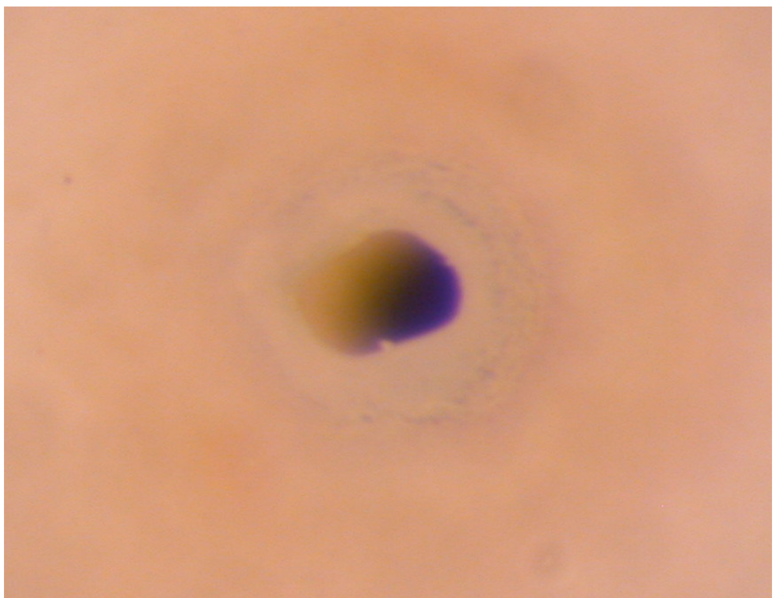

Figure 2.2. Optical photograph of a 100 μm diameter hole in 100 μm thick glass drilled using femtosecond laser ablation in 1 minute.

However, the resulting surface damage in the surrounding region is a major drawback, as shown in the scanning electron micrograph of Figure 2.3. When compared to previously published work, the results are very similar [30]. In fact, further testing in the literature concludes that the cause of the surface damage is glass redeposition. The identified solution was to place the target in a vacuum during ablation, resulting in very smooth, clean holes [30].

The results of the ablation studies suggest that while laser drilling is a potential solution, it requires a complicated processing setup. Aside from optimization, a special programmable stage is required to move the wafer to the location of each hole to be drilled after calibration of the stage for each wafer. Without optimization, a process time of 1 minute per hole was required. An entire wafer with 1000 devices and two holes per

device would require 2000 minutes per wafer, or more than 33 hours. The biggest drawback, however, is the complex setup required, placing the target in vacuum and feeding the laser beam into the chamber. While a femtosecond laser might work for this process, the added challenges do not appear worth the effort.

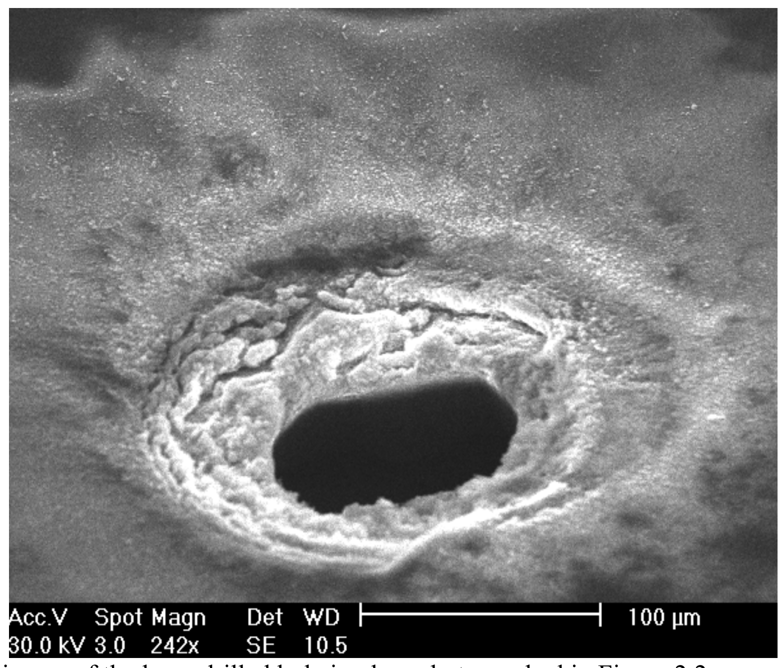

Figure 2.3. SEM image of the laser-drilled hole in glass photographed in Figure 2.2.

2.1.2. Mechanical drilling

Mechanical drilling using a manual drill press was also tested. A diamond bit was used to ensure high-quality cutting of the glass. Manual alignment using a custom optical setup allowed for visualization of the substrate but required a dedicated sacrificial mask to identify drilling locations. Unfortunately, the accuracy of the alignment is lacking due to human error and would greatly benefit from an automated stage with micrometer precision. This tedious process also resulted in the entire substrate cracking, reducing yield to virtually zero. A first hole drilled with 100 µm radius followed by a second hole of the same size within a distance of 1 mm would likely crack 500 µm-thick glass. Additional modifications such as the inclusion of a masking layer were not tested, though in principal this may absorb some of the shock during drilling of the substrate. However, the resulting surface was also not smooth, with microcrack propagation resulting in pits forming around the glass hole that polishing would not be able to easily correct.

Conventional approaches for drilling holes in glass do exist, but are not compatible with either batch-mode type fabrication or microscale requirements. Other commercial solutions, such as ultrasonic drilling, may be potential solutions in the future but are currently limited in resolution. A better solution for the batch-mode of machining glass is necessary, and it would be most beneficial if it were compatible with the current cleanroom processes used in MEMS fabrication, minimizing any external processing or complex tooling.

2.2. Glass-in-Silicon Reflow

The glass-in-silicon reflow process is a new process technique that provides a compelling solution to the aforementioned problems associated with machining glass. Conventional techniques for generating vertical interconnects rely on well-understood silicon processes, but have not been transferred to glass due to fabrication difficulties. The process detailed here avoids the challenges associated with the conventional techniques for generating holes in glass since the microfabrication occurs in silicon and not glass. The key to the technique is a glass reflow step that allows the glass to take virtually any shape and fill the pre-etched regions of a silicon wafer. This places the burden of fabrication on etching silicon, which is well known and results in high yield and fast etch rates using modern tools. Silicon, metal, or both can be incorporated in the glass substrates with this technique, resulting in whole wafers consisting of regions of these materials. The technique is used to form through-glass vias for vertical interconnects and cavity formation, enabling a new, vertically-stacked implantable structure demonstrated in the intraocular application. After removing a portion of the silicon mold, the end result is a wafer polished on one or both sides, as shown in the photograph in Figure 2.4. A magnified version of this photograph shows the inclusion of two square posts per glass substrate, as shown in Figure 2.5.

It is important to note that the wafer is constructed of just glass and silicon and it is completely solid. These wafers can be handled with minimal breakage if care is taken when handling them, especially ensuring no cracks develop at the edge of the wafer. The wafers are robust enough for double-sided processing using conventional lithography techniques, even though they have been thinned to between 150 µm and 250 µm. The

technique here can be extrapolated to other materials that may be molded, but there are certain disadvantages when using a polymer, for example, such as the lack of hermeticity and perhaps reduced biocompatibility.

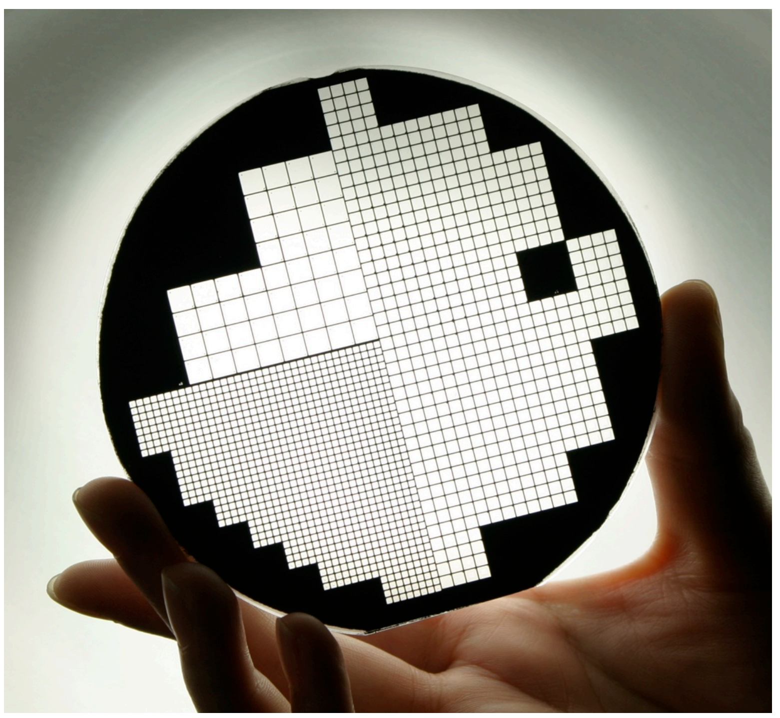

Figure 2.4. Photograph of a completed 250 µm thick 100 mm diameter silicon-in-glass wafer.

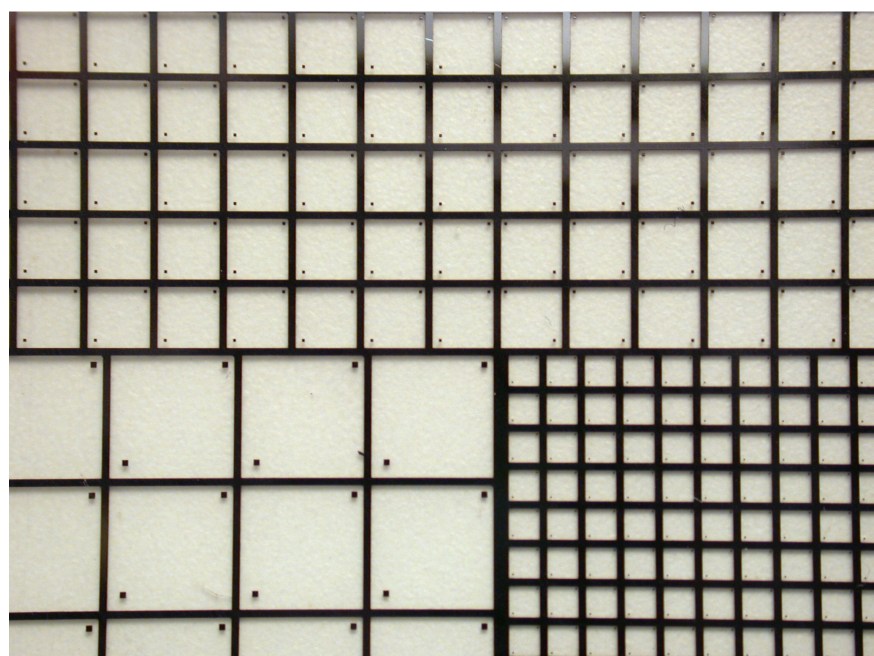

Figure 2.5. Magnified photo of glass-in-silicon wafer showing square posts in the corner of each glass die. The 1 mm x 1 mm die contains 50 µm posts while the largest 4 mm x 4 mm die contain 250 µm posts.

2.2.1. Process Flow

A process overview is shown in Table 2.1, highlighting the fact that only one mask is used to define the shape of the glass and two additional metals are used to provide lateral interconnect on each side of the wafer. Only seven steps are needed, all of which use common cleanroom fabrication tools and procedures. The process begins with a highly-doped silicon wafer to provide low-resistivity feedthroughs. Work thus far has been performed on commercially available p-type wafers with resistivities less than 0.01 Ω-cm.

Step	Description	Mask
1	Bare single-side polished silicon wafer, highly-doped; pattern photoresist	GLASS
2	DRIE etch to depth exceeding required final thickness	
3	Anodically bond borosilicate glass wafer in vacuum	
4	Reflow glass	
5	Front-side planarization and polishing	
6	Back-side wafer thinning and polishing	
7	Cr/Au deposition; release in EDP	M1, M2

Table 2.1. Glass-in-silicon process overview with defined masks.

The process flow is shown in Figure 2.6 and begins with a single photoresist mask, defining the inverse pattern of the resulting glass regions. Deep Reactive Ion Etching (DRIE) in a Pegasus STS tool utilizing the Bosch process is used to etch down to depths of typically half the standard wafer thickness of 500 µm. The practical limit approaches 450 µm, but physically depends on the etched surface area and remaining silicon thickness in order to ensure it will not fracture during subsequent steps. Anodic bonding of the silicon to a 100 mm glass wafer in vacuum is carried out in a Suss SB6e at 1000 V and 300° C. The vacuum essentially acts to apply a force within the sealed cavities, pulling the glass into the cavities during the subsequent reflow step, which begins at temperatures above the glass transition temperature T_g of 550° C.

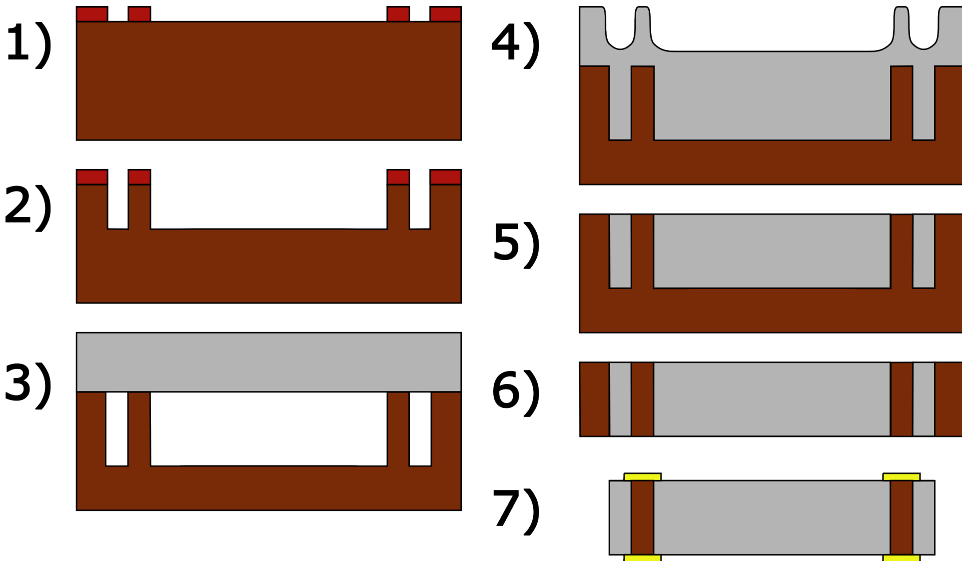

Figure 2.6. Process flow for glass-in-silicon, including double-sided metallization.

The furnace temperatures that have been tested ranged between 750 and 900° C; higher temperatures result in visible oxide growth on exposed silicon over time periods of eight hours. The actual parameters used during the reflow step can be further optimized to speed the process; as shown in Figure 2.7, the viscosity of borosilicate glass drops quickly as temperature increases and then plateaus. However, at higher temperatures, a longer cool-down period is required; otherwise, there is a risk of microcracks forming as the interior of the glass cools slower than the exterior surface exposed to atmosphere. The final steps are planarization of the glass surface until the silicon is flush with the glass, followed by chemical mechanical polishing (CMP) to bring the surface to the mirror finish required for later processing such as anodic bonding. Double-sided polishing is possible but requires a carrier wafer when used with a CMP designed for single-sided polishing, such as the IPEC tool used in this work. Other procedures can be used to speed thinning of the bulk silicon and bulk glass portions of the bonded wafer stack, such as wet silicon etching with potassium hydroxide (KOH). Similarly, the bulk glass can be pre-thinned before the planarization step using hydrofluoric acid (HF).

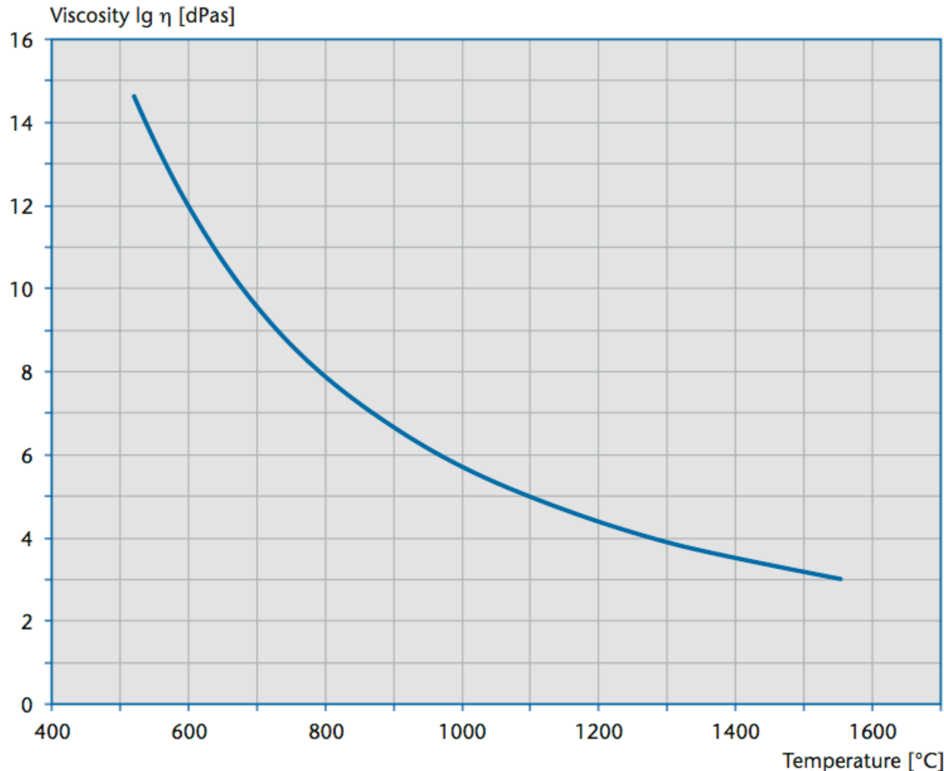

Figure 2.7. Borofloat viscosity versus temperature [34].

2.2.2. Feedthrough Resistance

The resistance through a round feedthrough has been calculated using the simple resistivity formulation of a cylinder in Equation (2.1), where R is the resistance of the feedthrough, h is the height of the feedthrough (equivalent to the thickness of the wafer), r is the radius of the circular post, and ρ is the resistivity of the bulk silicon wafer (0.01 Ω-cm).

$$R = \frac{\rho l}{A} = \frac{\rho h}{\pi r^2} \tag{2.1}$$

Hand calculations yield an expected ideal resistance of 3.18 Ω for a 250 µm thick substrate with 50 µm radius feedthroughs. A special test mask was designed to short two feedthroughs in series using a Cr/Au layer on one side and Cr/Au metal pads for probing on the other. The rest of the process flow was identical to that in Figure 2.6, with double-sided polishing. The resulting I-V curves showed a resistive feedthrough with resistances in the range of 2.2 Ω per feedthrough, close to the ideal calculated value. The

discrepancy may be simply due to a slightly lower resistivity for the silicon wafer, since the actual value from the manufacturer is not exact, but guaranteed to be below 0.01 Ω-cm. In fact, an ideal cylinder with the above dimensions but using 0.007 Ω-cm silicon would exhibit approximately 2.2 Ω of feedthrough resistance. A photo of the test wafer appears in Figure 2.8. A cross-section diagram illustrating the test circuit is shown in Figure 2.9. Probe tips are used to make contact to the gold pads.

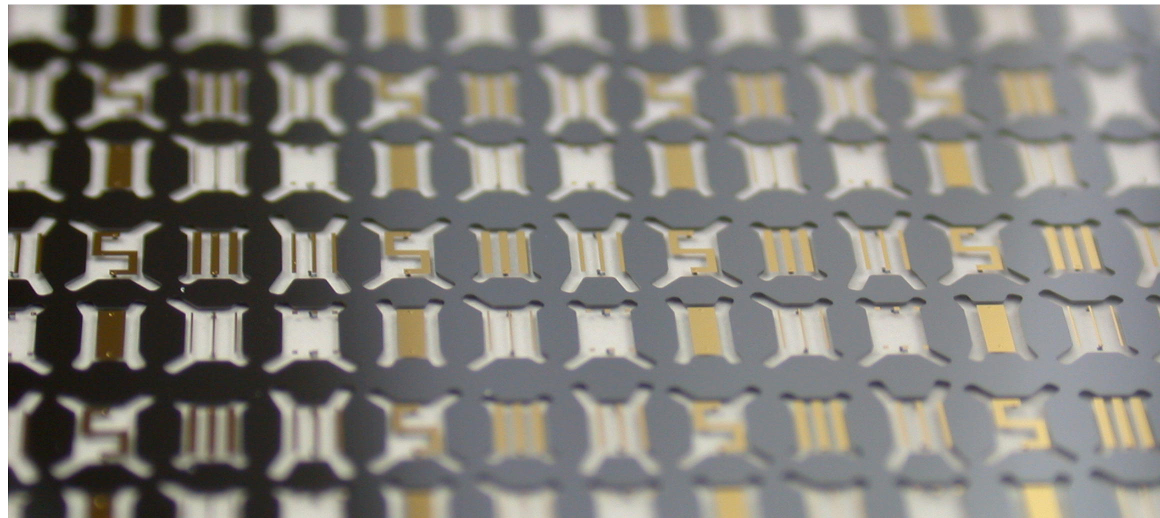

Figure 2.8. Wafer for testing feedthrough resistance.

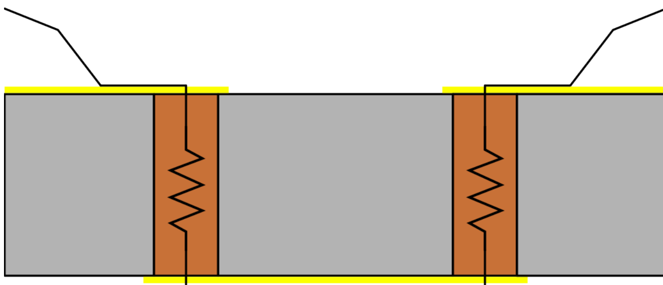

Figure 2.9. Cross-section illustration of test devices in Figure 2.8 showing the expected electrical path with probes.

2.2.3. Cavity Formation

In order to incorporate a cavity for an integrated circuit to reside in, the process was modified as shown in Figure 2.10. An additional mask enables a two-step deep reactive ion etch (DRIE). A first masking layer of PECVD oxide, up to 2 μm thick, is patterned in buffered hydrofluoric acid using photoresist as a mask. A second masking layer, using photoresist, is patterned on top of the oxide mask. After the first etch step is complete, the photoresist is removed, revealing the underlying oxide mask. The wafer is

then etched a second time, with the oxide selectively protecting the silicon from the plasma. Once the second etch is complete, all oxide is removed in hydrofluoric acid. Two separate masks are needed because of the etch depth since conventional photoresist applied using a spin-on process cannot evenly coat deep trenches. The rest of the process flow is identical to the standard glass-in-silicon flow in Figure 2.6 with subsequent reflow, planarization, grinding, and polishing steps.

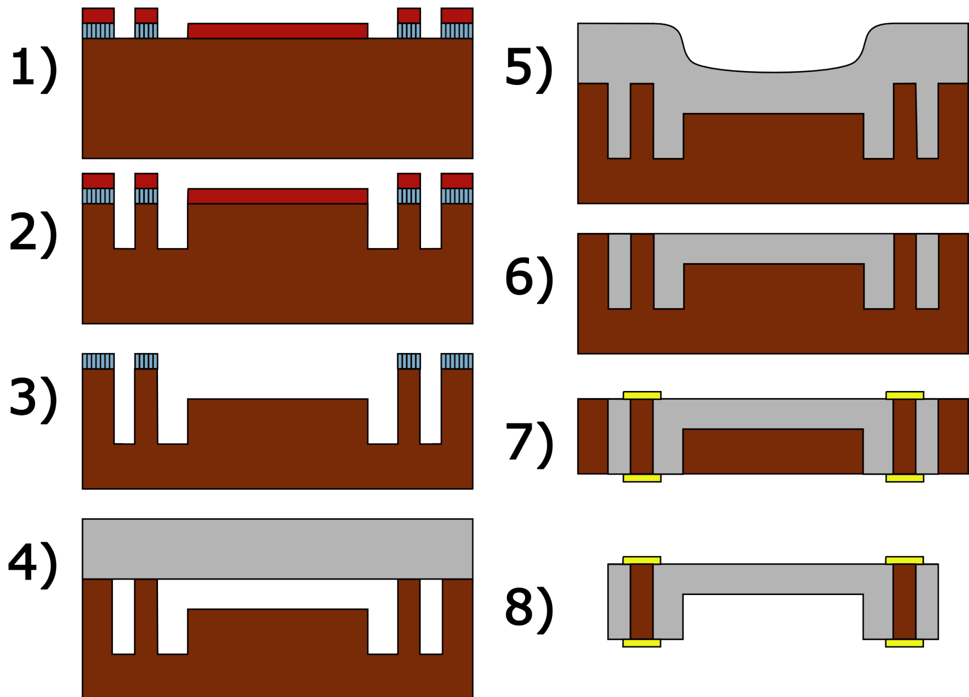

Figure 2.10. Glass-in-silicon process flow modified for cavity formation.

2.2.4. Metal Feedthroughs

Direct electroplating to silicon has been demonstrated for the purpose of vertical metal interconnects in this work. The modified process flow appears in Figure 2.11, introducing one additional mask. Prior to backside thinning, this mask is used to protect the entire wafer except the silicon feedthroughs. The glass-in-silicon wafer is then dry etched using XeF_2 (xenon difluoride) with photoresist masking the regions of the silicon to be preserved. The feedthroughs are removed quickly due to the small exposed area, leaving behind holes in the glass. The etch time needs to be sufficient to ensure that the removed silicon is below the reflowed glass, as shown in step 6 of Figure 2.11. Electroplating in conventional baths proceeds with the glass serving as the mold. Slight

overplating is desired since it ensures all the vias have been completely filled. The following steps continue with planarization and polishing on the front side and grinding and polishing on the backside. Cr/Au metal pads can also be patterned, protecting the metal feedthroughs during a release etch in ethylenediamene pyrocatecol (EDP) if necessary.

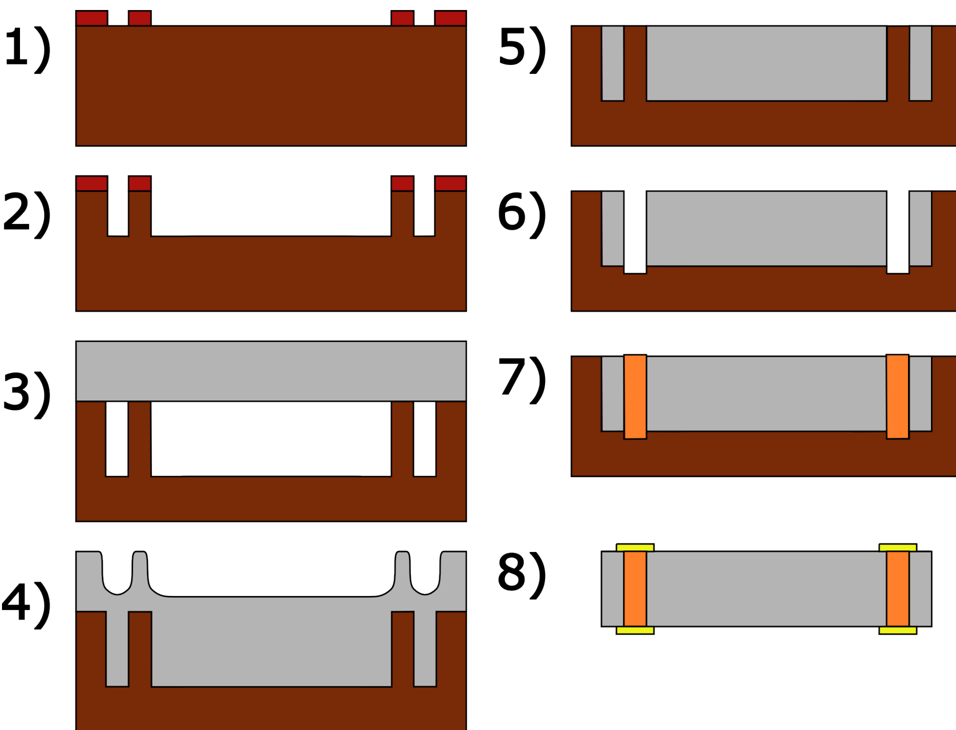

Figure 2.11. Glass-in-silicon process flow modified for electroplating metal feedthroughs.

SEM images were taken after etching the silicon completely from the feedthroughs, as shown in Figure 2.12. After electroplating gold for a short time period, it is clear that the metal successfully electroplated directly to the silicon surface at the bottom of the via, as shown in Figure 2.13. Though this has been demonstrated before by implanting dopants into the surface of the silicon [35], the presence of glass as the mold for the electroplating solution is unique. Furthermore, previous work in this area identified adhesion as a problem [36], which is not important here because the plating base, or seed layer, is removed once the silicon backside is thinned in a later step.

For the antenna, highly-doped silicon will not suffice due to its limited conductivity, which becomes an issue especially at high-frequencies. Therefore, metals such as gold or copper can be electroplated through the holes. In addition to the process

flow described above for metal feedthroughs, the process can be modified for more complex structures, such as a silver sheath and a copper core, for example.

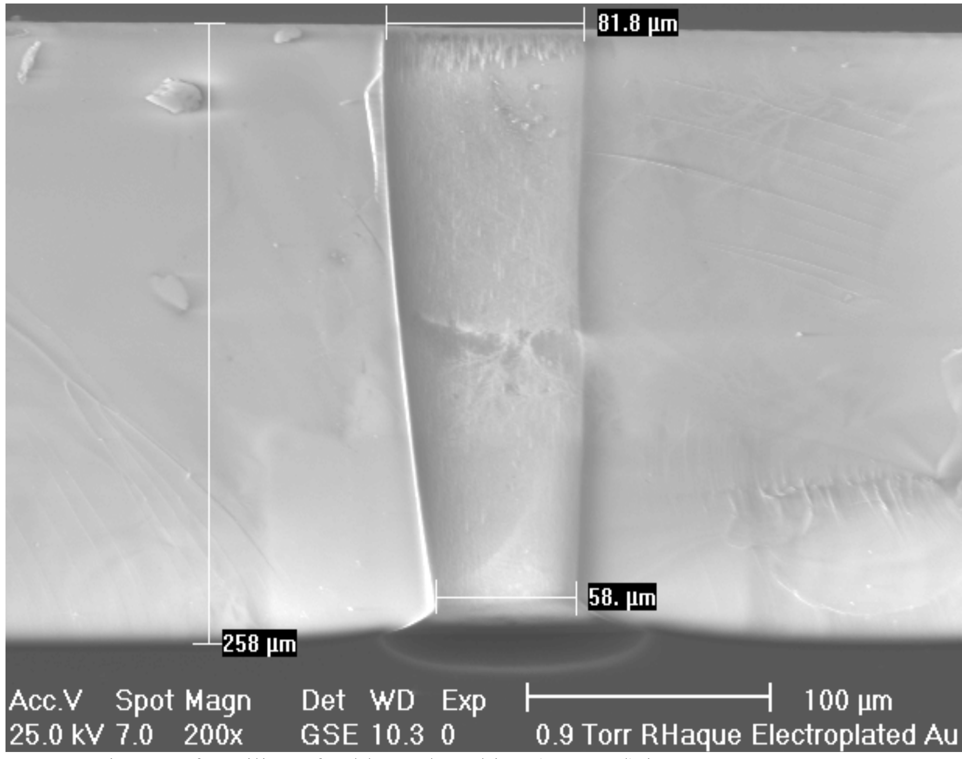

Figure 2.12. SEM image after silicon feedthrough etching (removal) in XeF2.

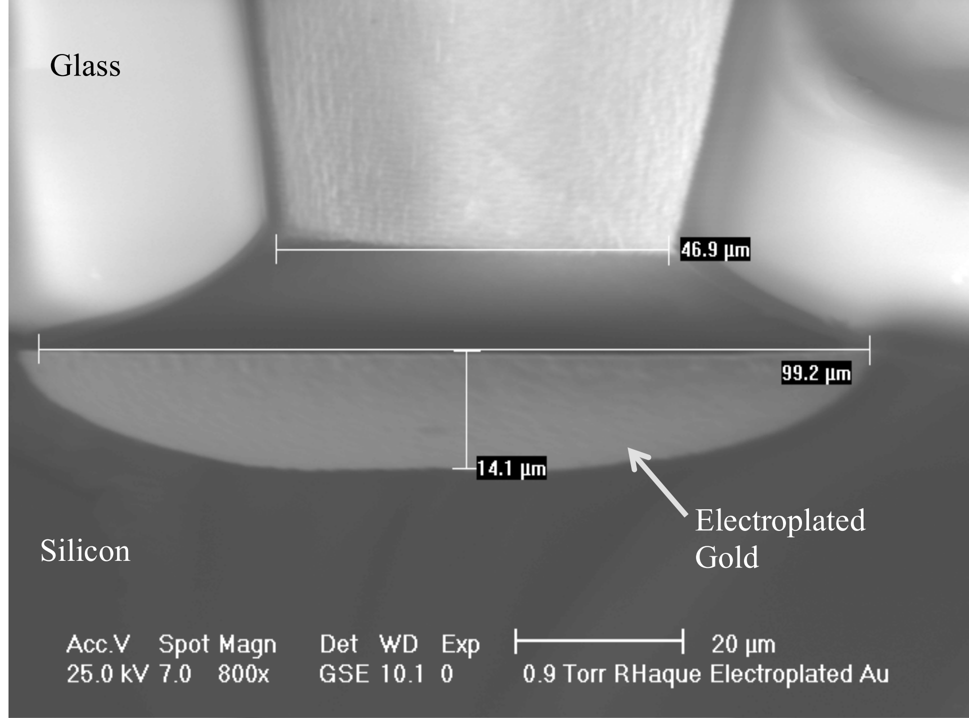

Figure 2.13. Bottom of the via showing gold after a short electroplating experiment, resulting in no voids.

2.2.5. Anodic Bonding

An additional feature of the particular glass used (borosilicate) allows anodic bonding between the glass and silicon. These bonds are of very high quality, hermetic, and very robust. Since the glass regions are embedded in one wafer, silicon can be anodically bonded at these locations, providing an excellent seal for devices such as pressure sensors, as demonstrated in Chapter 3. Chemical-Mechanical Polishing (CMP) is required for any surface that will later be anodically bonded to silicon in order to ensure bonding succeeds. The likelihood of a bond failure is high if the surface is rough since the bond relies on an electrostatic force to make intimate contact between the surfaces.

The inclusion of conductive feedthroughs could cause a short to develop, preventing an anodic bond from proceeding when silicon wafers are bonded to glass-in-silicon wafers. Care must be taken such that the bonding apparatus only makes contact with the glass areas and not the silicon areas electrically connected to the second wafer. A solution to this problem is to apply electrically conducting extensions to only the glass areas so that there is no shorting between the two silicon regions. A diagram to better illustrate this issue and the solution is shown in Figure 2.14.

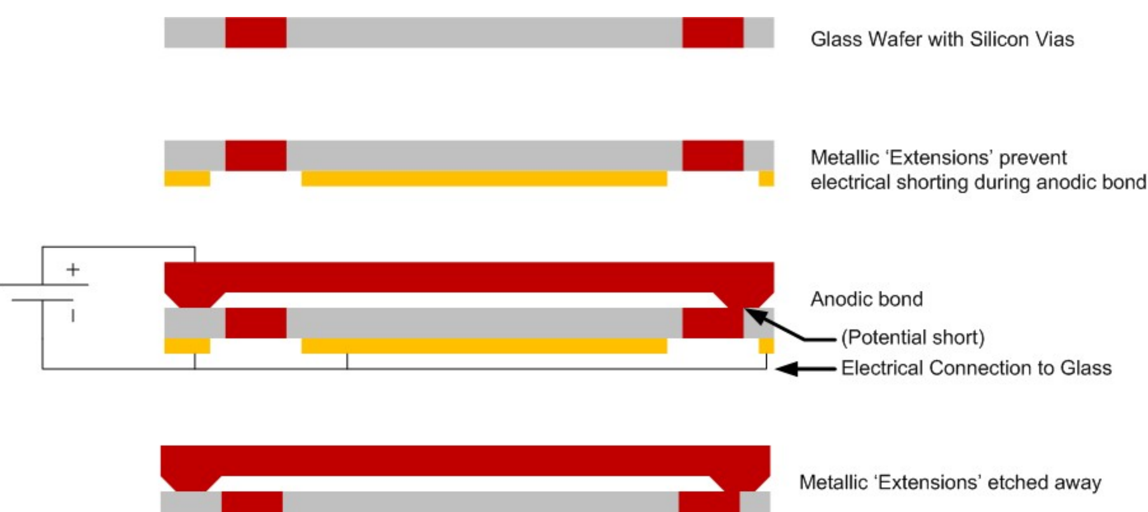

Figure 2.14. Apparatus for anodic bonding with a glass-in-silicon wafer.

The successful application of anodic bonding to the glass-in-silicon wafer with an aluminum spacer with thickness of 1.5 µm is discussed in connection with fabricating the pressure sensor in Chapter 3.

2.2.6. Related Work

A similar process flow to the one presented here was designed to produce lenses in glass using a silicon mold [37]. Timing the flow of glass was important in forming the correct radius of curvature for these lenses, and so the bulk of the work focused on the physical properties of reflowing glass at various temperatures. The silicon was also completely removed using a silicon etchant that preserved the glass, resulting in a glass wafer with embedded lenses.

A glass reflow concept was also previously used to seal a mechanical sensor with integrated silicon feedthroughs [38]. In this work, the glass was used both as a method of sealing the device and providing electrical isolation between electrical connections. The work demonstrated the ability to seal the device at vacuum while simultaneously providing excellent electrical isolation.

Other glass reflow work replicates conventional glass blowing but applied at the microscale [39]. In essence, this process can be thought of as the reverse of the glass-in-silicon reflow process. By sealing the cavities with atmospheric air or other gasses that have a higher expansion coefficient than air, the cavities generate an outward force as the gas expands during heating. A quick cool down step is used to solidify the glass in position before the trapped gas begins to contract.

2.3. Process Challenges

There are several unique challenges that have been overcome during the development of this process. The primary objective of the process development thus far was to increase the yield and robustness, and this has been achieved. Further optimization including faster reflow rates and reduced pitch is left to future work. In this regard, the absolute limits of the glass-in-silicon process are currently unknown.

2.3.1. Inadequate Filling

One of the biggest challenges with this process is ensuring complete glass filling. A photograph of inadequate filling after the reflow step is shown in Figure 2.15. The result of thinning such a wafer down, after the planarization step, is shown in the

photograph of Figure 2.16*,* clearly resulting in pits and even holes along the corner of a die.

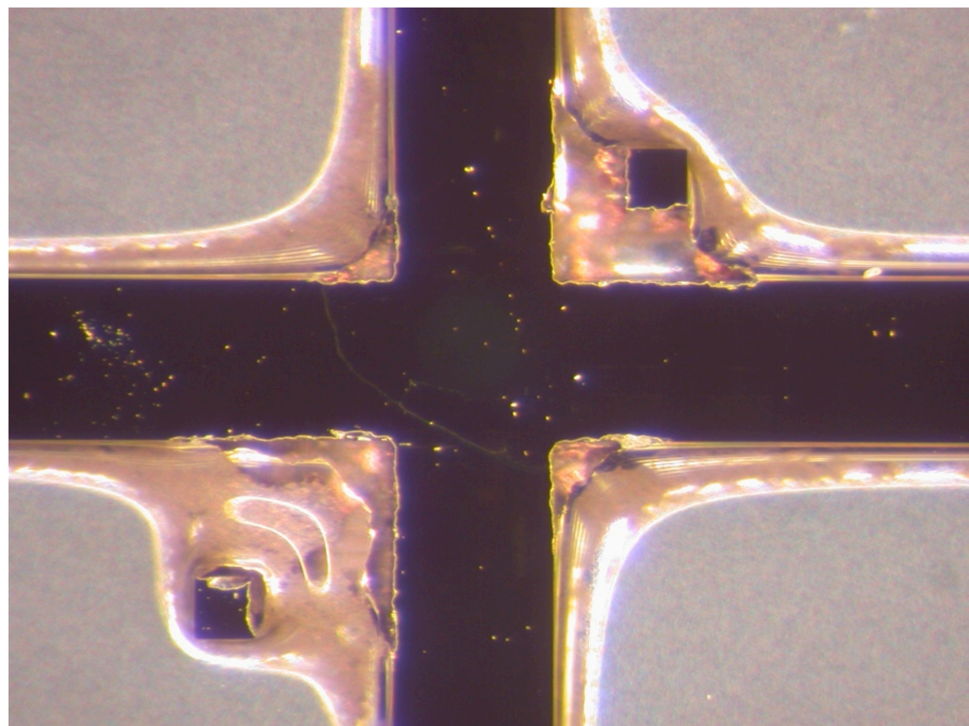

Figure 2.15. Photograph demonstrating incomplete corner filling, before planarization.

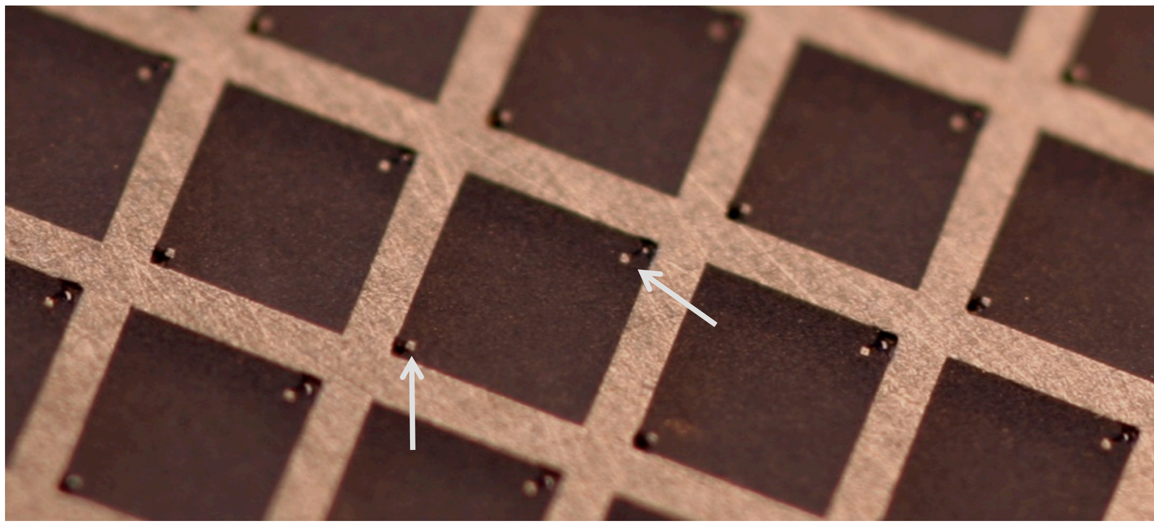

Figure 2.16. Glass-in-silicon wafer showing inadequate filling, after planarization but before polishing

It is theorized that the main reason why glass may not completely fill the mold is due to the lower energy of slow-moving glass. A combination of vacuum, reflow temperature and time, heating rate, and surface roughness is required for adequate filling, reducing the amount of energy acquired for the glass to move. Surfaces can also be

enhanced by a variety of methods, ranging from plasma enhancement to surface roughening. The material over which glass flows is extremely important, whether it is silicon or some other material grown or deposited (e.g., thermal oxidation or evaporated metals) due to the change in surface wettability. Certain materials also react with molten glass, diffusing into the glass and forming a chemical bond at the interface of the material and the glass. Other materials will not form a bond whatsoever and allow glass to flow easily over the surface. Combinations of materials are also possible, such as depositing material on the bottom surface of the silicon mold.

The pull-in force of the vacuum pulls the viscous glass in, while the stiction and friction forces of the glass flowing over the material counter this effect. At some point, the sealed volume reduces to such a small level that the strength of the pull-in force drops to virtually zero. It is entirely possible that glass flow stops much before this pull-in force goes to zero due to counter forces in the opposite direction from the adhesion forces associated with the flowing of glass or at sharp corners in large devices, and so on. The viscosity of glass further slows flow into narrow regions.

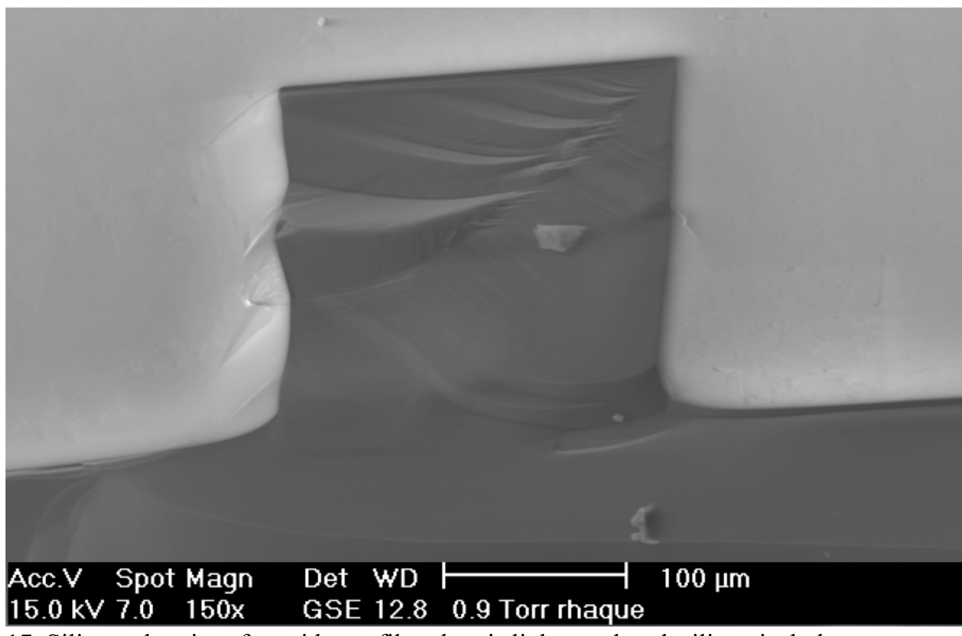

Figure 2.17. Silicon-glass interface side-profile; glass is lighter colored, silicon is dark.

Imaging the fill-effect and the boundary between the silicon and glass is important to determine how detrimental inadequate filling may be. In fact, a side-profile view along a sidewall, which shows complete filling, can give insight into how the interface

between glass and silicon is formed. Figure 2.17 shows an SEM of a sidewall before planarization. Here, no glass-fill problems are evident.

Energy-dispersive X-ray spectroscopy (EDX) was used to perform an analysis on the materials found in the corners where glass filling was a problem. Figure 2.18 is an image showing high quantities of trapped carbon. The only practical source of carbon is the polymer deposited during the passivation step of the Bosch process of DRIE. The presence of carbon indicates that the sidewalls of the silicon were not cleaned thoroughly, leaving behind polymer. During the bonding step or high-temperature reflow process, the polymer may melt and enter a gaseous state, reducing the amount of pull-in force available. In order to remove all potential sources of carbon, the process has been modified to include a long, high-power oxygen plasma treatment to burn off any polymer remaining on the sidewalls of the silicon mold prior to vacuum bonding. Further, additional cleaning of both the silicon and glass wafers in piranha etch (equal parts sulfuric and hydrochloric acid) helps ensure that no such deposits remain.

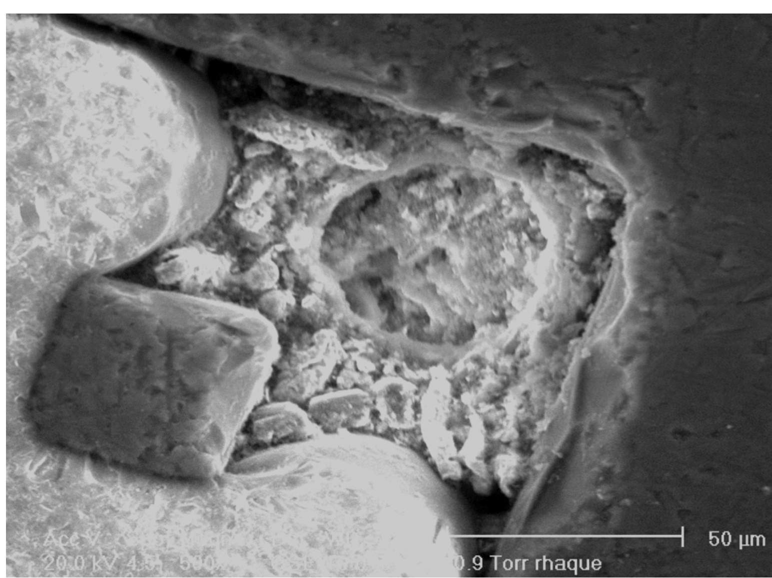

Figure 2.18. Top view of square silicon post showing buildup with high carbon-content

2.3.2. Surface Adhesion

In order to increase adhesion between the glass and silicon surfaces, several experiments were performed. It was believed that glass pull-in may cease well before the pull-in force was fully exhausted due to adhesion or friction forces that prevent or slow the glass from flowing. Platinum was deposited after DRIE of the silicon mold in order

to test if the glass adhesion improved, but no appreciable change was observed. Platinum was chosen because it has a very high melting point and does not form oxides easily. It is common to find platinum-lined crucibles carrying molten glass since the glass can flow over the platinum surface very easily.

Another experiment involved thermal oxidation after the silicon was etched. The purpose of this step was similar to that which artisans use when working with metal and glass. From conventional glasswork it is well known that glass does not stick to materials that are not oxidized. In fact, for copper wires embedded within glass such as in stained-glass lamps, a special pretreatment procedure is necessary. First, the copper wires are dipped in acid in order to remove any oxides on the surface of the wire. Then, the wire is inserted into a dedicated furnace to uniformly oxidize the copper wire. Once the wire has been removed, it can be dipped into molten glass, and when pulled out, the glass adheres to it evenly. Without the acid treatment, the glass will not adhere uniformly since oxidation of the wire is not consistent. Without the oxide, the glass does not adhere to the copper. For this reason, the silicon wafers, after etching in DRIE, were placed in a furnace and 1.2 µm thick thermal oxide was grown to improve the contact angle between the glass and the silicon dioxide surface. However, this step did not appear to improve the glass filling appreciably. It was determined that this step was most likely not worth the effort for an unobservable improvement.

DRIE can fluorinate the silicon surface, which may prevent native oxide from growing. In order to determine whether the presence of oxide had an effect, silicon wafers after DRIE were placed in BHF and then rinsed, dried, and bonded. These wafers still suffered from poor glass filling.

2.3.3. Gettering

Titanium was deposited for a very different reason, and some enhancement of the glass pull-in was observed. Figure 2.19 shows a photo of reacted titanium sealed within the glass cavities. Titanium serves as a getter, quickly forming oxides in the presence of various gasses. Once deposited and removed from the vacuum chamber, titanium quickly absorbs oxygen from the environment. However, when heated to the reflow temperature

of glass, titanium further reacts with nitrogen as well, forming titanium nitrides that are visible as a brownish-colored compound.

It was observed that this compound formed in sealed cavities, indicating the presence of nitrogen. By removing the nitrogen from the sealed cavity, it is possible that the vacuum in the cavity is further increased. Another possibility is that the titanium reacted upon contact with the glass and was drawn into it, forming titanium oxides. Complete glass-filling was achieved with either the titanium gettering or if the bonding tool was functioning at full capacity. Therefore, titanium can be used as a method of ensuring good vacuum is achieved in the sealed glass cavities prior to reflow.

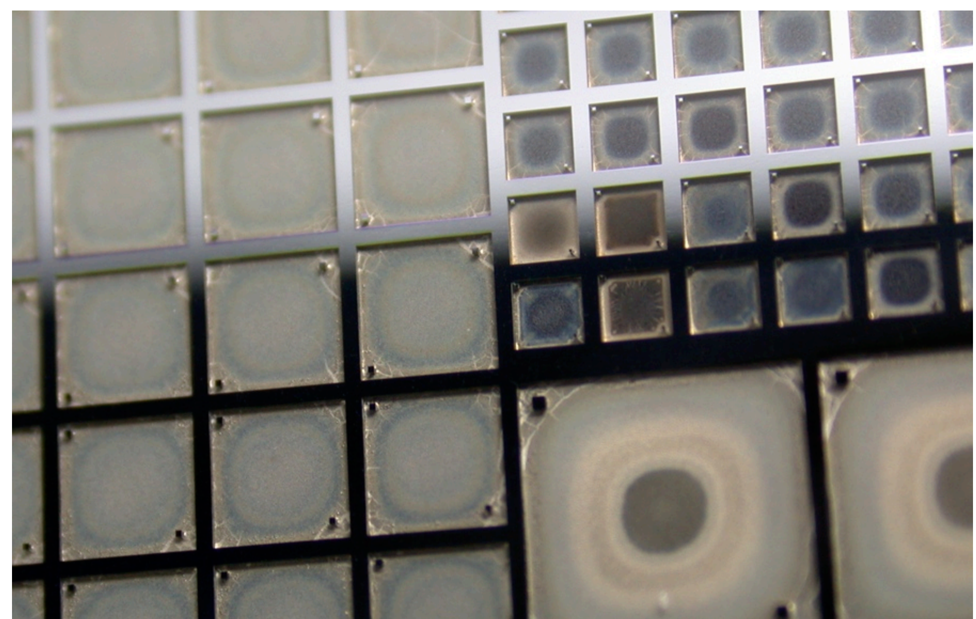

Figure 2.19. Planarized and polished silicon-in-glass wafer with embedded titanium. The ‘cracks’ are not in the glass but titanium and due to the intrinsic stress of deposited titanium.

2.3.4. Design Rules

The glass-fill problem in small features, such as corners, is one that can be avoided by design rules that maintain the silicon posts, used for vertical interconnect, at a minimum pitch of at least 100 µm. Rounded posts were found to have fewer issues than square posts. A thorough analysis of the limits of this process has not been performed at this time.

2.3.5. Wafer Stress

Wafer stress in these hybrid wafers is a concern; however, due to the similarity in thermal coefficients of expansion and the planarization steps, these wafers do not prematurely crack except in the case of incorrect wafer handling. The coefficients of thermal expansion (CTE) of silicon and borosilicate glass cross around 280° C and become significantly different at higher temperatures. Since the glass reflow process occurs at a much higher temperature, the critical state is the glass transition point T_g, when the glass begins to harden. Intrinsic stress is generated as the ambient temperature decreases while the wafer is cooling. The glass transition point (approximately 550° C for borosilicate glass) is critical in optimizing the reflow process to minimize stress variations through the wafer as well as reducing wafer bow. For tools such as the IPEC CMP used in this work, excessive wafer bow causes tool failure and, often, wafer breakage.

Bowing is virtually eliminated due to the amount of material removed during the planarization and polishing steps, as illustrated in Figure 2.20. As shown, an applied force during planarization pushes the wafer flat. The wafer attempts to return to the bow-shape and in turn exerts a higher force at the edges of the wafer. This causes these regions to be removed quicker than the center regions of the wafer. The resulting wafer is much thinner, but also as flat as the tool uniformity will allow.

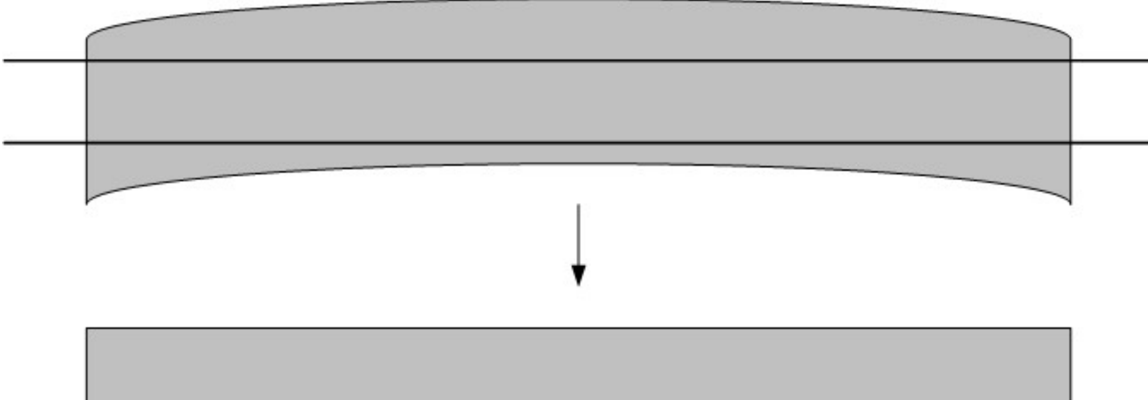

Figure 2.20. (Top) Wafer bow before planarization; (bottom) flat and thinned wafer after planarization

2.4. Glass-in-Silicon Advantages

This process enables several new possibilities; the following is a short list of new functions that can now be implemented relevant to the intraocular microsystem that previously were impossible or very challenging to accomplish.

2.4.1. Die Release

Since this method takes advantage of selectively removing silicon, it can be used for die separation instead of the conventional mechanical sawing methods. With this method, harsh vibrations, which can cause delicate microstructures to break, are eliminated entirely by using a gaseous etchant such as XeF_2. Furthermore, this is a batch-level process so that all die are simultaneously released in a single step, something not possible using conventional die singulation. If faster etch rates are desired and elevated temperatures are acceptable, ethylenediamene pyrocatecol (EDP) can also be used to selectively etch without a mask as long as important silicon is protected by a Cr/Au evaporated stack. EDP stops on highly-boron doped silicon and is therefore the preferred method of die release for pressure sensors since it will simultaneously remove bulk silicon and separate the glass-in-silicon wafer into individual die.

2.4.2. Material Properties

In conjunction with the device release, a broader, more general advantage becomes apparent due to the nature of having two very different materials coexisting in the same wafer. In this manner, the differences between these materials can be exploited laterally. For example, microfluidic devices can take advantage of the hydrophobic nature of silicon versus the hydrophilic nature of glass surfaces. Table 2.2 lists properties that are different between the two materials. Later, a demonstration of the usefulness of glass transparency is given in the form of optical communication and solar power generation for the microsystem. Furthermore, glass is non-conductive, and serves as a good substrate for antennas compared to silicon.

	Borosilicate Glass	Silicon
Transparency (Visible Light)	Yes	No
Thermal Conductivity	Low	High
Hydrophilicity	Yes	No
Crystalline	No	Yes
Acid Etch (i.e. HF)	Yes	No
Base Etch (i.e. KOH)	Slow	Yes
XeF_2 Etch	No	Yes
Plasma Etch (SF_6)	Very Slow	Yes

Table 2.2. Differences between silicon and borosilicate glass.

2.4.3. Feedthrough Hermeticity

The feedthrough should be hermetic since glass forms a chemical bond with the silicon; an additional evaporated metal can further ensure hermeticity. The metal stack also protects the silicon from being etched in ethylenediamene pyrocatecol, as explained in the next chapter. Figure 2.21 is an SEM image of a feedthrough pad showing the coverage of the Cr/Au stack.

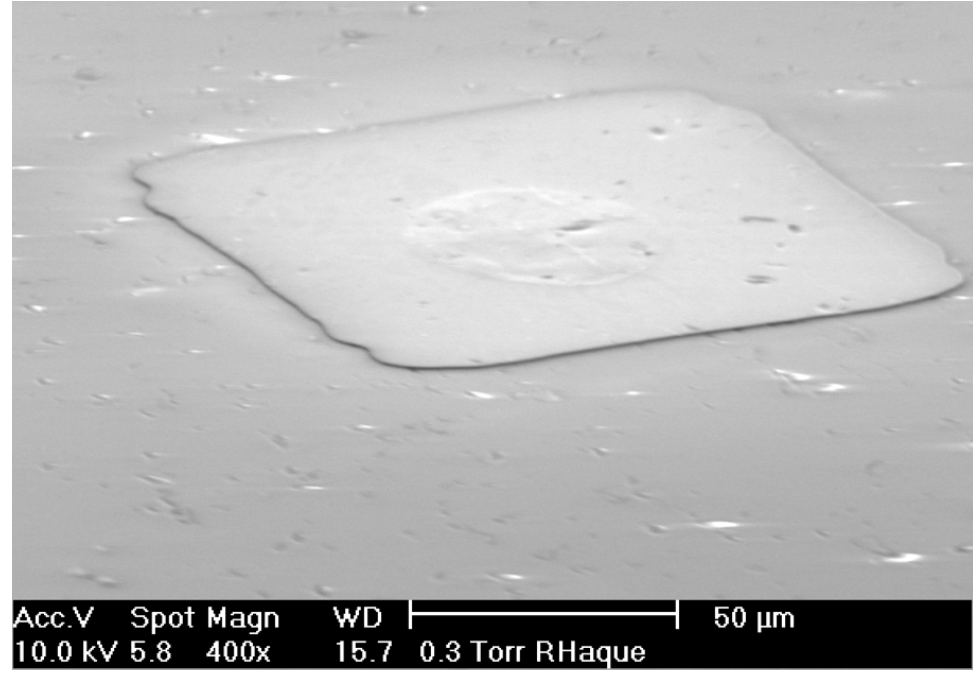

Figure 2.21. SEM image of Cr/Au pad over a cylindrical vertical 50 µm diameter silicon feedthrough.

2.4.4. Electrical Isolation

The glass-in-silicon reflow process has recently been applied to packaging a resonator [40]. In that application, it is important to have excellent electrical isolation in

order to reduce parasitic capacitances. Resonators typically operate with an applied electric field in an electrostatic mode, so any parasitics introduce noise and reduce sensitivity. A glass-in-silicon wafer with an embedded cavity was anodically bonded to an SOI (silicon-on-insulator) wafer to create a transparent cap with embedded silicon feedthroughs. Figure 2.22 shows a photo of the packaged die.

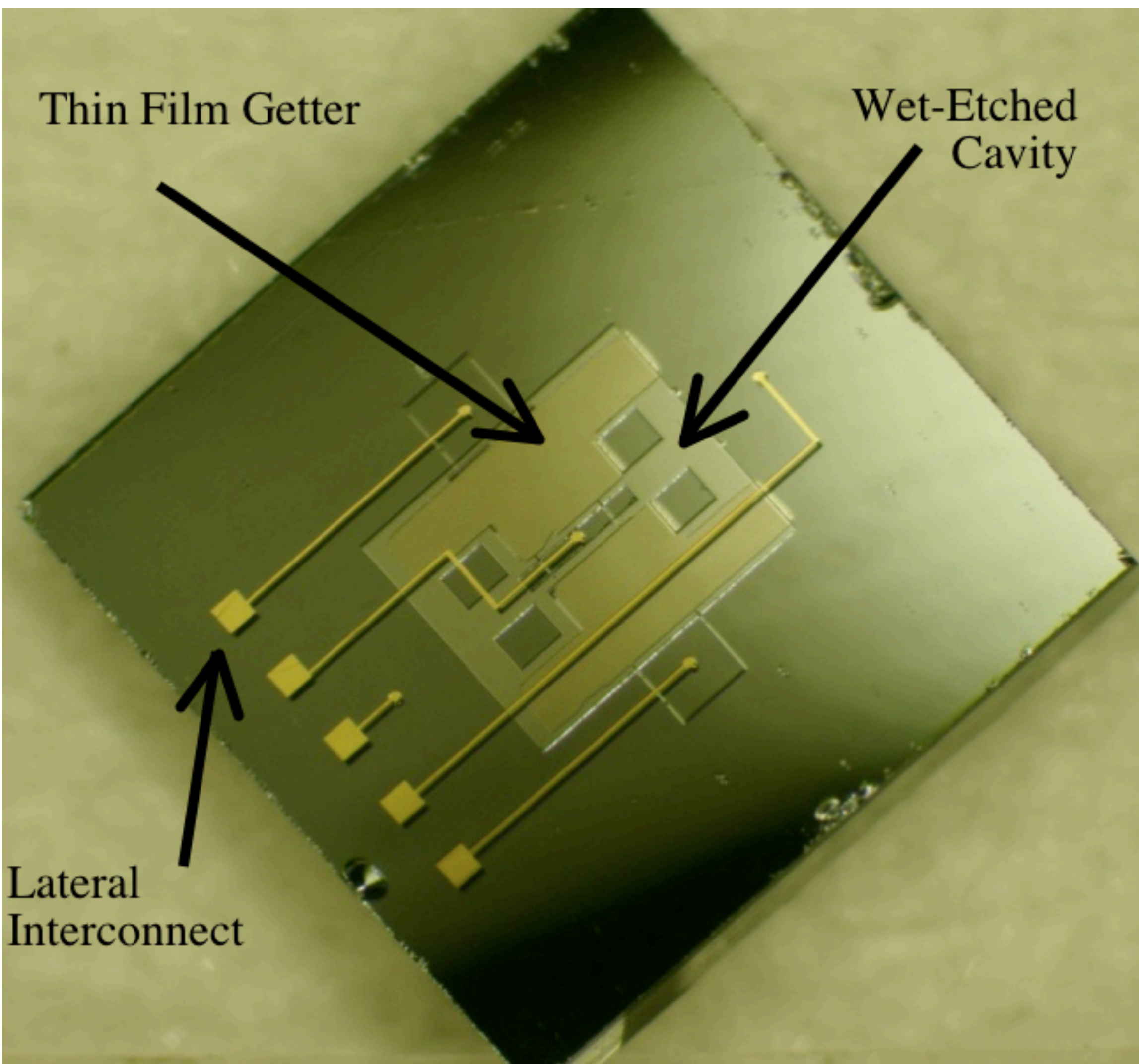

Figure 2.22. Photograph of a packaged and diced resonator sealed with a glass-in-silicon wafer. Silicon feedthroughs are embedded within the glass [40].

The packaged die was placed in an environmental chamber and temperature was swept while monitoring the quality factor. Results indicate that the packaged device is indeed hermetically sealed, although the vacuum within the sealed package could be improved. This was attributed to premature activation of the gettering material. Future

work will focus on improving the gettering activation method. Figure 2.23 shows a plot of the test results proving hermeticity. The conference proceedings from *Transducers 2011* contains more information about this work [40].

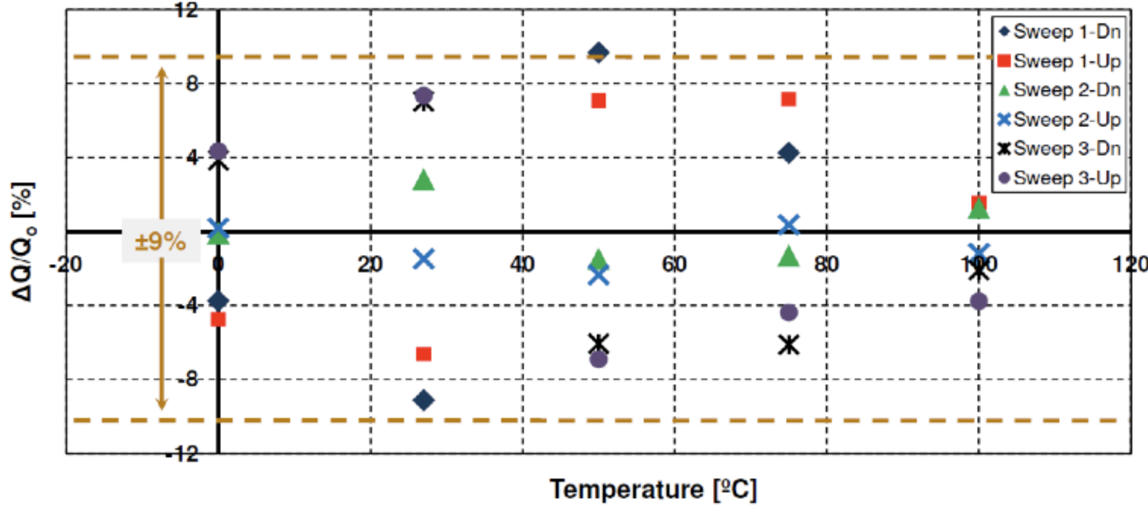

Figure 2.23. Plot of multiple temperature sweeps indicating hermeticity. The change in quality factor of the resonator for each successive sweep is within ±9% [40].

2.5. Packaging

The intraocular microsystem is comprised of up to three independently built modules fabricated on a glass-in-silicon substrate. In addition, an integrated circuit, fabricated using conventional CMOS circuitry is encapsulated within the microsystem. Two of the modules interact with the external environment, while the third provides an energy source. The pressure sensor, presented in Chapter 3, interacts with the local environment through a diaphragm that flexes with changes in pressure. The resulting change in capacitance is used to determine the pressure and is stored in the on-chip memory. The microbattery module is presented in Chapter 4 and includes a cavity in the glass-in-silicon wafer for the integrated circuit. Finally, the antenna module, described in Chapter 6, provides a wireless interface for communication purposes. It too is mounted on the external surface of the package in order to reduce potential sources of interference as much as possible. As each module is vertically stacked, lateral metal lines are used to transfer signals horizontally. Gold-gold contacts are used between each module to ensure good electrical connections. A cross-section demonstrating the modules and construction of the full microsystem along with the dimensions is shown in Figure 2.24.

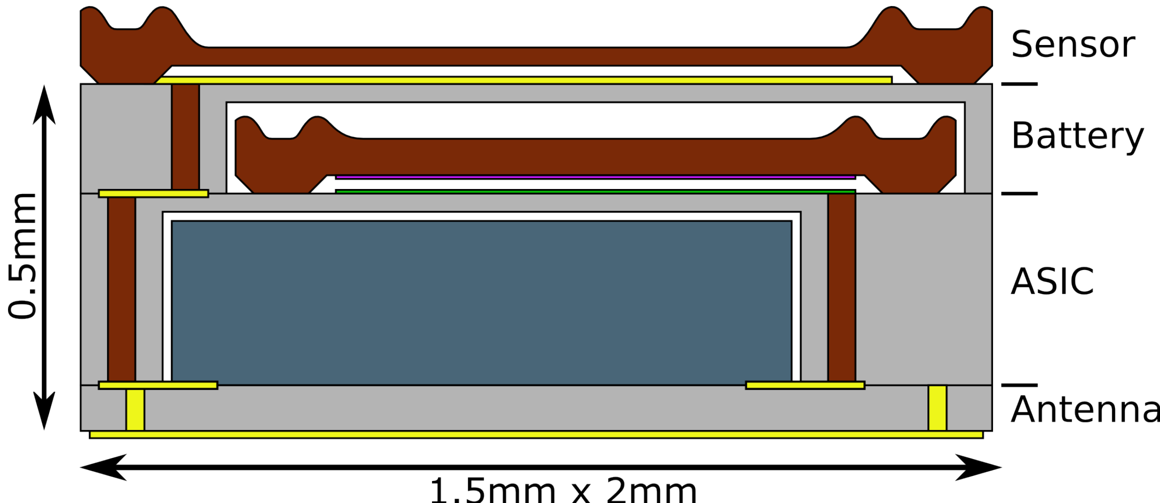

Figure 2.24. Cross-section schematic of the full microsystem.

Additional illustrations, in the form of 3D drawings, are shown in Figure 2.25 and Figure 2.26. Finally, a photo of a partially assembled microsystem appears in Figure 2.27.

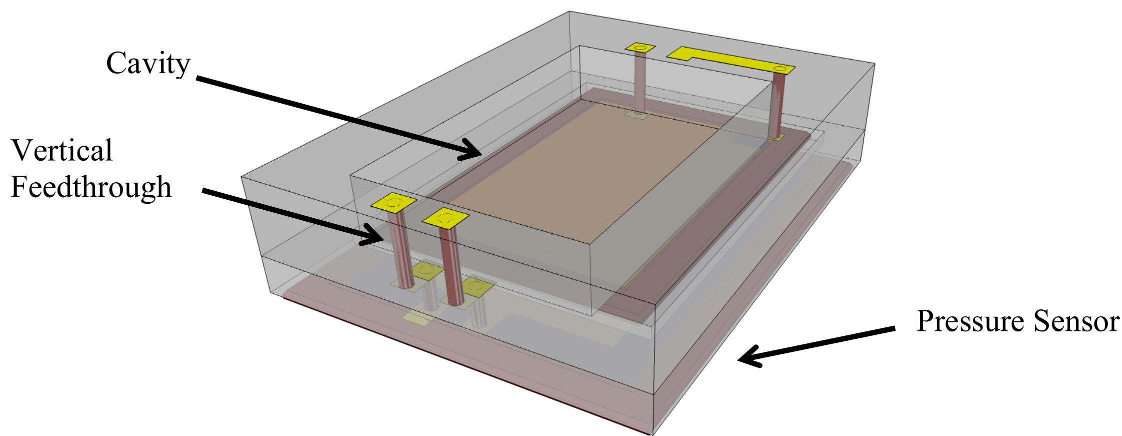

Figure 2.25. Isometric view of the IC cavity in the microbattery module; antenna connections not shown.

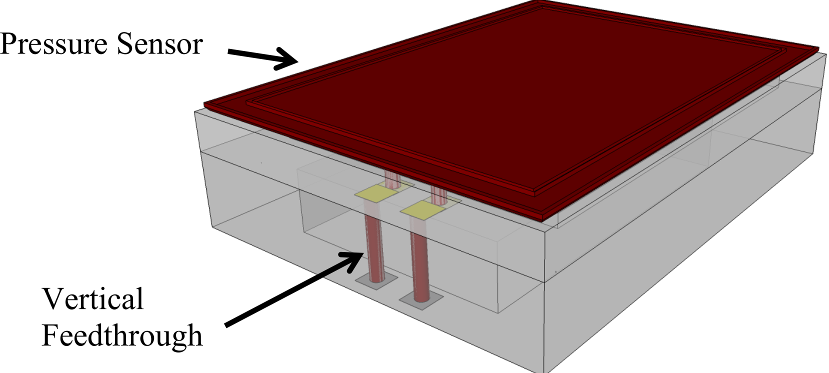

Figure 2.26. Reverse isometric illustration of the sensor; antenna connections not shown.

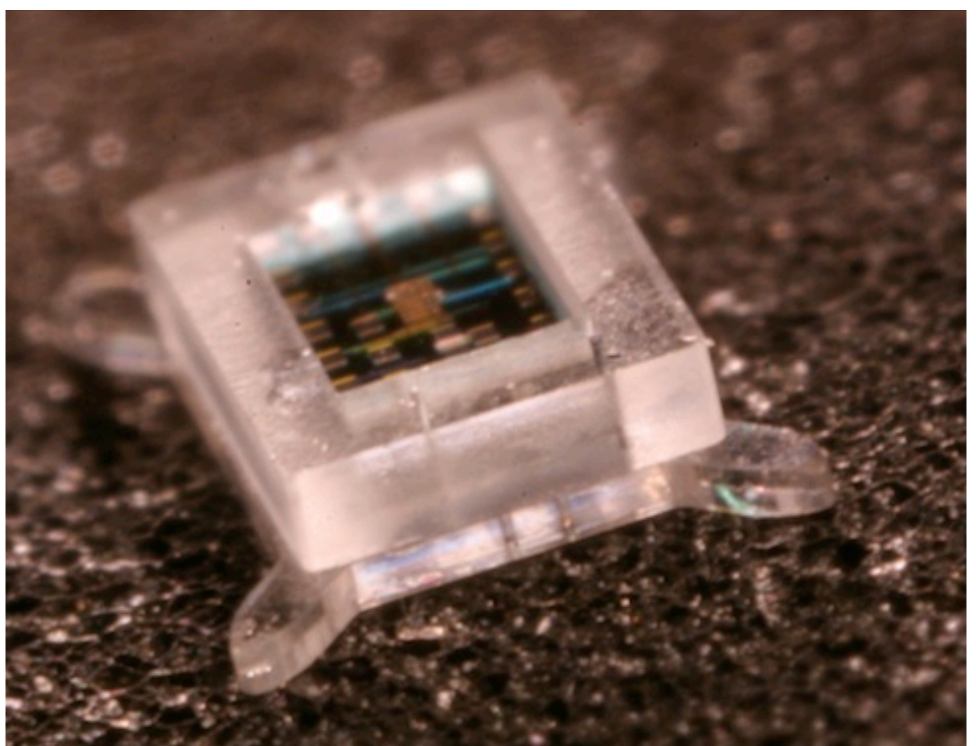

Figure 2.27. Photograph of a mockup of an intraocular microsystem with a custom ASIC (Chapter 5).

2.5.1. Sealing

In order to protect the sensitive microelectronics from the corrosive environment of the body, a hermetic seal would be most useful. However, of all the known microfabrication methods for hermetic sealing on the die level, very few are applicable for this particular application. The most limiting factor is the temperature limit of the microbattery, which is the boiling point of the liquid electrolyte, approximately 100° C. Conventional hermetic sealing techniques such as anodic bonding are not applicable for this reason. Eutectics, such as silicon-gold, also require a bonding temperature above 373° C. Even lower-temperature solders such as indium-tin still require 118° C. Compression bonding (such as gold-gold) requires high forces, which may risk damaging components such as the silicon diaphragm or glass substrate. Alternatives such as polymer or adhesive bonding suffer from some moisture penetration, making the seal less than hermetic.

A combination of two sealing approaches are being used in this microsystem. First, a biocompatible ultraviolet curable glue is used as an adhesive between the two modules. The ability of this adhesive to seal glass is well-documented within the

microfluidics community [41]. Furthermore, these adhesives tend to contract upon curing as the polymeric chains form. This is beneficial since it pulls together the two surfaces, creating a compressive force on the gold-gold contacts that are not perfectly flush with the surface. Test results have shown that the UV glue does not enter between two gold surfaces due to the hydrophobicity of gold. Finally, a coating of conformal parylene is used to encapsulate the entire device. Aside from providing an additional barrier, parylene is an FDA-approved material for implantable devices. Additionally, this coating ensures that in case any portion of the microsystem were to break, the parylene would hold the pieces together for removal as a single unit.

There are other options that are equally tedious for hermetic sealing of the assembled microsystem but may be worth pursuing long-term with dedicated tooling and equipment. For example, laser welding the glass substrates may be a viable option. By embedding an optically absorbent material between two layers of glass, heat is generated causing the glass to melt together. This seems practically a good solution and could provide a hermetic seal. This technique takes advantage of localized heating, so other methods that employ this approach may also be an option as long as the heat does not spread to the microbattery. Evaporated metal along the seam of the glass is another option – a very thin layer is known to provide a hermetic seal [42].

The need for a hermetically sealed package needs to be evaluated further. The pressure sensor must be hermetic, and it is by nature of the anodic bond. A non-hermetic seal would eventually cause the vacuum-sealed pressure sensor to fail. The seal used for electronics cavity should at least prevent moisture penetration since this could lead to corrosion of the sensitive electronics and premature failure. Ideally, a hermetic seal would also be used here as well; however, as previously stated, this is challenging with the current iteration of the microsystem. The current focus of the microsystem is to prevent moisture penetration using a layered approach with ultraviolet-curable adhesive between the modules and an outer parylene layer conformally wrapping the microsystem.

2.5.2. Safety

The safety of any implantable device is a concern that affects all chronic, long-term implants. For example, an inflammatory response in the iris to the implanted device

could prevent normal eye function. Infection should be preventable through proper procedures and sterilization of the microsystem prior to implantation and is not reviewed in this work. The potential for inflammation due to mechanical irritation, for example, can only be accurately determined during live animal studies.

Materials known to be biocompatible have been used in this work, especially glass and silicon, in order to avoid adverse reactions. The final packaged microsystem also includes a final conformal coating of parylene, a biocompatible and FDA-approved material. All three of these materials have been used previously in implantable devices. Some of the materials sealed within the microsystem package are potentially toxic, particularly the electrolyte and electrodes used in the power module. Typical electrolytes such as potassium hydroxide have not been used due to their known toxicity to living tissue. Details are provided in the discussion about the selected materials and electrolyte used in the power module in Chapter 4. However, the very small volume (approximately 15 nL) of the liquid electrolyte would likely not pose a significant problem.

Mechanical failures such as glass breakage or diaphragm rupture are also possibilities that need to be considered. Above all, any failure mode should not in any way create a problem that would compromise the normal function of the eye until the device can be removed. A simple explantation process that does not damage the eye is therefore beneficial. One foreseeable challenge that might occur during implantation of the device is the case where the haptics fracture and break off. In this situation, the parylene coating on the exterior of the device would bind the fractured component to the remainder of the microsystem, simplifying removal of the entire microsystem. Situations like this, when a portion of the device might fracture, are not expected to occur often; however, certain safety precautions should be taken to avert potentially dangerous and damaging situations from developing.

In developing the microsystem and specifically the package design, patient safety in the form of material choices and other sources of problems have been identified. In general, additional studies determining the biocompatibility of the individual materials may not be necessary since these materials are known to be biocompatible. However, when implemented as a complete microsystem, additional unforeseen challenges may become evident in live animal studies.

2.6. Surgical Implantation

While the material choices and design of the intraocular microsystem are important, the implantation procedure is equally important. A system-level approach is required to solve the problem of measuring intraocular pressure. Several important factors play into the application of the device, such as the implant location and orientation as well as the method of inserting the device.

2.6.1. Location

The iris is an ideal location for the implant since it is easy to access via surgical methods and is clearly visible during the operation. Incisions for intraocular lens implants and cataract surgery are similar to the incision proposed here for implanting the intraocular microsystem. Cataract surgery is a common procedure and is minimally invasive. Figure 2.28 is a modified image from Gray's Anatomy [43] indicating the planned location of the implant with regard to the cornea, the pupil, and the iris.

The tradeoff arising from placing the implant in this location is the potential for damaging corneal endothelial cells. The implant must therefore be relatively thin. However, as shown in the illustration, the cornea curves downward near the edge of the iris, suggesting that by moving the sensor closer to the center of the eye, a thicker implant may be possible. However, moving the implant closer to the center of the eye reduces the maximum dilation of the pupil, which may impact the patient's ability to see in dark environments.

2.6.2. Orientation

Another issue with the intraocular implant location is orientation, i.e., which surface is facing the iris and which is facing outwards. In the proposed implant, the pressure sensor diaphragm will be facing the iris. The raised regions around the silicon diaphragm, illustrated in Figure 2.29, are not significant in contacting the soft iris.

The choice of orienting the sensor in this manner is to ensure that the antenna is facing out towards the front of the eye. A signal radiating from the antenna from this position will avoid interference with the sensor, integrated circuit and battery, improving the quality and performance of the wireless signal.

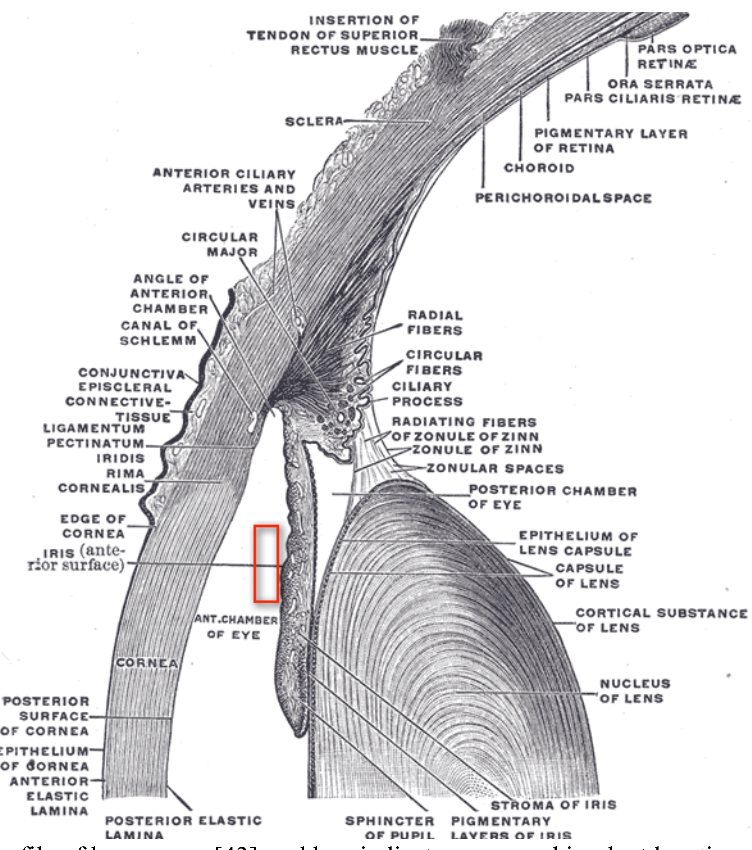

Figure 2.28. Side-profile of human eye [43]; red box indicates proposed implant location

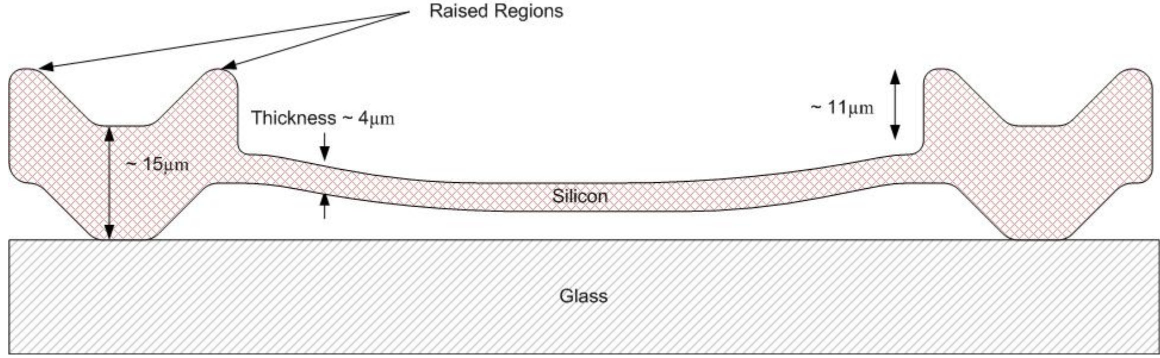

Figure 2.29. Illustration of the physical dimensions of the integrated intraocular pressure sensor.

Another benefit of this orientation is that the top surface of the integrated circuit is also facing out towards the front of the eye. This allows the solar cells located on the circuit chip to be exposed to ambient light from behind the antenna.

2.6.3. Haptics

The intraocular device is not perfectly rectangular. One of the advantages of the glass-in-silicon process is that arbitrary glass shapes can be used to form extensions that

may be used to aid surgical implantation. In this case, the extensions range from 250 μm to 500 μm in length and vary in angle from 45° to 22.5°, all with rounded edges. Each extension is positioned at a corner or center of an edge of the device, extending outwards. An illustration showing several different designs is shown in Figure 2.30.

The proposed surgical concept would allow portions of the iris to be folded over these haptics. The iris is very flexible, consisting of muscle and highly elastic collagen. The advantage with implantation in this manner is that there should be no damage to the iris, and the implant can be easily removed. Figure 2.31 shows a cross-section illustration of an implanted intraocular microsystem on the iris surface using haptics. An example of the haptics fabricated in this work can be seen Figure 2.32.

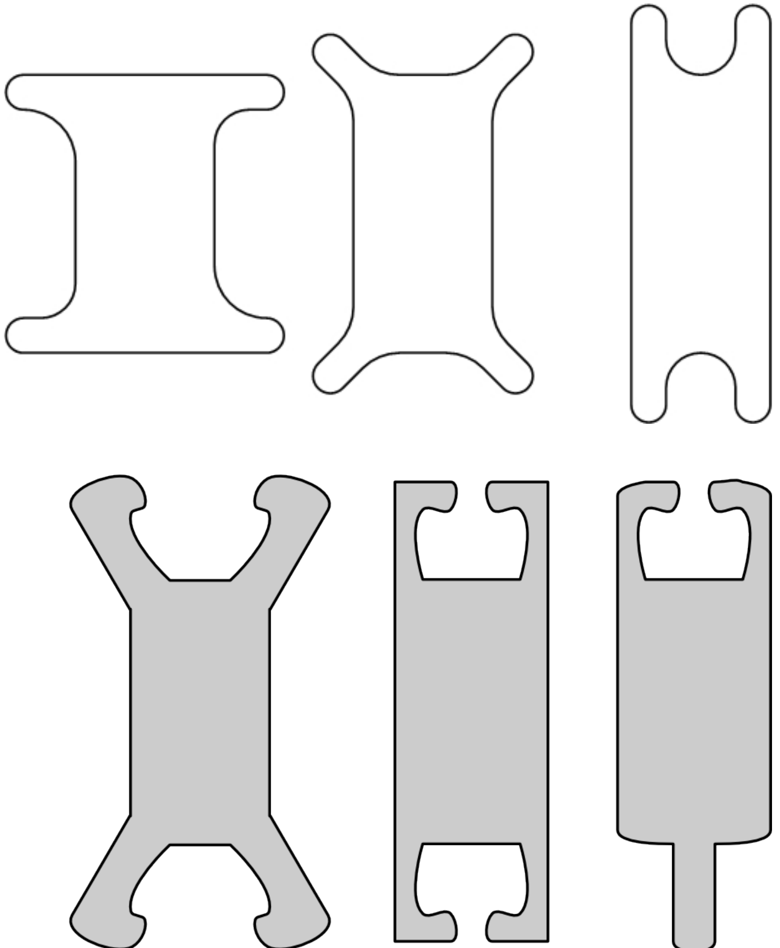

Figure 2.30. Several haptic designs, some fabricated and currently undergoing testing (top) and others for future implantation studies (bottom).

Figure 2.31. Cross-section illustration of implanted device demonstrating how the iris folds over the haptics of the implanted device.

In contrast, one of the most recent proposed intraocular implants suggests using a single hook to pierce the iris [44]. The single anchor point allows the sensor to be implanted in a single step but also suggests that it will be extremely challenging to remove the device if explantation is required, as in the case of device failure.

2.6.4. Initial Experiments

Several experiments, using human cadaver eyes, were conducted at the Kellogg Eye Center at the University of Michigan. Dr. Denise John was able to test different haptic shapes and orientations on the surface of the iris. Unfortunately, all tested human cadaver eyes required removal of the cornea since they were very clouded and made it virtually impossible to see the iris. Figure 2.32 shows the device prior to implantation above the surface of a human cadaver eye, while Figure 2.33 shows the substrate implanted on the surface of the iris.

Figure 2.32. A blank device with haptics is lowered near the surface of a human cadaver eye. Note the cloudiness of the cornea, making it difficult to see within the eye.

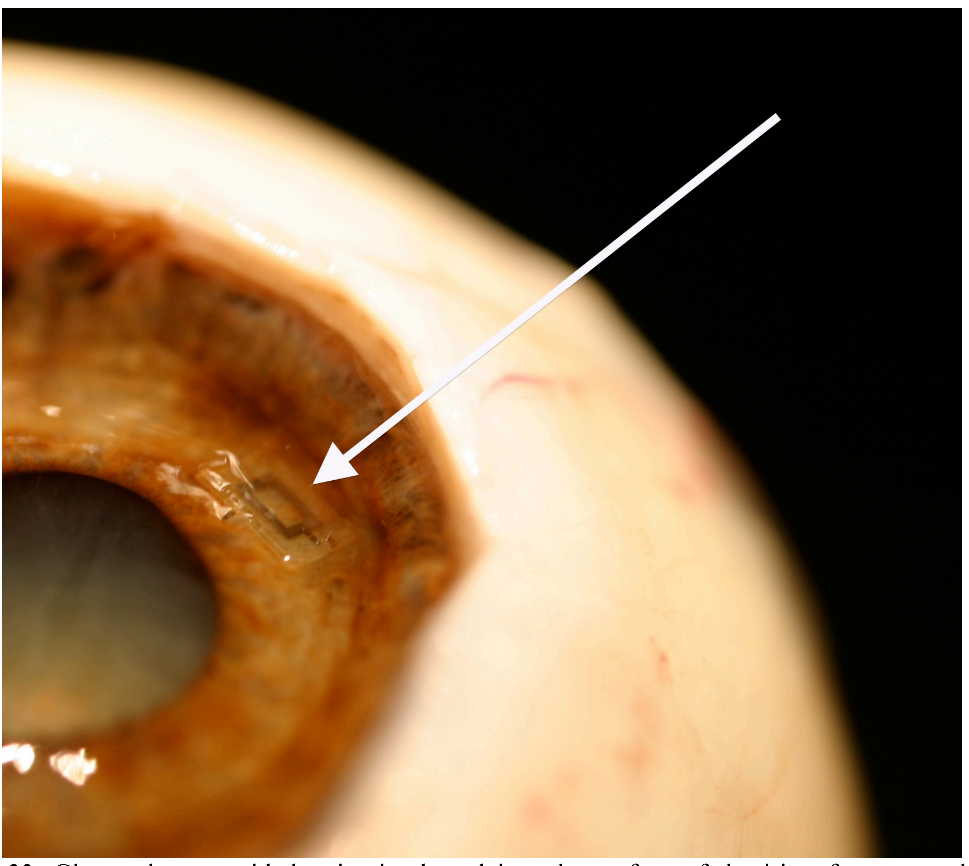

Figure 2.33. Glass substrate with haptics implanted into the surface of the iris, after cornea has been removed.

The next step is to test the haptics in live animals that will exhibit physical motion and more importantly test dilation and how it is affected by the presence of the device. This work is currently being undertaken under Professor James D. Weiland at University of Southern California in conjunction with the Doheny Eye Institute in Los Angeles.

2.7. Summary

This chapter has introduced the foundation of the intraocular microsystem, defining the overall construction of the entire intraocular microsystem. The package, system assembly, and surgical approach all determine the parameters that define the modules that make up this system. It is hoped that the work in this chapter can be implemented across BioMEMS in general, leading to the development of new and useful implantable devices. By targeting an intraocular application, the physical dimensions of this microsystem have been reduced to a scale that has not previously been possible. To this end, a glass-based process has been developed, keeping in mind biocompatibility and

robustness. Hermetic sealing is also an important aspect in order to protect sensitive components. The next several chapters introduce each of the modules that make up the intraocular microsystem, providing the necessary details.

The work in this chapter has demonstrated a new package design for implantable microsystems with distinct advantages that include minimally-invasive dimensions, transparency, and volume-efficient design. The sensor and antenna can be thought of as on-package components, mounted on the external surfaces, while the circuitry and power module are both mounted internally, affording protection from the external environment. The ability of the package to hermetically seal the sensor is of utmost importance, since this will affect the performance of the pressure data and the achievable lifetimes of the microsystem. The next chapter discusses the pressure sensor, which utilizes an anodic bond that has previously been demonstrated to provide the necessary hermeticity. The electronics cavity is not hermetic at this time; however, it is not known how good this seal must be. Long-term testing to determine the ability of the ultraviolet-curable adhesive and the parylene outer layer to prevent moisture from entering the cavity are necessary. Ultimately, a different solution such as solder-bonding may be required if the present seal is not sufficient.

CHAPTER 3

PRESSURE SENSOR MODULE

The purpose of the intraocular microsystem is to measure pressure within the eye. For this particular application, the specific parameters for the pressure variation are important and will determine the necessary functionality. As mentioned in the introduction, typical eye pressures vary from 10 to 21 mmHg above atmosphere [2]. Pressures above 21 mmHg are considered at risk for glaucoma. Pressure is increased in the eye two ways – an increase in intraocular fluid production, or a decrease in intraocular fluid evacuation. Intraocular pressure changes relatively slowly by the nature of these two mechanisms so values recorded every 15 minutes essentially constitute continuous monitoring.

This chapter begins with a discussion of the design of an implantable pressure sensor. The sensor is a capacitive, touch-mode transducer providing a highly linear response over the requisite range of pressures. Simulation using COMSOL, a software tool implementing the finite element method (FEM), is used to evaluate the maximum deflection, shape of the deflected diaphragm, and ensure the yield stresses of the materials are not exceeded. The full fabrication process is provided in detail, utilizing the new silicon-in-glass process described in Chapter 2. Finally, the sensor is tested in a closed environmental chamber and the capacitance of the sensor is recorded as a function of pressure. Surface interactions, a drawback of touch-mode sensors, induce a hysteretic effect, observed when sweeping the pressure in the chamber up and down repeatedly. The touch-mode hermetically-sealed capacitive silicon diaphragm sensor presented here was found to meet the design specifications for this application.

3.1. DESIGN

The structure of a pressure sensor consists of one moveable plate, or diaphragm, above a fixed substrate upon which a sensing electrode is formed. The deflection of the

diaphragm is controlled by the pressure difference on either side of the diaphragm. If one side is hermetically sealed in vacuum, then an absolute pressure sensor results with the measured pressure referenced to vacuum. When vacuum is not referenced, it is called a relative pressure sensor and measures gauge pressure. Relative pressure sensors are more challenging to operate due to the effects of damping and potential for contamination (e. g., trapped moisture) between the diaphragm and sensing electrodes. For this reason, absolute pressure sensors are preferred. However, in order to achieve accurate measurements, the local ambient pressure (typically atmospheric pressure) should also be measured and recorded at the same time. The absolute pressure sensor value is then subtracted from the atmospheric pressure value to determine the relative pressure.

This section begins with the specifications for the intraocular pressure sensor, defining the needed operation range and resolution. The physical operation of the pressure sensor is discussed, distinguishing between touch-mode and gap-mode pressure sensors. The necessary sensor interconnects are explained, and a technique used to avoid many of the associated challenges are discussed briefly, building on the work introduced in Chapter 2. Material properties such as intrinsic stress and yield strength and their effects on the diaphragm are explained. The interplay among all these effects resulting in a calculation of the expected gap is provided as well. Finally, this section ends with a discussion of surface interactions, which are present in touch-mode sensors due to the inherent physical contact of the capacitive plates.

3.1.1. Specifications

Intraocular pressure has a statistically normal range between 15 and 20 mmHg. A measurement range between 10 mmHg and 50 mmHg is therefore adequate for this application. This is a relative pressure value and does not take into account changes in atmospheric pressure. For example, a patient at elevation will experience a different atmospheric pressure than one located at sea level. For this reason, expanding the dynamic range further to account for atmospheric conditions a patient may experience is very important. The absolute pressure range for the intraocular pressure sensor is therefore set from 550 mmHg to 850 mmHg.

Pressure resolution is another important factor for sensor design. Typical tonometric methods, introduced in Chapter 1, have a measurement resolution of about 1 mmHg. An intraocular microsystem must therefore provide similar resolution. However, sensing pressure with a resolution of less than 0.5 mmHg may provide additional useful information, such as the monitoring of intraocular pulsatile flow.

Intraocular pressure is expected to change slowly, on the order of minutes, so a very slow sampling rate is sufficient. Obtaining the pressure at 15 minute intervals should provide adequate data; intraocular pulsatile flow can be captured with faster sampling rates. This flow has an intraocular amplitude of about 1 mmHg and a frequency directly correlated to heart rate [18].

The final specification is size and shape. The sensor was chosen to be rectangular rather than circular or square since this makes the best use of the substrate shape, which is rectangular as explained in Chapter 1. The thickness of the sensor is determined by the capacitive gap combined with the minimum diaphragm thickness required for adequate stiffness, resulting in a total thickness of approximately 30 µm, not including the substrate. Roughly half this thickness is the anchor and the other half is allocated to the gap. Determining the gap is described in a later section and depends on the required pressure sensitivity as well as the thickness of the flexible portion of the diaphragm. The sensor does not introduce any lateral size constraints and is therefore maximized to the available microsystem dimensions. By occupying as much of the available area as possible, the resolution of the sensor can be improved.

3.1.2. Transduction Method

Two methods of converting from the physical domain to the electrical domain are commonly used: piezoresistive and capacitive. Piezoresistors are formed in semiconductors by selective doping. When the material is mechanically deformed, the conductivity through the material changes. Typically, these types of sensors measure changes in stress. Capacitive sensors rely on a physical change in the distance between the two electrodes, resulting in a change in the electric field.

Transducing pressure to changes in stress or gap separation occurs in the mechanical domain. Piezoresistive sensors can be fabricated on a semiconductor surface

on which a bending force or pressure can be applied. As additional stress is applied, the resistance through the element changes. For capacitive sensors, gap changes are typically implemented using a diaphragm that deflects under applied pressure.

Capacitive sensors consume virtually no power, since there is no conductive path through an ideal capacitor. Piezoresistive sensors dissipate power proportional to the current flowing through the piezoresistive element and are therefore not preferred for energy-constrained applications. A discussion of the necessary readout circuitry appears in Chapter 5.

3.1.3. Touch-mode versus Gap-mode

Two operation modes for pressure sensors can be defined based upon the interaction between the diaphragm and the fixed substrate. When the moveable diaphragm never makes contact with the fixed substrate throughout its range of operation, the sensor is called a gap-mode sensor because the gap serves to transduce pressure into the electrical domain. As the gap decreases, the capacitance increases at a rate of $1/d$, where d is the gap distance. When the diaphragm remains in contact with the fixed substrate throughout the entire range of operation, it is called a touch-mode sensor. The total area in contact with the substrate changes with pressure, resulting in a change in capacitance. As pressure is increased, the diaphragm spreads out further, allowing more of the diaphragm to make contact with the bottom electrode.

A single sensing structure can be used in both gap-sensitive and area-sensitive modes, dependent only on the applied pressure. As pressure is increased from zero pressure (vacuum), the gap in the center of the diaphragm approaches zero. As pressure increases further, the center gap eventually reaches a minimum, set either by a mechanical stop or by physical contact of the diaphragm to the bottom electrode. If pressure is increased further, the diaphragm deforms further at the diaphragm edges, increasing the electrode area. Both gap-sensitive and area-sensitive modes are illustrated in Figure 3.1.

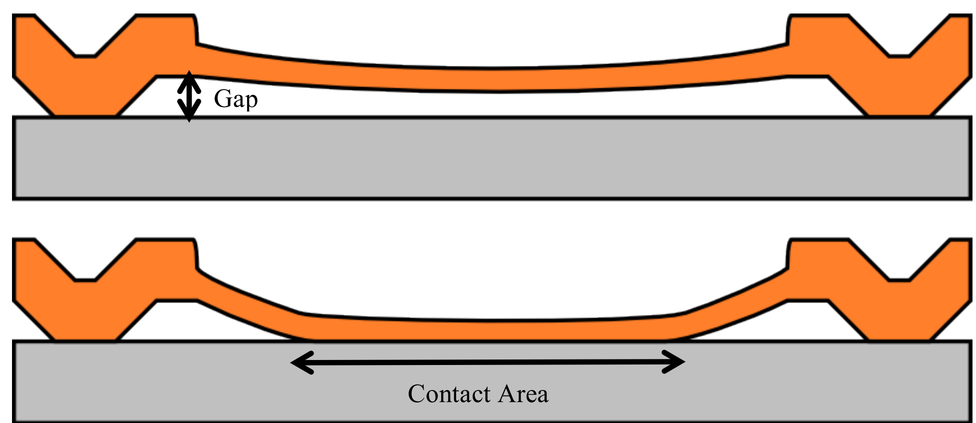

Figure 3.1. (Top) Gap-sensitive diaphragm cross-section; (Bottom) Area-sensitive diaphragm cross-section.

The gap capacitance, C, is defined in Equation 3.1 for a parallel plate capacitor as

$$C = \frac{\varepsilon_0 \varepsilon_r A}{d} \tag{3.1}$$

where A is the surface area, ε_0 is the electrical permittivity of vacuum, ε_r is the relative electrical permittivity of the gap materials, and d is the gap distance between the two electrodes that comprise the capacitor. Gap-sensitive capacitive sensors function based on deflection-induced changes in d, resulting in a capacitance that is proportional to this distance as shown in Equation 3.2.

$$C \propto \frac{1}{d} \tag{3.2}$$

One can easily observe that, for a parallel plate capacitor, this is not a linear function. On the other hand, an area-sensitive pressure sensor would vary with area as shown in Equation 3.3.

$$C \propto A \tag{3.3}$$

This is a linear function that should result in simplified readout circuitry. In the case of the energy and size-constraints of the intraocular microsystem, simplifying the circuitry can imply reduced power consumption. In order to facilitate further understanding of the area-sensitive mode, sensors in low- and high-pressure environments are illustrated in Figure 3.2.

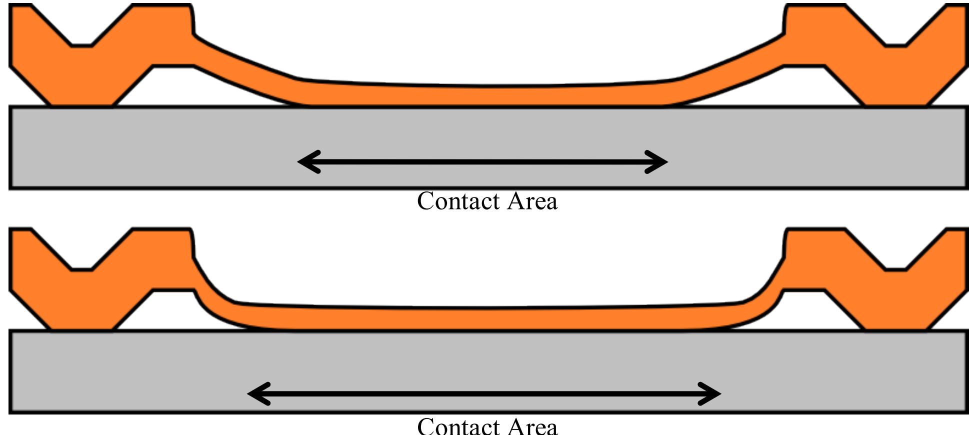

Figure 3.2. Cross-section profile view of diaphragm at two different pressures: (Top) low pressure environment with diaphragm in contact with bottom substrate; (Bottom) high pressure environment.

This type of sensor is preferable compared to a gap-sensitive (non-touch-mode) sensor from a fabrication standpoint due to the relaxed requirements on the design of the sensor. Gap-mode sensors are much more sensitive to process variation by nature; control of the gap is critical and depends on two independent variables: diaphragm thickness and initial gap. Touch-mode sensors must simply be in contact and any additional applied pressure is linearized above that point until the diaphragm shape and non-linear stresses begin to affect the curvature of the diaphragm.

Additional merits of the touch-mode sensor have been identified previously for use in a tire-pressure monitoring system [48]. The robust sensor design, built-in overpressure stop, and good linearity are the three main advantages identified for these sensors. More recently, work on enhancing the operational range of touch-mode sensors has been presented [49]. The work in this thesis does not suffer from saturation of the linear region due to the limited range of operation as well as the large size of the sensor.

3.1.4. Sensitivity

For gap-mode sensors, the highest sensitivity will occur as the gap is minimized. Therefore, it is crucial to design the sensor with the smallest possible gap in the expected range of operation. A built-in mechanical stop exists for these sensors and defines the upper limit of operation when the diaphragm makes contact with the substrate.

A larger diaphragm results in a larger change in area per change in pressure and contributes to the sensitivity directly. However, once the sensor has entered the area-

sensitive regime of operation, the base capacitance has already reached a large value due to the contacted area. This can pose a problem since the larger base capacitance reduces total sensitivity [50]. Reducing the base capacitance is therefore a priority for touch-mode sensors, something gap-mode sensors do not usually suffer from greatly. Other approaches have been proposed [49], but a simpler method is discussed here and suggested for future touch-mode sensors. Eliminating the initial contact area at ambient pressure can drastically reduce base capacitance C_0. This can be accomplished by removing a rectangular region from within the bottom electrode by using conventional metal lithography and therefore a simple change in the mask layout. Figure 3.3 is a top-view illustration showing the suggested solution with the ovular region indicating the part of the silicon diaphragm making contact with the bottom electrode. The remaining electrode should be present only immediately below the portion of the diaphragm that makes contact under applied pressures in the range of interest.

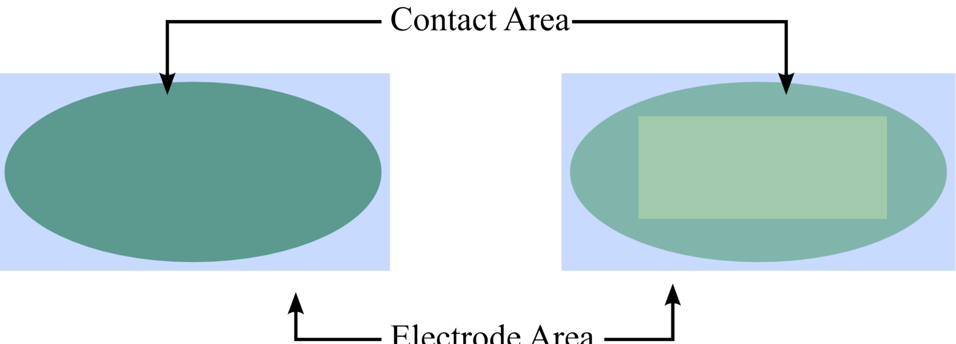

Figure 3.3. (Left) Normal area-sensitive electrode shown in blue rectangle with green oval depicting diaphragm contact area; (Right) Modified area-sensitive electrode, reducing base capacitance.

3.1.5. Interconnect

The internal electrode of a capacitive pressure sensor is typically sealed within a hermetic cavity, making it an absolute pressure sensor. Getting the electrical connection to this reference plate out of the sealed cavity is typically accomplished with the use of lateral interconnects. Chavan and DeHennis proposed two different and successful methods, the first utilizing a chemical mechanical polishing (CMP) process flow over layers of conductive polysilicon and insulating oxide [47], and the second using a silicon-gold eutectic feedthrough electrically isolated in a ‘tunnel’ of deposited oxides [52]. Both require complicated processing steps; DeHennis suggested methods to alleviate

alignment challenges such as a zig-zag shaped feedthrough, improving yield [52]. Chavan studied the minimum width of the silicon-glass anodic bonding region in order to achieve high yield [47]. The reason for the complexity of these feedthroughs is that they can be a major source of vacuum leakage and bond failure.

The only way to avoid lateral feedthroughs is to use vertical feedthroughs embedded within the substrate. This allows the entire bonding region to be flat and uniform without additional processing; the width of the bonding region can be reduced to 100 μm and possibly less if additional surface area is required for the sensing element [47]. The glass-in-silicon reflow process described in Chapter 2 enables embedded vertical interconnects and when applied to a pressure sensor, the diaphragm can be designed to utilize as much surface area as possible in order to maximize sensitivity. Due to the design of the microsystem, the entire surface exposed to the bodily fluid can then be used as the sensing element.

One of the main design goals for the microsystem is to minimize its total volume. The most efficient way to achieve this is to vertically stack its components. This provides several simplifications to the design of pressure sensors since it means that the most challenging aspect of typical designs, hermetically sealing around the lead from the glass reference electrode, is completely avoided. However, this does introduce the added complication of fabricating vertical interconnects that maintain hermeticity. Several previously mentioned solutions, such as laser drilling in glass followed by electroplating [30], were tested but found to be complex, expensive, and low-yield. In order to cost-effectively provide a batch-mode solution, the previously introduced glass-in-silicon reflow process was developed. The glass hermetically seals the vertical feedthroughs as it flows around the silicon posts. Evaporation of a thin-film metal layer over the exposed ends of the feedthroughs provides an additional hermetic seal [64] while simultaneously serving as an electrical contact pad. Pressure sensors based on the dissolved wafer process utilize a glass-silicon anodic bond to provide the final seal. This is advantageous due to the strength of the anodic bond, repeatability, high yield, and simplicity.

The glass-in-silicon reflow process wafer allows anodic bonding as well; however, one additional challenge is introduced. The vertical interconnect through the glass introduces an additional low-resistance path, traditionally not present during anodic

bonding with conventional glass wafers. Without the vertical interconnect, the glass uniformly increases conductivity as the temperature increases, allowing charged ions to move away from the glass-silicon interface. The conductivity through the feedthroughs is very high, however, skewing the electrical field across this interface. The resulting short-circuit essentially bypasses the desired bonding regions entirely, causing most bonds to fail. A solution developed here was to introduce one additional metal masking step consisting of a thick 1.5 μm evaporated aluminum layer on the surface of the glass but not in contact with any vertical silicon regions. This directs the electric field to the glass regions where there is no vertical interconnect, enabling anodic bonding to occur at the glass-silicon interface. Figure 3.4 illustrates this concept in more detail, showing a glass-in-silicon wafer ready for bonding to a silicon wafer. More about the pressure sensor process, including details about the metal spacer film, is described later.

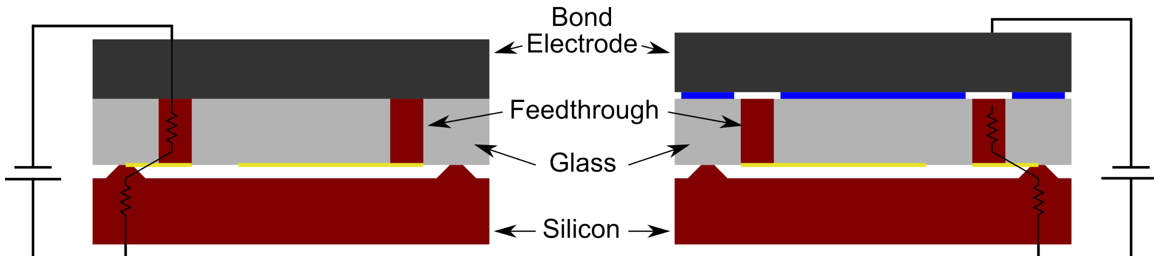

Figure 3.4. (Left) Short circuit path through vertical interconnects embedded in the glass-in-silicon wafer, placed between bond tool and silicon wafer. (Right) Thick aluminum metal layer, in blue, prevents short.

3.1.6. Intrinsic Stress

Intrinsic stress from the various materials used in the diaphragm can have a strong impact on deflection and sensitivity. The effect of stress depends on the thicknesses of stacked materials and the intrinsic stresses (introduced during fabrication) of the materials. Boron-doped silicon has a tensile stress of approximately 40 MPa [47] while thermal oxide has been found to contribute approximately 250 MPa compressive stress [47]. Calculating the composite stress of the thin boron-doped diaphragm with thermal oxide provides a useful approximation of how the combined stress affects the diaphragm. Equation 3.4 can be used to calculate a relative stress σ_c [50].

$$\sigma_c = \frac{\sigma_{si} t_{si} + \sigma_{ox} t_{ox}}{t_{si} + t_{ox}} \tag{3.4}$$

Using Equation 3.4, the composite stress for a 1000 Å-thick thermal oxide and a 4 μm thick boron-doped silicon diaphragm is approximately 33 MPa. The compressive stress of the oxide helps reduce the total stress in the diaphragm, which is helpful in controlling the touch-down point as described in Section 3.3.2. The thermal oxide on the diaphragm also provides electrical isolation in case the capacitor plates touch. For certain modes of operation, the thickness of this oxide also plays an important role in the base capacitance and sensitivity, as discussed in section 3.3.3.

3.1.7. Yield Strength

The maximum yield strength of boron-doped silicon has been previously reported as 7 GPa [47]. In order to ensure that this value is never approached, simulation models were used to ensure the maximum stress never exceeded this value. The maximum stress will appear where the largest bending of the diaphragm occurs. Discussion of the simulation results with additional detail is provided in a later section. If a fracture occurs, the vacuum would be quickly lost, causing the diaphragm to be released from the touch-mode operation and result in sensor failure. The safeguarding design margin is set to less than half of the maximum yield strength, so any value below 3.5 GPa is considered safe.

3.1.8. Deflection

Hand calculating the deflection of rectangular diaphragms is challenging, especially for large deflections where the total deflection is much greater than the thickness of the diaphragm [47], [54]. Understanding the dependence on material properties and geometry, however, can lead to important insights on the performance of the capacitive sensor. Equation (3.5) is the approximate center deflection y_0 for a rectangular diaphragm [54], where E is Young's modulus, ν is Poisson's ratio, a is the width (shorter side), b is the length, h is the thickness, and P is the applied pressure.

$$y_0 = \frac{(12Pa^2b^2)(1-\nu^2)}{Eh^3}\left(292.5\frac{(a^4+b^4)}{a^2b^2}+167\right)^{-1} \quad (3.5)$$

It is clear that the diaphragm thickness plays a very important role in determining deflection characteristics. Any small variation in the thickness can have a very strong

impact on the expected deflection. Dimensions in both the width and length play an important role as well of course, with the shorter dimension serving as more critical dimension, limiting the maximum deflection for the same pressure values. In order to provide a more detailed approximation, COMSOL was used to determine the maximum deflection and maximum stress versus pressure in the structure. The parameters for these simulations will be described in Section 3.3.

Controlling the total deflection is quite challenging because it depends on at least three independent variables. The first is the boron etch-stop thickness, which varies with furnace time at a fixed temperature and also with the distance from the solid boron oxide source. The second variable is the cavity etch depth, which is limited by the accuracy of the etch bath mixture (KOH), the temperature of the etch solution, and the etch time. Temperature variation and non-uniformity in the etch bath can result in significant etch depth variations from wafer to wafer and across a wafer. The third source of variation occurs during the final etch release step when the diaphragm is formed. Ethylenediamine pyrocatechol (EDP) is the preferred silicon etchant since it provides a very effective etch-stop based on concentration. However, etch rates of EDP are highly dependent on temperature and saturation of the solution. Furthermore, the etch-stop is not perfect; that is, the etch still continues, albeit much more slowly, beyond a boron concentration of about 1×10^{19} cm^{-3} [55]. Additional sources of variability in device sensitivity may include the inaccurate modeling of material properties of variables such as Poisson's ratio or Young's modulus for varying boron-doping densities in the silicon. Even if one can successfully take into account all these variables when designing a pressure sensor, the non-uniformity across-wafer and wafer-to-wafer variability can reduce yield. An optimal solution would be to use different diaphragm materials that allow better uniformity and process control or operate in touch-mode where most of these parameters have reduced effect. The pressure sensor presented in this work focuses on the latter approach, building on the expertise developed in the dissolved wafer process and improving sensor performance.

For this work, the diaphragm was set to the largest available surface area, limited only by the width of the anchor (bonded rim) regions, to maximize the sensitivity of the sensor. COMSOL was used to analyze the structure. The purpose of the mechanical

simulations was to determine the maximum expected deflection at ambient pressure and to ensure that applied pressures within the operating range do not cause the diaphragm to exceed the yield strength and fracture.

Aside from setting the initial dimensions of the diaphragm, the simulation tool allowed the testing of different diaphragm thicknesses, both in maximum deflection and to ensure the maximum yield stress is not exceeded. Optimization of the physical dimensions was performed during the simulation stage, where the target thickness of the diaphragm was determined and maximum stress could be checked to ensure the diaphragm will not fracture prematurely.

3.2. Surface Interactions

The interaction between the surfaces of the silicon diaphragm and the bottom metal electrode on the glass requires additional discussion since this effect is not present in gap-sensitive sensors. A hysteretic effect not present in gap-sensitive pressure sensors is observed in touch-mode sensors, as will be shown in Section 3.5.2. A brief discussion of the components that contribute to this surface interaction are discussed here, followed by potential solutions proposed in the literature.

3.2.1. Background

The study of interactions among surfaces when they come in contact is called tribology. Adhesion, friction, lubrication, and wear relative to the motion of another surface fall into this category. In the case of a touch-mode sensor, these effects need to be understood and evaluated.

MEMS operating in contact have been known to fail due to excessive surface-surface forces. Stiction is typically defined as the adhesion of two surfaces in contact to one another [57]. However, friction and wear are also relevant due to the scale of MEMS. In this work, only the adhesion forces are explored since friction is expected to be less than the spring force of the diaphragm and the applied pressure. Furthermore, friction usually involves lateral shear forces that are absent here. There are two main categories of stiction that may develop – during processing and release and during normal operation. Devices that avoid failure during processing depend on preventing contact

from occurring or having enough restoring force to achieve separation whereas touch-mode sensors deliberately require and operate in contact.

3.2.2. Adhesion Sources

Two main sources of adhesion relevant to touch-mode pressure sensors are capillary forces and surface energy. Moisture is an important source of capillary forces since oxides are hydrophilic and can adsorb water vapor [57]. Essentially, a meniscus forms at the edges of the contact area, resulting in a force that holds the two surfaces together. Surface energy, on the other hand, deals with the molecular interaction between two surfaces. Each material-material interface can be expected to exhibit a different surface energy. Some materials, such as Teflon-like coatings, exhibit lower surface energies whereas others increase the total surface energy of the system. Mastrangelo defined intersolid adhesion as the balance between the elastic energy of a bent beam and the surface energies. Equation (3.6) shows the total energy U_T of a cantilever beam [58], where E is Young's modulus of the beam, I is the moment of inertia for the particular shape, h is distance the beam bends to reach the opposing surface, s is the distance from the anchor to the point where the beam touches down, l is the length of the beam, w is the width of the beam, and γ_s is the surface energy density.

$$U_T = \frac{6EIh^2}{s^3} - \gamma_s w(l - s) \tag{3.6}$$

In the case of the touch-mode pressure sensor, studying this energy balance and adjusting the components to reduce the impact surface energy will undoubtedly reduce adhesion forces and the effects of stiction. However, when modifying the mechanical properties of a device such as a pressure sensor, the sensitivity will also change. Electrostatic forces may also be present, especially when the diaphragm is interrogated by applying an electric field across the dielectric, such as the case of a moveable plate capacitor. It has been reported that charge trapping at the interface of the dielectric can be a major source of stiction for electrostatic actuators [59]. Lesser forces such as van der Waal's interactions and hydrogen bonding are also sources of stiction.

3.2.3. Solutions

Multiple solutions have been proposed for combating the effects of stiction. Three principal methods have been identified previously [58]: surface texturing/ roughening, low-energy coatings, and fluorinated coatings.

Surface texturing involves the physical modification of the surfaces of the contacting materials. The main purpose of this technique is to reduce the contact area by introducing asperities, either locally or globally. Mechanically 'dimpling' the surface could be considered local (large-scale asperities) whereas surface roughening would be considered global. A dimpled surface is essentially a surface with raised regions that reduces the total contact area. Deliberately introduced during a specific processing step using lithography, the dimpling solution can still suffer from other drawbacks, such as a required flat surface and increased adhesion forces at the dimple [58]. Surface roughening may not require an explicit lithographic step and therefore may be a viable solution. Isotropic etchants such as XeF_2 have been used to roughen silicon, forming micropits in any exposed silicon.

Special coatings in the form of monolayers have also been explored. A self-assembled monolayer film such as octadecyltrichlorosilane has been studied and functions by silanizing the surface and making it hydrophobic. The resulting contact angle is greater than 90°, resulting in a capillary "push" [58]. This is important for the device presented here because the thermal oxide layer is known to be hydrophilic. Changing the surface to hydrophobic would help prevent moisture and humidity from forming an appreciable capillary force, especially critical for transducers open to the ambient environment. The monolayers also serve a second benefit by reducing the adhesion energy. Unfortunately, the stability and repeatability of these films has been shown to degrade due to contamination [60]. However, the hermetically-sealed pressure sensor in this work may not suffer from these problems since monolayer films have a finite source of contaminants and the sensor is sealed so no additional contaminants can enter [61]. Finally, atomic-layer deposition has also been explored to deposit a hard coating in the form of Al_2O_3 to reduce wear [62].

Teflon-like coatings, often byproducts of a plasma-based etch utilizing fluorinated compounds, can also reduce surface energies. Teflon is a common material used to

reduce friction and results in hydrophobic surfaces. However, the controlled deposition of these types of materials may be difficult due to the conformal nature of plasmas. Maboudian also suggests the use of a conductive layer on any contacting dielectrics, presumably in the form of an internal electrode dedicated to carrying away built-up charge from the contact area [57].

Finally, one potential solution to avoid electrostatic pull-in effects that can further exacerbate stiction is to alternate the direction of the applied electric field between sequential measurements. The net movement or alignment of charges in the dielectric and along the surface can be controlled in this manner and the average electrostatic force generated may be rendered ineffective.

The literature has explored many potential solutions to resolve the problem of stiction. Most rely on the fact that reducing the surface energy is of utmost importance. To this end, Mastrangelo recommends low-energy coatings as the best choice [58]. Incorporating such methods may be a simple matter of an extra deposition step. In combination with surface roughening, the adhesion of the materials making contact in a touch-mode sensor is expected to be dramatically reduced compared with devices where no attempt at reducing surface interactions is made.

3.3. Simulation

COMSOL, an FEM tool, was used to simulate the deflection, stress, and contact areas due to applied pressure. Simulation results develop a quick understanding of the maximum deflection and stress experienced by the diaphragm. The tool simply requires dimensions, applied forces, and material properties in order to conduct the simulations. However, in order to determine capacitance, a solution implementing multiple physics domains is necessary, requiring an FEM simulation in both mechanical and electrical domains. This is challenging for the tool because of the nature of a contact-mode sensor so an alternative method of determining capacitance is used. By simply calculating a surface integral of the deformed shape of the diaphragm and the gap, a close approximation of the capacitance can be determined. The effect of intrinsic stress on capacitance can also be determined.

3.3.1. Yield Strength

Mechanical simulations were used to ensure that no part of the diaphragm approaches the maximum yield strength of silicon, which could result in fracture and breakage of the diaphragm. The mechanical properties of the materials are important to evaluate such simulations correctly. Data for highly boron-doped silicon diaphragms were previously published and used with other finite-element modeling (FEM) tools such as ANSYS [47]. The required parameters are shown in Table 3.1. COMSOL was set up to allow contact and non-linear large-deflection modeling.

Young's Modulus (GPa)	170
Poisson's Ratio	0.066
Fracture Stress (GPa)	7
Density (kg/m^3)	2.328
Intrinsic Stress (MPa)	40
Thermal Expansion (K^{-1})	2.60E-06

Table 3.1. Material properties as used in simulation [47]

The maximum stress achieved for a vacuum-sealed device operating at well-above atmosphere (900 mmHg absolute pressure) was simulated and found to be below the stress fracture limit of 7 GPa. A safety margin of half the stress fracture limit was suggested earlier, setting the maximum acceptable stress to 3.5 GPa. This would take into account fabrication differences between die. This die variation may be due to sharper etch profiles, surface roughness irregularities, and variations in the stresses of the materials. As shown in Figure 3.5, the maximum simulated stress is below 0.25 GPa, well below an order of magnitude of the safety margin. Therefore, no compensation is necessary to ensure the sensor will not fracture during normal operation due to excessive stress. It is important to note that this stress value is plotted for various applied pressures up to 900 mmHg and across only one edge of the diaphragm because this is where the maximum stress is expected to occur. The von Mises stress over the entire diaphragm is shown in Figure 3.6, showing where the maximum stress occurs at the maximum applied pressure of 900 mmHg across the top surface of the diaphragm. The diaphragm edges are fixed and unmovable. The simulation solves the deflection of the diaphragm from the applied pressure.

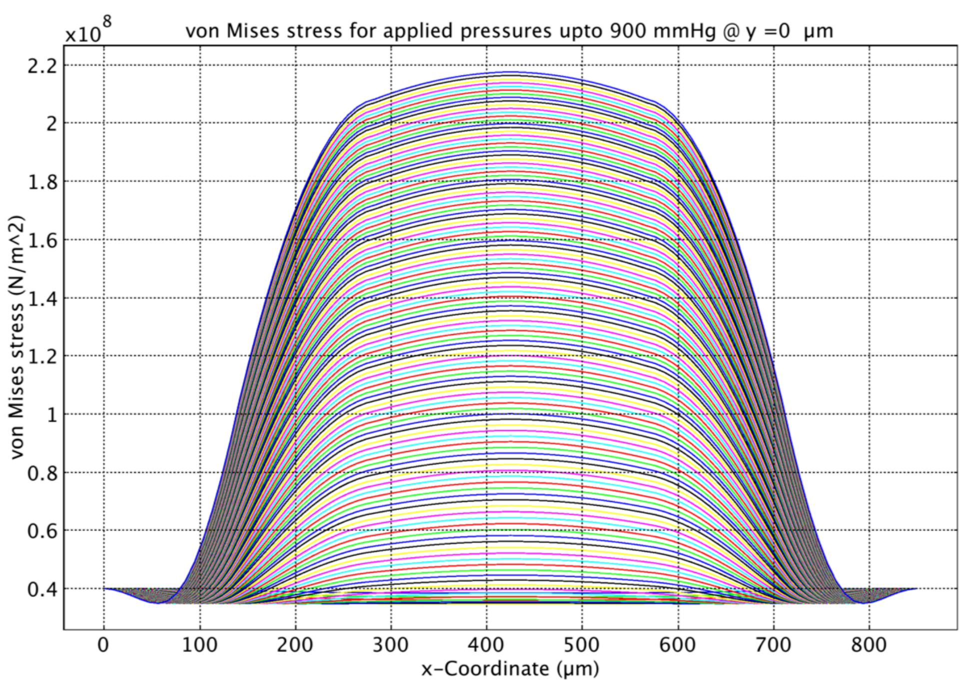

Figure 3.5. Stress plot over increasing pressure along x-dimension of short side of diaphragm.

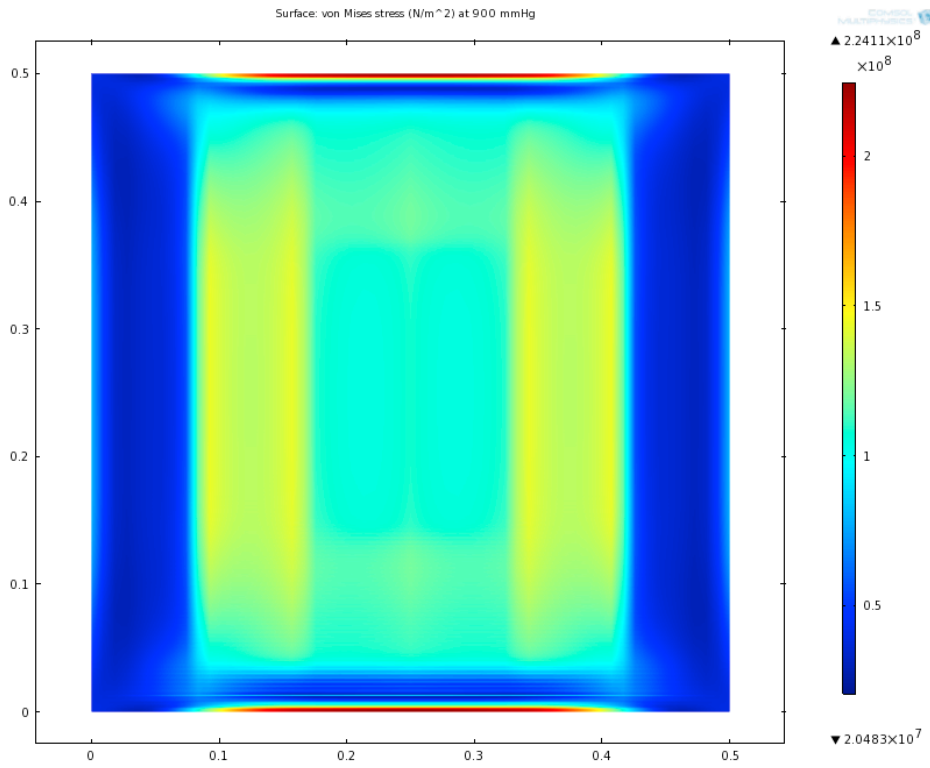

Figure 3.6. Stress across bottom surface of the diaphragm. The dark blue regions indicate zero or low stress, evident in the corners. Maximum stress (red) occurs on the short side of the diaphragm.

Simulation parameters are shown in Table 3.2 for a fixed diaphragm thickness of 4 µm. The cross-section of the deflected membrane appears in Figure 3.7 along the

center of the diaphragm. Figure 3.8 provides a 2D model of the deformed shape of the sensor at an applied pressure of 900 mmHg.

Height	1650 μm
Width	850 μm
Thickness	4 μm
Maximum Deflection	~15 μm
Maximum Stress	0.224 GPa

Table 3.2. Simulation results for specific height, width, and thickness

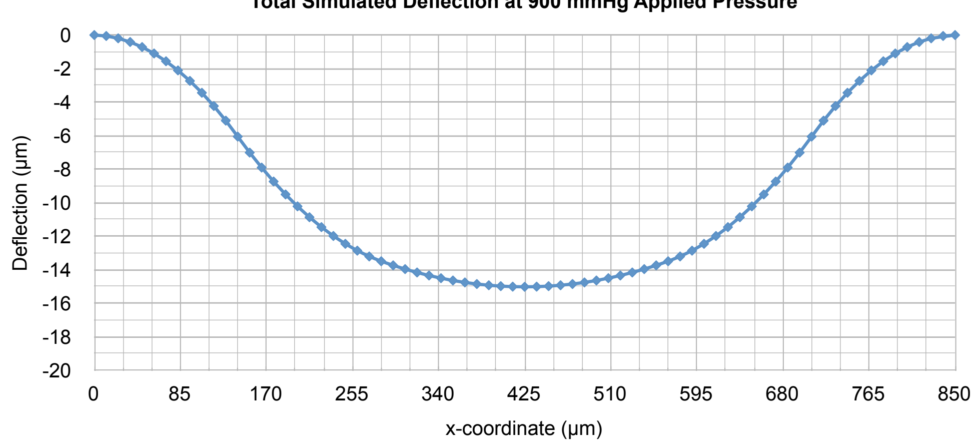

Figure 3.7. Total deflection for an applied pressure of 900 mmHg for a cut-plane along the center of the diaphragm (y-coordinate = 825 μm).

Diaphragm Deflection at 900 mmHg

Figure 3.8. 3D plot of diaphragm deflection.

3.3.2. Intrinsic Stress

Intrinsic stress and the effect this stress can have on the total deflection was discussed in Section 3.1.6. COMSOL was used to simulate diaphragms with and without intrinsic stress. It is clearly shown in Figure 3.5 compared to Figure 3.9 that the maximum stress is reduced from 389 MPa to 224 MPa when intrinsic stress is included. The simulation results confirm that intrinsic stress has little impact on the deflection of touch-mode sensors, but it does shift the response of the sensor, as shown in Figure 3.10. In other words, the larger the intrinsic stress of the diaphragm, the smaller the contact area.

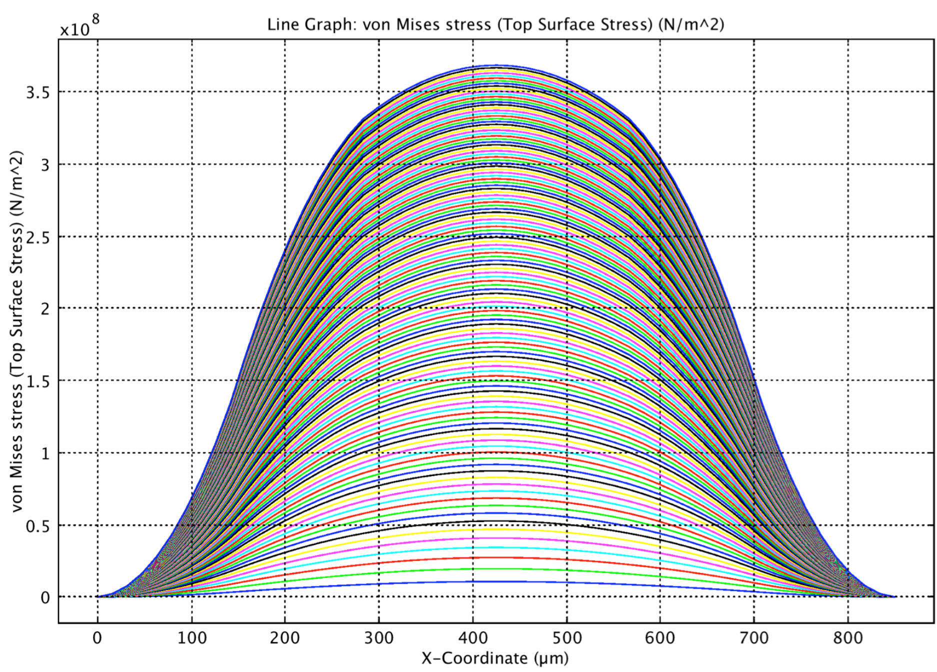

Figure 3.9. Stress of diaphragm without intrinsic stress included in the material properties. Note the increased maximum stress as compared to Figure 3.5.

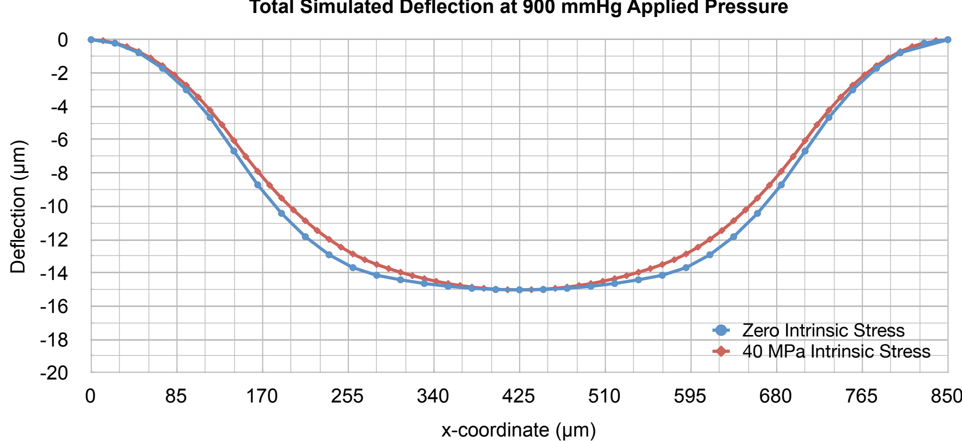

Figure 3.10. Comparison plot showing deflection of diaphragm with zero intrinsic stress and with 40 MPa intrinsic stress at the same applied pressure, resulting in reduced contact area.

3.3.3. Capacitance

Because Equation 3.1 assumes a parallel plate structure in order to accurately calculate capacitance, it is invalid for the deformed diaphragms of gap-sensitive pressure sensors, which are not perfectly flat. For area-sensitive pressure sensors, the capacitance may be more accurate assuming the contact area is known since this area closely models a parallel plate capacitor. In order to avoid possible error, a mathematical solution based

on FEM simulation results was adopted. Equation 3.7 is used to calculate capacitance using a surface integral over the x and y dimensions and the average deflection of each element used in the FEM simulation.

$$C = \varepsilon_0 \varepsilon_r \iint \frac{1}{d}\, dx\, dy \tag{3.7}$$

Increased accuracy is attained by expanding Equation 3.7 to include the series capacitance of the gap and the thin silicon dioxide used as a mechanical stop and insulator on the diaphragm. This equation is shown in Equation 3.8, where t_{ox} is the thickness of the insulating layer and ε_{ox} is the permittivity of silicon dioxide.

$$C = \varepsilon_0 \iint \left(d + \frac{t_{ox}}{\varepsilon_{ox}} \right)^{-1} dx\, dy \tag{3.8}$$

The results of this data are shown in Figure 3.11. As can be clearly seen, the sensor has three distinct modes of operation. Also note that the sensitivity of the sensor depends on the thickness of the isolation oxide. For a 1500 Å thick oxide, the sensitivity in the touch-mode region is about 20 fF/mmHg while for a 1000 Å thick oxide, the sensitivity is approximately 26 fF/mmHg. Therefore, a thinner oxide will increase the sensitivity of the sensor but will also increase the base capacitance by about 10 pF.

Similarly, the effect of internal stress on total capacitance is important to understand. Figure 3.12 shows that for the same oxide thickness of 1000 Å, the touch-down point, or pressure at which touch-down mode commences, has shifted drastically by about 250 mmHg. The actual stress of the diaphragm or the thermal oxide is not critical; rather the composite stress will determine the touch-down point. If the stress is too high, then the sensor measurements at the lower range will result in non-linear behavior. It is therefore important to ensure the composite stress of the diaphragm is below a certain threshold value. A thicker thermal oxide or oxide with higher stress will help offset this problem, as suggested by Section 3.1.6. It was calculated that thermal oxide of thickness 1000 Å shifts the composite stress from 40 MPa to 33 MPa. A thicker oxide would again improve this value but at the cost of reduced sensitivity as explained earlier in this section.

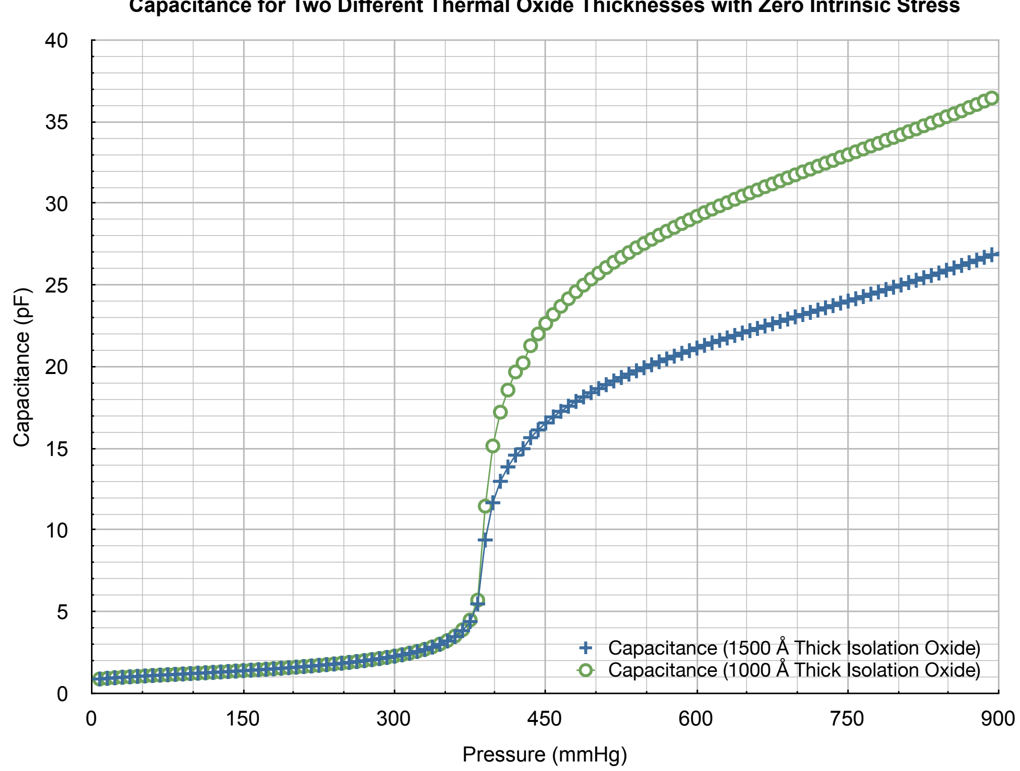

Figure 3.11. Simulated capacitance for a range of pressures without intrinsic stress.

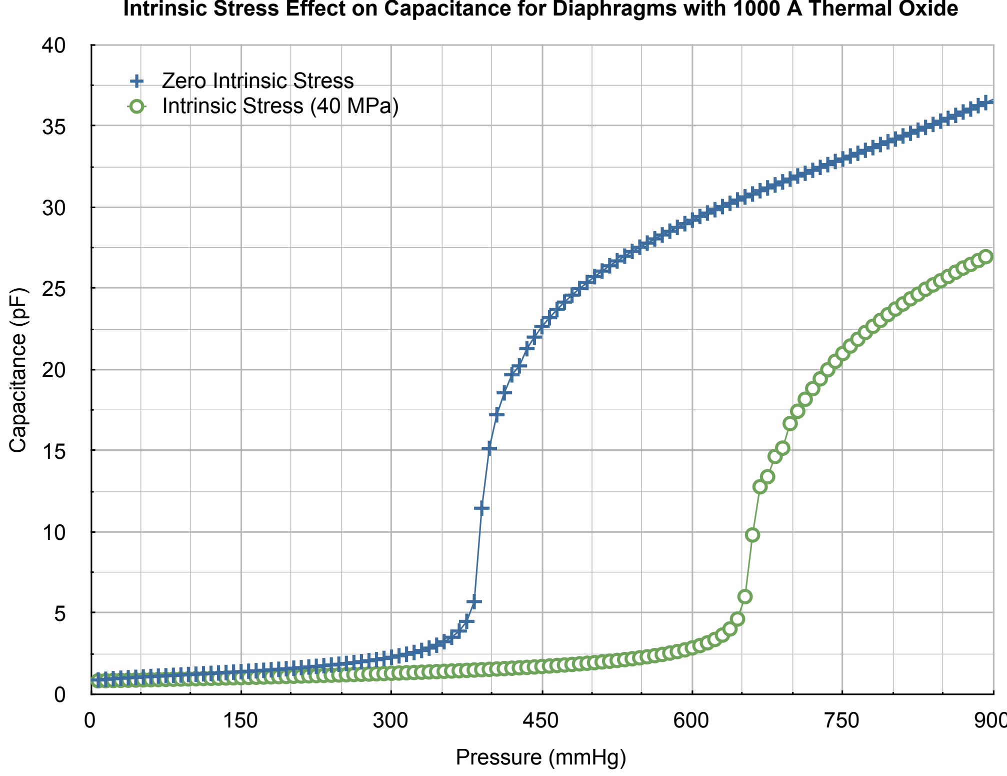

Figure 3.12. Effect of intrinsic stress on capacitance. The touch-down point, or the pressure at which touch-mode begins, shifts to much higher pressures.

3.4. FABRICATION

The fabrication process is similar to previous work but with some major simplifications and the inclusion of vertical feedthroughs. The substrate of the pressure sensor is a glass substrate fabricated using the silicon-in-glass process, providing two highly-doped silicon posts as electrical interconnect. The pressure sensor itself is designed using the dissolved wafer process (DWP) in order to remove the bulk silicon, controlling diaphragm thickness [53].

3.4.1. Layout

For this work, the diaphragm area was set to 1650 µm x 850 µm to make the most use of the available surface area and maximize sensitivity. The layout of the pressure sensor appears in Figure 3.13. The corresponding layer definitions appear in Figure 3.14. In this particular design, the two feedthroughs are circular, with diameters of 100 µm and centers spaced from the edge of the substrate by 250 µm.

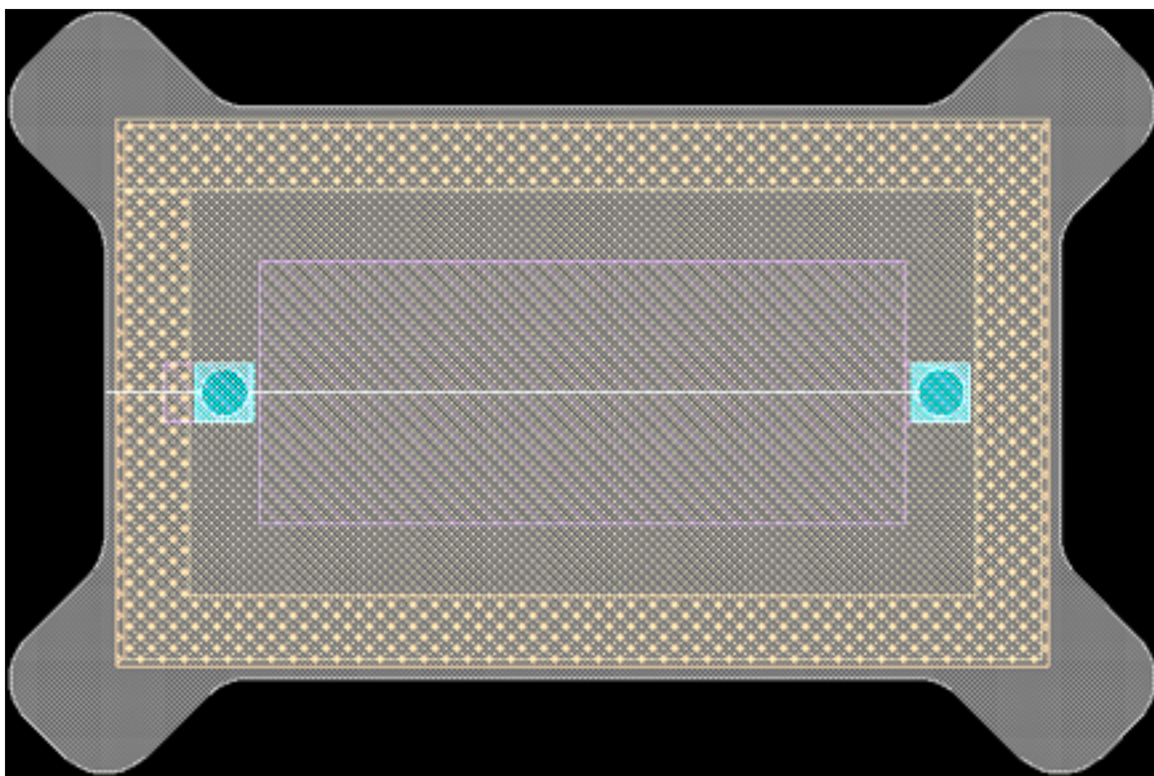

Figure 3.13. Layout of one pressure sensor

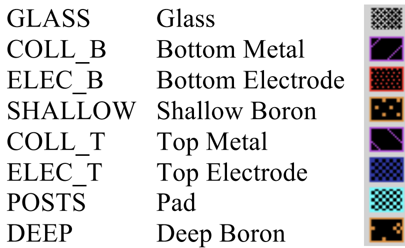

Figure 3.14. Selected layers shown in the layout of Figure 3.13

The full wafer layout appears in Figure 3.15, realizing 828 die on a single 4" wafer. Reducing areas used for alignment marks and moving the die closer together might have allowed for the inclusion of additional die. The two empty regions along the horizontal center of the wafer contain only alignment marks.

Figure 3.15. Full wafer layout

3.4.2. Process Flow

An overview of the process flow is shown in Table 3.3, and a detailed process flow appears in Figure 3.16. The process begins by growing a 1.2 μm thick thermal oxide on single-side polished silicon wafers. SPR 220 photoresist is spun on both the backside and front of the wafer to protect the oxide from the following oxide etch step. The mask labeled TRENCH is exposed on the front and then the wafer is etched in buffered hydrofluoric acid (BHF) until the silicon is exposed. The resist is then stripped, and the wafer is etched in KOH for approximately 18 minutes at an expected etch rate of 0.9 μm/min using the remaining thermal oxide as a mask. A preliminary silicon test wafer is used to determine the exact etch rate and also to activate the solution in order to achieve a 15 μm etch depth. Once the silicon etch is complete, the oxide mask is stripped and the wafer is piranha cleaned. A 0.7 μm thick thermal oxide is then grown, followed by spin-on of AZ 9260 photoresist to a thickness of 14 μm, allowing the resist to flow over the non-planar top surface of the silicon. The DEEP mask is then exposed and developed on the front-side. The wafer is once again dipped in BHF to etch the oxide, stripped and cleaned, and placed in a furnace to form a 15-μm deep boron etch-stop. The borosilicate glass that has formed is then stripped in hydrofluoric acid (HF), followed by another pre-furnace clean and a 0.7 μm oxide growth. Thick 9260 resist is again spun on the wafer, exposed with the SHALLOW mask, and etched in BHF to expose the silicon that forms the diaphragms of the pressure sensors. After resist stripping and cleaning, the wafer is placed once more in the boron diffusion furnace to form a 4-μm thick etch-stop for the diaphragm. No drive-in step is used here. Once the wafer has been cleaned and the borosilicate glass is once again removed, the wafer is placed in the furnace for approximately 20 min at 1000° C in order to grow a 1500Å thick thermal oxide to serve as an electrical insulator. The short run time prevents boron from diffusing beyond the initial 4 μm depth. The wafer is exposed with thick 9260 resist and the regions which do not require electrical isolation are etched in BHF. This completes preparation of the silicon side of the pressure sensor.

Step	*Description*	*Mask*
1	KOH etch using oxide mask	TRENCH
2	Deep boron diffusion for anchors	DEEP
3	Shallow boron diffusion for diaphragm	SHALLOW
4	Oxide and titanium deposition	GETTER/INSULATOR
5	Anodic bond to Silicon-in-Glass substrate	
6	Aluminum etchant to remove BOND_JIG	
7	Cr/Au to protect feedthroughs in EDP	POSTS
8	Wafer thinning in DRIE or HNA followed by EDP release	

Table 3.3. Pressure sensor process flow overview.

Figure 3.16. Pressure sensor process flow. Fabrication steps and masks outlined in Table 3.3.

The preparation of the glass side of the wafer requires an electrode to serve as the non-moving plate of the capacitive sensor. AZ 9260 is used as the resist, and COLLECTOR_B is exposed on the glass-in-silicon wafer. After development, the wafer is placed in vacuum, and 500 Å of Ti, 500 Å of Pt, and 1500 Å of Au are deposited. Liftoff in acetone removes the metal in unwanted regions. Bonding of the two wafers can now proceed after the thick 1.5 µm Al spacer is deposited on the backside of the glass-in-silicon wafer to ensure no shorts during bonding can occur, as explained previously. Alignment of the two wafers is accomplished with the Suss MA/BA-6 configured in the

bond-alignment mode and silicon-silicon bond mode with image capture enabled, rather than the silicon-glass mode. The thinned glass-in-silicon wafer is temporarily fixed to a dummy glass wafer with stiction forces by placing a drop of deionized water and bringing the two wafers together. During the actual bond step, the high temperatures will cause the water to evaporate allowing easy removal of the glass wafer. This dummy glass wafer is used to spread the electrical field across the surface of the glass-in-silicon wafer to ensure a good bond can be formed. The bond is carried out in a Suss SB6e until the bond current drops to 1.5 mA at 1000 V. 50 kPa of pressure is applied at a temperature of 300° C. Once the bond is complete, the dummy glass wafer is removed, and the bonded wafer stack is placed in an Al etchant in order to strip the aluminum that was used as a spacer. Finally, thick 9260 resist is spun on the back side of the wafer bond stack and the POSTS mask is exposed. 250 Å Cr/1500 Å Au is evaporated after a quick dip in BHF to strip native oxide. Liftoff removes the Cr/Au stack except over the electrical feedthroughs, protecting it from the following etch step. The final step is device release in ethylene-diamene pyrocatecol (EDP) at 95° C until completion. The etch stops on oxides, heavily-doped silicon, and Cr/Au.

3.4.3. Results

Fabrication of the devices went well, with a very high yield of sensors that visually showed deflection, indicating a vacuum-sealed cavity. The high yield may be due to the small number of steps in the process flow as well as the lack of lateral feedthroughs, improving the likelihood a strong anodic bond is formed. Photos of the completed devices appear in Figure 3.17. Scanning electron microscopy (SEM) images were taken in order to better visualize the side profile, Figure 3.18, and the surface of the glass that holds the silicon-in-glass wafers together, shown in Figure 3.19. The SEM images were taken with a Philips XL30FEG configured in the environmental mode (ESEM), which reduces the maximum magnification but allows non-conductive materials to be imaged. The SEM images were taken while in vacuum; hence the diaphragms are not deflected.

Figure 3.17. Four pressure sensors fabricated with the silicon-in-glass process. Two sensors in the center show the deflected diaphragm and two sensors on the left and right show the backside of the sensor.

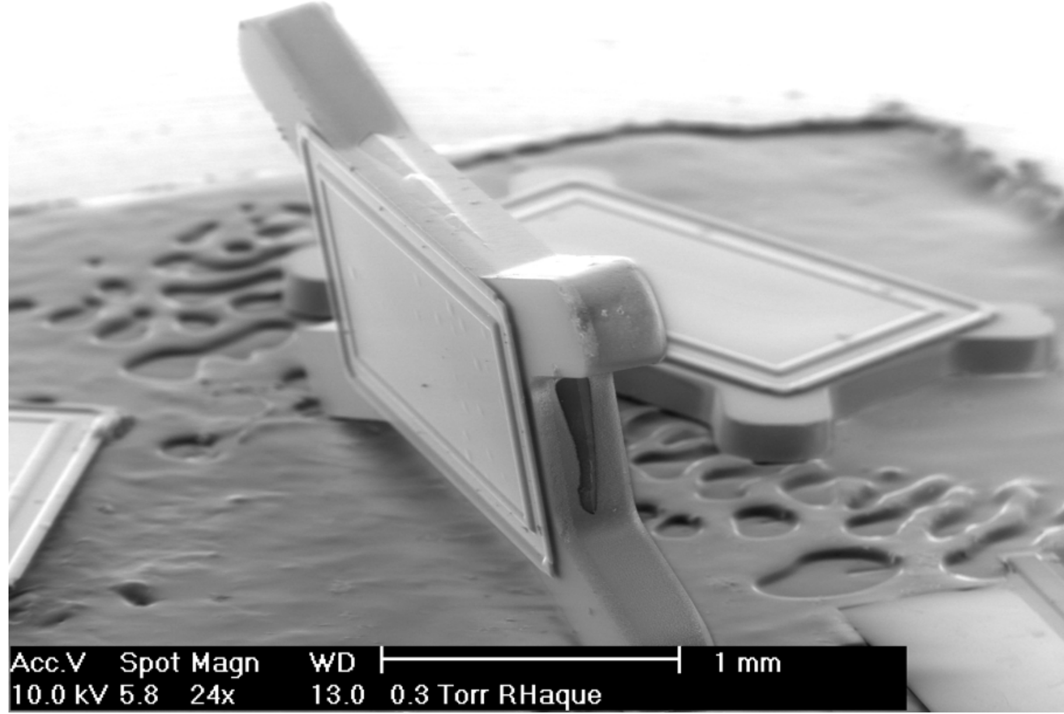

Figure 3.18. SEM image showing the side profile of the pressure sensor.

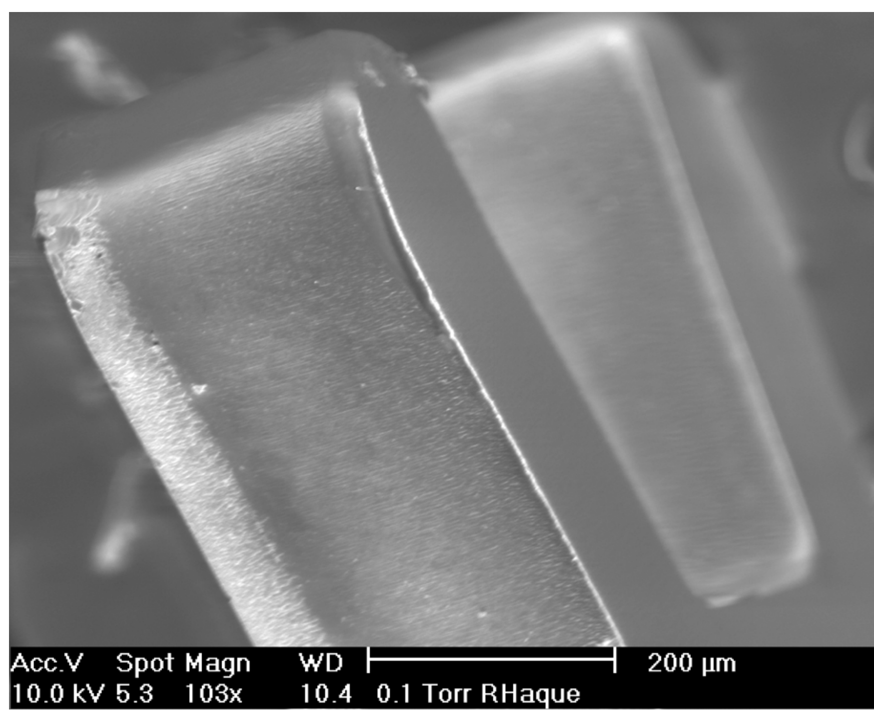

Figure 3.19. Magnified side-view profile of the embedded glass haptics.

3.5. TESTING

Pressure sensors were tested in a custom-designed, sealed aluminum pressure chamber. The small chamber allows testing of three devices simultaneously with six pass-through leads sealed with a vacuum-tolerant epoxy. Measurements were taken using an HP 4284A LCR meter with a sampling rate of 1 MHz and 4-point averaging. The chamber is controlled by a Positive Shut-Off Pressure Controller/Calibrator, model PPC2+ (DH Instruments) to regulate and control pressure within the chamber. Data presented in this section was collected using either this test setup or a vacuum probe station.

3.5.1. Touch-Mode

The sensors were placed in a vacuum probe station and the capacitance was recorded over a range of pressures from close to vacuum to an atmosphere. Figure 3.20 shows the three easily identified regimes of operation. Before the sensor approaches the bottom plate, there is very little capacitance measured, implying the gap between the plates is still large. In the middle region, the sensor behaves with extremely high sensitivity to changes in pressure, as expected when the gap is very small. The final,

third region of operation is also evident, after the two plates have touched, showing reduced sensitivity but increased linearity. The tested pressure sensor behaves as expected, mimicking the simulated results and clearly showing the gap-mode and touch-mode operation regimes.

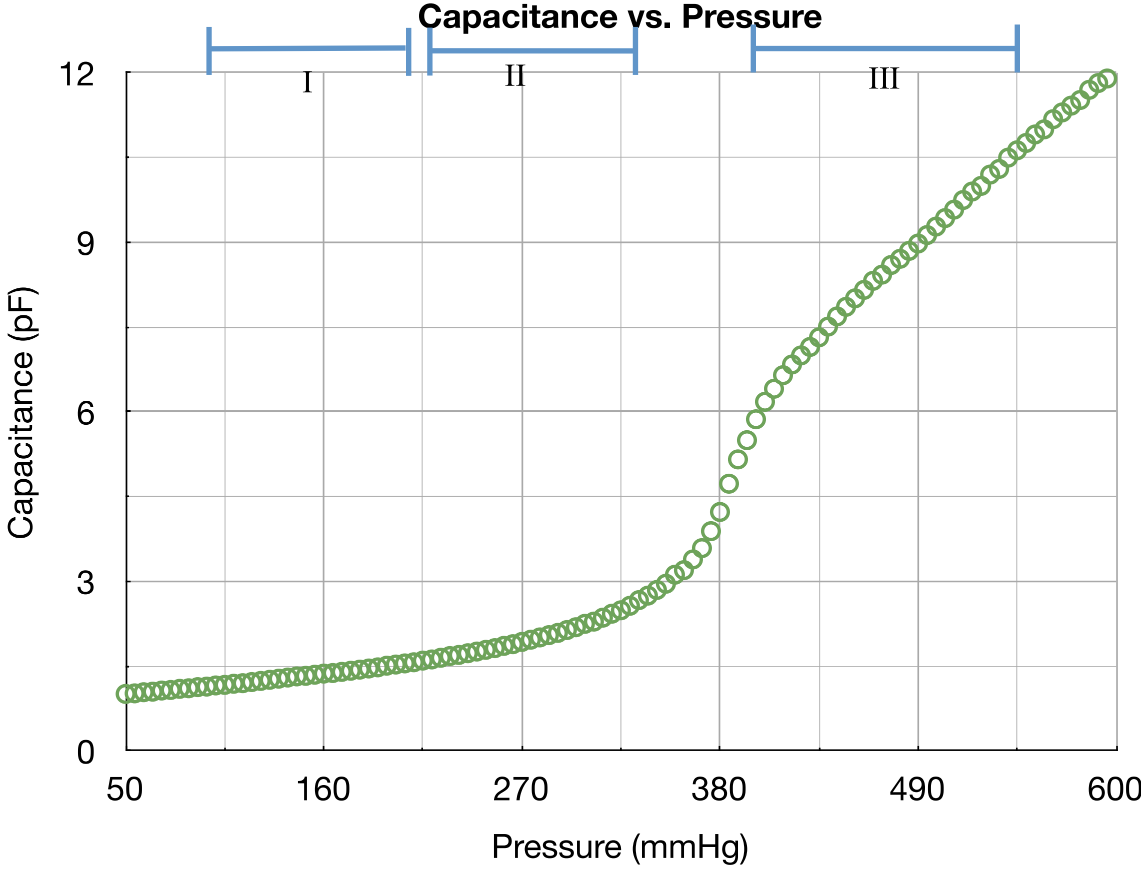

Figure 3.20. Pressure sweep for a single pressure sensor. The three distinct modes of operation are present: (I) large-gap, (II) gap-sensitive, (III) area-sensitive

3.5.2. Hysteretic Effect

As shown in Figure 3.21, a hysteretic effect is observed during multiple sweeps. During this test, the pressure in the sealed chamber was swept from 750 mmHg to 550 mmHg, then back up from 550 mmHg all the way through to 850 mmHg, and then back again to 750 mmHg. There is some measurement inaccuracy in the pressure regulation mechanism and test setup due to manual recording of the data. The error sources are discussed in detail later. An average capacitance difference of 0.05 pF throughout the overlapping regions (opposite sweep directions) was found for the same pressures, as shown in Figure 3.22.

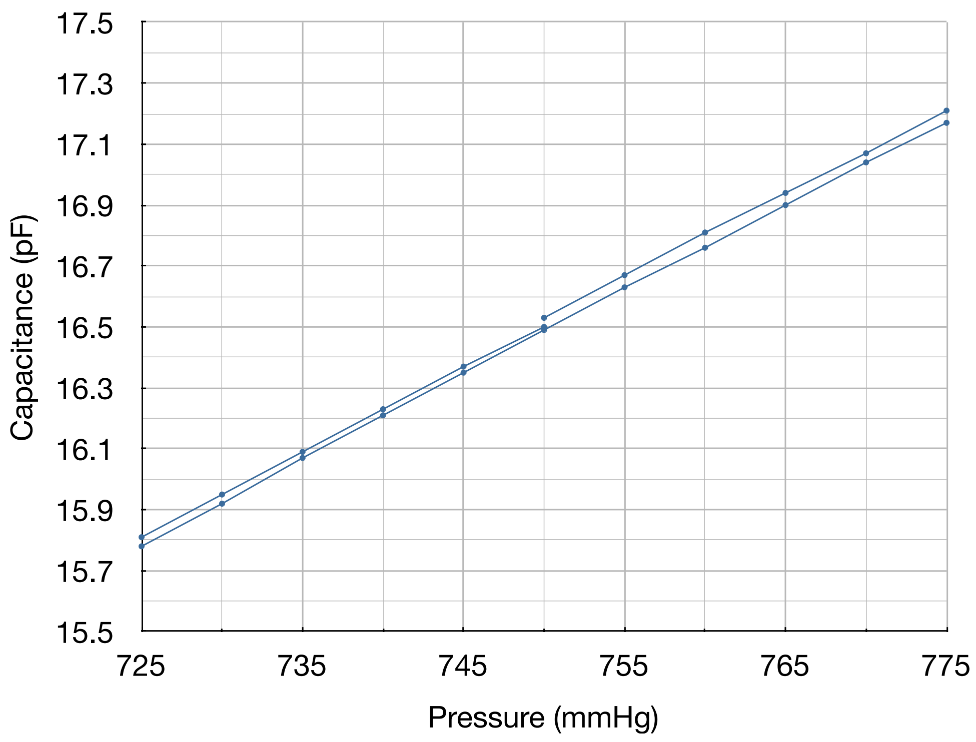

Figure 3.21. Pressure sweep plot magnified around ambient pressure point clearly showing hysteresis.

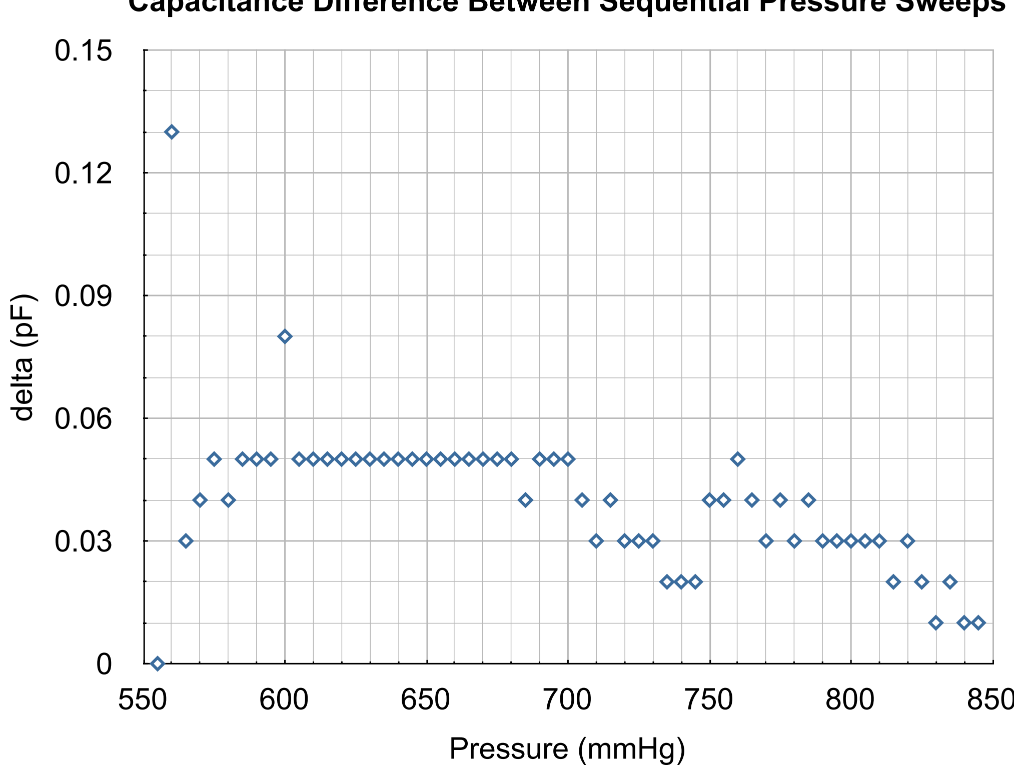

Figure 3.22. Plot of capacitance difference between successively measured data during an increasing pressure sweep minus decreasing pressure sweep.

A 0.05 pF, or 50 fF, offset in the measured pressure exceeds the required pressure resolution of 1 mmHg. However, with correction that takes into account the effect of the hysteresis and the artificial fixed offset induced in the data [56], it is estimated that this error could be easily reduced to well below the measured error, resulting in a resolution meeting the required 1 mmHg specification.

Further evaluation of the test setup will help pinpoint the source of error and understand deficiencies introduced by the equipment. A pressure regulator with a built-in pressure sensor was used to control the chamber. The accuracy in the sensor or control algorithm used in the tool can be verified with a secondary pressure sensor. This was accomplished using a Mini-Convectron, model 275 (Granville-Phillips) connected to a T-fitting between the sealed test chamber and the PPC2+ regulator. Figure 3.23 is a plot of this data and shows a distinct non-linearity not present in the intraocular pressure sensor data.

Voltage vs Pressure Sweeps (750 to 550 to 850 to 550 mmHg)

Voltage (V)

5.6
5.55
5.5
5.45
5.4
5.35

550 600 650 700 750 800 850

Pressure (mmHg)

y = 0.0007x + 5.0126
R^2 = 0.9965

Figure 3.23. Pressure sweep plot as measured by Mini-Convectron.

Figure 3.24 shows a similar plot to Figure 3.22, plotting delta voltage over a pressure sweep of the Mini-Convectron. It was found that for every 5 mmHg, the voltage changed by 3.5 mV resulting in a 0.7 mV/mmHg sensitivity. The maximum shift is 2.6 mV, which is equivalent to approximately 3.7 mmHg. This large offset occurs as the regulator passes through ambient pressure while the average error across the entire set of data is 0.8 mV, equivalent to a shift of 1.1 mmHg.

Figure 3.24. Plot of voltage difference between increasing pressure and decreasing pressure sweeps in the test chamber, measured with Mini-Convectron.

As shown in Figure 3.25, the steps between each successive pressure setting tends to have a linear trend up or down depending on the direction of the sweep. The above testing of the tool setup indicates that the performance of the capacitive sensor can only be evaluated down to a pressure resolution of around 1 mmHg, which is the targeted resolution. Further testing using a much more accurate setup is necessary to evaluate sub-mmHg accuracy. Hysteretic error introduced by the regulator may be calibrated out at a later time to improve the error inherent in the system itself.

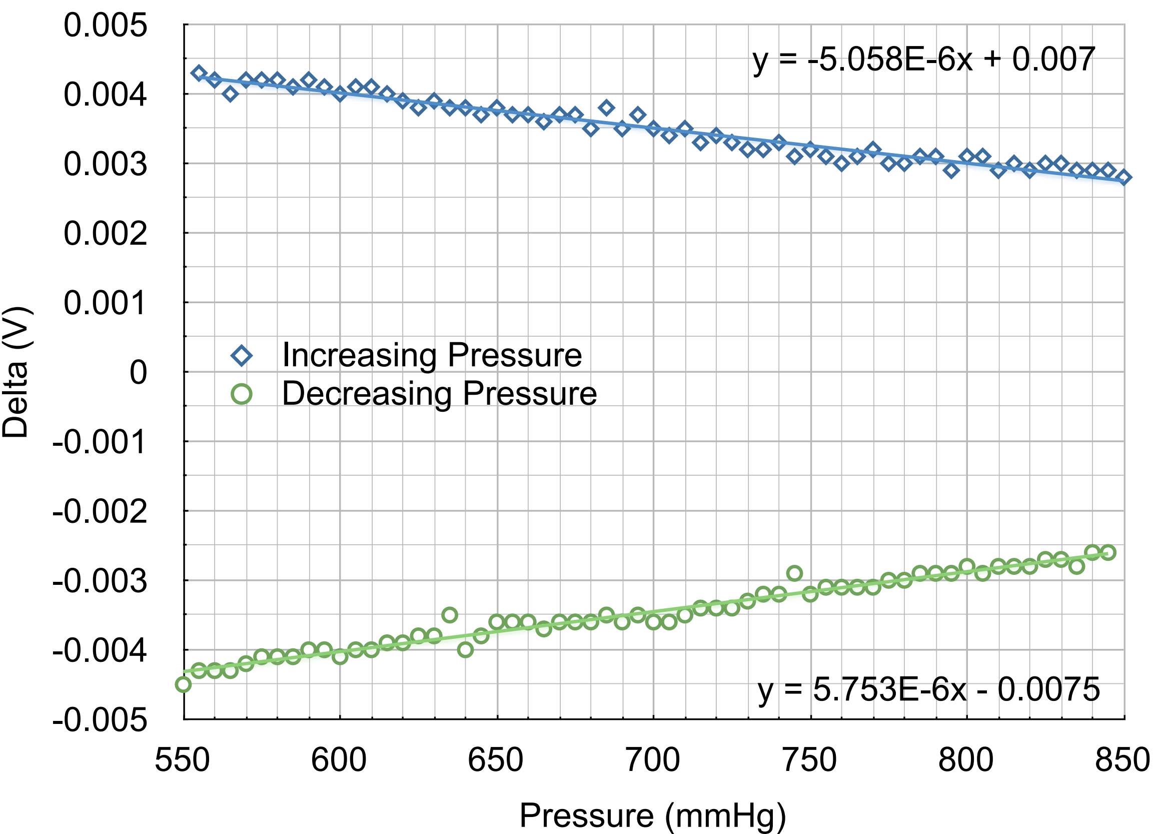

Figure 3.25. Difference between sequential steps of pressure change.

3.5.3. Resolution

The resolution of the fabricated pressure sensors depends on the measured sensitivity. In the touch-mode region, sensitivity was measured to be linear, with a value of 26 fF/mmHg, derived from the slope of the curve in Figure 3.20. Sensitive external bench-top test equipment can measure down to 0.5 fF [50], resulting in a minimum resolvable pressure of approximately 0.02 mmHg.

3.5.4. Discussion

SEM images of purposely-destroyed sensors were used to determine diaphragm thicknesses. Figure 3.26 shows the diaphragm thickness, as measured using an SEM, for the pressure sensors. The thicker region, listed here as 16.7 μm, is the thick boron-doped regions used as the anchor and rim for the diaphragm. The thinner region, listed here as

4.28 μm, is the diaphragm thickness. Measurement inaccuracy due to alignment of the sample is expected so these values should only be used as an approximate measurement.

Additional data was also used to verify that these sensors were in fact operating in touch-mode. The photographs in Figure 3.17 make it appear as though the diaphragm shows no curvature changes until it approaches the edge of the diaphragm, corresponding to a touch-mode type sensor rather than a gap-mode sensor, which should exhibit no observable flat spots on the diaphragm. An Olympus confocal scanning laser tool provided precise deflection data. The results, shown in Figure 3.27, can then be compared with the simulation data in Figure 3.7 of the same region of the diaphragm. The side-profile of this data is just as predicted by the simulation.

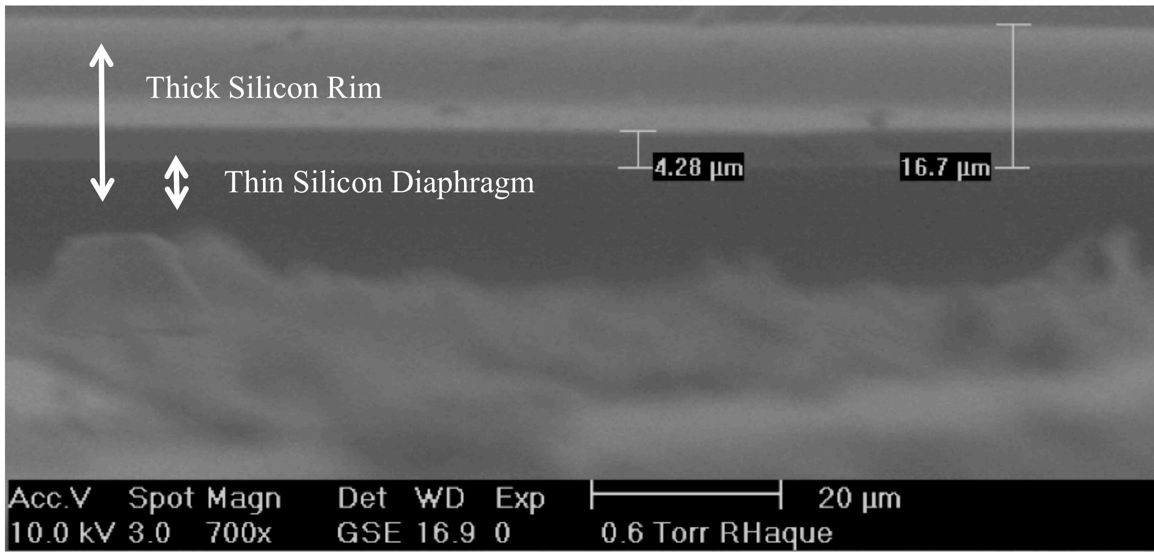

Figure 3.26. SEM image used for measuring diaphragm thickness by comparing thin silicon doping with thick silicon doping regions, such as the rim of the sensor.

Long-term testing can verify the effects of creep and device stability. As pressure increases, the angle between the anchor region and the diaphragm increases. This can be a potential source of fracture if the stress induced exceeds the fracture limit of the diaphragm. However, as mentioned previously, all simulation results indicated that the maximum stress is an order of magnitude less than the fracture limit of silicon and so diaphragm breakage during normal use is not expected. None of the fabricated pressure sensors have failed in this manner.

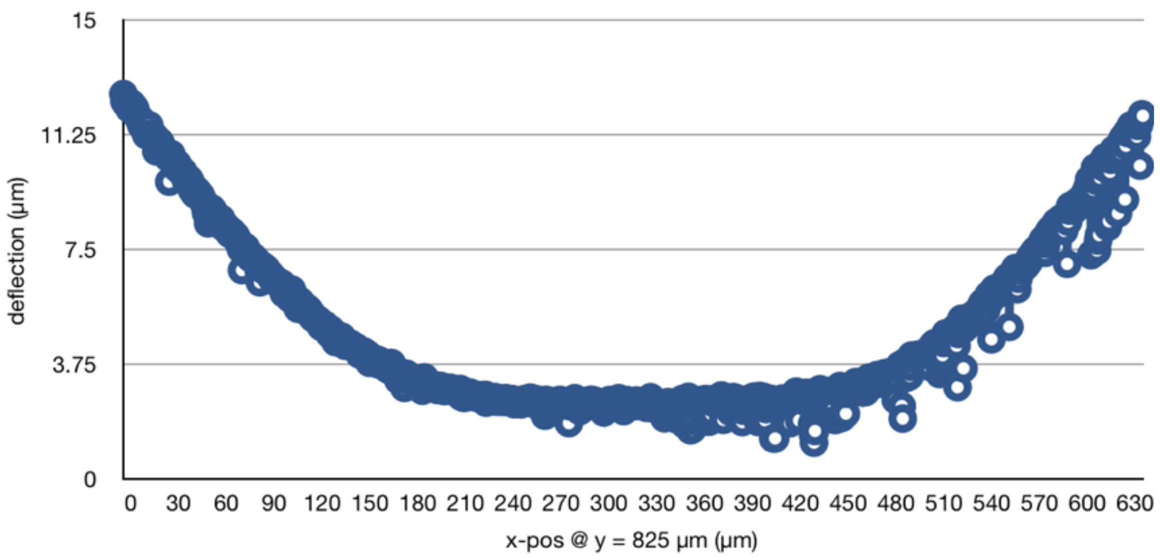

Figure 3.27. Olympus scanning confocal laser for touch-mode pressure sensor

3.6. Summary

This chapter has discussed the development of a pressure sensor for the intraocular application. The main limitations are dimension and geometry, but as previous work suggests, meeting the required specifications is possible. This work also demonstrates an application of the glass-in-silicon reflow process by incorporating vertical interconnects. This approach reduces complexity in fabrication and still maintains hermeticity. Sensors with high linearity and sensitivity have been fabricated utilizing touch-mode with the only potential drawback of hysteresis. Previous work on stiction analysis [57] and more recent work focused on techniques for overcoming the resulting hysteresis in pressure sensors has been reported in the literature [63].

One of the important optimizations that would improve this sensor is a reduction in the base capacitance. This can be accomplished by forming an electrode on the glass-side that has the center portion removed, since this region is a fixed capacitance and never changes with an applied pressure above ambient. In other words, the portion of the diaphragm that makes contact with the bottom electrode for touch-mode operation at an atmosphere of pressure is removed. The work here is the first known implantable pressure sensor based on touch-mode operation and utilizing vertical interconnects.

Overall, the resulting pressure sensor module is promising. The robust, high-yield process improves the reliability and general operation of the sensor. The work resulting from this chapter suggests that an implantable pressure sensor scaled to dimensions of 2

mm x 1.5 mm is not only feasible but also practical because of the high measured sensitivity of 26 fF/mmHg. Each sensor must be calibrated due to minor variations introduced during fabrication, but the linearity and sensitivity are expected to be consistent. Continuing work for this module should focus on reducing the base capacitance using the method mentioned in this chapter, reshaping the bottom electrode.

CHAPTER 4

POWER MODULE

One of the fundamental requirements of continuous monitoring devices is the availability of a suitable power source. Without one, it becomes virtually impossible to record and/or store data over long periods of time. An ideal power module for the device would include a built-in energy-scavenging unit to continuously or periodically recharge an on-board battery. Several challenges exist in implementing a microbattery: material choices (electrodes and electrolyte), process flow and fabrication, and post-fabrication thermal limitations on the packaging. In terms of energy scavenging, solar power is a viable solution in this particular application since the device is located within the eye and is exposed to ambient light.

The intraocular power module, together with the integrated circuit (ASIC) described in the next chapter, provides a complete, testable, and self-powered controller ready for integration within the microsystem package, with connections to both the antenna and pressure sensor. This chapter begins with a discussion of the microbattery work that was done. The second part of the chapter focuses on photovoltaic energy scavenging techniques. An electrostatic scavenger is also discussed along with alternative power sources such as ultra-capacitors and commercial thin-film batteries.

4.1. Previous Microbattery Work

Research groups such as Oak Ridge National Laboratories and Argonne National Laboratories have been working on thin-film microbattery technologies for some time. The resulting research has spawned several spin-offs, but there are still relatively few thin-film battery suppliers and fewer still that target microbatteries for implantable applications. One example of a company commercially supplying thin-film batteries is Cymbet Corporation, with products currently on the market supplying up to 50 μAh, all packaged using surface-mount technology (SMT) [65]. A company that provides small

implantable batteries is Quallion; however, their smallest product is approximately 12 mm long and 3 mm in diameter, supplying 3 mAh. Both of these batteries are rechargeable.

There has been a variety of published work on microbattery and thin-film electrochemistry reported in the literature. After extensive review of the published microbatteries, it can be concluded that virtually none offer the high-quality sealing characteristics required for implantable applications, and they often have poor performance in terms of number of recharge-discharge cycles [66], [67]. Quallion comes closest to meeting the requirements for implantable systems; however, their smallest battery is still quite large and is not compatible with embedding within a 1 mm^3 microsystem.

Much of the published work has focused on a single component of the entire microbattery, typically the anode or cathode, in order to increase efficiency, reduce charging times, or increase useable current. For example, in [68], the authors present techniques for creating silver oxide nanoparticles, used in silver-zinc batteries, with the goal of providing higher charge and discharge currents. In general, the trend in the literature is to increase the surface area of the electrodes by way of MEMS fabrication techniques [69] and, more recently, by focusing on unconventional techniques [70]. Work has also progressed on implantable batteries that operate without a package and instead use the body's fluids as a natural electrolyte [71].

One of the biggest challenges in the literature is to hermetically seal the batteries. For an implantable battery, this is obviously a basic requirement since the external environment is a highly conductive medium. Otherwise, there is always the possibility of the battery electrolyte or other components leaking into the body. For lithium batteries, in particular, the encapsulation technique must be hermetic since lithium will react violently on contact with moisture [72]. This particular effort used parylene to provide a sealing coating over the package; however, some moisture will travel across any polymer (though as the authors note, parylene is better than other polymers previously used). Interestingly, coin-cell batteries are also not hermetically sealed since they are packaged using a compression bond over a nylon gasket [73]. Another polymer that has been used in microbatteries as a spacer and adhesive is benzocyclobutene (BCB), chosen for its ease

of fabrication; however, this approach is primarily applicable to disposable and low-cost batteries [74]. Table 4.1 provides an overview of some microfabricated batteries in the literature, their capacity, dimensions, and chemistry.

Reference	***Chemistry***	***Active Area***	***Capacity***	***Voltage***
[79]	Au-Zn	0.51 mm^2	1.33 µAh	1.5 V
[74]	Pt-Al	100 mm^2	64 µAh	0.8 V
[70]	Ni-Zn	64 mm^2	5.28 µAh	1.7 V

Table 4.1. A sampling of published microbatteries.

As part of a collaborative project at the University of Michigan under the WIMS ERC, a silver-zinc thin-film battery was developed [75]. There are two major shortcomings with this design, however. The first concern is the toxicity of the material used for the electrolyte (potassium hydroxide). Even though the battery is sealed within the device, this particular electrolyte is known to etch silicon and glass, albeit slowly at body temperature. The second concern is the battery package, which is not conducive to implantation or embedding within the microsystem. Further, although the package is claimed to be hermetic, the silicone gaskets and polycarbonate clamps used do not provide sufficient leakage protection [75], especially on the microscale. Finally, these particular batteries are assembled by hand; a batch-mode fabrication technique would be preferable in order to save costs in the long-term.

4.2. Design

Three desirable properties are important for any implantable microbattery design: a hermetic seal, low toxicity, and rechargeability. Size constraints and manufacturability are additional optimization goals. As a result, the previously designed pressure sensor was used as the core design structure for the battery, with changes to include electrodes and fill-ports for electrolyte loading. The electrochemistry chosen is silver-zinc due to its high performance and ability to operate as a rechargeable cell. Toxicity is addressed by replacing the potassium hydroxide with a non-toxic solution (saline). Finally, sealing techniques similar to those used for the pressure sensor presented in the previous chapter were used to achieve hermetic sealing. Details on the selection of the necessary battery components are provided in the following subsections.

The issues of size and manufacturability were resolved by using conventional microfabrication techniques. According to [75], commercial solutions were not viable because if batteries were scaled to microsytem levels, the battery package alone would occupy 85% of the volume and 35% of the mass. The low efficiency of conventional batteries, ranging from 20% for rechargeable batteries to at best 40% for non-rechargeable types [76], serves as another motivating factor. Finally, since MEMS-based fabrication techniques are batch-mode, manufacturing such microbatteries at low cost should be possible.

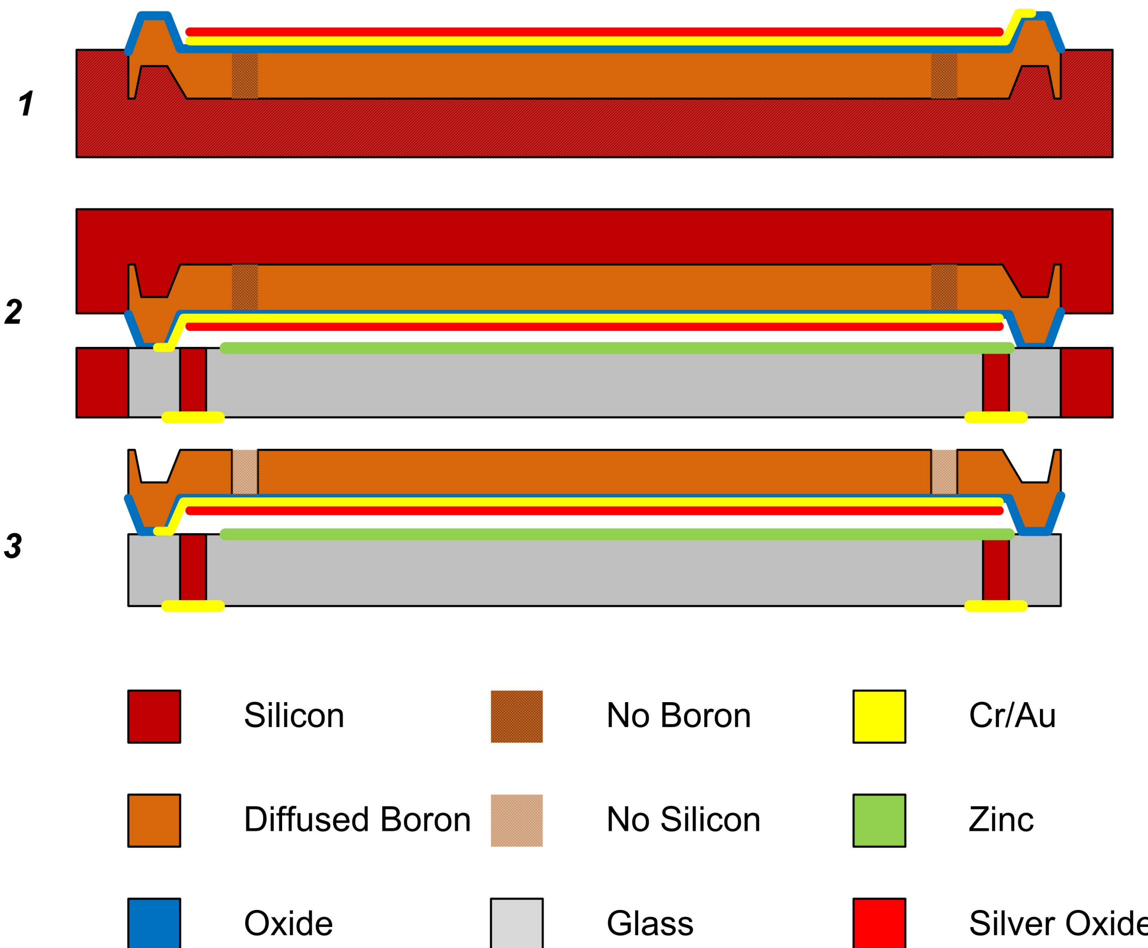

Figure 4.1. Proposed process flow for the microbattery with vertical interconnect and fill ports.

4.2.1. Layout

The fabrication of this device is similar to the pressure sensor and makes use of the previously demonstrated glass-in-silicon process. There are some limitations, however, depending on material choices. Figure 4.1 shows a process flow for the

microbattery. In step 1, silicon cavity etching, deep boron diffusion, oxide growth, and deposition of Cr/Au/AgO are shown. Step 2 uses an anodic bond to a glass-in-silicon wafer containing a previously-deposited Zn electrode. Finally, the devices are released, simultaneously opening the fill-ports to expose the oxide cavity seals.

The oxide cavity seals are specially designed regions that lack thick boron-doped silicon. During the release step, ethylenediamene pyrocatechol (EDP) attacks undoped and low-doped regions of silicon. Since these regions lack boron-doping, the silicon is removed up to the oxide. Here, the etch stops because EDP does not appreciably attack oxides.

Figure 4.2 presents a top-view of the microbattery. The right half of the figure shows the glass-in-silicon wafer while the left half of the figure shows the silicon side of the battery. For the glass substrate side: Step 1 is the starting wafer, followed by aluminum deposition on the backside for bonding in Step 2. Step 3 deposits a conducting Cr/Au pad to connect the top half of the battery to one of the vertical interconnects to the glass substrate. Step 4 shows the bottom Zn electrode and its corresponding connection to the other vertical interconnect. For the silicon side: Step 1 shows the silicon cavity etch. Step 2 shows the selective deep boron diffusion, followed by the oxide growth in Step 3. Step 4 is after the metals (and silver oxide electrode) have been deposited.

The fill ports can be better seen in Figure 4.2 on the left half of the figure. During Step 2, they are masked and protected from boron diffusion. Step 3 is a thermal oxide coating, forming the oxide seal that will be pierced later when loading the electrolyte.

4.2.2. Electrochemistry

Choosing an appropriate electrochemistry can be challenging, and there are many criteria that are used to define batteries. For example, in Figure 4.3 and Figure 4.4, the discharge curves are shown for several different types of batteries with two different metrics, the first fixing the battery mass and the second fixing the size. Lithium-based chemistries are typically the best choice because of the high-energy density these chemistries exhibit in practical use. Another useful aspect of these plots is the cell voltage stability during the useable lifetime of the battery. Sudden drops near the end of the lifetime may be more difficult to detect for voltage monitors, whereas a flatter curve

may help on-board regulators operate at their peak efficiency for a longer period, increasing the useable lifetime of the battery. Finally, one interesting observation that serves as a kind of “fingerprint” for silver-zinc batteries can be seen in the plot of Figure 4.3: the initial higher voltage output of the battery for a short time period before it drops to a second, flat voltage level. This is due to the AgO instead of just Ag_2O reacting with the electrolyte; once the AgO has completely decomposed to Ag_2O, the lower voltage level is observed [78].

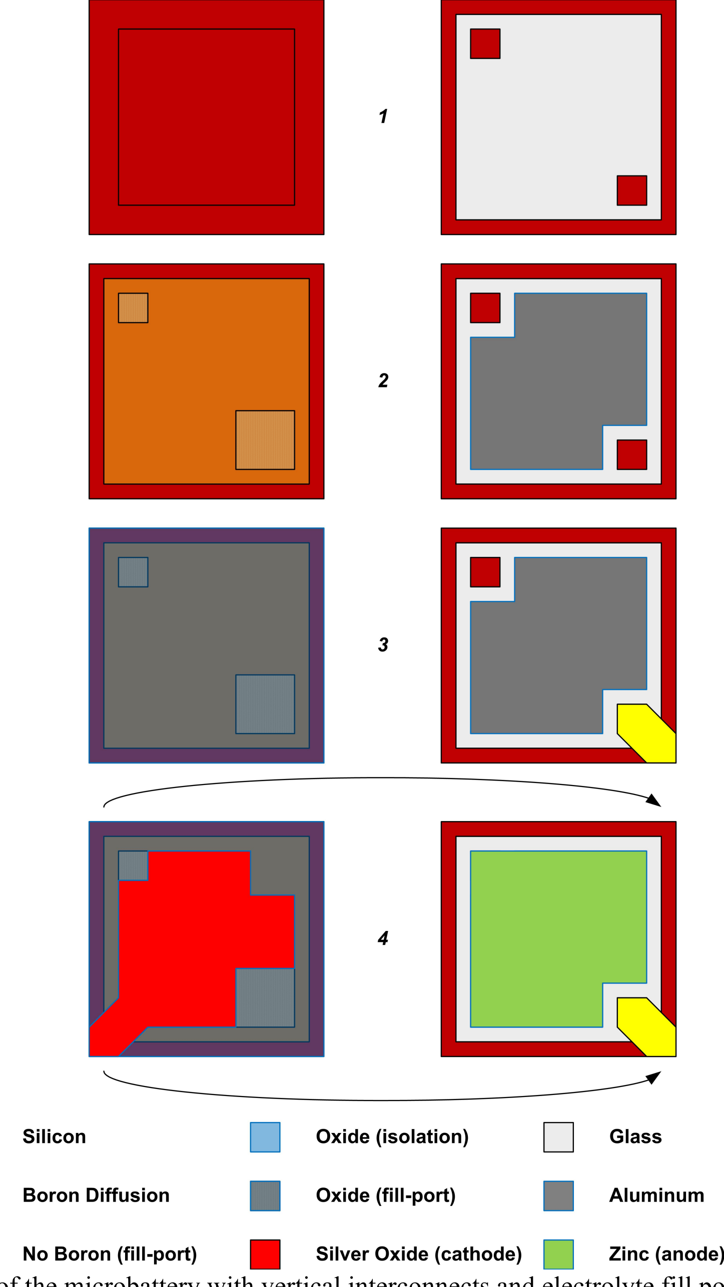

Figure 4.2. Top view of the microbattery with vertical interconnects and electrolyte fill ports.

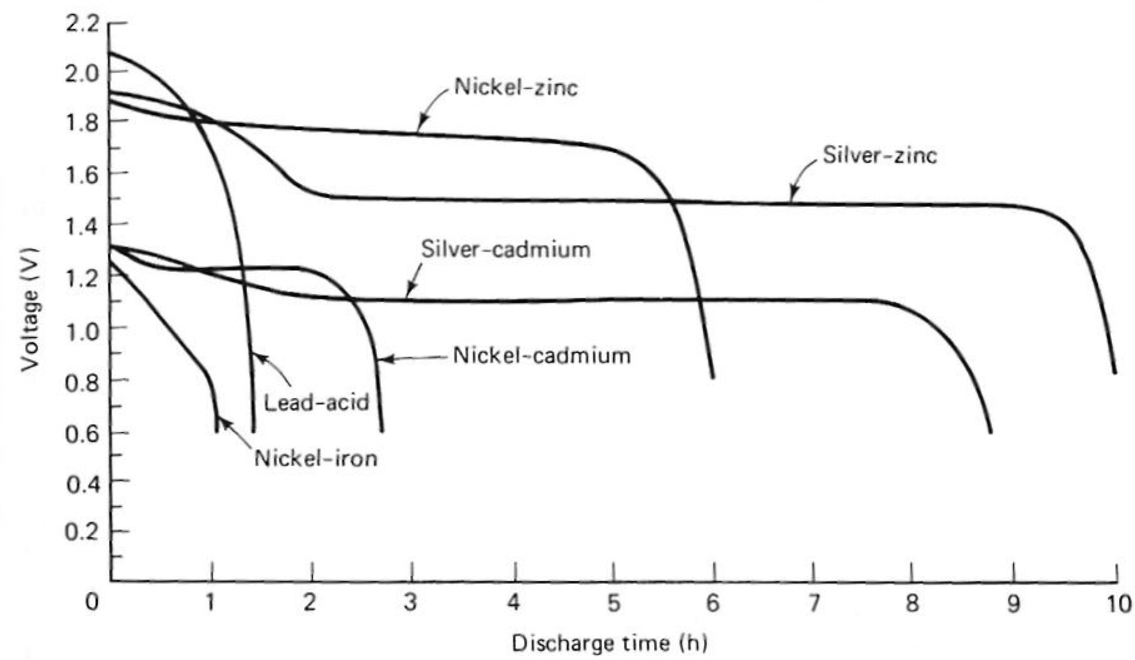

Figure 4.3. Typical battery discharge curves for the same mass and discharge rate [77]

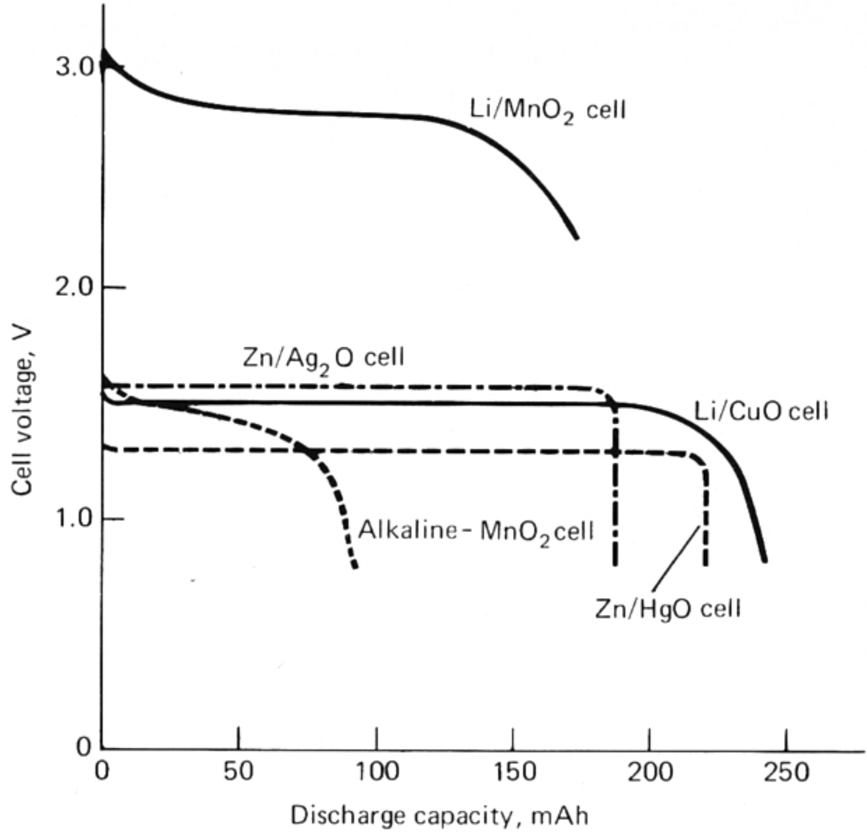

Figure 4.4. Typical battery discharge curves for same-sized batteries (11.6 mm diameter x 5.4 mm) [78]

From the data presented in Figure 4.3 and Figure 4.4, several chemistries become strong choices. A higher voltage supply (as seen in the previous figures) typically means a higher power level and therefore higher energy density, so the lithium-based chemistries appear as the best option. Chemistries such as the alkaline-manganese dioxides produce a variable voltage during discharge that may prove more difficult to regulate. In Figure 4.5, these same chemistries have been plotted with the energy density measurements, showing mass and volume for different types of batteries. Primary batteries are not rechargeable while secondary batteries are rechargeable; the upper right quadrant shows those chemistries with higher energy density. Silver oxide batteries, considered to be both primary and secondary, have a good volumetric density and therefore are conducive to smaller systems than other chemistries. A distinction in the plot between prismatic, or small-form factor, batteries, and cylindrical, the more common battery style such as D-cells, indicates that the packaging method can affect performance.

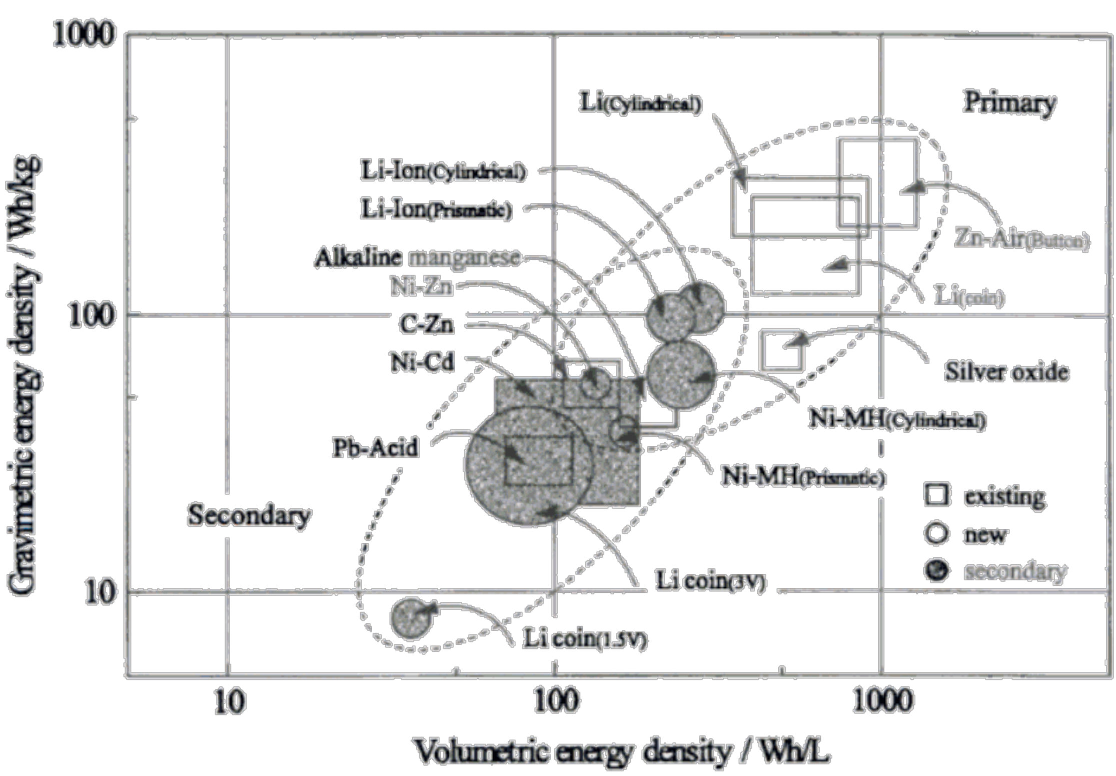

Figure 4.5. Energy density map for small batteries [76].

4.2.3. Electrochemical Reactions

This section gives a brief overview of the expected chemical reaction and the theoretical maximum available energy for the standard silver-zinc chemistry. First, the basic equation for cell potential is shown in Equation (4.1).

$$E^{\theta}_{cell} = E^{\theta}_{cathode} - E^{\theta}_{anode} \tag{4.1}$$

The standard half-cell potentials for silver oxide and zinc, followed by the expected cell potential calculation, are shown in Equation (4.2):

$$\begin{aligned}
&2\mathrm{AgO} + \mathrm{H_2O} + 2e^{-} \longleftrightarrow \mathrm{Ag_2O} + 2\mathrm{OH^-} && E^{\theta} = +0.57V \\
&\mathrm{Ag_2O} + \mathrm{H_2O} + 2e^{-} \longleftrightarrow 2\mathrm{Ag} + 2\mathrm{OH^-} && E^{\theta} = +0.345V \\
&\mathrm{Zn} + 2\mathrm{OH^-} \longleftrightarrow \mathrm{Zn(OH)_2} + 2e^{-} && E^{\theta} = -1.245V \\
&E^{\theta}_{avg\ cell} = 0.345 + 1.245 = 1.59V
\end{aligned} \tag{4.2}$$

It has also been found that the Ag_2O capacity is 231 mAh/g and 1650 mAh/L and the Zn capacity is 820 mAh/g and 2870 Ah/L for powders, which would appear to indicate that silver oxide is the limiting factor by mass and volume, but this is not the case since Zn suffers from additional issues (such as shape change, explained later) [78]. Also, the chemical reaction that provides the initial high voltage is not calculated since it raises the battery voltage in practice to a value of approximately 1.7 V to 1.8 V. This only occurs for a short portion of the entire discharge curve since it is based on AgO decomposing into Ag_2O. Capacity is limited due to the low conductivity of the selected electrolyte (saline). The overall reduction in battery voltage is quite large, as shown in the testing section, reducing the cell potential to between 800 mV and 900 mV.

4.2.4. Electrolyte Loading

One of the important features of the designed battery is the post-fabrication electrolyte loading procedure. During the fabrication process, the boron regions that define the silicon battery cavity are masked to leave two small undoped areas. When running the dissolved wafer process, these undoped regions etch away, and the etch stops on the thermal oxide layer below. These thermal oxide layers can be subsequently

pierced or removed, and electrolyte can then be loaded into the shallow cavity between the two halves of the battery. If one oxide cap is pierced while the device is submerged in a solution of saline, then the saline will be pulled into the cavity if bonding occurs in vacuum, just as with the pressure sensor. If the battery is not sealed in vacuum, a second port can be used as a vent hole to allow trapped air to escape as it is displaced by the liquid electrolyte. Once electrolyte loading is complete, epoxy can be used to seal off the loading ports.

The challenge with the proposed concept for electrolyte loading is due to size constraints. Originally, it was proposed that the fill ports be loaded externally by piercing the thermal oxide with microsyringes; however, this proved extremely challenging. The main difficulty occurs because there is trapped gas (air or nitrogen) inside the battery cavity from the bonding step, which must be displaced before fluid can enter. Vacuum-sealed batteries should not have this issue and future designs may even eliminate one of the loading ports to increase the total surface area dedicated to the electrode.

4.3. Materials

There are many different types of electrochemical cells available. Three factors were used to narrow down the choices: energy density, material availability, and rechargeability. The previously shown plots of energy density versus volume and mass clearly show the lithium-ion based chemistries to be most effective and an obvious choice. However, since there is no easy access to lithium and its compounds within standard MEMS cleanrooms, this choice was eliminated. The next-best chemistry that is also rechargeable is silver-oxide and zinc chemistries. Both silver and zinc are easily available, so an initial study of silver-oxide was conducted and analyzed using x-ray diffraction (XPS) analysis.

4.3.1. Zinc

Zinc is a common choice for electrochemical cells due to its material properties [77], [78]. In a typical MEMS cleanroom, the electron-beam evaporation of zinc is possible, but it is usually segregated from CMOS fabrication. Deposition is currently

limited to 2000 Å per single run due to limitations of the tool, but it is possible to deposit more over multiple runs if necessary.

Zinc nanoparticles, rather than evaporated zinc, were used in a previous work [75]. The advantage of this technique is the increased surface area as well as the ease of application, since its deposition is from a spray aerosol in a can manufactured by 3M. This particular method may not be useable in the cleanroom environment since the resulting aerosol spray includes petroleum distillates and other solvents. However, this is a simple way to deposit large surface areas of material.

The limiting factor of Ag-Zn batteries is the zinc – in macroscale devices, battery capacity loss is due to corrosion, evolution of hydrogen, and shape change [78]. Conventionally, hydrogen has been controlled in the past with the addition of mercury. Shape change is the result of material migration. In order to compensate for these effects, a reduced battery volume and a less corrosive electrolyte (saline) is used in this work. Similar to the macro-scale solution for decreased cycling performance due to shape change of the anode, more zinc can be deposited than necessary.

4.3.2. Silver Oxide

Silver oxide can be generated by way of reactive sputtering a silver target in the presence of oxygen [82], [83], [84]. In this process, silver sputtering occurs in an environment that contains a very specific ratio of argon to oxygen such that prior to the accelerated silver atoms reaching the surface of the target, oxygen in the chamber reacts with it to form silver oxide. Depending on the ratio of argon to oxygen, different silver oxide compounds are possible: AgO and Ag_2O. Both compounds are unstable and the potential to release oxygen and decompose into silver occurs at elevated temperatures (greater than 300° C), although at room temperature the films are stable. This is one of the major drawbacks of using silver oxide, since it may restrict later high-temperature steps during packaging.

The actual ratio that preferentially forms AgO versus Ag_2O in the literature is somewhat imprecise so an experiment on decomposition temperatures was carried out. Based on the data provided in [82], [83], [84], higher flow rates of O_2 should create more AgO. Several test runs were conducted with auger spectroscopy using XPS to verify the

material deposition. The testing section of this chapter, and in particular Figure 4.9, will discuss the results in detail.

The ratio of oxygen to argon is defined by Equation (4.3).

$$r = \frac{[O_2]}{[Ar] + [O_2]} \tag{4.3}$$

The thermal limit before silver oxide in the form of AgO decomposes to silver and oxygen was reported in the literature to be approximately 300° C [85], [86], [87], [88]. The decomposition of Ag_2O also leads to the formation of AgO above certain temperatures. Increasing the temperature beyond this value then leads to the decomposition of AgO to pure silver. One possible explanation for this behavior in the literature, though not confirmed independently, is worth mention here:

> "Namely, for a thin layer, the activation energy for the AgO to Ag_2O reduction is larger than the one for decomposition of Ag_2O into Ag. On the other hand, for powders the situation is opposite. We believe that this discrepancy may be either due to the dimensionality effects or to strains accumulated in the thin film." [87]

This may better explain the experimental results, which showed that anodic bonding at temperatures of 300° C is not an issue. The decomposing chemical equations are presented in [86], and are repeated here. The reaction described in Equation (4.4) is the first decomposition; the intermediate product indicates that there is a mixture of AgO and Ag_2O, depending on the temperature. Equation (4.5) describes the reaction from Ag_2O to Ag.

$$\mathrm{AgO} \rightarrow x\mathrm{AgO} + (1-x)\mathrm{Ag_2O} \rightarrow \mathrm{Ag_2O} \tag{4.4}$$

$$\mathrm{Ag_2O} \rightarrow x\mathrm{Ag_2O} + (1-x)\mathrm{Ag} \rightarrow \mathrm{Ag} \tag{4.5}$$

What is not clear from the listed reaction is the relative stability of each step. In the literature, regardless of the reported decomposition temperature, Ag_2O is much more stable since it has a higher decomposition temperature, so Ag_2O is the preferred active electrode material. Interestingly, anodically bonding at 300° C may serve as an advantage since it may convert AgO to Ag_2O directly.

Several tests were conducted on a hotplate in a normal atmospheric environment. It was observed that silver oxide did indeed decompose, indicated by a change from a transparent brownish color (silver oxide) to a solid metallic grey color (silver). Further tests were conducted in a much more controlled manner in the cleanroom approximating actual use during bonding. In this experiment, a glass wafer with silver oxide was anodically bonded to a blank silicon wafer. Though the applied temperature was 300° C, the silver oxide was perfectly preserved based on simple visual inspection to determine if pure silver was observed. Furthermore, the transparency of silver oxide was maintained. It was concluded that the bonding process does not cause silver oxide to decompose into silver. These simple experiments confirmed the results reported in [83].

The actual deposition process was completed in an Enerjet sputter tool, beginning with a pure argon environment with a base pressure of approximately 7 mTorr. Before any silver is sputtered on the surface of the device wafer, pre-sputtering for approximately 1 minute cleans the target of any organics, nitrides and oxides that may have formed on the surface during storage in the cleanroom environment. Next, the oxygen valve is opened, and controlled to a specific ratio of $r = 0.7$, as defined in Equation (4.3), by using dedicated built-in flowmeters. Once the oxygen begins to flow, the plasma can be easily observed to have changed color, possessing more of a bluish tinge as opposed to the more purplish glow in a standard silver (pure argon environment) sputtering process.

Previously, silver was deposited using a physical vapor deposition and then oxidized in a high-oxygen content environment [75]. The drawbacks with this approach are the multiple steps required to form silver oxide, but more importantly, the fact that oxidation occurs from the outer exposed layers towards the inner protected layers. Depending on oxygen diffusion rates and the thickness of the evaporated silver, the inner layers of the metal may never be oxidized to silver oxide. These are not concerns when reactively sputtering silver in an oxygen-rich environment. In fact, one of the advantages of this process is the ability to first deposit pure silver to serve as a current collector, before introducing any silver oxide. It has been noted, and verified, that silver oxide itself is not a good conductor, so thin films of the silver oxide may prove to be beneficial.

Normally, graphite is mixed in with the silver oxide to serve as a current conductor in order to aid current transport; this may be unnecessary for a thin-film approach [77].

4.3.3. Electrolyte

Electrolyte options vary, but typically a solution containing potassium hydroxide (KOH), a strong base, is used with silver oxide batteries. However, KOH is known to slowly etch both silicon and glass. More importantly, KOH is toxic to the body and can even cause permanent eye damage [89]. Specifically, in the case of eyes, experiments have shown that 5% KOH is an extreme irritant and corrosive in rabbits while human data has shown that alkali burns can occur quickly after exposure and may even result in loss of vision [90]. Previous microbattery work used KOH in concentrations up to 28% [75]. In order to avoid this issue, other, safer electrolytes should be used.

The most obvious alternative is saline, simply sodium chloride at 0.9% by volume, which is similar to that found in the human body and used for intravenous solutions [91]. The disadvantage of using saline is reduced conductivity as compared to other alkaline solutions. There are two potential ways to compensate for this: the sodium chloride concentration can be increased to 12% where maximum conductivity occurs, or the gap can be reduced between the cathode and anode, thereby reducing internal resistance [80]. The resistance of the cell results in a direct drop in the maximum voltage that can be supplied from the calculated standard electrochemical cell potential of 1.5 V. Mixing in additional compounds such as hydrogen peroxide can increase battery power significantly, as has been demonstrated in aluminum-based batteries using conventional saltwater for marine applications [81]. Another possibility, currently used in a commercial battery provided by Quallion LLC, is a siloxane-based electrolyte, or more specifically, liquid siloxane with organoborate salts [66].

It is possible to use an electrolyte that is not a liquid but rather is a gel or type of ceramic that allows the conduction of ions and also simultaneously serves as a separator. A key advantage of this type of battery is that it can be used during typical solder reflow processes and does not have the same temperature limitations as a liquid-electrolyte based microbattery. This may suggest a microbattery could be sealed using conventional bonding techniques at temperatures above 100° C.

4.3.4. Other Materials

Lithium-based chemistries have not been ruled out for this particular battery design. As mentioned earlier, they do have the highest energy density per mass, ignoring air-electrode batteries that are not possible in a sealed and implanted application. A collaborative study with Professor André Taylor of Yale University was initiated in order to combine the battery structure developed here with the proposed ink-based deposition process Prof. Taylor and his research group have developed. This type of material deposition should yield thin-film lithium batteries with even higher energy density than silver-zinc chemistries. The ink-based deposition technique is convenient for bulk wafer-level processing as well.

4.3.5. Challenges

Low-temperature bonding techniques are important for the overall intraocular microsystem, since the microbattery with liquid electrolyte sets the upper thermal limit. The boiling point of the liquid electrolyte limits the maximum temperature for later processing steps to less than 100° C. Additional issues were discovered in later processing steps due to the formation of various intermetallic compounds. As shown in Figure 4.6, zinc shows a high propensity for mixing with metals such as gold at temperatures below the anodic bonding temperature of 300° C. In the original design, a Ti/Pt/Au stack was used as a current carrying layer below both electrodes. In the case of zinc this is not necessary since it is a good conductor. However, this layer is required for silver oxide since it is a very poor conductor. Once the Ti/Pt/Au stack was removed from the zinc side, no change in the coloration of the zinc was observed.

Finally, the proposed battery design does not include a separator, which serves as a physical barrier to dendrite growth. The reason this was not included in the first-generation microbattery is because such formations tend to occur during recharge, a process that should only occur for short periods of time with a constant energy harvesting solution. Future batteries may include a coating of Nafion, a spin-on material that allows ion transfer, over the Zn anode. Other optimizations are expected in any final microbattery involving the electrolyte concentration, cell dimensions, and/or thicknesses of the deposited materials.

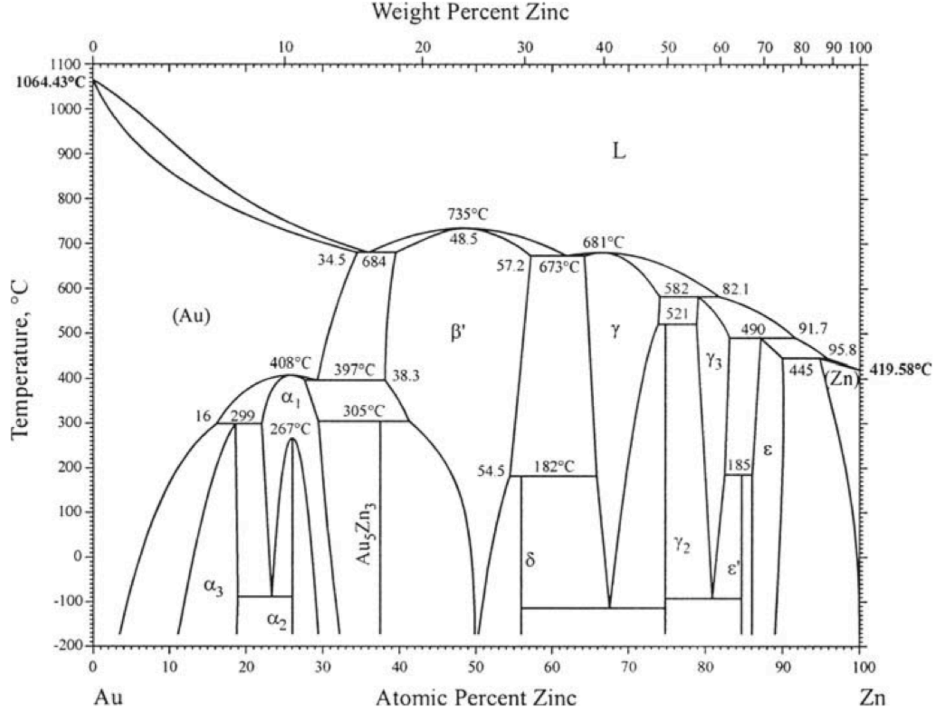

Figure 4.6. Au-Zn phase diagram [92]

4.4. Fabrication

The source wafers used for the battery are glass-in-silicon wafers thinned to approximately 250 μm and standard 500-μm thick silicon wafers for the cathode-side of the battery. A built-in cavity is formed that is about 200 μm deep. Figure 4.7 shows a photo of an early test run of a fabricated microbattery that did not function.

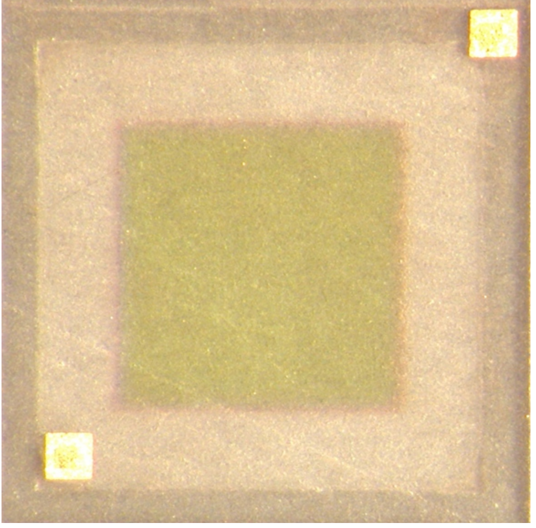

Figure 4.7. Fabricated microbattery test run. The two gold pads provide connection to the electrodes.

In addition to the details provided previously about the deposition techniques for the various electrode materials, simple liftoff was used. Zinc liftoff is almost instantaneous when using thicker resists, while silver oxide tends to form stronger and more conformal coatings. Ultrasonication along with the use of thicker resists alleviated this challenge. Double-sided liftoff (meaning lift-off on both the front and back) of the glass-in-silicon wafer has proven to be reliable, though resist must manually be spun-on since the wafers are too fragile for automated resist spinning. Once the glass-in-silicon wafer is patterned with zinc and the silicon half of the battery is patterned with silver oxide, the two wafers are aligned and then anodically bonded in vacuum at 300° C using a Suss SB6e.

4.5. Testing

During this work, only bench-top testing of flooded cells was performed. These bench-top tests validated the material choices, test setup, and data collection procedures developed. Future work involving fully-fabricated microbatteries would test the energy density, instantaneous current limitation, rechargeability, and self-discharge rate. But the work here establishes the feasibility of a silver-zinc microbattery for the intraocular microsystem.

4.5.1. Silver Oxide Analysis

As mentioned previously, reactive RF sputtering was used to deposit silver oxide electrodes. In order to verify the presence of silver oxide and its form (AgO versus Ag_2O), XPS analysis was conducted. The plot in Figure 4.8 shows strong peaks for silver, oxygen and some carbon, indicating minor contamination.

In order to determine if the Ag 3d orbital is bound to a single oxygen, two oxygen atoms, or none, another plot of this region is required, as shown in Figure 4.9. As noted in [83], the presence of Ag_2O can be determined by peaks occurring at a binding energy of above 368 eV whereas Ag is present below 368 eV. A plot showing the energy at which Ag, AgO, and Ag_2O can be found in Figure 4.10, demonstrating the difficulty of determining if pure Ag, AgO or Ag_2O exists. The plot does show that thermal decomposition is a useful technique for determining this. As temperature is increased,

the curve shifts from AgO to Ag_2O, and then finally to Ag once the threshold value (400° C as reported) is reached [93].

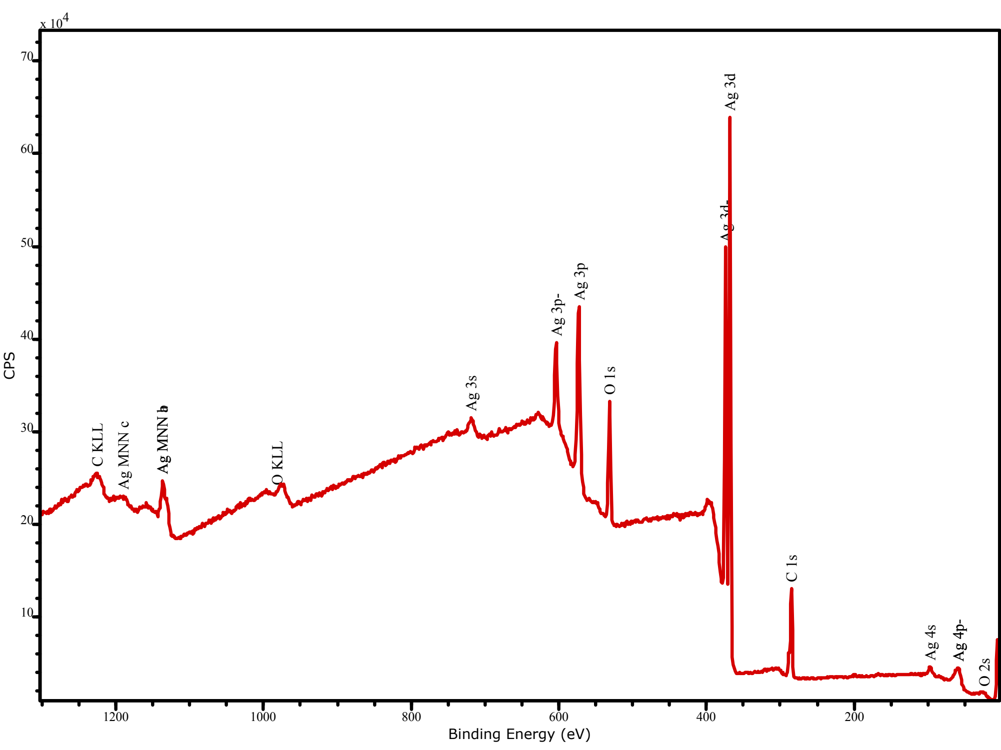

Figure 4.8. XPS analysis of as-deposited reactively sputtered silver oxide.

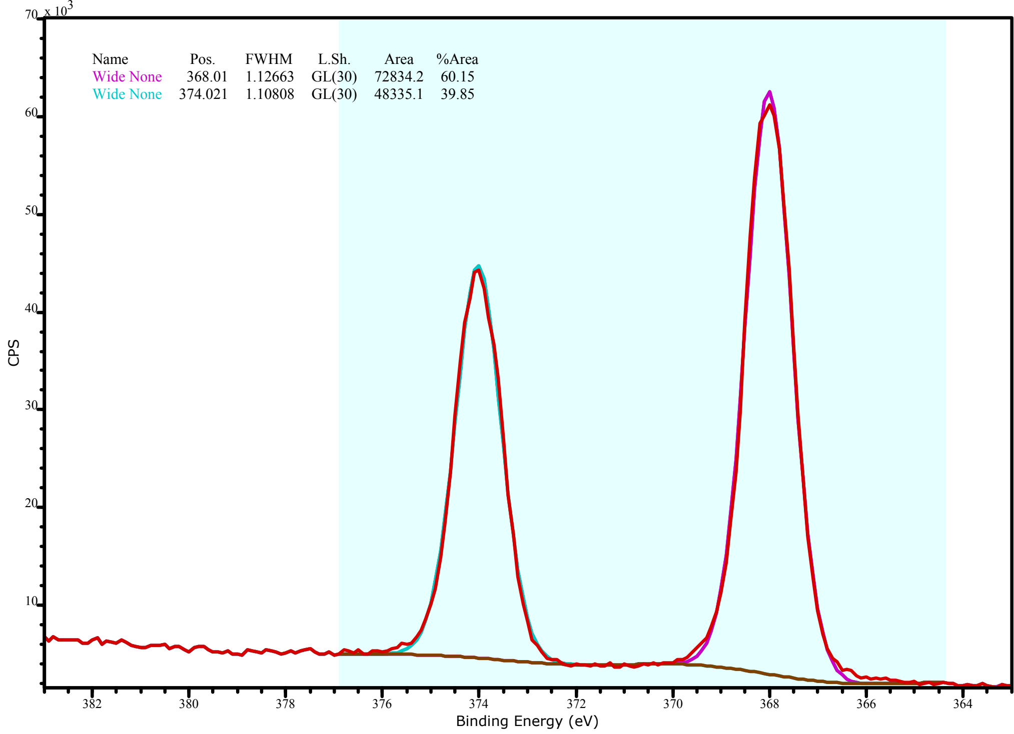

Figure 4.9. Binding energy of 3d orbital of Ag of as-deposited reactively sputtered silver oxide.

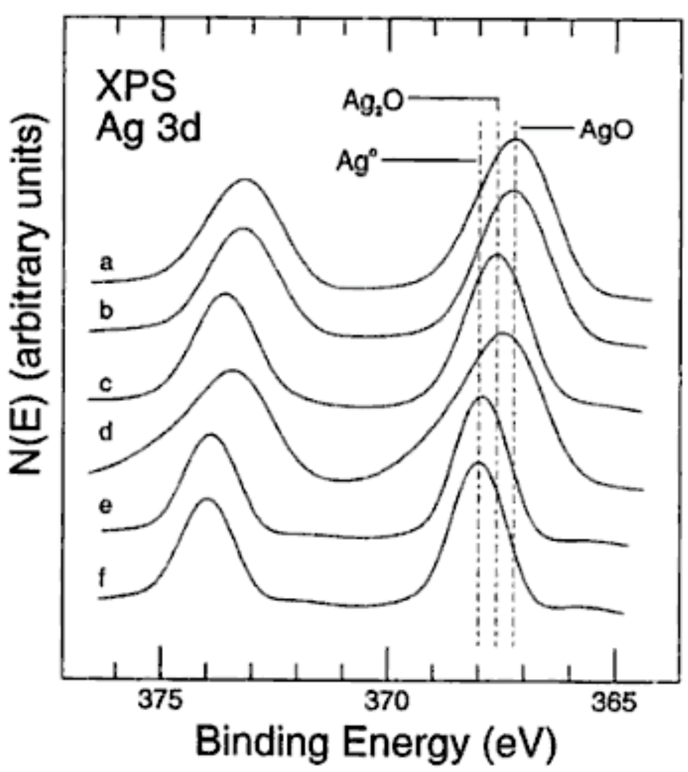

Figure 4.10. Auger peaks after annealing; (a) is no annealing, (f) is above 400° C [93]

4.5.2. Experimental Setup

In this test, silver-zinc batteries were placed in a flooded-cell. This means there is no limitation in the amount of electrolyte available and there is no possibility of saturating the solution. A 1 L beaker of deionized water in which 9 grams of NaCl was dissolved was used for the saline electrolyte (0.9% NaCl). Silver oxide and zinc were deposited on blank glass slides with no other materials present. A pure silver base layer to provide a current collecting and conductive layer was deposited on the glass slide prior to silver oxide deposition.

A silver/silver chloride electrode was used as the reference when connecting to the third electrode of a Keithley 617 Electrometer. The connections are shown in Figure 4.11. In this test setup, the electrometer was connected directly to a resistor box serving as a fixed load and an Ag/AgCl electrode.

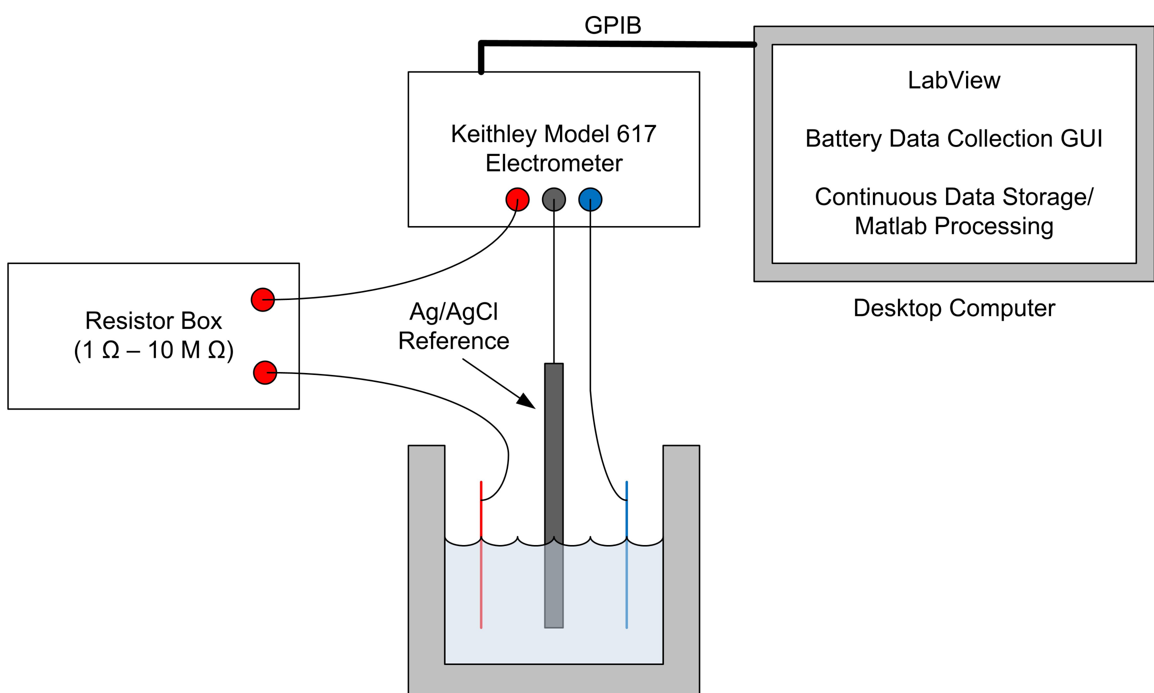

Figure 4.11. Test setup configuration for flooded-cell experiments

A Keithley Model 617 Programmable Electrometer was used, configured to measure voltage and current by switching between the two modes once every second. The settling time is listed as 15 ms for current measurements in the nA range, and the input impedance is greater than 200 TΩ in the voltage mode [94]. The connections were made with Triax shielded cables, which provide a single shield that operates as a ground with dual signal-carrying wires within the sheath. The reference electrode was connected to the shield wire to normalize the measurements to the saline solution and ensure the voltage potential measurement occurs across the two electrodes of interest.

A LabView program was written to control the GPIB port of the Keithley Programmable Electrometer to alternate between voltage and current reading of the cell under test. The electrometer is an extremely sensitive device and was configured to measure the voltage through an adjustable resistor load box. A standard resistor box showed signs of fluctuating resistances and so by providing both the voltage and current, power can be directly calculated at an almost instantaneous point in time. The data from LabView was exported to a plain text file for easy import into MATLAB for plotting purposes, resulting in the plots shown in the next section.

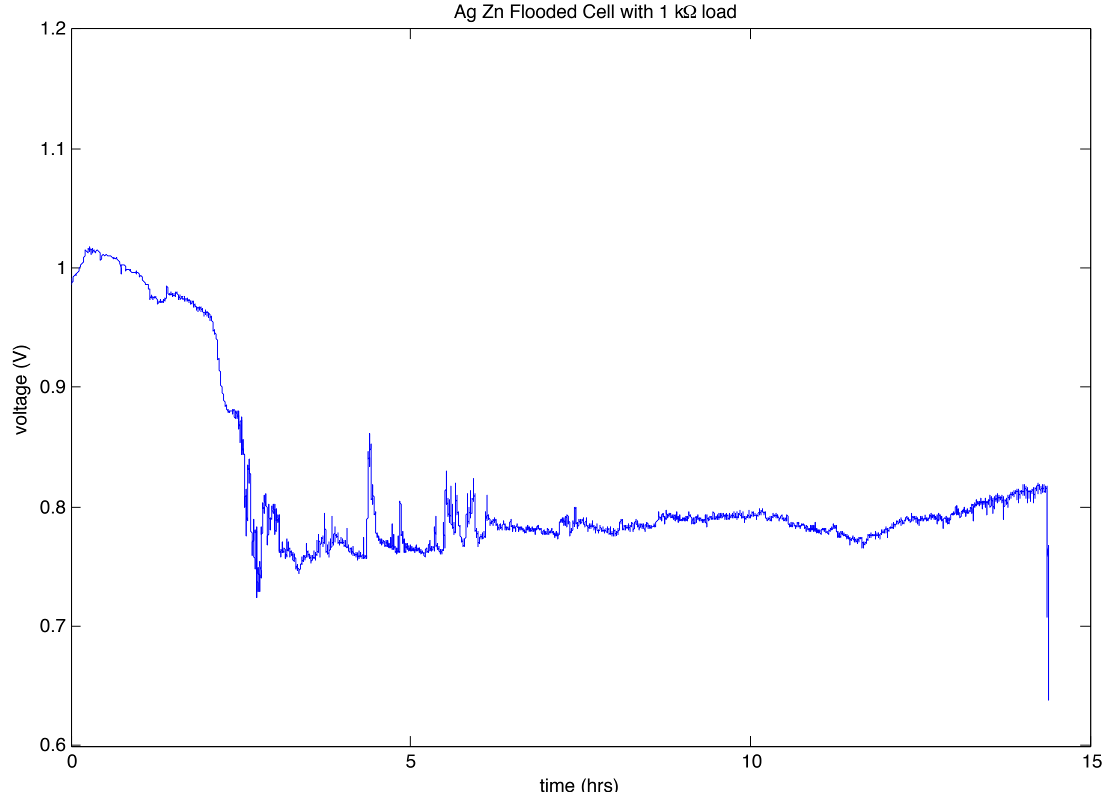

Figure 4.12. Plot of silver-zinc battery voltage with a fixed 1 kΩ load.

4.5.3. Benchtop Testing Results

Testing results indicated that the cell does indeed operate, though at a much lower voltage than a KOH-based electrolyte solution, as expected. Regardless, the data proves successful operation of the battery cell. Figure 4.12, Figure 4.13, and Figure 4.14 show plots from the flooded-cell experiments on glass slides with electrodes deposited on an area of approximately 60 mm x 25 mm. The translation of the bench top data to a microscale system using these dimensions is calculated later. In Figure 4.12, the battery voltage is plotted against time, showing no appreciable drop-off in voltage even after 15 hours with a 1 kΩ load. It also exhibits the telltale silver-zinc behavior with the initial higher-voltage generation at around 1 V and then the drop-off to a second-level operating point, as seen in Figure 4.3.

Figure 4.13 shows the demonstrable power output for these cells at almost 100 nW supplied to a 100 MΩ load. The plot indicates a smooth, mostly flat curve. This plot was generated from the instantaneous voltages and currents that were recorded by the

LabView software through the Keithley electrometer. This eliminates most fluctuations of the actual load through the resistor box.

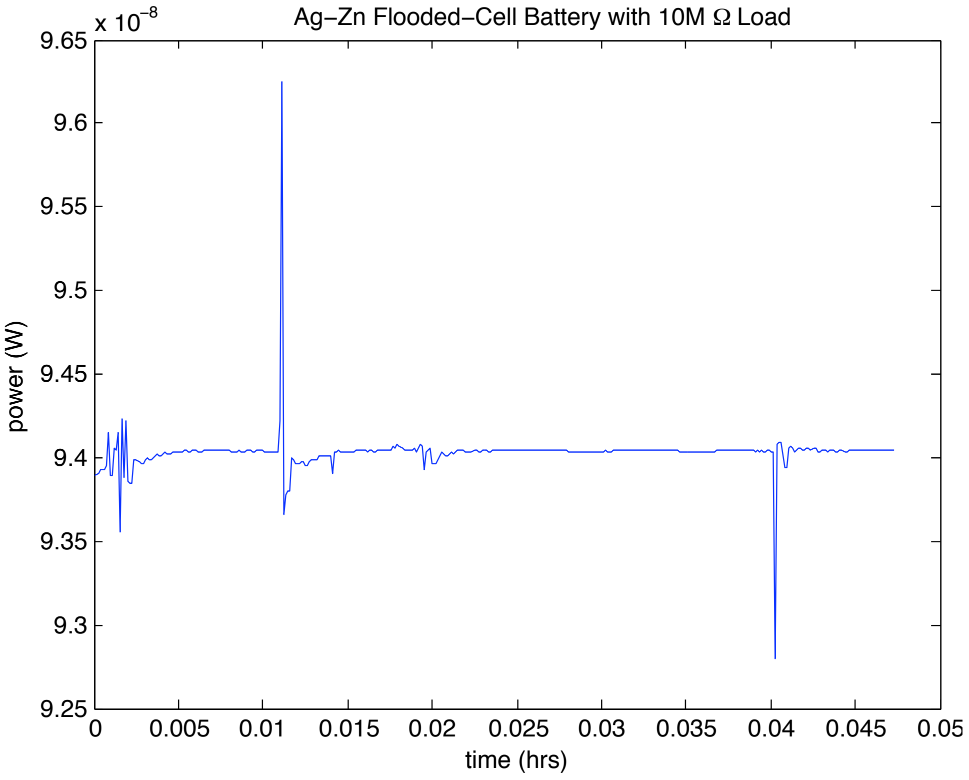

Figure 4.13. Flooded-cell test showing flat power supply of almost 100 nW.

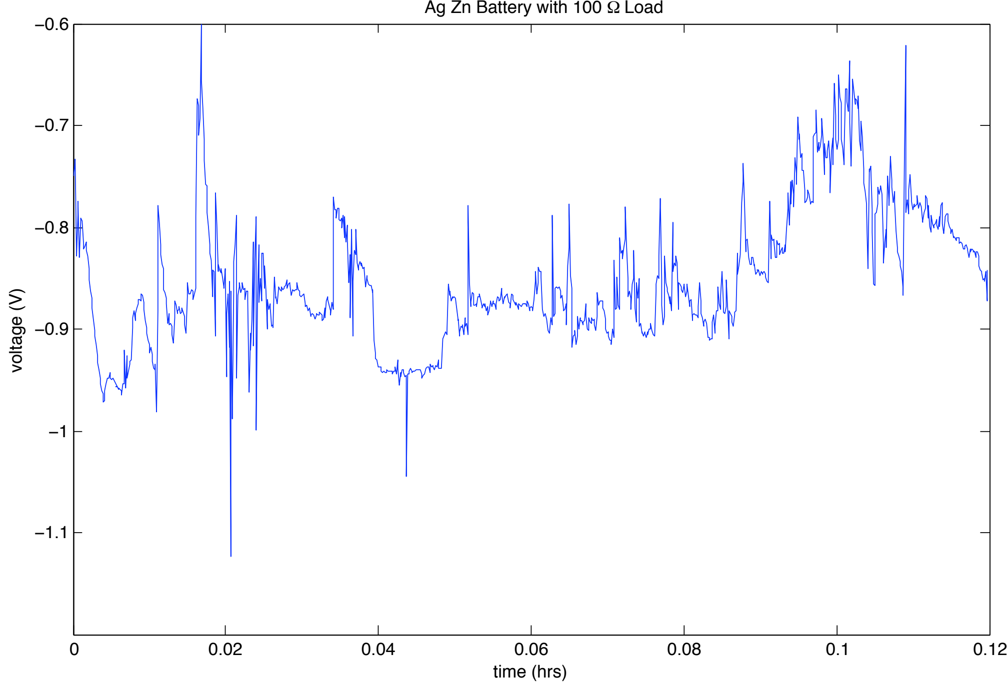

Figure 4.14. Flooded-cell test with 100 Ω and voltage fluctuations due to the current draw.

The plot in Figure 4.14 shows the instability in the voltage supply at higher currents, demonstrated via a fixed load of 100 Ω. This shows the limitation in the current density for this particular electrochemical cell and may not translate directly to smaller-scaled microbatteries. It does show that the silver-zinc chemistry is indeed powerful enough to provide large currents, here sourcing approximately 8 mA.

Increasing the electrode thickness increases the total available electrode material and should therefore increase the lifetime of the battery. Increasing electrode surface area would increase the peak available current, but keep the capacity the same. Finally, a well-defined endpoint for the voltage supply could yield longer life, such as until battery voltage drops to below 0.7 V.

Before providing calculations based on this data, however, there are two major flaws in assuming that a microbattery will operate in the same exact fashion as the flooded-cell approach. The flooded-cell provides no solute-saturation limit in supplying electrolytes and allowing more reactive species to enter the solution. This is a rough approximation since the completed microbattery will have an extremely small volume, on the order of tens of femtoliters. The second assumption is that recharging will work with this particular chemistry though this was not explicitly tested. A preliminary calculation for battery capacity is based on the 1 kΩ load and an average 0.8 V for 15 hours indicates a capacity 12 mAh. The total active electrode area is approximately 60 mm x 25 mm. Recalculating the current capacity for a per unit-area specification results in a value of 8 $\mu Ah/mm^2$. The electrode thicknesses are approximately 2000 Å for both electrodes.

The experiments presented here were used to understand the electrochemistry and show that the required electrode materials can indeed be deposited in a conventional cleanroom without using any exotic solutions. It has also been demonstrated (in experiments described earlier) that the high-temperature limit for subsequent process steps is 300° C, above which the silver oxide electrode would begin to spontaneously decompose into pure silver. The main limitation associated with these results is the lack of testing to determine the battery performance as a function of the volume of the electrolyte. The data presented here is based on flooded-cells and may not extrapolate to microscale devices in a linear fashion.

4.6. Alternative Power Sources

There are several alternative solutions for providing a micropower source for the intraocular application, but all have some disadvantages. Conventional battery techniques applied to the macroscale suffer from inadequate sealing and inefficient use of the available volume. Applying conventional electrochemistry to a micro-scale based system such as the microbattery discussed above alleviates most of these challenges but introduces the operating temperature limitation. The microbattery with liquid electrolyte cannot be exposed to temperatures above 100° C; hence, the need to explore additional options for long-term power sources. The following sections examine a commercial microbattery alternative and a non-electrochemical based solution in the form of an ultracapacitor.

4.6.1. Cymbet Microbattery

A commercial lithium-based microbattery has also been successfully used for the intraocular microsystem. The custom-fabricated design provides about 1 μAh at a nominal voltage of 3.8 V in a 1.4 mm x 0.9 mm package. This rechargeable battery is fabricated using a proven commercial process. The thin-film battery is typically used to provide a power source for backup memory on printed circuit boards [95]. The successful use of this microbattery in this application is published elsewhere [96].

The Cymbet battery is solder reflow compatible, meaning it does not have the temperature limit that conventional liquid electrolytes would impose. However, the packaging technique used in the intraocular application may require higher temperatures applied over extended periods of time beyond that expected during solder reflow.

The Cymbet battery uses a toxic electrochemistry based on lithium and an unknown electrolyte, which may prove problematic if it were to leak out. The commercial version of this battery is currently not used in and not intended for implantable applications. Another limitation is that the peak current that can be supplied is limited to 40 μW [96], which is not nearly sufficient enough to drive the wireless transmission electronics referred to in that work. Finally, the voltage supplied is very high, more than 3x larger than a typical low-voltage processor would require. Special electronics are required to step-down the voltage to useable levels and provide regulation.

Secondly, and possibly more problematic, is that the recharge voltage is 4.1 V, requiring this voltage to be generated (boosted) on-chip. The extra down-converter and boost-converter would both be sources of additional inefficiencies in the power subsystem for the intraocular application. Therefore, an alternative to the lithium-based microbattery is suggested, even though it has some distinct advantages such as the increased temperature range the device can withstand and its proven (on a commercial level) functionality.

4.6.2. Ultra-capacitors

Another interesting possibility is the use of ultra-capacitors, also called supercapacitors. These devices are a type of hybrid component that behaves like a capacitor in that they can supply very large instantaneous currents and can also be charged very quickly. The total stored energy density is still less than an electrochemical cell, but is many times better than a standard capacitor. Other advantages of the ultra-capacitor include a much higher ability to withstand multiple charge and discharge cycles as compared to electrochemical cells. Also, the materials used in typical ultra-capacitors are not typically toxic, do not require corrosive electrolyte solutions, and do not suffer from an overcharging condition or self-heating issues.

The main disadvantage of these devices is the complex electronics required to control discharging of the ultra-capacitor. As charge is drawn out of the device, its potential drops, unlike an electrochemical cell that can maintain its potential for most of its life. This means that a voltage regulator that can handle a very large input voltage range is required. Unfortunately, because of the nature of the physics behind the ultra-capacitor, it exhibits a high self-discharge rate. This means that even without supplying any power to an external circuit, the ultra-capacitor will lose its stored charge at a much faster rate than an electrochemical cell.

Overall, while ultra-capacitors are an interesting solution to the power storage problem and provide distinct advantages in terms of improved energy density, these may be outweighed by the complexity of the power circuitry required to correctly utilize them. The typical voltage supplied by these devices is considered low-voltage, but will still likely require a step-down converter to reach the more useful voltages used in low-power circuits.

4.7. Energy Scavenging

There are at least three methods of energy scavenging available within the eye that may generate appreciable power. The first is solar power, which is readily available due to the location of the device and the transparent nature of the eye. The second is the most common technique: wireless transfer of power via electromagnetic means, either using far-field RF or near-field inductive links. The third is mechanical-based energy scavenging that operates on the pulsatile pressure of the eye. With every heartbeat, the intraocular pressure varies about 1 mmHg [18]. If the pressure sensor is sensitive enough, this 1 mmHg can translate to a useable energy source in the form of an electrostatic energy generator.

Compared to the other two techniques, solar (photovoltaics) appears to be the most viable and useful approach since scavenging occurs at all times when light is available. Secondarily, electrostatic scavenging from changes in intraocular pressure is also worth further exploration, even at low power outputs, because the heart is constantly beating. This section reviews all three approaches.

4.7.1. Electromagnetic

Electromagnetic means of powering implantable devices have been studied and presented in the past. In fact, one of the more recent intraocular designs implemented an RF-based wireless power transfer [97], while most other intraocular designs have utilized inductive links [98]. The older devices suffer from excessive size, sometimes affecting the field of view due to the required size of the coils for an inductive link. More details about power drop-off versus distance are provided in Chapter 6, where the discussion is based upon the power required for wireless communication. There, the case is made that an RF solution is preferred in order to minimize the size of the receiving antenna. Previously published work demonstrates that power transfer via an RF link is viable and can be successfully used to recharge an on-board power supply, in this case a large capacitive array [97]. The drawback with even the latest design utilizing RF power transfer is the fact that the resonant antenna has to be several millimeters long. In the space-constrained eye, this can be problematic.

Since electromagnetic solutions for power transfer have been well studied and both types have been explored in the literature, independent work on these techniques was not carried out during this thesis research. However, future work on an RF-type solution for power transfer, but operating at a much higher frequency in order to alleviate the constraints on the antenna size, could be worthwhile. As frequency increases, the size of the receiving antenna decreases, but the signal may also be attenuated by the tissue. A thorough analysis of the applied frequency versus attenuation needs to be carried out since the literature is somewhat conflicted about actual data above several GHz. Electromagnetic fields in body tissue is discussed in Chapter 6.

4.7.2. Solar power

Photodiodes are semiconductor elements formed using p-n junctions that generate current as light impinges on them. Normally, a built-in voltage exists at the junction, creating a depletion region. The distance the depletion region extends into each doped (p or n) region depends on the doping concentration. When photons strike this depletion region, the electron-hole pairs generated within it and within a minority-carrier diffusion length of it are swept to their respective regions – holes to the p-region and electrons to the n-region. The wider the depletion region and the surrounding diffusion length, the greater the number of photons that will be collected and contribute to the current, called the photocurrent, through the photodiode. As light intensity increases, more photocurrent is generated, but the junction voltage reaches a maximum as the diode becomes strongly forward biased. The structure of a photodiode is simple, since it is based on a diode; the variations on doping concentrations, diode area and layout of the doped regions, and even top-level metal routing, can affect the overall performance.

CMOS solar cells are challenging to build but are not impossible, even with sub-micron features. The biggest drawback is that the process is fixed and not optimized for photovoltaic energy conversion, so there is no way to adjust doping profiles and concentrations. Also, the wavelength of captured light typically travels deeper than the active region of the silicon surface. One work in particular tested multiple layouts and found the diode between the well and the substrate to be the dominant contributor to photocurrent generation because it is a deeper structure [100]. Though this result was

determined using a 0.35 μm process, it is reasonable to assume that process nodes utilizing even smaller (shallower) structures would be likely to generate even less photo-current near the surface than with deeper diode structures.

The Phoenix processor, mentioned in the introduction and described in Chapter 5, also incorporates solar cells [96] and successfully used them to trickle charge an on-board battery. The total area the solar cell occupied is only 0.07 mm^2 and was constructed with deep n-well to p-well and p-well to n-active diodes.

Single photodiodes used to generate a supply voltage are constrained to a maximum voltage of approximately 0.5 V, not nearly enough to recharge most batteries and sufficient only for circuits operating in subthreshold mode. A special voltage boosting circuit is required, often dissipating power as it converts from a low input voltage to a high output voltage. For integrated circuits, an inductor is not easily available so capacitor-based circuits are typically used like the Dickson charge pump. A recent study concluded that voltage doublers are more efficient than a similarly designed Dickson charge pump, with a maximum conversion efficiency of about 60% and 50%, respectively [99]. This much loss coupled with the low efficiency of CMOS solar cells means that the expected power output would be low. Based on this very brief overview, it appears that CMOS solar cells are a feasible option for generating power in an intraocular application, and indeed it is has been shown to be a viable option for the energy-autonomous Phoenix processor.

It is worthwhile to explore alternative photodiode structures in CMOS as a way to improve the conversion efficiency between solar power and electrical power. However, in a standard CMOS process node, the only options are to improve circuit topology or optimize layout of the solar cells since the doping concentrations and depths cannot be adjusted. Another, less explored, alternative is to modify the photodiode structure itself. For example, there have been some attempts at introducing multiple diodes to generate the supply voltages directly, eliminating a voltage-boost circuit. One technique proposes a low-voltage rail of $-V_{dd}$, a ground rail of 0 V, and a $+V_{dd}$. Two different photodiode structures contribute charge to each supply rail, effectively doubling the voltage harvested using solar power in conventional CMOS [101].

The work here attempted to build a solar-cell array that connected three photodiodes in series using a conventional CMOS process. This would allow higher voltages to be generated using standard photodiodes, which are typically limited to about 500 mV. Only a process node that supports a deep n-well layer can allow series-connected diodes; otherwise, either a p-region or n-region is always tied to one supply rail or the other. The deep n-well allows for the creation of an n-well 'tub' in which a p-type region can be defined, completely isolating it from other active devices in the p-substrate. The deep n-well is typically used in CMOS structures to eliminate noise through the substrate by providing a conductive region that surrounds the active device [104]. Here, it is used to isolate the sequential photodiodes such that the intermediate node voltage can rise above the fixed voltage of the substrate. As the n-well is biased further, the parasitic diodes between the n-well and the p-type substrate prevent the well from leaking back into the substrate. A modified vertical NPN-type transistor is used as the solar cell. This topology was chosen because of the similarity the NPN transistor has to the desired final structure. As shown in Figure 4.15, the NPN emitter and collector are shorted together, forming a diode-connected bipolar transistor.

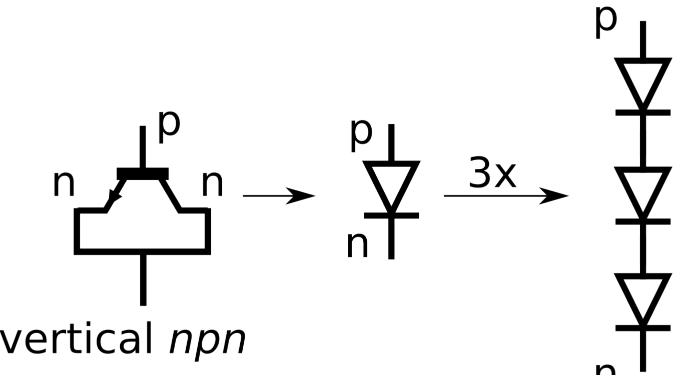

Figure 4.15. A solar cell constructed of three diode-connected NPN transistors in series.

A cross-section of the device clarifies the isolation between each diode and demonstrates how each photodiode is connected to the next. As shown in Figure 4.16, three NPN transistors are laid out next to each other. The emitter and collector regions (drawn symmetrically here, but in the actual device this is not the case) are shorted together and connected to the next stage. The p-region of the prior diode forces the n-well of the following region to move up in potential the same amount as the p-region.

The n-well and the base of the NPN are shorted together and are connected to the previous stage. The first stage is a substrate contact to ground.

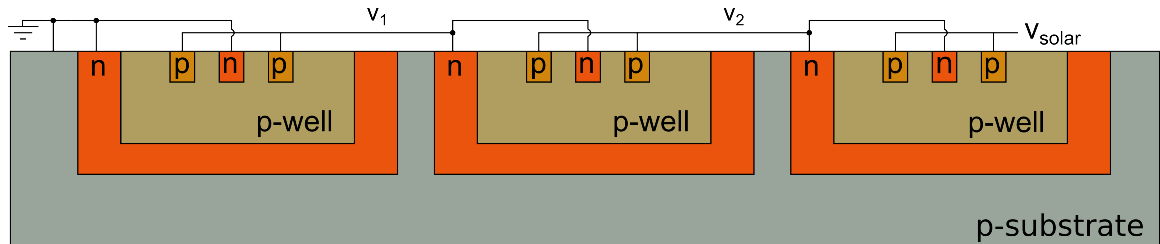

Figure 4.16. Cross-section of three photodiodes (vertical NPNs) connected in series. The orange region is the n-well, with the brown regions identifying the p-well located within the n-well.

One of the major challenges with this particular structure is understanding the parasitic diodes and making sure none are inadvertently forward-biased. Furthermore, it is known that the dominant photodiodes are typically deeper in conventional sub-micron CMOS processes [100]. It is therefore difficult to estimate how much power, if any, can be derived from this structure before it either leaks off into the substrate due to parasitics or dissipates before an appreciable voltage can be generated.

Figure 4.17 shows a circuit diagram of all the diodes in the solar cell array, including parasitics. Parasitic photodiodes are highlighted in red with the desired photodiodes in blue. Nodes v_1 and v_2 correspond to the node voltages shown in Figure 4.16. Prior to fabrication, it was unknown if the parasitic NPN transistors would contribute much if any current flow due to the low doping concentration of the base. However, because each isolated diode was fabricated close together, the series resistances through the collector and emitter may be low enough that an appreciable current may flow through the NPN, configured as a common-base. This would essentially create a short, setting v_2 equal to v_1 equal to the substrate voltage, which is ground, and render the entire photodiode stack non-functional except the last stage connected to V_{solar}.

The triple-stack photodiode structure was fabricated in standard TSMC 0.18 µm mixed-signal CMOS process. Since the TSMC process kit does not provide any photodiodes, standard parameterized-cell active components must be modified manually. The modified layout includes an additional layer, called RPO or Resist Protect Oxide, which prevents silicide formation over light-sensitive regions of the diode. The silicide would attenuate light and needs to be removed [102]. The wiring layout above the top

surface of the photosensitive regions was modified to allow more light to pass through. Recent work has calculated an optimal metal layout for unit photocells allowing the metal routing to also function as a capacitor but was not implemented here [103]. Finally, a layer is added to remove the passivation material that usually exists above the photodiode so light can strike the surface unaltered.

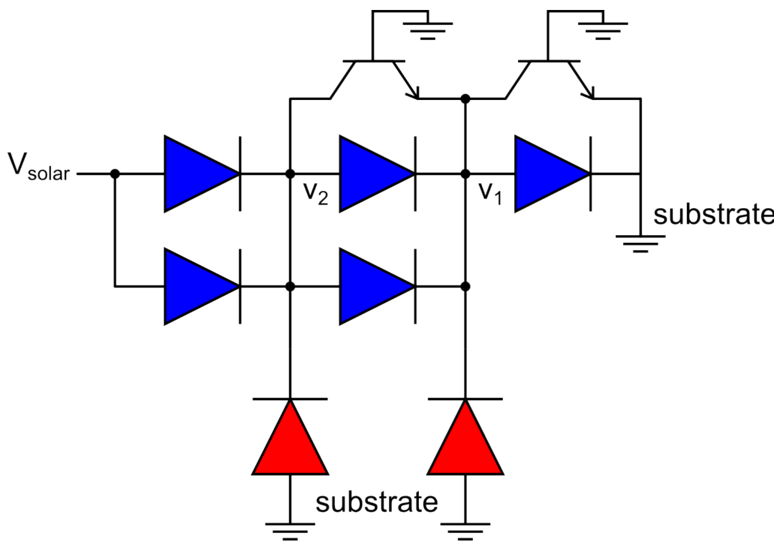

Figure 4.17. Circuit model of diodes in the triple-stack solar cell structure. Blue diodes are the desired photodiodes while red photodiodes are parasitic. NPN parasitic transistors are also formed between closely-spaced deep n-well regions.

Figure 4.18 shows the layout of a single cell, modified from an NPN-type transistor. As can be easily seen, the layout for each region of the transistor is not symmetrical since the device was designed to optimize the performance of an NPN transistor. Future versions should further optimize this structure so that the top-level metal routing is simpler and also maximizes the total photosensitive regions. In this work, the layout was minimally modified in order to ensure that the test devices functioned as intended, since they are essentially diode-connected NPNs in series. Only a few select layers are shown, including one metal layer (METAL1) and the contacts (CONT) to the diffusion regions. The mapping of these layers is shown in Figure 4.19. The NWELL layer defines the n-doped well, while layer DNW defines the deep diffusion 'tub' in which the NPN transistor sits inside. Layer DIFF is the diffusion region; the layers PIMP and NIMP indicate p-type doping and n-type doping respectively. Finally,

RPO is the layer used to identify regions where the resist protect oxide should be removed to prevent silicide formation.

Figure 4.18. Layout of modified NPN transistor, occupying about 24 µm x 24 µm.

Figure 4.19. Mapping of layers as used in the solar cell of Figure 4.18 and Figure 4.20.

The layout of the full solar cell includes three NPN devices in series, as explained earlier. Figure 4.20 shows the layout of several of these solar cells, wired in parallel. In other words, there are 27 total cells, each consisting of 3 photodiodes in series.

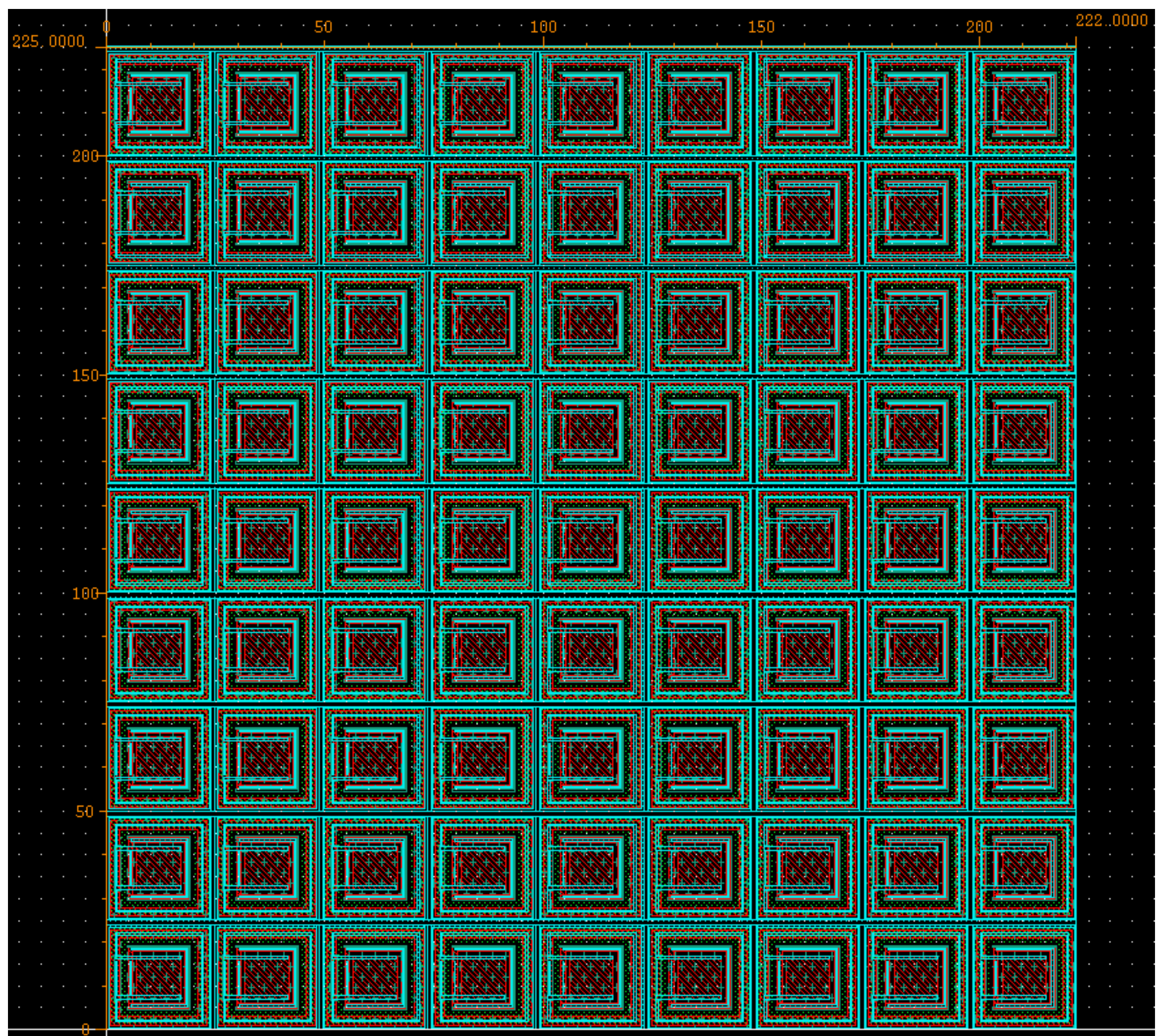

Figure 4.20. Layout of a 9 x 9 solar cell array, consisting of 27 total solar cells in parallel. The array measures 222 μm x 225 μm.

The simulated results indicate that a large voltage can be generated with such a structure. Figure 4.21 shows the expected DC output voltage for various light intensities, approximated with a current source placed in parallel with the NPN solar cell, representing the photocurrent. The current source is a only approximate, designed to mimic the photocurrent generated in a photodiode.

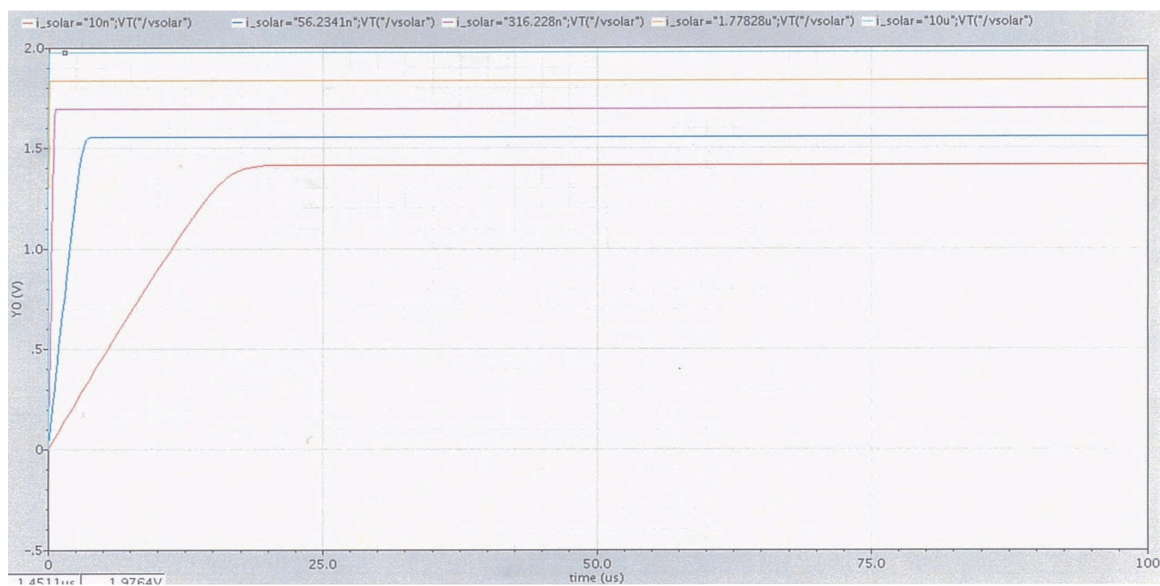

Figure 4.21. Plot of simulated voltages generated through the solar cell stack at different photocurrents. Note that all currents plateau and the lower the photocurrent, the slower to buildup the voltage.

Actual test results indicate that there may have either been a short developed between two sequential devices or some other layout error that prevented the open circuit voltage from reaching the simulated value. Figure 4.22 shows the open circuit and short circuit test results from a 9 x 9 solar cell array.

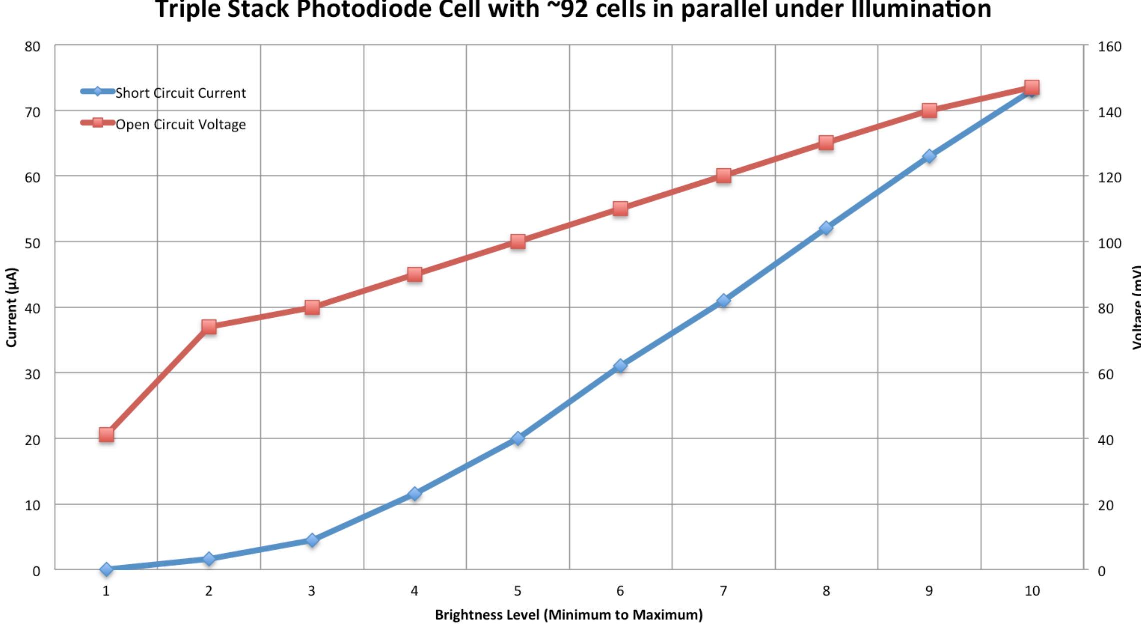

Figure 4.22. Output of full solar cell array showing both short circuit current and open circuit voltage.

In order to better quantify the performance of the photodiode, an I-V curve of a single photodiode array was taken using an HP 4155A semiconductor parameter analyzer under no illumination (ambient room lights off) and full illumination (microscope stage light on full). Under no illumination the photodiode stack performance mimics that of a standard diode and demonstrates a reverse breakdown voltage of 1.5 V. However, once light is applied, the breakdown voltage shifts closer to the origin, occurring at approximately 250 mV. The plot appears in Figure 4.23.

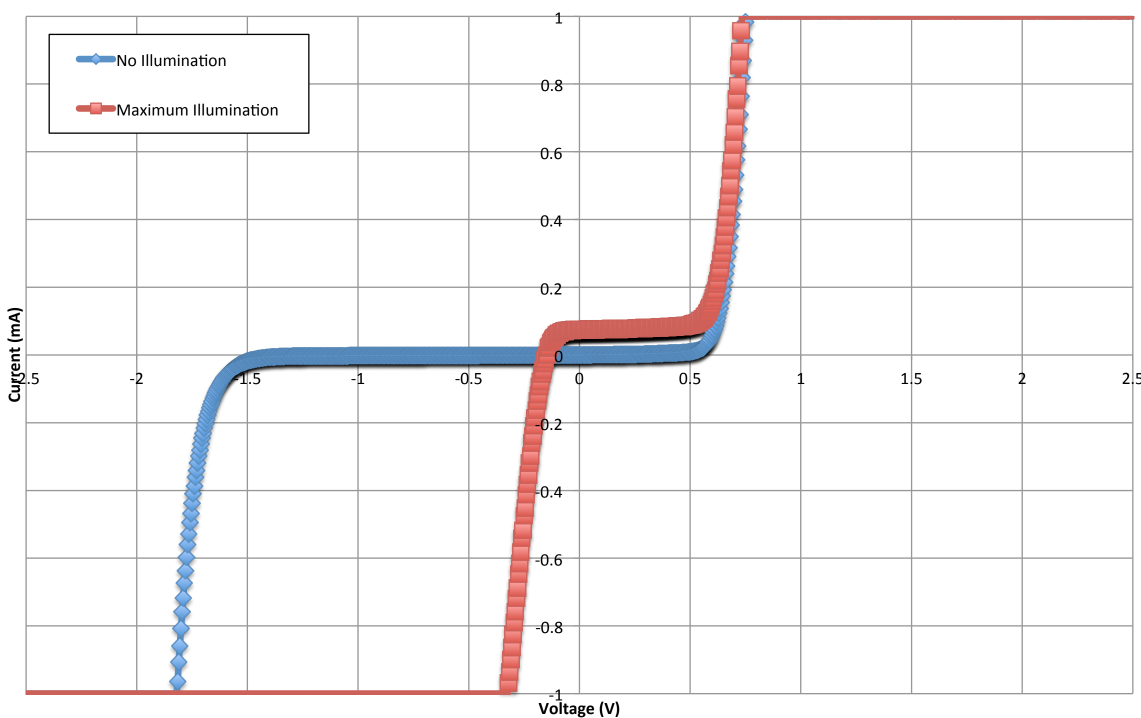

Figure 4.23. I-V characteristic of full photodiode array.

The results indicate that the photodiode has failed, and there are many potential sources of failure. An error in the layout is difficult to capture because this cannot be checked using standard design tools, such as Layout Versus Schematic, since the layout of the solar cell array is custom. The primary failure mode of the photodiode is attributed to an appreciable amount of leakage current passing through the NPN transistor between sequential stages as shown in Figure 4.17. A secondary possibility is that the distance between sequential n-wells is not sufficient, allowing some leakage to occur into the substrate. This may be due to imperfect sidewalls at the junction of the shallow-trench

isolation (STI) region and the doped regions. This can lead to significant leakage and stress mismatch [104]. Furthermore, these sidewalls can contribute a significant dark current [106]. A simple solution in layout requires a dedicated doped region formed as a ring around each of the photosensitive regions [107], capturing stray charges. A third possibility is that an additional unidentified parasitic diode, having its silicide layer removed, is inadvertently forward-biasing itself as the voltage generated increases. Future work should focus on determining leakage sources and ruling out whether the amount of current generated in the desired photodiodes is enough to overcome any efficiency loss in the photodiode itself. If the efficiency losses can be overcome with changes in layout, then the triple-stack photodiode structure may be a viable option resulting in much higher solar conversion efficiencies than conventional single photodiodes with dedicated voltage boosting circuits in standard CMOS.

This section discussed some early solar cell work and a new solar cell design useful for power-limited microsystems such as the intraocular microsystem. In this particular application, the solar cells would be used to trickle charge an on-board power source such as a microbattery. The results of the solar cell indicated additional studies need to be carried out with dedicated test structures to determine the source of failure.

4.7.3. Power Generation from Pressure Variation

It has been shown by previous studies that the pressure within the eye fluctuates about 1 mmHg per heartbeat [18]. As the heart rate increases, the amplitude of the pulsatile ocular pressure stays virtually the same but occurs with increased frequency, correlated directly with the heart rate. Energy generated from this source will be consistent and always present, as opposed to the case of the solar cell, which is limited to the times when the patient has his or her eyes open. Furthermore, solar cells operate more effectively in brighter light conditions such as the outdoors, as opposed to standard indoor lighting.

In order to better assess the maximum possible energy available due to a 1 mmHg pressure fluctuation in the eye, Equation (4.1) gives the total energy E of a capacitor C in terms of voltage V while Equation (4.2) shows the definition of a capacitance in terms of its gap g and electrode area A, as described earlier in Chapter 3. Equation (4.3)

rearranges pressure P in terms of gap changes by expressing it as force F divided by area. Furthermore, the force F can be defined in terms of a spring constant k and the total displacement of the diaphragm, where g_0 is the gap when no pressure is applied minus g. Finally, Equation (4.4) combines all the above equations and describes the relationship of the energy generated $E_{generated}$ with respect to pressure variations betweeen P_1 and P_2.

$$E = \frac{1}{2}CV^2 \tag{4.1}$$

$$C = \frac{\varepsilon A_{electrode}}{g} \tag{4.2}$$

$$\begin{aligned} P &= \frac{F}{A} = \frac{k(g_0 - g)}{A_{diaphragm}} = k\frac{g_0}{A_{diaphragm}} - k\frac{g}{A_{diaphragm}} \\ g &= -\frac{PA_{diaphragm}}{k} + g_0 \end{aligned} \tag{4.3}$$

$$\begin{aligned} C &= \frac{\varepsilon A_{electrode}}{-\frac{PA_{diaphragm}}{k} + g_0} \\ E &= \frac{\varepsilon A_{electrode}}{-\frac{PA_{diaphragm}}{k} + g_0}\frac{V^2}{2} \\ E_{generated} &\approx \frac{k\varepsilon}{2} \cdot \frac{1}{(P_{final} - P_{initial})} \cdot \frac{A_{electrode}}{A_{diaphragm}} \cdot \left(V_{final} - V_{initial}\right)^2 \end{aligned} \tag{4.4}$$

The important result from the final derivation of Equation (4.4) is that although there is a relationship between pressure-generated energy, the change in voltage on the capacitor can be quite substantial and increases quadratically. One of the major drawbacks of electrostatic generators is that an initial voltage $V_{initial}$ must be applied. This means either an on-board power supply in the form of a microbattery or photodiodes are necessary for an electrostatic generator to work.

Electrostatic energy generators operate on the principle of charge sharing. At the beginning of a charging cycle, a voltage is placed on the variable capacitor. The power supply is then disconnected, and the variable capacitance increases as the gap decreases,

causing the potential on the capacitor to increase. The charge is then shared with another capacitor, $C_{storage}$. A simple circuit diagram showing the electrostatic energy generator appears in Figure 4.24 along with the function of the circuit at each stage of an energy generating cycle.

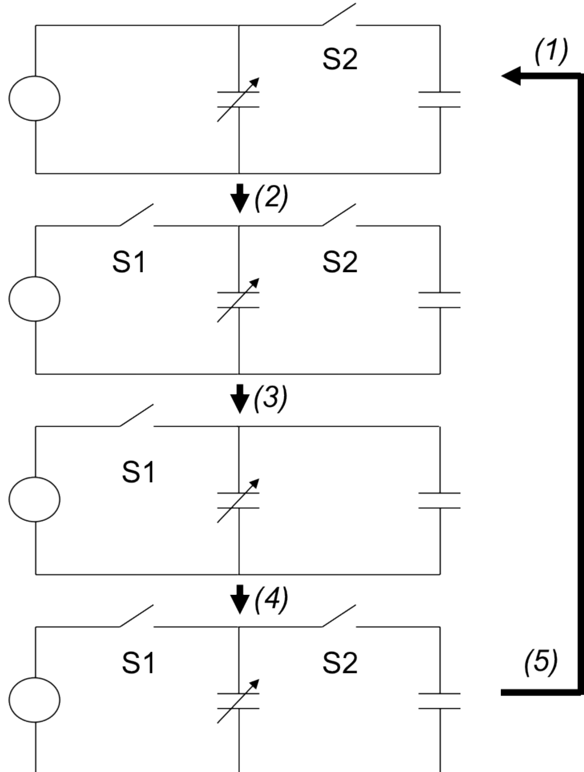

Figure 4.24. An electrostatic energy generation circuit demonstrating function at each stage of an energy generating cycle.

The first phase is the charge phase, with S1 closed and S2 open, allowing an initial charge to be placed on the variable capacitor. The second phase is the change in capacitance, while both switch S1 and S2 are open; the voltage on the variable capacitor $C_{variable}$ rises at this point. The third phase is the transfer phase, with S1 remaining open and S2 closed, allowing the charge to be shared across both capacitors $C_{variable}$ and $C_{storage}$. Finally, the fourth phase returns the capacitor to its original position, with both S1 open and S2 open. It is important to note that the energy generating cycles are non-resonant, meaning no specific frequency must be applied for it to operate at its peak efficiency although there may be ways to conserve and amplify mechanical energy in the diaphragm plate since it behaves like a spring.

There has not been mention of a fully-integrated electrostatic energy generator in the literature. This is most likely due to the parasitic losses in a small microsystem solution using discrete devices, which have been used in the past to demonstrate an electrostatic system. These previous designs have suffered large enough inefficiencies that very few practical devices have resulted [109]. It is unlikely that a microscale electrostatic generator has been demonstrated, combining both an integrated circuit and a microscale energy harvester such as the one suggested here, utilizing the pressure sensor as a generator when it is not used as a sensor.

A simple electrostatic energy scavenger based on diodes acting as pseudo-switches is shown in Figure 4.25. The diodes take the place of switches, avoiding the inherent losses as well as the additional drive and timing circuitry necessary [110]. However, CMOS fabricated diodes are also lossy, and the leakage rate will determine the minimum amount of current that must be generated per cycle for the circuit to make appreciable power.

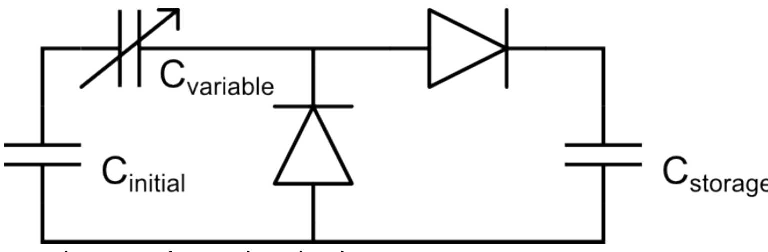

Figure 4.25. Electrostatic energy harvesting circuitry.

The simulation results indicate that the generator, based on the size of $C_{storage}$, can be strategically designed to take approximately 15 minutes to fully charge the capacitor. Figure 4.26 shows the voltage of a large $C_{storage}$ of 1 nF charged by a capacitor that changes 16 fF per cycle of pressure in the eye at a rate of 1 Hz or 60 beats per minute. The minimum current generated during operation is 6 pA, more than half as much power as generated when no voltage exists on $C_{storage}$, or about 14 pA. This reduced power generation is most likely due to the difficulty of placing more charge on the fully charged $C_{storage}$, making it more difficult to generate power once the capacitor is full.

Previous work demonstrated an efficiency of 71.8%, requiring external components such as an inductor [111], but did demonstrate a system for recharging a lithium-based battery. There has also been precedent for building an implanted

electrostatic generator that mounts to the wall of the heart, utilizing the heart's physical beat as the source of the energy [112]. The biggest drawback with this device is that it is a resonant device and generates peak power at only one specific frequency.

After listing these shortcomings, it still appears that electrostatic energy generation by way of intraocular pulsatile pressures may be a viable method. Even if the device can only produce fW of power, this may still be useful for purposes such as providing power for memory retention. Since the source of the power (the heart) is always present, a memory powered by this scavenging circuit will remain powered at all times, unlike solar cells or even an electrochemical cell with limited lifetimes and recharge cycles. Furthermore, another limiting factor will be the initial voltage placed on the variable capacitor. Iterative simulations showed that an initial voltage of 10 V provided the best efficiency but this may be challenging to achieve in low-voltage process nodes that cannot sustain a maximum voltage of 5 V even with special processing. Finally, another alternative that avoids placing a voltage across $C_{initial}$ is to use electret type capacitors since they maintain a fixed polarity across the gap.

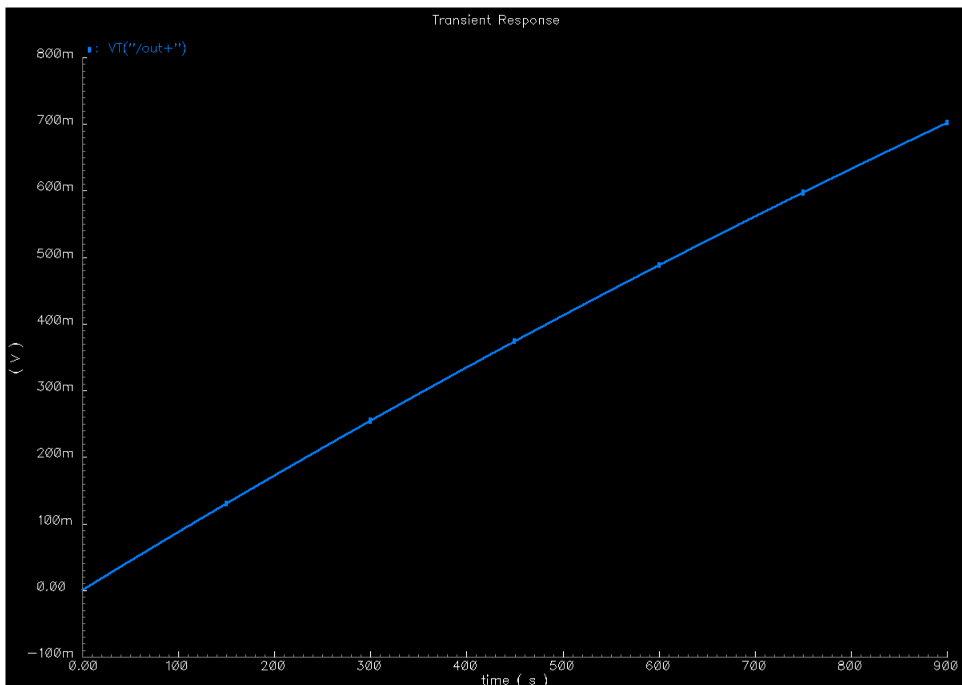

Figure 4.26. Plot of the output voltage over a period of 15 minutes. The electrostatic generator charges from 0 V to 0.7 V. The total energy stored is 245 nJ.

Before an electrostatic energy harvester such as the one described here can be built and used as part of an intraocular implant, there are several challenges that must be overcome. The first is an efficient switch that does not leak power between $C_{storage}$ and whatever load circuit exists after the switch. Simulation results indicated that any load on the other side of a standard MOS transistor operating as a switch was prohibitively large, disabling charging of $C_{storage}$ completely using the electrostatic mode. Therefore, good isolation between the charging circuit and the load is required when the circuit is powering up. Secondly, a very large capacitor must be fabricated that is currently not easily feasible in CMOS, at least at a reasonable cost. In lieu of a CMOS solution, the capacitor can be fabricated using a MEMS solution. Finally, the leakage through the diodes needs to be reduced substantially in order to generate an appreciable amount of power.

4.8. Summary

A microbattery has been designed with the main design goals of biocompatibility, small size, high energy density, cleanroom compatibility, and batch-mode fabrication. The materials chosen were based on the electrochemistry of zinc and silver oxide, with an electrolyte of saline. The electrochemistry choice was further based on rechargeability and the materials available in a standard MEMS foundry, such as the Lurie Nanofabrication Facility. Zinc is simple to evaporate directly onto substrates, while silver oxide requires a reactive sputtering technique to convert pure silver into silver oxide during deposition. Several challenges were addressed, mostly based on thermal budget, limiting subsequent processing steps to a maximum temperature of 300° C, which is high enough for anodic bonding. The overall design of the battery makes use of the proven design of the pressure sensor with vertical feedthroughs to help in stacking the ASIC and battery together. Testing on a macro-scale in a flooded-cell saline environment yielded a battery utilizing 2000 Å-thick electrodes on glass slides providing power to a 1 kΩ load for 15 hours. Extrapolating to the microscale yields an expected 8 $\mu Ah/mm^2$ current density.

Alternatives to the proposed microbattery were also presented, including a commercial thin-film lithium-based microbattery and the use of an ultra-capacitor, a sort

of hybrid between standard capacitors and a battery. The advantages and disadvantages of both were reviewed.

Energy scavenging techniques have also been discussed, including electromagnetic, solar, and pressure-induced mechanical scavenging. Both solar and electrostatic methods were looked at more closely. The brunt of the design effort and testing was spent on solar applications, a unique approach for implantable applications that is only relevant to devices exposed to ambient light or implanted just below the surface of the skin. An electrostatic energy harvester has been designed and simulated, although it is expected to provide an extremely low power output on the order of fW.

The work in this chapter has looked at several potential solutions to provide long-term power storage within the intraocular microsystem. A microbattery based on silver-zinc chemistry was also designed and fabricated though a second run is necessary to collect the necessary data and verify operation. Of the alternatives that were presented, the most appealing is the Cymbet microbattery due to its proven manufacturability and demonstrated use in the intraocular application. However, the main challenge that must be overcome is the toxicity of the materials used in this approach. Animal studies exploring the toxicity of the microbattery can yield useful data and it is entirely possible that the amount of toxic material is so small that it may prove inconsequential with regard to federal government testing standards. Additionally, if a protective coating or package seal can be used that eliminates any chance of leakage, this commercial battery may become a viable and preferred alternative. Energy scavenging in the form of solar power is not only practical but also proven in previously published work, allowing the intraocular microsystem to function in an energy-autonomous mode requiring zero external power. Other alternatives like mechanical scavenging techniques are not suggested until the sensitivity of the pressure sensor can be increased further.

CHAPTER 5

INTRAOCULAR CIRCUIT DESIGN

Previous chapters have discussed the various components of the intraocular microsystem, including the pressure sensor and power supply. This chapter focuses on the integrated circuitry that ties all the components together, providing functions such as the conversion of pressure to frequency, signal readout, power management, and wireless communication. The interface to the antenna module is described here as well, although the antenna module itself is discussed in the next chapter. The main purpose of the work here is to provide a demonstrable solution for the integrated circuit portion of the microsystem. An ASIC (Application Specific Integrated Circuit) was fabricated with the simplest functionality in mind while demonstrating useful low-power circuit techniques. An optical receiver was built to serve as a trigger to advance the state of the finite-state machine controlling the microsystem. A loaded ring oscillator is used to convert capacitance (transduced from pressure) to frequency, followed by counters to divide the resulting clock. Finally, a pulse generator was designed to create fast, short-duration pulses with fast rise and fall times to drive the external antenna directly.

A second chip with different functionality and operating at extremely low power was developed in collaboration with University of Michigan Professors David Blaauw and Dennis Sylvester and their students. This processor, called Phoenix, is an advanced microcontroller with extremely low power consumption made possible by operating its transistors in the subthreshold regime. The processor provides memory, wireless communication, a power regulator in addition to solar cells used to trickle charge a thin-film microbattery. Only a very brief discussion of this microcontroller is provided here since the details have been published elsewhere [96].

The ideal processor would be a combination of the two ASICs presented here, utilizing the optical interrogation technique and wireless communication method of the

simplified ASIC but implementing the memory and power management schemes of the Phoenix processor.

The purpose of the integrated intraocular circuitry is to provide two functions: conversion of the pressure data to an electronic digital format and the subsequent wireless transmission of this data to the external world, either in real time or on demand. This chapter begins with detailed descriptions of the circuitry designed and fabricated as a part of this thesis work and then moves on to show test results. A later section in this chapter discusses the contributions of the Phoenix processor to the intraocular microsystem. Finally, a short discussion of the components needed for an ideal intraocular microsystem is included to identify what remains in terms of future development work.

5.1. Controller

Simple control logic in the form of a finite state machine is all that is necessary for the intraocular microsystem. Four states are required: State 0: idle mode, State 1: 5 pF reference test mode, State 2: pressure sensor input, and State 3: 1 pF reference test mode. States 1 and 3 utilize the two on-chip reference capacitors and are used for calibration. Switching between multiple states is achieved using an optical trigger, implemented with a photodiode connected to a Schmitt trigger. This technique replaces the typical constantly powered wireless receiver that waits for a wakeup signal while continuously burning power. A photovoltaic-based solution is ideal in this particular application because rather than consuming power at all times, the optical trigger operates only when an optical source exists. In this implementation, the only static power consumption occurs in the Schmitt trigger and the controller during the idle mode.

The controller is implemented as a 2-bit counter and must be continuously powered otherwise the current state will be lost. Future versions should not require constant power if the wakeup state from idle is well-controlled. Furthermore, a modified optical trigger may source power from the optical source itself, eliminating the need for static power dissipation in the Schmitt trigger. This means that the entire controller circuitry could consume virtually zero power if redesigned with these features in mind. During States 1 through 3, the entire system is active, with the three-stage ring oscillator loaded by the respective capacitor.

A 9-bit counter is connected to the output of the oscillator, providing a single pulse by resetting itself when the counter rolls over to the 10th bit. Nine bits is equivalent to a clock division of 512, slowing the clock frequency down so that enough time is available between successive pulses to recharge the output pulse generator. The counter output pulse is used to drive a pulse generator, which further sharpens the rise and fall times. The pulse generator is fully digital and drives the antenna directly without a dedicated power-amplifier stage. The following sections describe the optical trigger, the conversion of capacitance to frequency via a loaded ring oscillator, and the pulse generator. Figure 5.1 shows a block diagram of these components and how they are connected to each other. Note the external device, which contains a receiving antenna and an LED to trigger the optical wakeup receiver.

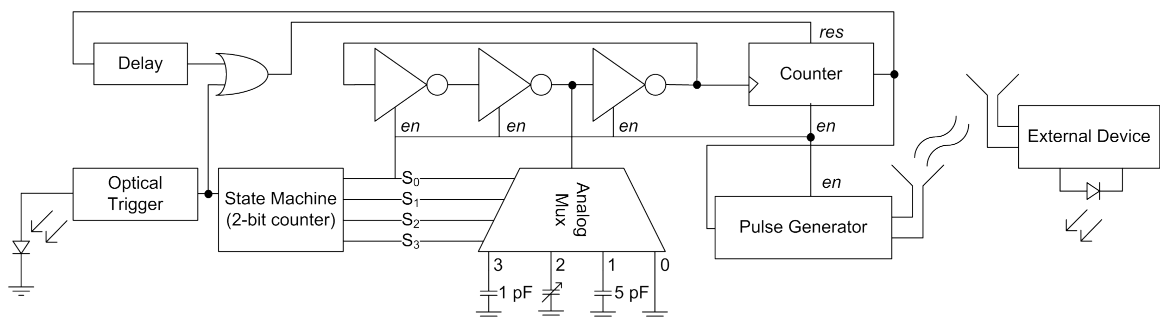

Figure 5.1. Overall block diagram of fabricated integrated circuit.

Eliminating components and removing functions that can be implemented externally achieve the majority of power savings. No dedicated wireless receiver is included since it is unnecessary and places the burden of analysis and data capture on the external receiving device. By using a finite-state machine, no instruction memory or programmability is included, thereby simplifying the design but also forcing a single specific mode of operation. The external receiver must be prepared to receive signals wirelessly and communicate with the implant using the optical pulse output from an LED. The implanted finite-state machine only changes state based on an externally applied optical pulse that provides a 'data acknowledge' signal indicating a successful data transmission. In essence, simple bi-directional communication is achieved by way of a wireless link and an optical link. The data itself is also simply time encoded without using any additional circuits.

5.2. POWER OPTIMIZATIONS

The ASIC designed here also implements multiple circuit-level power-saving solutions. The first adjustment is to utilize high-V_t devices. These active transistors are fabricated with a thicker gate oxide, increasing their threshold voltage but more importantly, reducing their leakage current during the off-state. Typical circuits that require high-speed functionality utilize the standard V_t devices. Pad drivers and circuits that interface with the pad where electrostatic discharge protection may be needed are better served by the high-V_t devices in a standard design.

Another optimization technique used is power-gating, which inserts header and footer transistors into the power rail of each circuit. This creates an internal voltage supply $V_{internal}$ that may be switched on or off as the need arises. The controller sets the state of the power-gating transistors through an ENABLE signal. During State 0, the idle state, this signal is set to digital low, disabling the internal power rail. The power switch itself, however, is not enough to ensure controlled logic functionality since the missing supply voltage can cause the internal nodes to float. Floating voltages are not desirable in a fully-digital design since later stages could be forced into possibly turning both PMOS and NMOS devices on at the same time, creating a large leakage path directly between the supply rails. If the following stages are not power-gated, the result could be problematic in terms of power consumption but also in terms of digital errors. In order to avoid this, at least one and possibly two transistors are used to gracefully power-down blocks by simply forcing the output node to a known voltage, such as digital low, and dumping excess charge into the intermediate power rail (e.g., $V_{internal}$) to ground and a zero state. Relieving charge on the power rails also ensures no spurious signal can inadvertently be generated as the block powers down. For example, the D-latch in the clock divider circuit includes an enable switch, allowing it to be powered off during idle mode. Again, in order to ensure no leak states are induced, the output of each stage is forced to a known value. The drawback of using a power-gating technique includes slower operation, since less current is delivered to the logic circuitry, and the addition of up to four more transistors per logic circuit. Both of these issues are not important in this particular design since the speed of the circuitry is not critical for this application and area is not at a premium since the overall circuitry is very simple.

Finally, for high-current stages such as the pulse generator, a special power-gating solution is implemented. The main challenge here is the additional resistances that are included in the power supply path due to the header and footer transistors during normal, powered operation. They reduce the voltage supply rail and dramatically affect the slew rate of the transistors since less drive current is available. This effect was so detrimental it meant either raising the supply voltage, which would increase the total leakage power as well as dynamic power, or simply eliminating the header and footer transistors and disabling power-gating. Unfortunately, the latter solution is not ideal since the pulse generator is the major contributor of leakage power during the idle state due to the size of its devices. Another problem with this block is that due to the large transistors used in this circuit, an enormous current is required on startup. If the state machine enables the block during normal operation, it is very likely that the local power draw will inadvertently reduce the power rails' voltages and possibly cause a loss of state or other malfunction.

An alternative solution was developed to alleviate these challenges, resulting in a form of power-gating but with full-swing of the voltage rail. A large capacitance is inserted into the local power rail of the block, after a power-gating transistor. This capacitance serves as a local power supply and is charged through the current-limiting power-gating transistor. This approach is ideal for this particular application because the pulse generator is never required to provide an output immediately when the enable signal is set high since the digital counter connected to the ring oscillator must first count up to 9 bits, providing a delay on the order of milliseconds, depending on the frequency of the oscillator. On the 10th bit, the counter resets itself, generating a pulse that is sent to the pulse generator, increasing slew rate and boosting drive current. The circuit diagram used to implement the internal charging capacitor is shown in Figure 5.2.

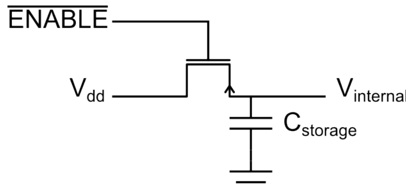

Figure 5.2. Power sub-circuit showing how the internal voltage supply is maintained during non-idle modes. When ENABLE goes high, the circuit charges Cstorage slowly to Vdd. Cstorage allows the local circuitry on Vinternal to dissipate current quickly.

The capacitance $C_{storage}$ must be quite large since during the pulse transmission, this capacitor behaves as the only power source, discharging up to 5 mA during the pulse and slowly recharging through the power-gating transistor between pulses. $C_{storage}$ consists of both metal-insulator-metal (MIM) capacitances and MOS-based capacitances that vary in value based on the voltage stored. The PMOS switch device pulls the voltage on the capacitor ($V_{internal}$) all the way to the supply voltage (V_{dd}). The MIM capacitance is approximately 24 pF with another 36.8 pF stored in the MOS capacitance directly below the MIM capacitance. The total area consumed by this 50 pF capacitor and the digital circuitry for the pulse transmitter occupies 182.5 μm x 97.5 μm. The layout is shown as a part of the discussion on the pulse transmitter in a later section of this chapter. Simulations indicating power draw through two different pulse generator circuits were also conducted to verify the utility of the previously mentioned high-V_t devices and their use in power gating. Figure 5.3 shows the pulse transmitter without the high-V_t devices while Figure 5.4 shows the high-V_t devices included in both the ENABLE and the idle (SLEEP) state for the pulse generator. In these plots, the pulse generator is artificially triggered.

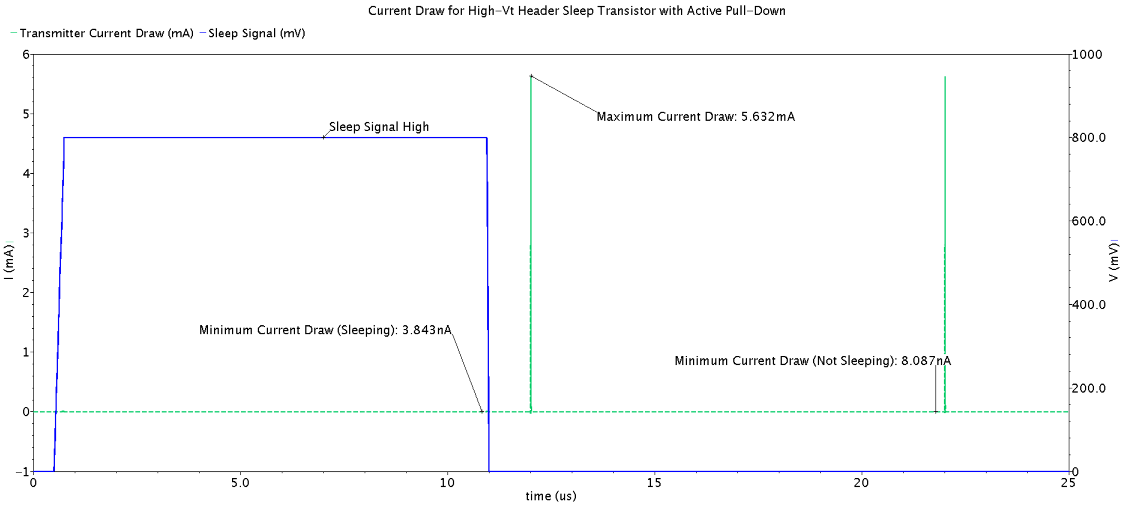

Figure 5.3. Plot of current draw through the pulse generator circuit for both idle and non-idle states. The two peaks during the non-idle state indicate a pulse transmission.

Similar to the transmitter, a chip-level power-gated capacitor is also implemented with its own $C_{storage}$. Since the rest of the circuit blocks do not consume much dynamic current, they are all connected to the same internal voltage node and are switched off

during idle mode, when ENABLE is digital low. In this case, the total MIM capacitance is 14.8 pF while the MOS capacitance is 5.7 pF, resulting in a total storage capacitance of about 20.5 pF. The only two blocks that remain powered at all times are the optical trigger and the finite-state machine.

Several studies of the total power consumption of the system were carried out in order to optimize the current draw and provide a predictor for total power consumption. The results of this simulation data are shown in Figure 5.5 during a non-idle state with all components powered at 800 mV. Figure 5.6 shows those same blocks but in the idle state.

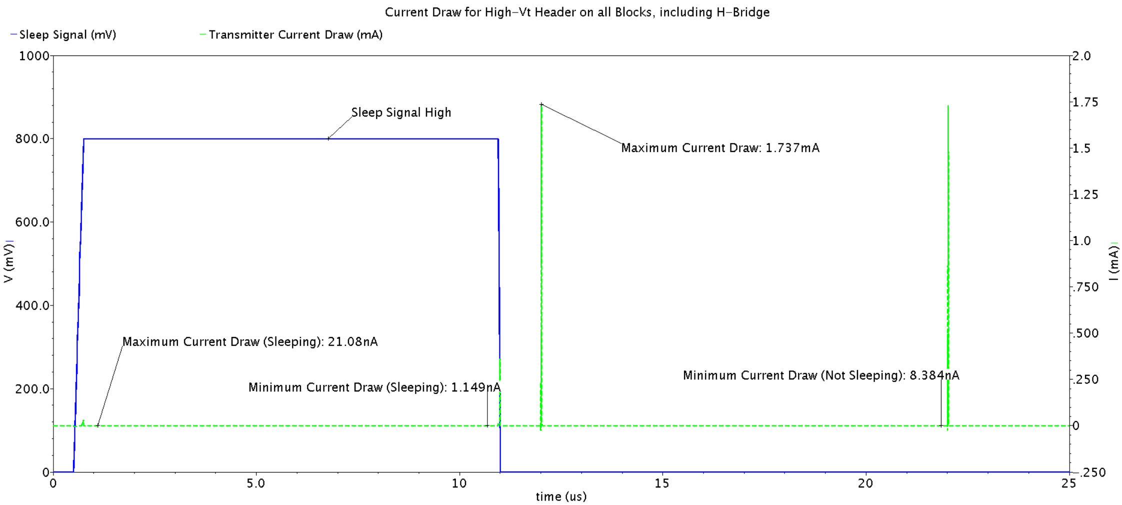

Figure 5.4. Plot of current draw through the pulse generator circuit for both idle and non-idle states, but with power gating as described in this section.

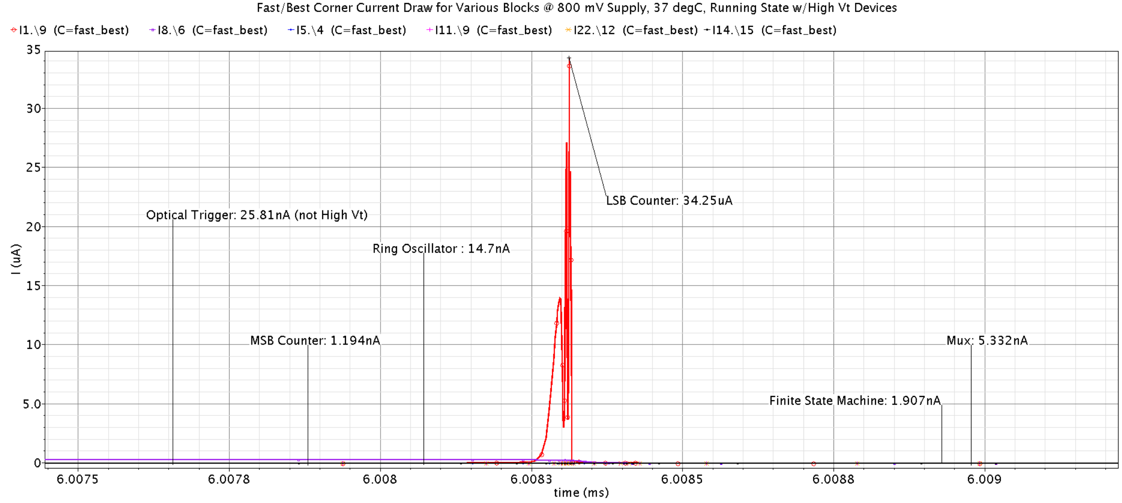

Figure 5.5. Plot of current draw when ENABLE signal is high and all blocks are powered.

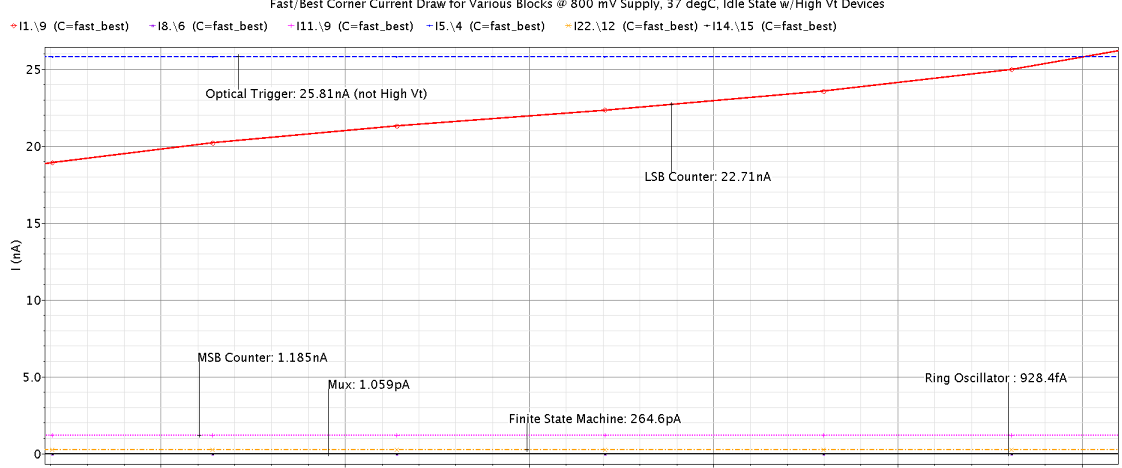

Figure 5.6. Plot of current draw when the ENABLE signal is low and most blocks are powered off.

5.3. Optical Trigger

The optical trigger is designed to avoid a constant power draw on the supply used for generating a wake-up signal. The main component of the optical trigger is the photodiode, fabricated in the standard CMOS process provided by TSMC. The only process change in the layout is the removal of a silicide layer, which attenuates light, and the glass cut layer used over pads to remove dielectric over the photodiode. Normally, the silicide layer is important for standard active devices (i.e., diodes and transistors) since it prevents light from affecting the functionality of the circuit and increases the conductivity of contacts.

The photodiode generates photocurrent from an external light source that passes through a high-pass analog filter configured with a DC-blocking capacitor and a resistive path to ground. This ensures that only pulsatile optical signals will be able to pass through to the Schmitt trigger. The high-pass filter utilizes a simple analog technique to eliminate potential ambient optical sources, such as room light, which otherwise could falsely trigger the system. For an optical frequency above about 24 Hz, the human eye cannot distinguish an oscillating on-off image, resulting in what would appear to be a constant signal. Furthermore, many environmental sources of optical pulsations exist at about 60 Hz, due to the AC frequency of building power supplies in the United States. To ensure that no inadvertent triggering can occur, the high-pass filter cutoff frequency is

set above 500 kHz. This value is chosen to be just below the upper limit at which conventional low-cost LEDs can turn on and turn off [113][114].

The pull-down resister of the high-pass filter ensures that the input of the Schmitt trigger is nominally set to zero, especially upon startup when power is initially applied. This avoids a dedicated startup circuit for the finite state machine. The Schmitt trigger is used to shift the switching point of the device as compared to a standard inverter so that an appreciable pulse is generated that can be detected by the input of the finite-state machine. The switching point is adjusted by deliberately inducing hysteresis. In other words, the purpose of the Schmitt trigger is to increase the width and smooth the pulse prior to passing the signal on to the finite state machine. A block diagram showing the optical wake-up trigger is shown in Figure 5.7.

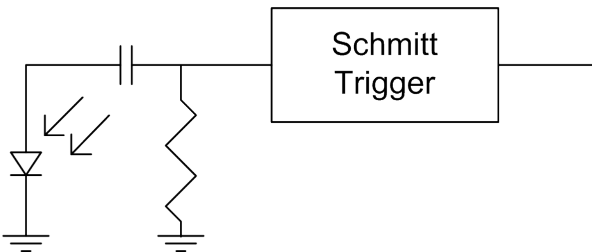

Figure 5.7. Optical trigger block diagram – an optical light source generates a photocurrent in the photodiode, triggering the Schmitt trigger after passing through a high-pass filter.

The actual circuit implementation appears in Figure 5.9. Here, D1 is the photodiode, implemented in a standard TSMC 0.18 µm process. The process kit provided by TSMC includes a diode component called "pdio" which signifies a diode that is formed between the P+ region and the NWELL region. This diode, providing a total active area of 1.2 nm^2 and perimeter of 140 µm, was modified to suit the purpose of a photodiode. Removal of the RPO (silicide) layer and inclusion of a glass cut layer is necessary. The wiring layout was also modified: instead of covering the active diode area, contacts were placed along the edges of the diode. The physical dimensions of the diode are about 36 µm x 36 µm. The circuit model of the diode also includes a shunt resistor of 1×10^{-10} $\Omega/\mu m^2$.

Figure 5.8 shows a cross-section of the photodiode and a parasitic diode that contributes a photocurrent for longer wavelengths of light. The diode is placed in an n-

well, available only in this particular version of the TSMC 0.18 μm process since it is used to provide additional shielding for RF circuits.

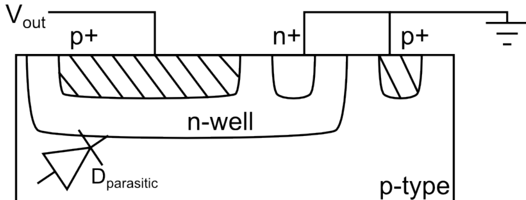

Figure 5.8. Cross-section of the photodiode, showing a parasitic photodiode. This diode does not function since the n-well and substrate are held at the same potential.

Transistors M1–M6 are high-threshold devices, limiting the static leakage current through the transistors in the off-state, a critical feature of the overall circuit design that effectively reduces power consumption, even during idle mode when the circuit block is fully powered.

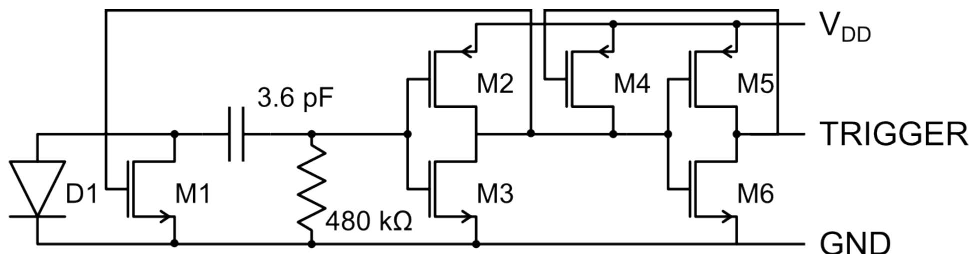

Figure 5.9. Circuit implementation of the optical trigger, showing the high-pass filter and Schmitt trigger.

The high-pass filter consists of a 3.6 pF capacitor and 480 kΩ resistor, resulting in a cutoff frequency f_c as calculated in Equation (5.1). The purpose of the high-pass filter, as stated previously, is to prevent ambient or environmental optical sources from inadvertently triggering the circuit.

$$f_c = \frac{1}{2\pi RC} = \frac{1}{2\pi(480\text{E}3)(3.6\text{E}-12)} = 92 \text{ kHz} \tag{5.1}$$

It is important to note transistor M1, since this device discharges the photocurrent after the pulse has been detected in the first stage of the Schmitt trigger. This ensures that the Schmitt trigger is not doubly-triggered and also provides a means by which photocurrent is drained off, preventing potential damage if excessive voltage were to buildup on the plate of the capacitor.

The high-pass capacitor is a MIM (metal-insulator-metal) capacitor with a 2 fF per square micron capacitance available as a special option in the TSMC 0.18 μm CM018 (mixed-signal) process at additional cost as compared to the nominal 1 fF per square micron capacitance. Only two capacitors sized 1.8 pF each are necessary, consuming 1800 μm^2, not including the area required for interconnect. The resistors are fabricated using an NWELL conductive layer below the STI (shallow trench isolation). Twenty resistors in series each consuming 100 μm^2 were required to generate the necessary resistance of 480 kΩ.

Transistor M4 is the main functional transistor of the Schmitt trigger, shifting the switching point by adjusting the width to length ratio (W/L). As M4 is strengthened, it increases the hysteresis of the Schmitt trigger. However, if the transistor is enlarged too much, the gate capacitance essentially loads the output of the Schmitt trigger requiring a resizing of transistors M5 and M6. Iteratively simulating the circuit in order to determine optimum transistor sizes was essential to ensure that the optical trigger functions as expected.

The AC response of the photodiode is critical in understanding the intrinsic filtering effect of the diode itself. It is presumed that the photodiode has an upper cutoff frequency determined by the intrinsic capacitance of the diode itself, setting the upper-bound on the signal that the diode can effectively pass through to the high-pass filter without attenuating the signal. The simulation plot of the photodiode AC response and the high-pass filter after the photodiode appears in Figure 5.10. It is clear that in order for the optical trigger circuit to function correctly, a pulsating optical source must oscillate at a frequency between 32 kHz and 850 kHz.

Simulations of the complete circuit indicate functionality for the desired range of input frequency. The plot in Figure 5.11 shows the digital output of the TRIGGER port of the optical trigger circuit. Eight different frequencies emulating an input optical signal were tested. Only those signals that had a frequency of 100 kHz or higher successfully generated a full voltage digital swing for a supply voltage of 800 mV. All signals below 100 kHz failed to generate any signal whatsoever with the circuit successfully suppressing any noise on the output, as evidenced by the signal staying flat with no extraneous spiking of the TRIGGER port.

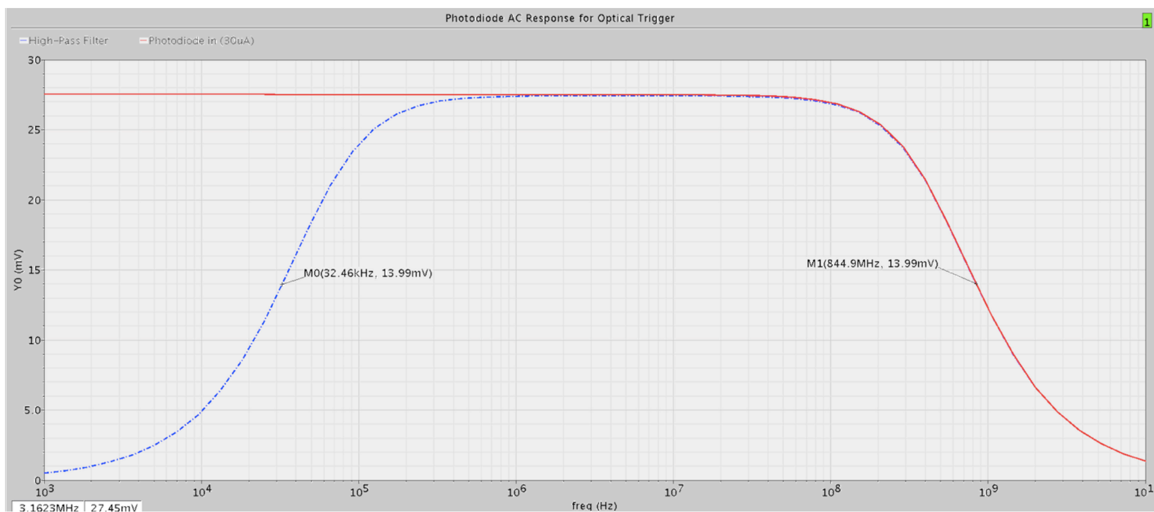

Figure 5.10. Photodiode and high-pass filter AC response as used in the optical trigger, showing a bandpass filter effect effectively passing signals between 32 kHz and 845 MHz.

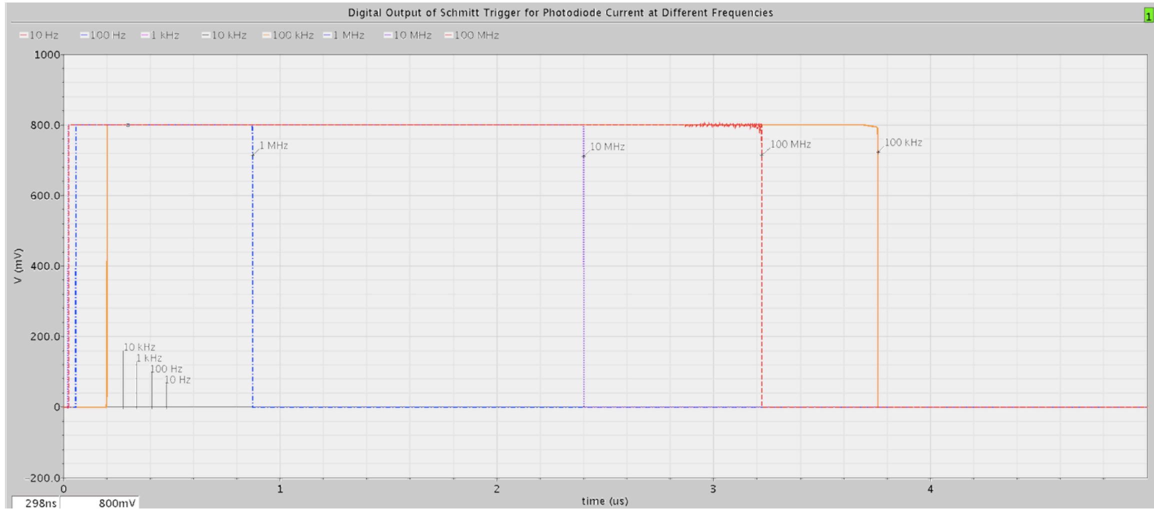

Figure 5.11. Simulation plot of optical trigger circuit showing operation with different optical pulse frequencies. Only signals above 100 kHz effectively generated a digital pulse.

The total area consumed by the passive components dominates the layout of the optical trigger circuitry. The photodiode itself was kept small, although increasing the size will increase the sensitivity to lower light levels since more photocurrent will be generated. Figure 5.12 shows an image of the completed layout, consuming a total area of approximately 110 µm x 80 µm. The active circuitry appears in the lower-left region while the left side is the photodiode.

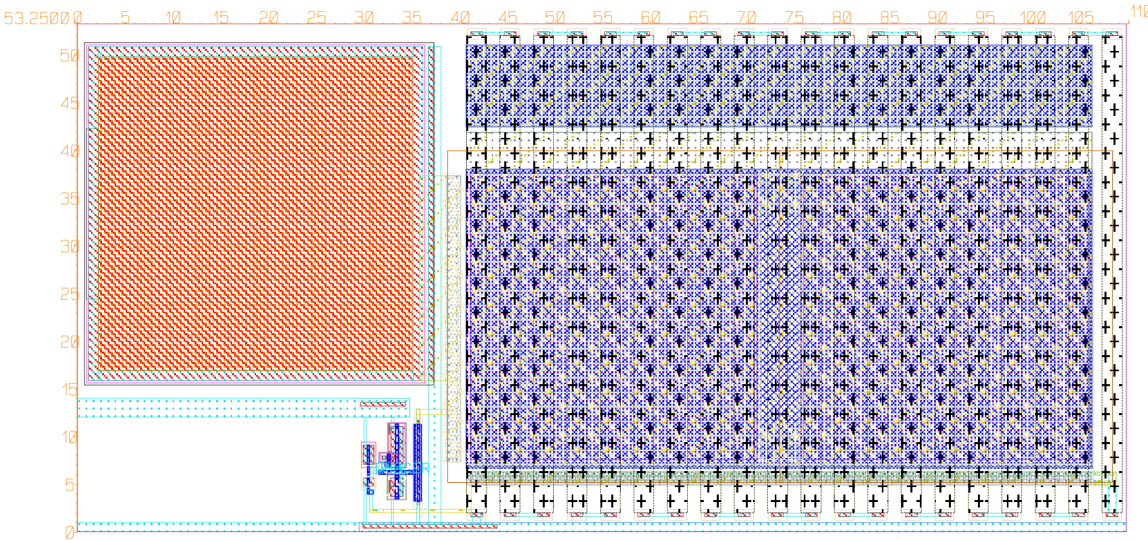

Figure 5.12. Layout of the optical trigger circuit, showing that the majority of the 110 µm x 53 µm dimensions are reserved for the passive components (prior to the 40 µm marker). Active circuitry appears lower-left of center while the photodiode appears on the left side and appears as an orange square.

5.4. Capacitance-to-Frequency Conversion

Capacitance-to-frequency conversion is a common circuit function that has been studied since the earliest days of MEMS sensors. The main purpose of such circuitry is to convert capacitance into a more useable form, such as an analog voltage, or in this case, a pseudo-digital signal such as frequency. A square-wave oscillating signal can be used to encode capacitance as frequency over time. Frequency, in turn, can be converted to a digital word using a counter and a reference clock over a fixed aperture of time. In this work, a simple ring oscillator is used to convert the capacitance of the pressure sensor into a frequency. This method relies on the fact that a larger capacitance on the output node of an inverter results in an increased delay and a lower oscillating frequency. In a three-stage ring oscillator, if one of the stages is deliberately loaded by a pressure-variable capacitor, the entire ring delay will be proportional to that capacitance and hence to pressure. Current-starved ring oscillators operate at low power levels by effectively introducing a resistance in the supply path in the form of two additional transistors, the header and footer. This limits the maximum voltage swing of each stage of the ring oscillator, reducing the total dynamic power consumed. During idle mode, the ring oscillator is turned off by disabling the header and footer transistors using a dedicated ENABLE signal generated by the controller. A buffering inverter is used to isolate the capacitive parasitics of the next circuit block.

Figure 5.13 shows the implemented circuit schematic. Transistors M11 and M12 are the header and footer transistors respectively. Both ENABLE and its complement are available directly from the controller with only a driver circuit. Two back-to-back inverters provide buffering with sufficient current for driving the gates of multiple transistors (not shown). Two transistors, M9 and M10, are used to force the internal nodes of the ring oscillator to a known value during the idle state. M9 pulls the internal V_{dd} source to ground while M10 pulls the output node to ground, setting a known state when idling and ENABLE is disabled. Without this, a sizeable leakage current might occur in later stages since the output would be unknown and could behave as an analog input to the following digital stages. Forcing a digital high or digital low state eliminates this problem, as explained in the previous section.

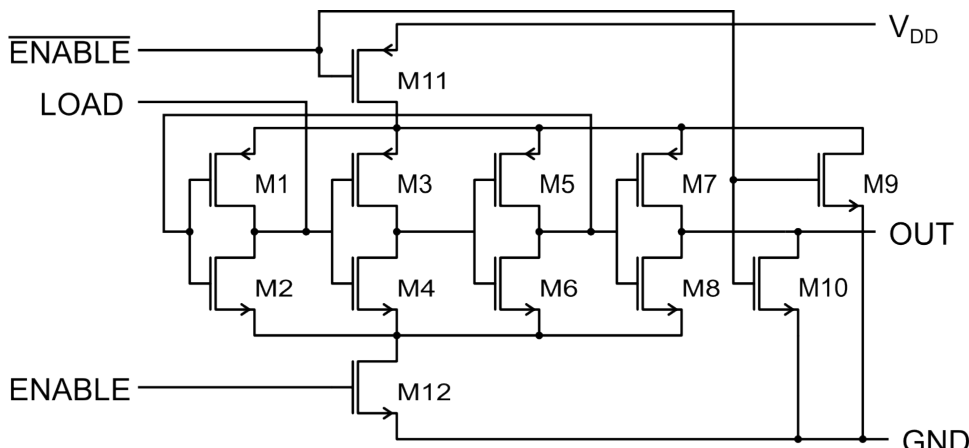

Figure 5.13. Circuit diagram of the ring oscillator with dedicated ENABLE and LOAD inputs used to turn off the oscillator during idle mode and for checking various capacitive loads.

Transistors M7 and M8 serve as a driver for the next stage and do not actually contribute to the ring oscillator function. Only transistors M1-M6 form the ring oscillator itself. Configured as a 3-stage ring, the capacitive load is introduced onto the intermediate node (output node of transistors M1 and M2) in order to reduce parasitic capacitance as much as possible. The ring oscillator method works by changing the load capacitance at a particular node within the ring. The gate capacitance of the next stage as well as the junction capacitances of the source and drain of the current inverter also contributes to this load capacitance but it is fixed in value. In order to induce an adequate measurable change in frequency, these parasitic capacitances must be limited to only a

small fraction of the loaded capacitance applied at that node. Minimizing the transistor sizes as much as possible aids in this process.

The 12-transistor ring oscillator is mostly minimum-width layout and therefore consumes an area of only 13 μm by 26 μm, as shown in Figure 5.14. As clearly evidenced in the layout, many transistors, especially those part of the ring oscillator itself, were lengthened, increasing their resistances and reducing their drive currents to reduce dynamic power. This reduces the oscillation frequency because of the reduced drive current available and increased gate capacitances between stages.

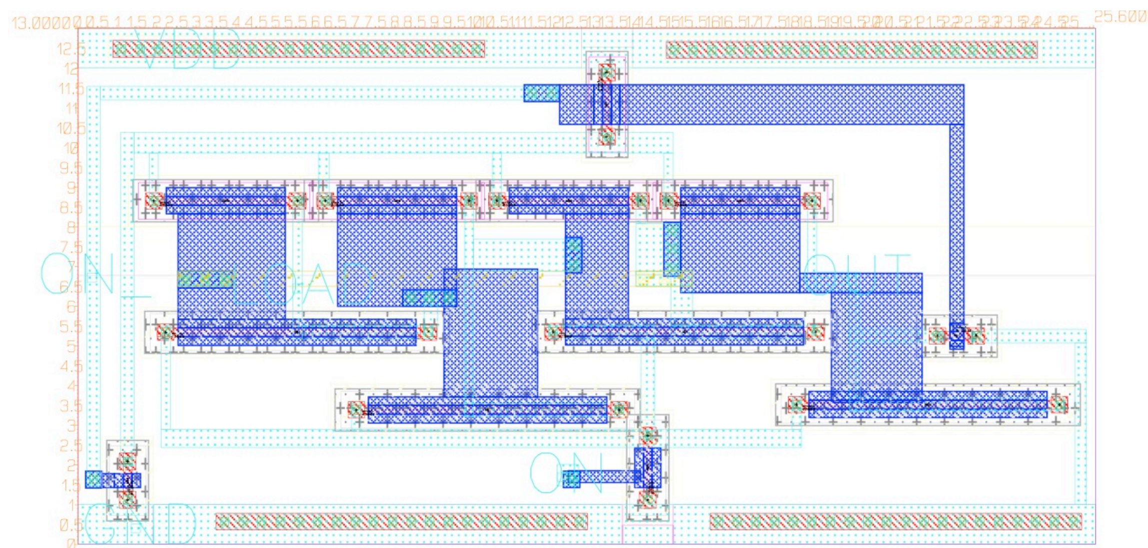

Figure 5.14. Layout of the ring oscillator, showing 12 transistors in a total area of 13 μm x 26 μm.

Simulation results for the ring oscillator indicate a non-linear behavior as capacitance increases. This makes sense since the transistors themselves behave nonlinearly as current draw increases and the load changes. In an effort to maintain simplicity, no look-up table or linearizing circuit was used to compensate for nonlinearity; instead, this burden is placed on the external readout. Figure 5.15 shows a plot of the frequency output of the ring oscillator calculated from the period for different load capacitances.

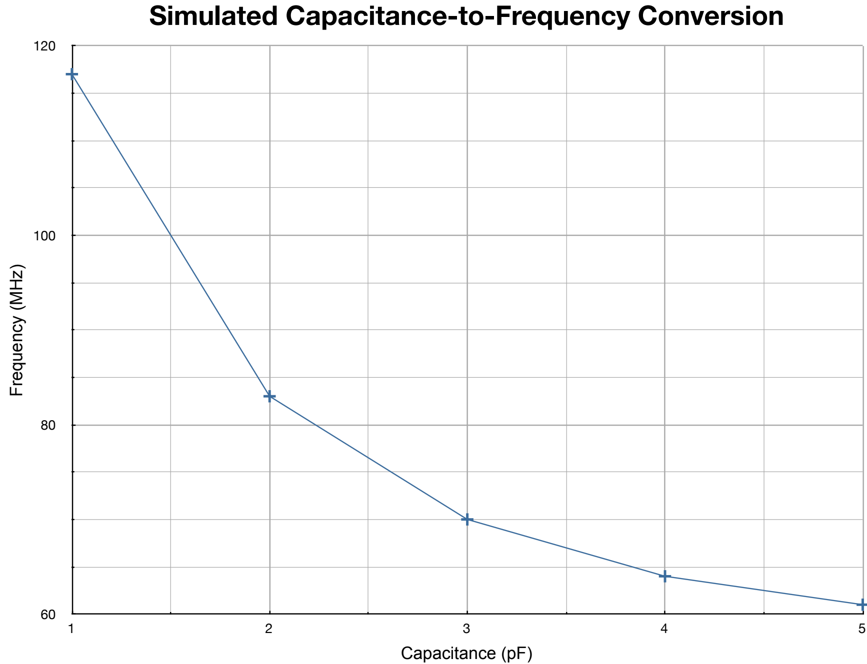

Figure 5.15. Simulated ring oscillator frequency output with varying load capacitances.

Additional simulations were conducted on process corners as well since it was estimated that the ring oscillator would be heavily impacted by any shifts in threshold voltage and other process parameters. Figure 5.16 shows a plot testing three process corners and the resulting oscillator outputs. Here, the actual ring oscillator output waveforms are shown, indicating that throughout the process corner differences, the waveforms are still stable. Three different load capacitances were also tested.

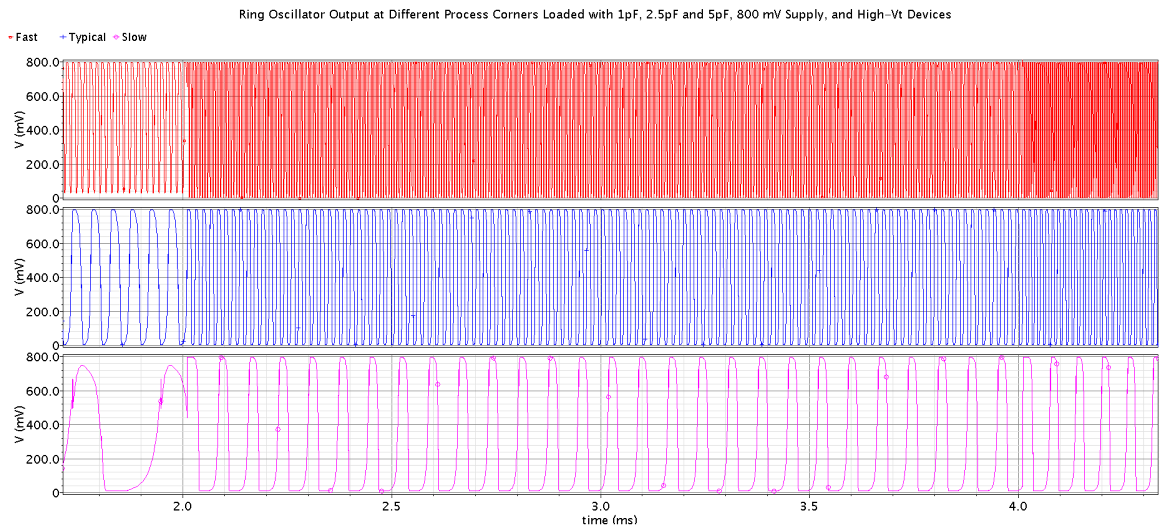

Figure 5.16. Ring oscillator output over various process corners with 1 pF (less than 2 ms), 2.5 pF (2 ms to 4 ms), and 5 pF (greater than 4 ms) load capacitances.

5.5. Pulse Generator

The transmitted wireless data is not encoded prior to wireless transmission in the conventional sense, avoiding additional circuitry. Techniques such as frequency shift keying and phase shift keying require some sort of modulation circuitry to encode the data into a change in frequency or change in phase, respectively. The data in this work is encoded as time between successive pulses, or pulse position modulation (PPM). The external receiver can derive a data point based on just two pulses or can accept multiple pulses, taking an average to reduce noise. After receiving a valid data point, the external device outputs an optical pulse on the LED, causing the implanted ASIC to advance to the next state, either evaluating another capacitance or entering the idle state. Therefore, the external device (the wand) acts as the controller, initiating and collecting data for as long as necessary. It is also important to note that the signal captured is still in the analog domain since there is no direct conversion to a digital form. The clock division provided by the counter simply increases the period between successive pulses so that they are detectable by the external receiver and to allow enough time for the pulse generator to recharge its local power supply. The secondary purpose of the counter, in future versions of this circuit topology, is to convert the frequency into a single digital value by comparing it to a fixed clock. This digital value can then be stored in on-chip memory. Calibration of the pressure sensor data is done in the external device.

The wireless transmitter is the most power-consuming component of the intraocular microsystem; therefore, optimization of its performance is critical. Instead of implementing previously demonstrated yet complex wireless systems, a simpler approach was taken once again. Encoding of the data, prior to transmission, is accomplished using PPM as described above. Multiple advantages for this particular application result from this decision. First, the complexity of the transmitter is reduced and the burden of signal detection is placed on the external receiver where power consumption can be higher and power sources and processing power are easily available. Secondly, the transmitter power of the implant is reduced as various circuit components are eliminated, such as an on-chip oscillator. Finally, the circuit design of the transmitter can be made all-digital, eliminating power loss through inefficient analog sub-circuits, especially when fabricated in low-power, sub-micron digital process flows.

The function of the pulse generator is twofold: to reduce the pulse width of an incoming pulse, and to reduce the rise and fall times of the pulse. In order to accomplish this, special circuitry is required to drive power into the antenna. The circuit schematic of the pulse generator is based on splitting the input signal into two parallel paths, introducing a slight delay in one, and then combining the two signals together. Only three types of logic functions are required: buffering in the form of inversion, NAND, and a NOR. Figure 5.17 shows the schematic of the pulse generator including the driver stage. Transistors M1 and M2 are NMOS devices used as the drivers while R_{pullup} forces the output stage high. In the non-idle states and when no pulse is sent to the input In, the transistors M1 and M2 are off, consuming only a small amount of leakage power. Multiple buffering inverters are used to drive these large transistors with the desired rise and fall times.

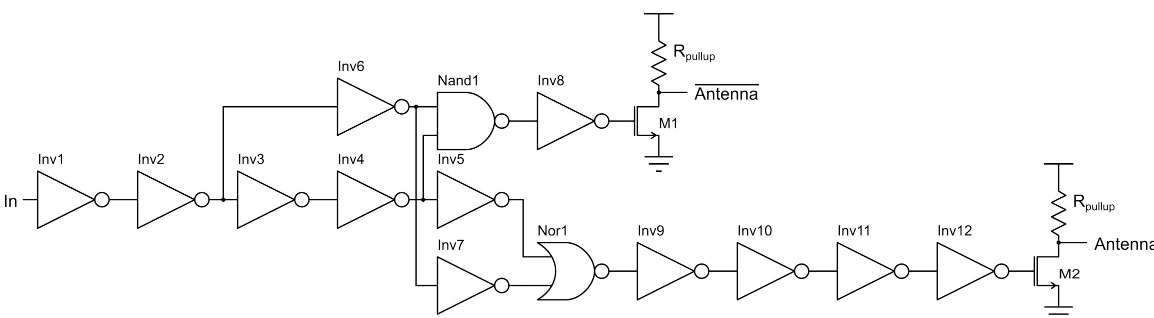

Figure 5.17. Schematic of the pulse generator. The input pulse is buffered, split, and buffered again before driving two different halves of the differential antenna.

Simulations with circuit models of the physical antenna were used to optimize the output driver stage of the pulse generator. Although the accuracy is not guaranteed the simulations do provide insight into the behavior of the driver in the presence of a real antenna load. This method, called co-solving, requires the extracted electrical parameters of the antenna. This was accomplished by simulating the modeled antenna in Ansoft HFSS, a finite-element modeling tool geared toward electromagnetics. The antenna simulations are discussed in more detail in Chapter 6.

Ideally, the driver would be perfectly matched to the antenna, transferring all power with minimal loss. Any reflections due to an impedance mismatch will reduce the effectiveness of the antenna. Also, the pulse shape of the output waveform depends greatly on the load. Figure 5.18 illustrates this dependence on load clearly.

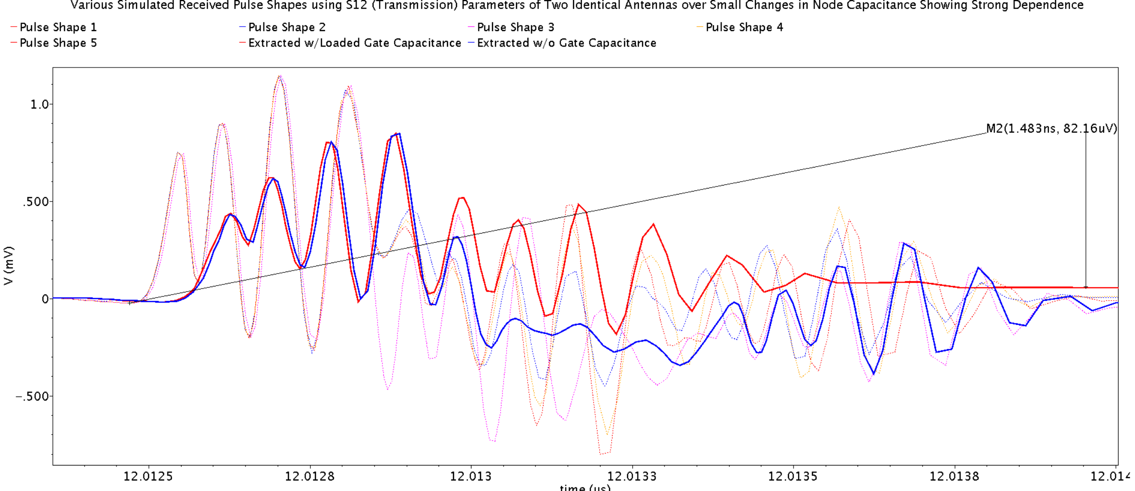

Figure 5.18. Various waveforms at the output of the driver stage for different load capacitances. Note the variety in pulse shapes.

The layout of the pulse generator is shown in Figure 5.19. It is quite obvious that the bulk of the circuit block consists of capacitance in the form of both MIM and MOS structures used for the local power supply, for the previously described power-gated technique. Only the lower-left hand corner, consuming an area of approximately 50 µm x 25 µm is the actual digital logic.

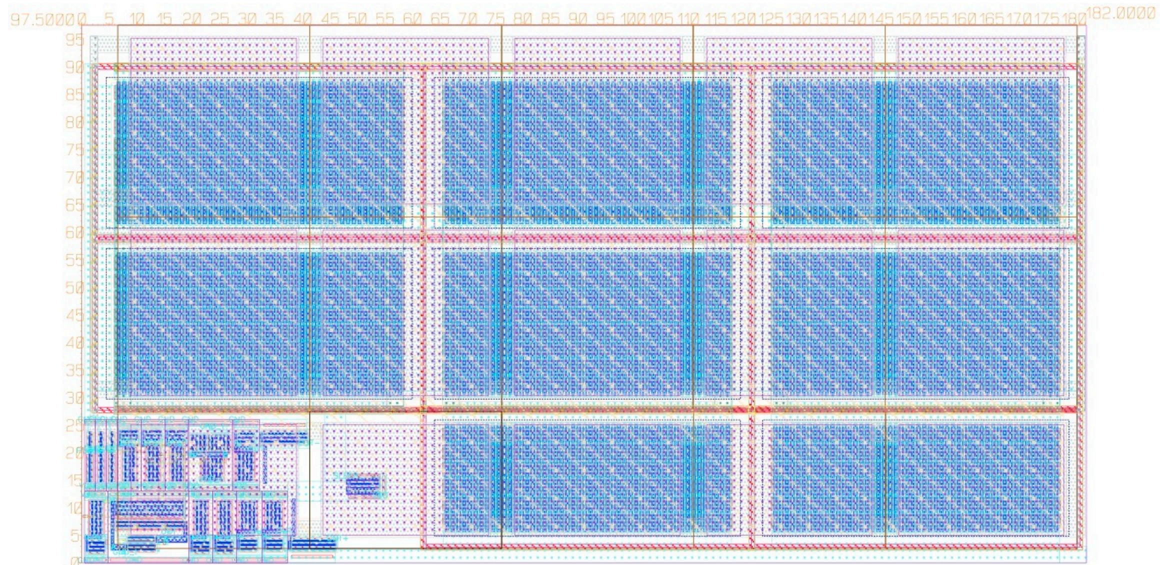

Figure 5.19. Layout of the pulse generator. The bulk of this block consists of the internal capacitor - only the lower-left corner is active circuitry with the rest of the area dedicated to MOS and MIM capacitance.

5.6. System Layout

The layout of the entire system appears in Figure 5.20 and consumes only 158 µm x 258 µm. The remaining area of the available circuit area of 1.4 mm x 0.9 mm can be dedicated to solar cells as described in Chapter 5. Only six output pads of 85 µm x 85 µm are required: two ground pads, one voltage supply, two antenna output pads and one sense input for the capacitance to be measured. The test chip used here includes many more pads, output driver circuitry, and input multiplexors to provide methods of probing the internal circuitry.

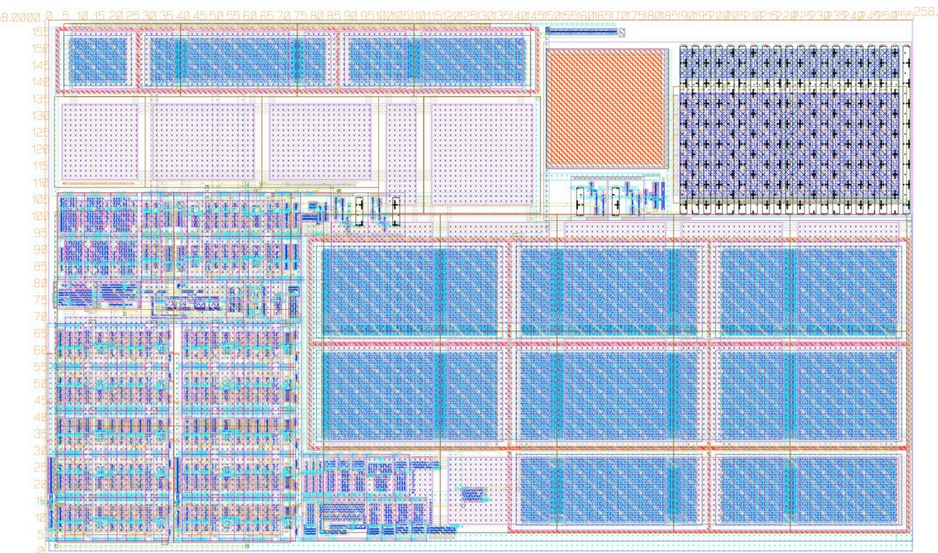

Figure 5.20. The overall circuit layout, measuring 258 µm x 158 µm. The top-right corner contains the optical trigger, the top-left corner is the built-in reference capacitor array, and the left-side is mostly digital logic for the counters and ring oscillator while the bottom-right is the pulse generator and its internal storage capacitor.

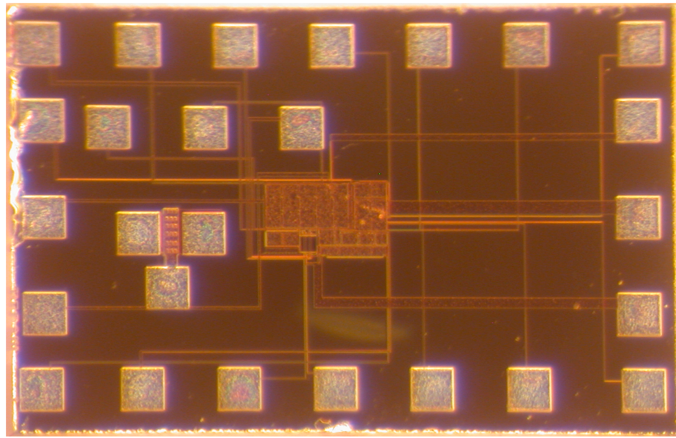

Figure 5.21. Die-level photograph of the 1.4 mm x 0.9 mm test chip. Only the center area is active; in future versions, unused die area will be dedicated to a solar array.

A die-level micrograph is shown in Figure 5.21. The six pads, three each on the left and right sides, are the main functional pads. Many additional test pads for probing the circuit are also included. Only the very center of the die contains the layout shown in Figure 5.20.

5.7. Test results

The simplified ASIC was tested using LabView. A separate breadboard was used to build a circuit capable of driving an LED with the desired rise and fall times, mimicking an external receiver. An NPN transistor with an LED is connected to its emitter, controlled by an external pulse generator connected to the base. The Agilent 33250A Function Generator is limited to 5 ns minimum rise and fall times and was used to drive the LED through the NPN. On every falling edge, the optical trigger activated and the chip would change states. As described in the optical trigger section, a high-pass filter was used to filter out slowly changing signals. A 5 ns rise/fall time is equivalent to a 200 MHz signal and should pass without attenuation.

Additional pad driver circuitry was incorporated in the actual fabricated circuitry in order to avoid limiting circuit functionality due to parasitic loading. The custom LabView program provided a visual indicator of which state the finite-state machine was in and provided digital outputs for values of interest, such as the output of the ring oscillator and the 9-bit counter. The following figures show the output of the ring oscillator as it responds to the optical input. Figure 5.22 shows what happens when the optical trigger signal is generated after power-up, advancing the system from the idle mode (State 0) to the 5 pF reference mode (State 1) and turning the ring oscillator on. Figure 5.23 shows the transition when the optical trigger signal advances the system from the 1 pF reference state (State 3) to the idle state (State 0), powering-down the ASIC. Figure 5.24 shows how the waveform of the ring oscillator changes as the state changes between two active modes. The first part of the waveform (State 2) is loaded with a larger capacitance, hence the lower frequency while the second part of the waveform (State 3) is after optical triggering a much smaller capacitance, thereby increasing the oscillation frequency to 2.99 kHz.

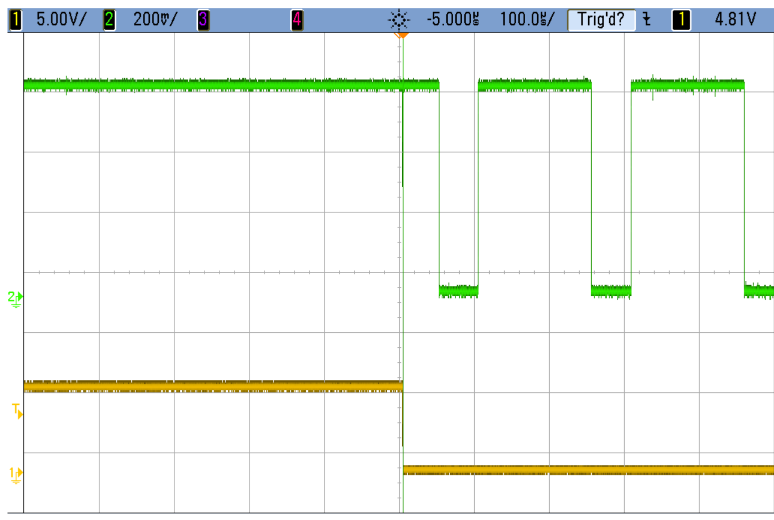

Figure 5.22. Ring oscillator startup (top), entering State 1 after optical trigger (bottom).

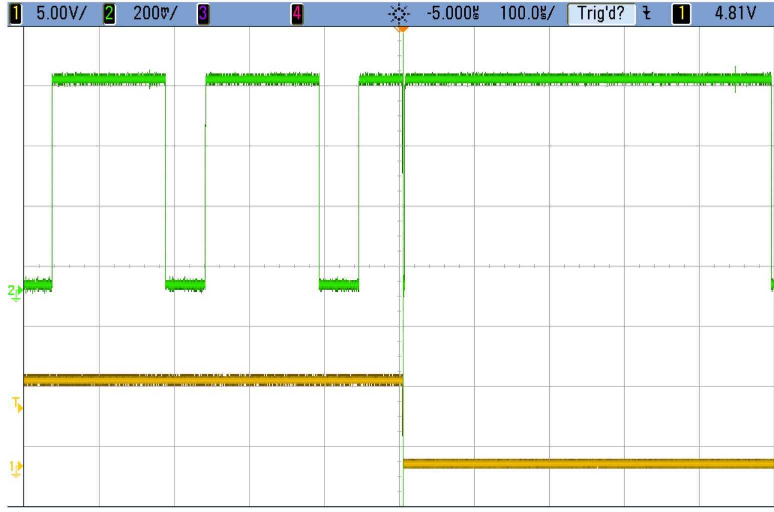

Figure 5.23. Ring oscillator power-down on receipt of an optical trigger signal.

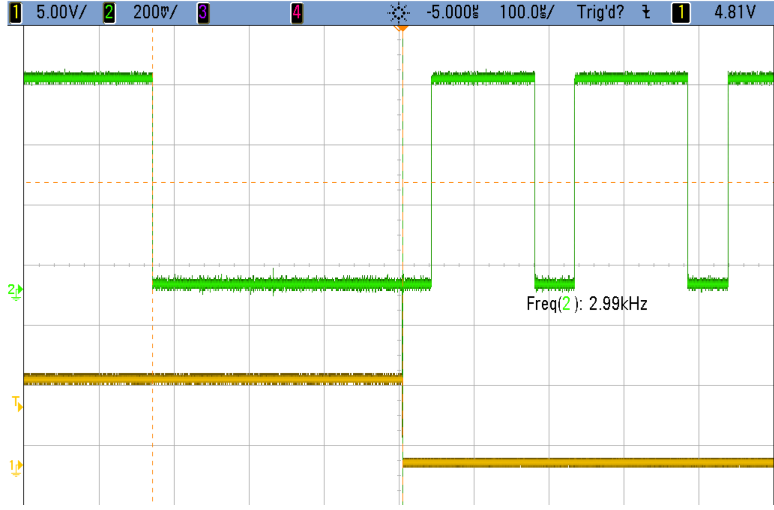

Figure 5.24. Ring oscillator switching between two different capacitive loads, from a larger capacitance (State 2) to a smaller capacitance (State 1), after optical triggering.

The main function of the capacitance-to-frequency conversion relies on a variable capacitance. In order to test the functionality of the circuitry, various fixed capacitors were applied to the sensing input of the ASIC. However, these capacitances do not include any additional parasitic capacitance induced by wiring to the chip itself associated with bench-top testing and therefore may not be very accurate measures of the chip's performance. In order to partially address these issues, the internal reference capacitors were also measured to help approximate the included parasitic capacitances associated with the test bench. Data collected with the ASIC connected to various capacitances is shown in Figure 5.25. The zero pF entry indicates an open-circuit input and therefore includes just the parasitics on the input node. Subsequent measures include this parasitic value. As a comparison, the internal calibrating capacitances are shown in Table 5.1. The parasitic capacitance is minimized for these values since the capacitors are internal to the chip. From this data, it can be extrapolated that the parasitic capacitance is in the range of approximately 10 pF for data collected using the test bench.

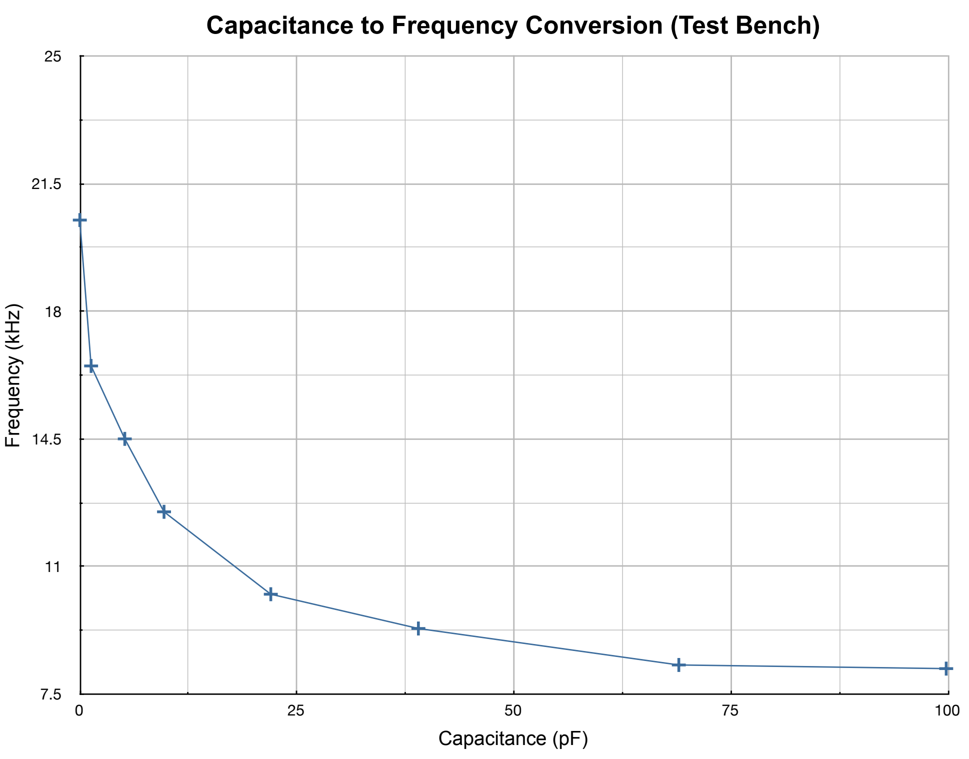

Figure 5.25. Plot of capacitance-to-frequency conversion using a test bench setup. Zero pF represents open-circuit connection; this is result of just parasitic capacitance applied at the input node.

In order to evaluate how data can be extracted from the measured data, a plot of curve-fitted data is shown in Figure 5.26. Here, the plot is generated by approximating the expected curve as determined by simulated results. The two on-chip reference capacitors are then used to set the upper and lower bound of the curve and are also fitted to determine the accuracy of this calibration technique. The bounds used in this plot are measured from an actual test chip and shown in Table 5.1.

Capacitance (pF)	*Frequency (kHz)*
1 pF	109 kHz
5 pF	39 kHz

Table 5.1. Table of capacitance-to-frequency conversion for same supply voltage used in Figure 5.25.

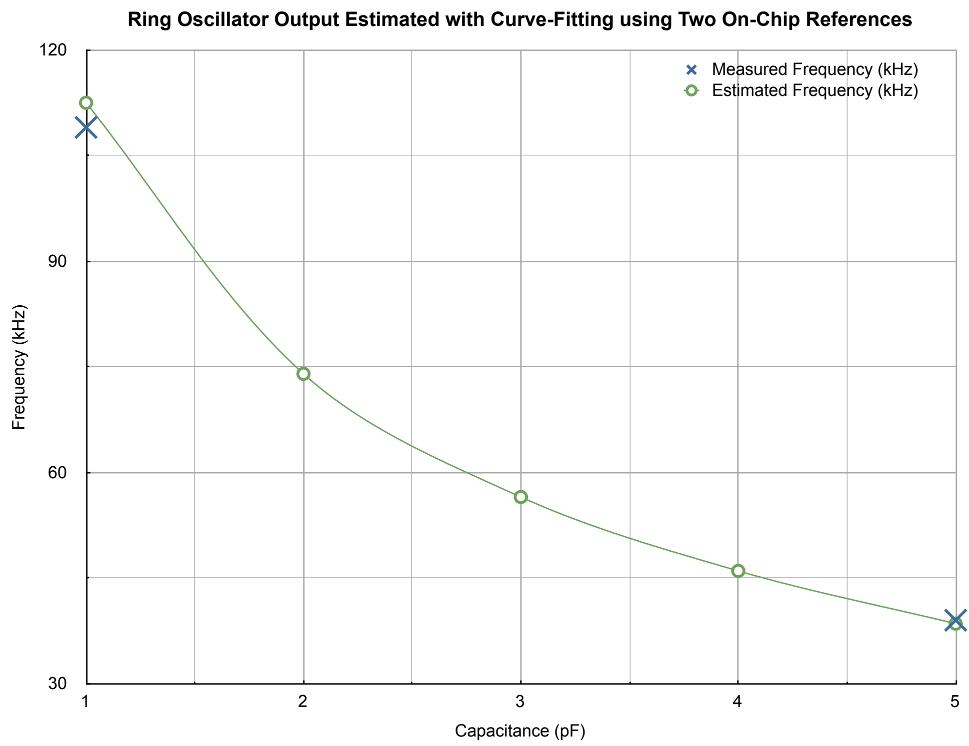

Figure 5.26. Estimated capacitance-to-frequency conversion using two on-chip references of 1 pF and 5 pF.

5.7.1. Power Consumption

The measured power consumption is actually much less than that indicated by the simulation results. An estimate in the nW range was calculated by the simulation tool for a supply of 800 mV. In the fabricated chip, two separate power rails were utilized, one for the core chip and one for the test circuitry, allowing for the power consumption of the core to be measured independently. An extremely sensitive electrometer (Keithley 617) was used to measure current in all stages of use. Table 5.2 highlights the minimum and

maximum measured power consumption for a voltage supply of 800 mV, the intended operating supply for which the chip was designed. However, additional testing found that the minimum supply voltage is 700 mV while maintaining full-chip functionality. At this supply level, current draw for the entire chip in the idle state dropped to approximately 50 pA, resulting in a total power consumption of 35 pW. This extremely low idle state power consumption is possible due to the power-saving measures described earlier in this chapter but comes at the cost of a slower ring oscillator.

State	***Current Draw***
Idle	120 pA
State 1 (maximum)	50 nA
Current draw when pulse generated (wireless communication)	31 µA
Current draw during pulse generation from internal storage capacitor (simulated)	~5 mA for ~1 ns

Table 5.2. Current consumption of the ASIC during various states while at a supply voltage of 800 mV. For comparison, the simulated current draw from the local storage capacitor is included.

One of the challenges that needs to be addressed is the total power consumption during expected operation of the microsystem. Two factors contribute to this: the first is power consumption while the ring oscillator is operational, and the second is the total expected energy consumed during a readout of the sensor relative to the idle time. The instantaneous power draw from the supply is often a limiting factor and so this data shows that the power module must sustain at least an equivalent peak current draw of 50 nA. Figure 4.12 shows the output of a silver-zinc chemistry sustaining currents of up to 1 mA. While this much power is not required, it is important to note that silver-zinc chemistry is known for its ability to provide large instantaneous currents when necessary. Similarly, the Cymbet microbattery can provide pulsed discharge currents of up to 100 µA [65].

In order to determine the total energy consumed during a sensor readout, the total time required to accomplish this task must be known. Data is encoded in time, requiring multiple measurements to determine an accurate data point was captured. As an example, one test chip with an 800 mV supply provided a pulse output frequency of 1.3 kHz, or approximately 770 µs periods. In order to capture data accurately, 256 cycles (8-bit accuracy) can be used. Within 197 ms, a single capacitance value can be captured, so for three measurements (two reference capacitances and one pressure sensor reading), a total of about 591 ms would be required. The current draw during this time could be up to

50 nA resulting in total energy consumption of 24 nJ with the 800 mV power supply. During the idle mode, energy consumption is 86.4 nJ over 15 minutes. Combined, the total energy consumption for a single operating cycle of 15 minutes including one data readout is 110.4 nJ. Over the entire period of one day, there are 96 such readings, so 10.6 μJ is consumed per day in just readout and idle mode. Reducing the power supply will increase the time required for each data readout because the ring oscillator output will be slower but will also reduce the idle mode power consumption further so an optimum supply voltage can be found balancing between these two operation modes.

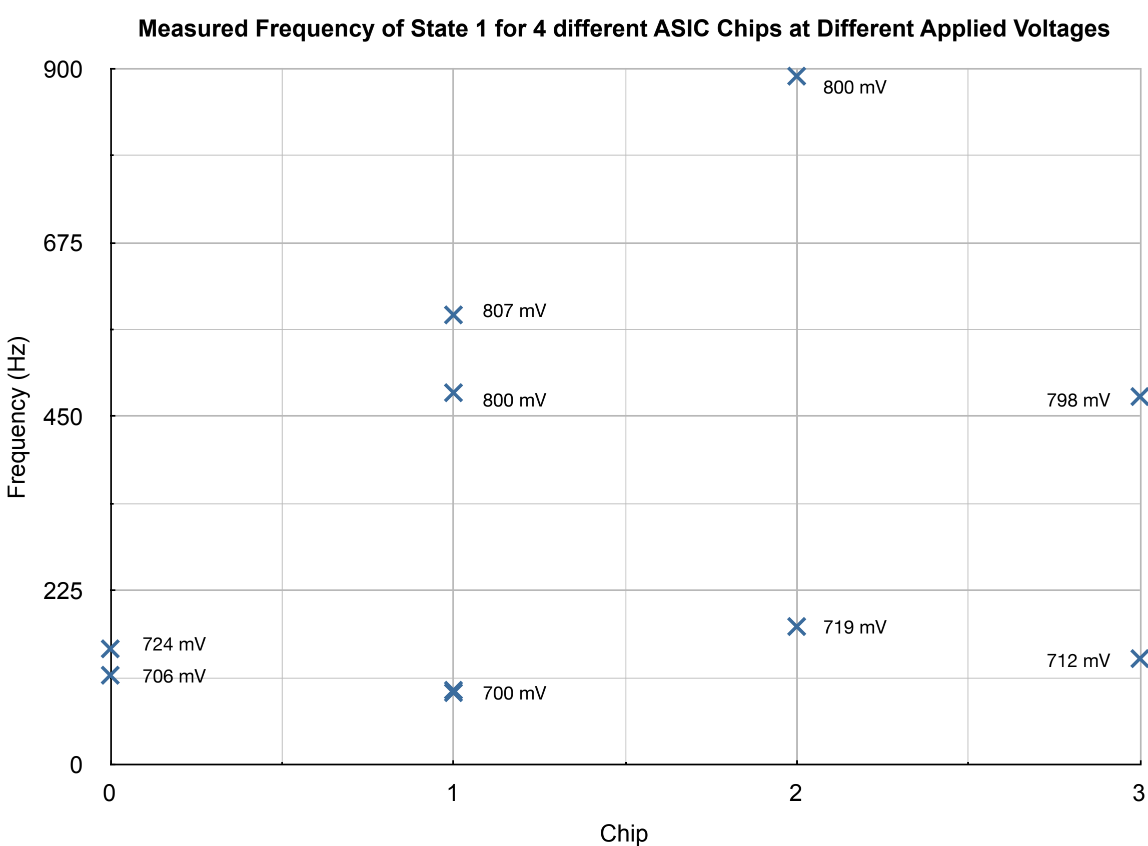

Figure 5.27. Data showing four different ASIC chips tested at various power supply voltages.

Another issue that needs to be taken into account during actual use is the dependence of frequency on voltage supply. Figure 5.27 shows a plot of four different ASIC chips tested in State 1, one of the internal reference capacitor calibration states. The reference frequency is found to vary considerably for different supply voltages. Of course, there is also great variance from wafer-to-wafer, but this is expected since there is no on-chip regulator to isolate the oscillating frequency from the voltage supply. The

dependence of the measurement frequency on the supply is one parameter addressed during calibration of each individual microsystem. The use of two calibration capacitors bracketing the span of the measurement capacitor allows compensation for variations in the sensing capacitance (for a given pressure) as well as for variations in the supply voltage or device currents. The external readout device can therefore account for the change in frequency due to changes in the voltage supply, such as when the battery begins to lose charge.

Operation was successful up to power supply voltages of 1 V and should be possible at even higher levels but at an increased power consumption because the ring oscillator operates at an increased frequency. The actual voltage supply will vary between 800 mV and 700 mV when used with the microbattery presented in Chapter 4. In the future, if a voltage regulator is included, it may be wiser to set the power supply within the subthreshold regime, such as 400 mV, and operate at that potential. In this chip, no on-chip regulator was included in order to minimize complexity and power consumption.

5.8. PHOENIX PROCESSOR

The Phoenix processor, developed by the research groups of Professors David Blaauw and Dennis Sylvester, operates in the subthreshold regime [115]. This chip incorporates some of the latest work on implementing a low-power clock for capturing data after minutes-long intervals [116]. The Phoenix processor operates at a subthreshold supply of 0.45 V, resulting in a very low power consumption of 3.65 nW during the idle state. This latest version of Phoenix implements a dual inductive coil technique with on-chip antennas as well for wireless communication and solar cells for trickle charging an on-board microbattery. The chip is described in detail elsewhere [117].

5.9. IDEAL ASIC

This chapter has discussed an ASIC implemented during this work for the intraocular application. Although the goal of the device was to provide simple functionality, it lacks some of the circuitry needed to provide all of the necessary

functions for the intraocular application, represented well by the Phoenix processor. A review of the expected use of the intraocular microsystem helps to define the ideal ASIC.

The microsystem should record intraocular pressure every 15 minutes, storing the pressure data in an on-chip memory. Once a day, the patient would download the data to a hand-held wand. This wand would automatically transfer the data directly to the physician's office. Once there, specialized software can review the data, alerting the physician to any anomalies in pressure. The pressure data can also be simply stored for review at the next appointment, helping the physician make well-informed decisions about the success of the ongoing treatment and any changes that may be necessary.

In order to accomplish these functions, the need for several circuit blocks is immediately apparent. First, a low-power memory source is required to store the data. The larger the size of the memory the better, allowing patients to exceed the once-a-day requirement if necessary. In the case of the user exceeding the memory limit, the ASIC should note that some data has been lost, retaining only the most recent data. A very low-power timer operating during the idle state is also required in order to wakeup the controller every 15 minutes to take a pressure reading. A digital conversion from capacitance is also needed so that the value can be stored. In addition, a wireless communication link is necessary.

5.10. SUMMARY

This chapter has reviewed the circuitry used to interconnect all the various components of the intraocular microsystem. A simple, extremely low-power ASIC has been designed and fabricated, consuming only 35 pW in the idle state. An optical trigger is used for receiving signals from an external monitoring device, avoiding a constantly-powered wireless wakeup receiver. The conversion between capacitance and frequency was accomplished using a simple ring oscillator with 9-bit counter serving as a clock divider. Finally, a mostly-digital pulse generator was developed to transmit pulse-position modulated pressure data to the outside world. Initial testing indicates extremely low power consumption and also shows the functionality of the finite-state machine and optical trigger.

The ASIC presented in this chapter demonstrated excellent power-consumption values; however, it does not contain any memory, a basic requirement in order to capture data continuously over long periods of time. SRAM-type memories will add modest amounts of additional power consumption, but Phoenix has shown this to be manageable. If non-volatile memories can be used, such as FeRAM, then this will further alleviate the power requirements for these types of chips. For the time being, in order to compensate for the additional memory power draw, subthreshold digital techniques such as those used in Phoenix will continue to push power consumption down. Certain blocks, such as the pulse generator, may not operate at all if converted to subthreshold designs due to the lower supply rail and slower operation, so power-gating with a local capacitor may need to be used. All of the components necessary to build an ideal ASIC have been described in this chapter, making it clear that such an ASIC is not only feasible but practical as well.

The work in this chapter demonstrated a simple ASIC designed to convert the data to a time-encoded pulse. Though this technique is amenable to low-power designs, an alternative intraocular ASIC was also developed collaboratively called the Phoenix processor which implemented sub-threshold logic for power savings. Phoenix demonstrates the upper-level solution, incorporating memory, power distribution, full processor, and capacitance conversion circuitry. Between these two functional ASICs, the feasibility of low-power electronics for an intraocular application has been demonstrated. One major challenge in implementing such circuitry is the ability to power the device and this has been addressed in both ASICs by implementing ultra low-power solutions and by incorporating energy scavenging solutions as described in the previous chapter. An energy-autonomous mode is not only practical but has already been demonstrated with on-chip solar cells. Therefore, the ASIC, not including the wireless communication circuitry, of the intraocular microsystem is complete and ready for implementation.

CHAPTER 6

WIRELESS MODULE

One of the top priorities for developing a successful implantable microsystem is minimizing power consumption due to the challenges of supplying and storing energy. The wireless components of implantable devices are typically the largest power consumers, depending on how often they are used. In the case of the intraocular microsystem, wireless communication is used on a daily basis for data readout. Devices such as pacemakers can make use of large batteries when placed in the chest or abdomen; however, in smaller implantable microsystems, such as the intraocular application, the useable volume must be minimized to aid surgery and reduce impact on the patient. It is well known that wireless data transmission is the dominant source of power dissipation for low-power nodes [117]. Therefore, the entire wireless subsystem, from the application layer to the low-level physical layer must be carefully optimized in order to reduce the required power as much as possible.

The work reported in this chapter describes a simplified communications method that is tailored to the specific problem of transferring small amounts of data from an implanted sensor over a very short distance. This well-defined problem allows several critical simplifications to reduce power consumption. The performance of the resulting system should be better than with other, more common, communication protocols. For example, since very little data is transmitted, low data rates are possible, and complicated precision circuits such as phase-locked loops become unnecessary. In-depth design of a wireless subsystem taking into consideration all potential tradeoffs has not been a typical approach in the past because wireless subsystems have been implemented as complete independent solutions. Here, in order to save as much energy as possible, analysis begins with the electromagnetic foundation for communication, resulting in a new perspective on the entire wireless subsystem.

The use of an energy storage/generation component, such as a microbattery or harvester, helps alleviate some of the power challenges in certain cases, especially if it is used only after the wireless link has been established. However, power sources are limited and the relatively large amounts of energy used during wireless communication must still be eliminated. On-board power storage and energy generating solutions have been discussed in Chapter 4.

This chapter begins with an overview of the current wireless techniques for biomedical devices found in the literature. This is followed by a discussion of the shortcomings of these particular techniques in order to define the need for a new approach. The following sections then discuss properties important to implantable electronics and methods of building on these for optimum antenna design. Simulation results then lead to a layout and process flow for fabricating the intraocular antenna module.

6.1. Conventional Implantable Wireless Techniques

This section describes the most common wireless communication techniques for implantable biomedical devices, including their advantages and drawbacks. First, near-field communication systems are described, followed by common narrowband radio techniques, which have become popular for applications that require higher data rates than inductive links can provide. For those applications that require high data rates as well as simultaneous wireless power transfer, dual-link solutions are another alternative.

Before continuing, the difference between near-field and far-field needs to be defined to determine the boundary between these two types of links and their very different behaviors. Equation (6.1) presented in [119], [120], defines the boundary $R_{far\text{-}field}$, in terms of wavelength λ. For values of r, where r is the distance between transmitter and receiver, approaching $R_{far\text{-}field}$ both near-field and far-field effects are expressed. For this reason, values of r much greater or much less than $R_{far\text{-}field}$ are typically considered to possess qualities of only one or the other domain. An alternative definition is presented in [121], shown in Equation (6.2). In this expression, the largest dimension D of the antenna is used to define the interface between the near-field and far-

field. In this work, the first definition in Equation (6.1) is used to set the value of r where the far-field begins and near-field ends.

$$R_{far-field} = \frac{\lambda}{2\pi} \tag{6.1}$$

$$R_{far-field} = \frac{2D^2}{\lambda} \tag{6.2}$$

Fundamentally, an electromagnetic field is dominated by either an electric field or a magnetic field at the source of its generation. As the electromagnetic field propagates, the field begins to present both electric and magnetic components. The distance from the radiation source at which this occurs is the boundary between the near-field and the far-field. Therefore, depending on the communication distance between the source and receiver and the particular wavelength of the applied field, it may be better to operate either in the near-field or the far-field regime.

6.1.1. Near-Field Systems

Typically, inductive and capacitive links are considered near-field communication techniques because they operate with either a mostly magnetic or mostly electric field within the region close to the antenna. Inductive coupling is the favored choice for communication with implantable devices [125], [126], primarily due to the larger amount of power that can be transferred safely across tissue and the enhanced signal fidelity [127]. This approach is advantageous in the body because the magnetic permeability of body tissues is virtually the same as air and therefore results in little, if any, attenuation. The major drawback with this approach is the limited range inherent in these types of links. As the size of the antenna is reduced, this problem is further exacerbated. Previous analysis has shown that coil or antenna sizes approaching 2 mm and below are less efficient for near-field communications [127], [130]. The next section demonstrates how this can be determined and the minimum limits of an inductive link.

Inductive links typically operate on the principle of a coupled inductive-capacitor (LC) tank oscillation, where two inductors are linked as in an air-transformer. A resonant frequency for the LC tank can be obtained from the simple expression shown in Equation (6.3).

$$f = \frac{1}{2\pi\sqrt{LC}} \tag{6.3}$$

By exciting the inductor at this particular frequency, a large voltage can be induced in the LC tank. A more useful expression is the quality factor Q, which includes the load and parasitic resistances of the active circuitry that the LC tank is required to power. Q is described in Equation (6.4), where R is the parasitic resistance of the LC tank and R_L is the load resistance.

$$Q = \frac{1}{\frac{R}{2\pi fL} + \frac{2\pi fL}{R_L}} \tag{6.4}$$

The quality factor is an indicator of how much voltage 'amplification' can be achieved by operating at resonance. Further information can be found in reference [131] and in other sources that describe RFID (radio frequency identification) tags in more detail. There are other near-field approaches besides resonant tanks, such as introducing a material that changes the magnetic field of an inductor based on a change in applied pressure; however, this approach was found to be less effective [132]. More recent work has studied the limits of inductive links and proposed an approach to mitigate losses due to reduced coil sizes by matching loads dynamically; this has been claimed to enter a new domain between near-field and far-field, demonstrating a combination of effects [128], [129].

It is common practice to use capacitive pressure sensors to provide the capacitance portion of the LC tank. This sensor causes a shift in frequency as the capacitance varies, as shown in Equation (6.3). The main advantage of this approach is that power is externally coupled via the magnetic field to the implantable system so no internal power source, or active circuitry, is required. The disadvantage of this approach is the limited range of transmission and the requirement that power must be applied constantly in order for communication to function. Such an approach has previously been applied to an intraocular pressure sensor [133].

Another challenge with inductive links is the size of the antennas involved. Typically, large coils can be used externally, but the internal receive coil is limited in dimension by the implant location, with an intraocular application being more

challenging than many other implantable applications. In [131], the optimum antenna diameter is discussed in terms of magnetic field strength. As the radius of the transmitting coil decreases, the magnetic field strength increases, but the readout range begins to roll-off earlier. Therefore, an optimum coil radius can be calculated for a given coil transmit distance [131].

Many different types of inductive links have been used in the past, ranging from passive to active devices. The simplest method is more of a detection scheme, which works well for transferring analog data as a frequency shift but may not be as attractive when used for transmitting digital data. The general operation is based on the detectable changes in the impedance of the external coil due to changes in the generated electromagnetic field in the presence of the implantable device [131]. Another option is the use of pulsed fields, whereby the external coil generates a magnetic field for only a short time, allowing the implant to charge up an internal energy store, such as a capacitor. Once the external field turns off, the implant then generates its own electromagnetic field modulated with the data to be transmitted. Sweeping frequency around the resonance point of the implanted device, commonly used in RFID tags, allows the external device to detect the internal load [134]. Backscattering techniques have also been used in the past successfully, extending the operating range of these devices beyond those of simple LC resonant devices by increasing the signal-to-noise ratio. This technique operates by load modulation, whereby the implantable device dynamically shifts the frequency or phase once power has been delivered to the implant. This can be accomplished by switching in a resistive load, for example, using active circuitry. The different loads can be interpreted as different data bits. Much more detail and a comparison of the various near-field techniques can be found in [131].

Though most of this discussion has focused on inductive links, there is another technique to achieve near-field communications that is based on capacitive, or electrostatic, communication. Though this technique is not commonly used, it has been demonstrated to be a viable option [135]. The limitations of this approach are its very short range due to potential attenuation and reflection from dielectrics and conductors in range of the transmitter or receiver. The electric field is strongly affected by lossy dielectrics and is therefore not a good choice, especially for implantable electronics, as

will be explained later in this chapter. The implementation is simple, requiring only a capacitor for communication, although typical topologies are more complex [135].

6.1.2. Far-Field Systems

Far-field communication techniques operate with a full electromagnetic wave, having both magnetic and electric components. Where high-data rates are required, such as in recording neural spikes from multiple sites and sending the data off-chip, far-field links are used due to their higher data rates and less susceptibility to interference. Within far-field techniques, by far the most common wireless transmission schemes are based on narrowband radios. The basis of this technique is to generate a carrier wave that operates at a specific frequency, and then modulate that carrier wave. The most common modulation schemes are frequency shift keying (FSK), amplitude shift keying (ASK), and phase shift keying (PSK). The carrier wave requires a precise on-board frequency generator and support components that operate at the higher frequencies, such as a mixer. One option to increase data rates is to introduce multiple channels around the main operating frequency. Other approaches may also be incorporated, such as in the case of neural applications, where the main operating frequency is as high as 6.7 GHz [136].

6.1.3. Dual-Link Systems

Some of the more recent work [137], [138] has focused on dual-link type wireless techniques. In this approach, two different frequencies are used, one for power transfer and one for communication. A slight variation to this theme allocates one specific frequency to a particular direction of communication [139]. The goal of dual-link approaches is to optimize the two different links for their specific purposes. For power transfer, near-field low frequency inductive links are used. For data transfer, far-field high frequency radio links are used. The benefits of this approach include the ability to use low-frequency coils to transfer power through a magnetic field, which is not affected by the tissue, while avoiding the limitation of low data rates. Higher frequency signals inherently allow faster data transfer, and with larger bandwidth, more data can be sent across multiple wireless channels. In the case where different frequencies are used for

each direction in a bidirectional wireless system, the benefit is the increased signal-to-noise ratio afforded by the design.

6.1.4. Non-Conventional Approaches

There have been a few interesting developments using atypical wireless techniques. Most were born out of a need for high-data rate communications rather than being motivated by the power limitations or miniaturization requirements of this work. The typical approaches have been focused on pushing communication frequency higher using conventional wireless techniques in portable electronics, e.g., 2.4 GHz radios [140], in order to attain higher data rates. Another solution that has been proposed and implemented more recently is based on ultrawideband (UWB) techniques, due to their highly efficient and high-speed data transfer capabilities. UWB operates across many frequencies, hence the name "wideband" as opposed to conventional wireless techniques (called narrowband). A cochlear implant has been implemented that uses UWB to communicate across the skin, with data rates of 1.2 Mb/sec [141]. There is quite a bit of promising work in this regime, and it remains to be seen if more high-data rate applications, such as neural prostheses [142], will take advantage of the benefits of UWB over more conventional narrowband techniques. The next section discusses ultrawideband in more detail, describing its benefits and the reasons why it has been selected for the intraocular microsystem.

6.2. Ultrawideband (UWB) Systems

Ultrawideband is described by the Federal Communications Commission (FCC) as any wireless transmission that operates with a 500 MHz or greater bandwidth. The FCC further stipulates that compliant devices must not exceed a power output of -41 dBm/Hz for the frequency range of 3.1 GHz to 10.6 GHz to reduce the potential for interference with other devices operating in those frequency ranges, as shown in Figure 6.1. This low-power output limitation has often been cited as equivalent to electrical noise generated by standard consumer electronics.

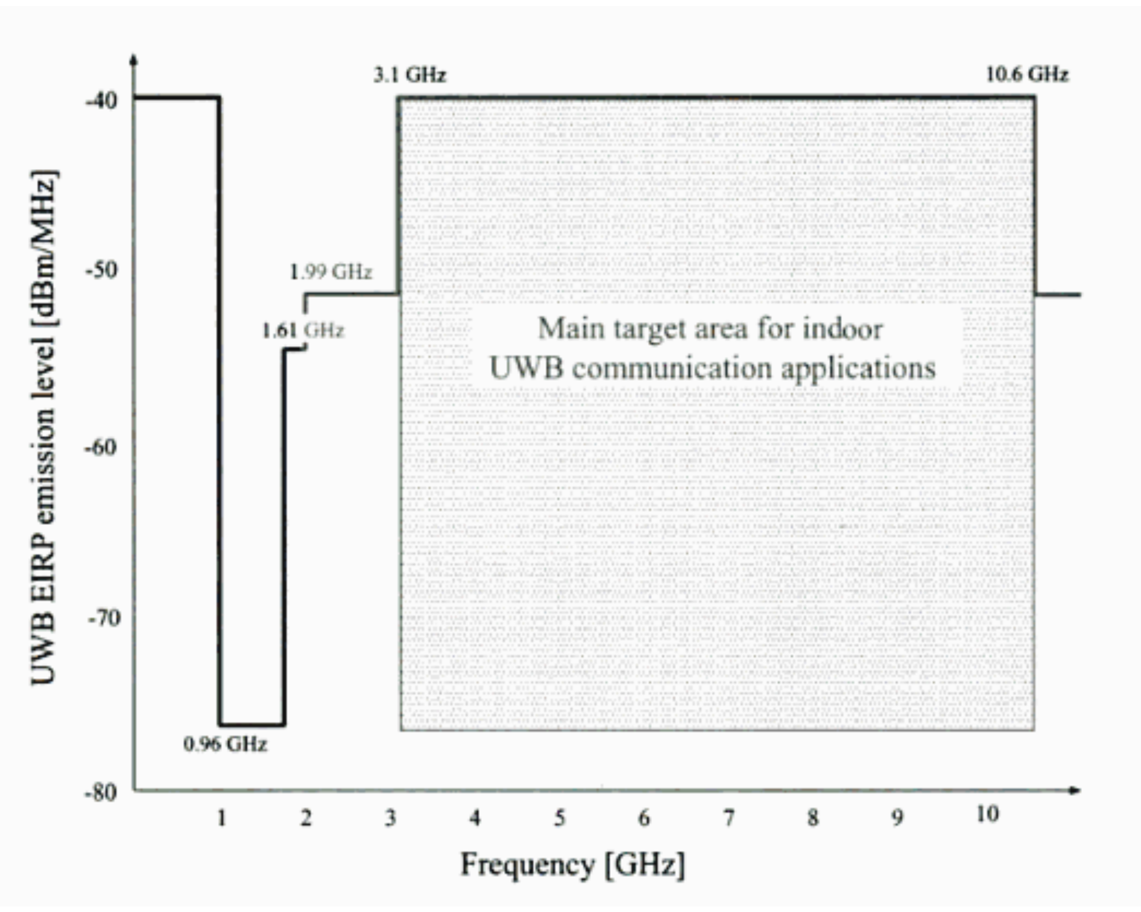

Figure 6.1. FCC emission mask for ultrawideband devices [143]

Ultrawideband has become very popular in the last two decades and will undoubtedly be studied in much greater detail in the future. Most recent studies of energy-efficiency in terms of wireless transmission (though not for implantable devices) have been focused on ultrawideband. This technique can be considered the opposite of typical radio transmissions in that rather than operating on a single frequency, ultrawideband operates with a large frequency bandwidth. As such, energy is distributed over the entire bandwidth. There are many advantages to ultrawideband communication, such as high data rates due to the wider allocated bandwidth and channel capacity. Other advantages include difficult signal hijacking (i.e., eavesdropping on communications), reduced chance of interference, and the ability to do ranging (to determine the distance between transmitter and receiver akin to radar). Most importantly, and highly relevant, is the much simpler transmitter circuitry that can be implemented entirely using digital circuits. In the case of implantable devices, UWB has been described in the literature, although mostly for high-data rate techniques [141].

The main advantages that led to UWB as the preferred wireless approach for the intraocular application include the potential for low-power, small size, and simple wireless subsystem architecture. Small size has been attained by pushing the operating frequency higher than almost any other reported implantable device but also because of the electromagnetic properties of the tissue, as will be explained in this chapter. There are drawbacks, of course, including the attenuation electromagnetic signals experience when travelling through the tissue. It is important to determine the tradeoff between signal integrity and other restrictions on the device, e.g., volume or maximum available dimensions. For implants that may not be so restricted by size, such as an intracranial sensor, UWB may not be the optimal solution whereas an inductive link may be.

6.2.1. Circuits for UWB Communications

The typical UWB transmitter consists of two main components: a pulse generator and a power amplifier. The pulse generator is designed to take an incoming data bit and convert it into a pulse that distributes energy across many frequencies. This pulse is then passed to an integrated digital amplifier, which may be as simple as a fast-switching high-current buffer stage with a direct connection to the antenna. The power amplifier must also provide any impedance matching required to ensure that energy is not reflected back from the antenna, reducing the efficiency of the signal generated. Many designs have utilized off-chip impedance matching to optimize power transfer to the load; however, in this application, such an option is not possible due to size constraints. The circuit design and simulation of a pulse generator is described in detail in Chapter 5.

An external receiver has not been designed as part of this work but is typically much more complicated than the transmitter. In the case of the intraocular microsystem, it is recommended that standard off-the-shelf components be used to build an UWB receiver, since it is neither a high-data rate nor a long-range application requiring complicated circuitry.

6.2.2. Antenna Co-Design

The main advantage of being able to design the antenna and the circuitry is that both can be tailored to one another for optimal performance. Most antennas have a

characteristic input impedance (Z_0) based on geometry and medium (the material in which the antenna will radiate) that is typically converted to a common standard impedance (i.e., 50 Ω) using a dedicated matching network. This allows circuitry with a different impedance to efficiently interface with it [120], [121], reducing reflections and power loss. The most efficient transfer of energy occurs when both the input and output are matched [145].

The conversion from double-ended (differential) output to single-ended output is typically carried out by a component called a balun (*bal*anced to *un*balanced) with the purpose of removing shunts to ground through coaxial shields, for example [120]. These baluns may be complicated and hard to design for wideband systems as opposed to narrowband systems, where the balun only has to operate at a specific frequency. Transmission line theory can be used to easily calculate required passive or active components [120].

Both matching and balancing (single-ended components) are avoided in this particular work by matching the impedance of the antenna on-chip at the output driver level and by implementing a differential output that drives a differential antenna. This work will therefore bypass the standard 50 Ω characteristic impedance for both input and output impedances that are typically found in wireless systems since the choice of 50 Ω is based on air-core coaxial wire [151] and the impedance which corresponds to the minimal energy loss for that particular transmission line.

6.3. Wireless Link Analysis

This section explores some electromagnetic theory to help define the most common techniques with a goal of developing a method of comparison. There are two main categories of wireless links, as previously described, defined by the range and wavelength of the signal. In the near-field, either electric or magnetic fields are dominant. In the far-field, the electric and magnetic fields are related to one another by the intrinsic impedance η of the medium in which the electromagnetic wave is present. This detail becomes important when designing far-field antennas for implantable devices. For near-field devices, an antenna can either be designed to generate a magnetic or

electric-dominant field. On the other hand, a far-field electromagnetic wave can originate from any type of antenna.

Another important variable that has a direct impact on near-field and far-field effects is the frequency of the signal applied to the antenna. As frequency increases, the defined near-field region shrinks, moving closer and closer to the source antenna.

The type of antenna is also an important parameter, especially if the radiating element is a coil or wire. Coils radiate strong magnetic fields while wire antennas, such as dipoles, present a stronger electric field [145]. As explained earlier, the far-field of both these types of antennas is identical in that both appear as combined electromagnetic waves, involving both magnetic and electric properties.

6.3.1. Power Transfer Efficiency

To evaluate the wireless efficiency and the useful range of far-field and near-field links, a simple MATLAB script was used to calculate the implanted coil radius versus the transferred power ratio for near-field inductive links and far-field links at a fixed frequency. Several assumptions were made to generate Figure 6.2. For the near-field calculations, a quality factor of 10 was used for both the input and output coil along with an extremely low coil resistance on the receiving coil, a large load resistance, single turn antenna, and perfect alignment of the transmitting and receiving coils. The transmitting coil diameter was fixed at 2 mm for two different receive coils, 2 mm and 4 mm. In some studies, it has been found that the alignment of coils has a strong impact on the link quality, an especially important observation since perfect alignment is difficult to achieve, especially for implanted coils [144]. The assumptions made in the far-field case are gains of 1 for both the receive and transmit antennas and isotropic radiation (no directivity). This results in plotting the standard $1/r^2$ dependency in free-space. The assumption of free-space operation has two very important effects: first, the wavelength in free space is vastly different than that in the body (as will be explained later), and second, no attenuation of the signal due to the lossy medium (tissue) is taken into account.

In several works, the signal drop-off for inductive links is listed as $1/r^2$ [127], [131], and the effect of this drop-off is readily apparent in the plot. In fact, one reference

claims that the drop off is much as $1/r^6$, due to resistive losses in the conductors becoming more apparent when operating at high frequencies for smaller coils [147]. From this, several conclusions can be drawn. First, as the receive coil reduces in size from 4 mm to 2 mm, the drop-off of inductive power transfer begins at a shorter distance. Secondly, plotting the same equations but sweeping different variables, Figure 6.3 shows there is an optimum coil radius that occurs at the same value as the required read range. This implies that the optimum power transfer to a 2 mm implanted coil, an approximation used for the intraocular application, occurs at a read range of 2 mm.

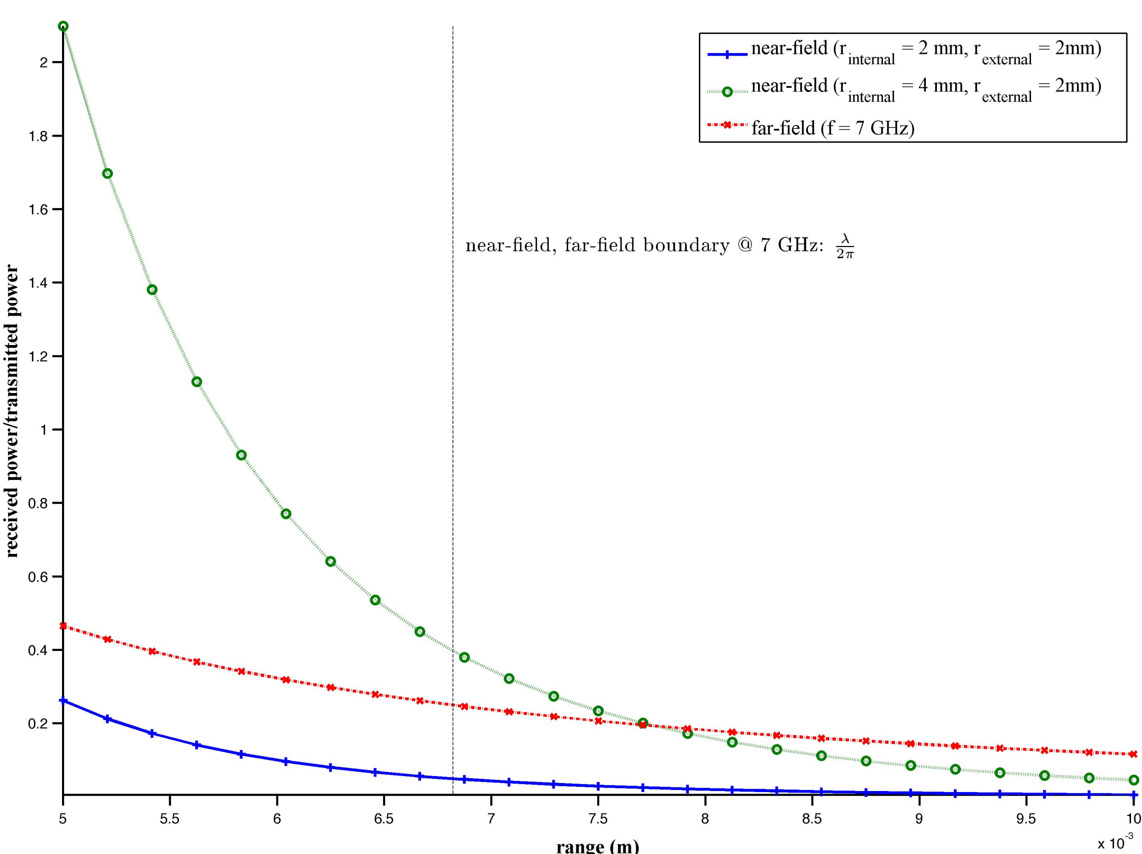

Figure 6.2. Transfer efficiency in near-field and far-field; note far-field cut-off (Friis transmission validity)

In order to calculate the far-field power transfer, the Friis transmission formula was used [120], [121], as shown in Equation (6.5). Several simplifications, as noted above, were made, leading to the simplified version here.

$$\frac{P_{received}}{P_{transmitted}} = \frac{\lambda^2}{4\pi x^2} \tag{6.5}$$

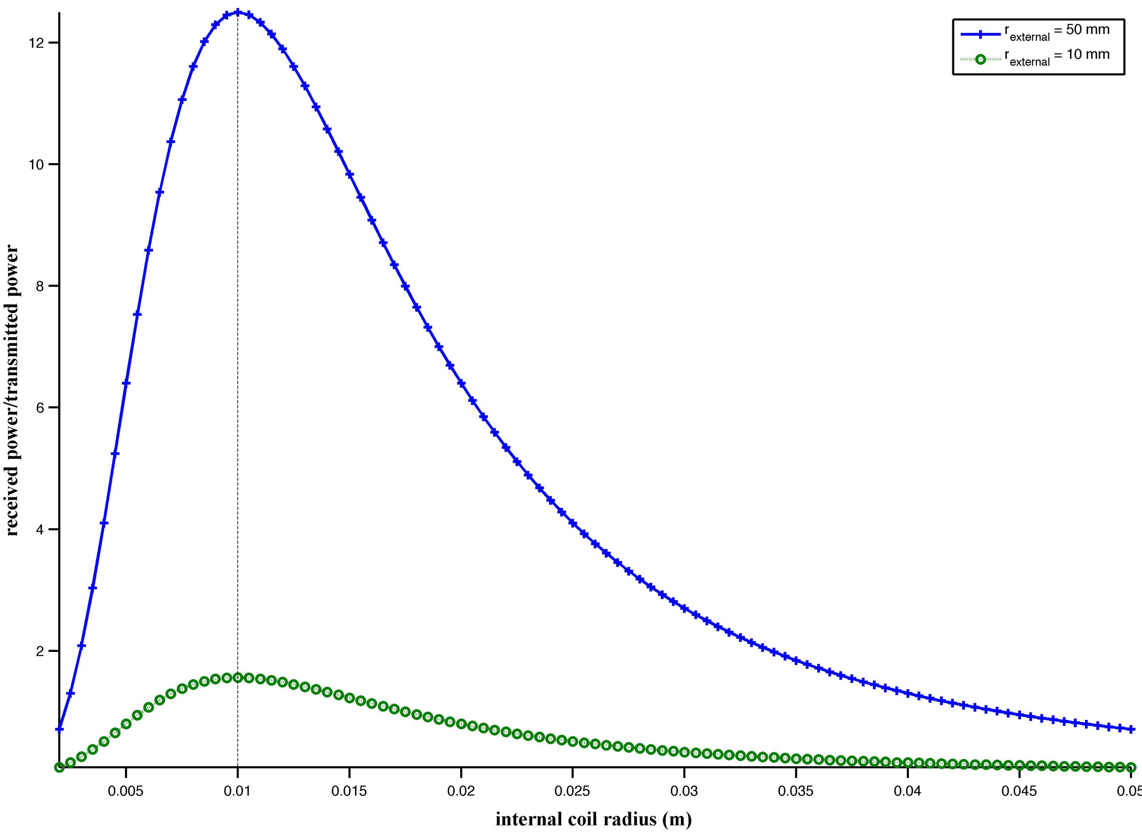

Figure 6.3. Near-field power transfer efficiency for various internal coil radii and fixed range of 10 mm

Equation (6.5) shows a dependence on wavelength (see Equation (6.9) for definition) and also on the distance *x* between antennas. To calculate near-field effects, the following equations were used [127], [131]:

$$\frac{P_{received}}{P_{transmitted}} = k^2 Q_1 Q_2 \tag{6.6}$$

The derivation for this form of power transfer is shown in [148]. The equation assumes perfect alignment; *k* is defined as the coupling coefficient between the two coils, and considers the effect of the mutual inductance to be represented as an energy storage field. In this case, the quality factor becomes important, where Q_1 is the quality factor of the transmitting coil and Q_2 is the quality factor of the receiving coil. The definition of the coupling coefficient is described in the following equation, but with some limitations in its application. The approximation in Equation (6.7) is only true when the transmit coil size is less than or equal to the receive coil [131].

$$k = \frac{r_{tx}{}^{2} r_{rcv}{}^{2}}{\sqrt{r_{tx} r_{rcv}} \left(\sqrt{x^{2} + r_{rcv}{}^{2}} \right)^{3}} \tag{6.7}$$

The radius r for both coils is the same while the distance between coils is x. An equation for Q for the receiver is provided in [127]. However, for the purpose of this approximation, Q_1 and Q_2 were simply set equal to each other and to a value of 10, which can be considered an average value for on-chip inductors [149]. Combining Equation (6.6) and Equation (6.7) yields the power calculation used to approximate near-field power transfer, shown in Equation (6.8).

$$\frac{P_{received}}{P_{transmitted}} = \left(\frac{r_{tx}{}^{2} r_{rcv}{}^{2}}{\sqrt{r_{tx} r_{rcv}} \left(\sqrt{x^{2} + r_{rcv}{}^{2}} \right)^{3}} \right)^{2} Q^{2} \tag{6.8}$$

The main conclusion to draw is that below a certain receive coil radius, inductive links cannot transfer as much power as antennas operating in the far-field over the same transmit distance. One alternative, which may be explored in the future, is evident in Equation (6.8) – improving Q has a square-law dependency on the transferred power. If there is a way to construct extremely high-quality-factor coils, then these inductive links may be useable at smaller radii. The limiting factor will most likely be the conductivity of the metals used in the coil and the skin effect.

Overall, this section has described and compared the dominant types of wireless techniques used with implantable devices. A preliminary discussion of electromagnetic properties and how they are affected in the body was also provided to help define limits and specifications for an improved wireless communication technique. It is clear from the previous section that far-field techniques are a better choice when device size limits the maximum internal coil size. If the device size could be increased to accommodate larger coils, then inductive links are a better choice.

In general, as the frequency of the electromagnetic wave increases, the loss increases. Some of these effects are due to dielectric relaxation [145] of water and other molecules in tissue that respond to an applied electric field. Since there are no strong magnetic fields in the body, however, magnetic permeability is virtually the same as in

air. This by itself lends credence to choosing the near-field inductive link as explained earlier. Similarly, it is important to note that any antenna designed to operate in the far-field will still radiate in the near-field, and therefore any attenuation in the near-field will also affect the strength of the signal in the far-field. This means that antennas that are inherently magnetic in the near-field will be virtually unaffected by the body tissue, since the body's magnetic permeability is close to that of free-space. For this reason, an implantable dipole antenna is most likely not a good choice.

6.4. Electromagnetics

The antenna serves as the link between the electrical domain and the physical domain, and as such, its efficiency and properties are paramount to the device. In the case of ultrawideband (UWB) transmissions, the designs of these antennas are different from conventional narrowband antennas due to physical differences in electromagnetic propagation – instead of propagating an electromagnetic wave at a specific frequency, wideband antennas are designed to operate over much larger bandwidths. Simulation tools have been used to approximate the response of these antennas when implanted in lossy tissue by including the electromagnetic properties in the simulation tool. Several different antennas have been designed for different material properties in order to test antenna efficiency, to correlate simulation results with actual results, and for implantation studies.

6.4.1. Electromagnetic Properties

Several important design parameters are presented later but depend on the definition of a few basic principles, such as the definitions of wavelength, wave velocity, and the effects of the medium. Equation (6.9) defines wavelength in meters, where f is the frequency and c is the speed of light in free space.

$$\lambda = \frac{2\pi}{k_0} = \frac{c}{f} \tag{6.9}$$

This equation assumes free-space conditions. k_0 is called the wavenumber of free-space, and is defined in Equation (6.10).

$$k_0 = 2\pi f \sqrt{\mu_0 \varepsilon_0} \tag{6.10}$$

This value can also be used to calculate velocity of the wave by calculating the wavelength from the period of 2π. In free-space, this yields the speed of light *c*, as shown in Equation (6.11).

$$c = \frac{2\pi f}{k_0} = \frac{1}{\sqrt{\mu_0 \varepsilon_0}} \approx 3 \times 10^8 \text{ m/s} \tag{6.11}$$

It is important to note that the speed of light depends on both the permeability μ and permittivity ε of the medium through which the wave is propagating. Wave velocity is different for each medium, due to the dependency on these two parameters. This strongly impacts the ability of antennas to propagate through materials such as a lossy dielectric like tissue. Another useful equation relating these two values is the intrinsic impedance, η with units of ohms, as defined in Equation (6.12). For free space, the intrinsic impedance is 377 Ω.

$$\eta = \sqrt{\frac{\mu}{\varepsilon}} \tag{6.12}$$

6.4.2. Electromagnetic Fields in Living Tissue

Electromagnetic waves at microwave frequencies transmitted through tissue are attenuated due to the complex-valued dielectric properties associated with the medium. This is a major drawback, implying that energy is dissipated and lost into the tissue as heat, causing signal degradation. It is also worth noting that each type of tissue exhibits a different characteristic complex impedance.

Microwave frequencies can also be dangerous due to excessive tissue heating. This issue is covered in great detail by government regulation and studies carried out on Specific Absorption Rate (SAR) and the various related standards. For UWB, the FCC has placed restrictions on the output power, limiting the total amount that can be radiated to extremely low levels. Specific further studies on UWB implants and the biological safety need to be conducted, though the FCC has defined medical imaging devices as a specific application of UWB, thereby potentially implying that the extremely low output power of UWB does not pose a health risk.

In terms of wireless transmission, as the transmit frequency increases, the wavelength drops, allowing a smaller antenna to be used as shown in Equation (6.9). Since a small surface is required (the maximum single dimension is 2 mm to ensure a minimally-invasive surgery), a small antenna is required. This in turn implies a higher frequency must be used. In the body, the propagation of electromagnetic waves is slowed, reducing the wavelength further and thereby shrinking the required antenna dimensions. As an example, a standard quarter-wavelength dipole antenna sized at 2 mm would operate at a frequency of 37 GHz in air. However, in the case of an implantable device, the biological system serves as an advantage, reducing the required frequency by way of the dielectric effect. It is therefore possible to build an implantable antenna that fits within our dimensional requirements, operating in the upper UWB range of 7 to 10 GHz, and as high as 9 to 10 GHz, the preferred range of operation due to size constraints on the antenna.

6.4.3. The Dielectric Effect

The dielectric effect can be considered a method of antenna miniaturization [146]. The technique works by slowing down electromagnetic propagation, which changes the wavelength of the electromagnetic wave. This effect is due to the change in intrinsic impedance η of the medium, which is very different from free space and must be calculated for each medium.

Wave propagation in dielectrics can be defined in terms of the wavenumber, which will change based upon the medium. Equation (6.13) shows this relationship.

$$k = \omega\sqrt{\mu\varepsilon} \tag{6.13}$$

Permittivity can also be complex, as defined in Equation (6.14).

$$\varepsilon = \varepsilon' - j\varepsilon'' \tag{6.14}$$

Now, Equation (6.13) can be rewritten as shown in Equation (6.15).

$$k = \omega\sqrt{\mu\varepsilon'}\sqrt{1 - j\frac{\varepsilon''}{\varepsilon'}} \tag{6.15}$$

These equations can be used to calculate two important parameters, the attenuation coefficient (α) and phase constant (β), as shown in Equation (6.16).

$$\alpha = \mathrm{Re}\{jk\} = \omega\sqrt{\frac{\mu\varepsilon'}{2}}\left(\sqrt{1+\left(\frac{\varepsilon''}{\varepsilon'}\right)^2}-1\right)^{1/2}$$
$$\beta = \mathrm{Im}\{jk\} = \omega\sqrt{\frac{\mu\varepsilon'}{2}}\left(\sqrt{1+\left(\frac{\varepsilon''}{\varepsilon'}\right)^2}+1\right)^{1/2} \quad (6.16)$$

Lastly, the loss tangent is described as the ratio between the complex and real parts of permittivity, as shown in Equation (6.17). The loss tangent *tan* θ is the value often reported once measurements have been made for a particular material.

$$\tan\theta = \frac{\varepsilon''}{\varepsilon'} \quad (6.17)$$

The characteristic impedance, redefined due to the complex valued permittivity, is shown in Equation (6.18).

$$\eta = \sqrt{\frac{\mu}{\varepsilon' - j\varepsilon''}} \quad (6.18)$$

The result of all these equations can be used as a general 'rule': "…the wavelength is shorter and the velocity is lower in all real media than they are in free space" [145].

Another useful equation in terms of attenuation is shown in Equation (6.19), which provides a simple relationship between attenuation and the electric field, E_0, in a complex dielectric.

$$E_0 e^{-1} = 1/\alpha \quad (6.19)$$

Any antenna that is implanted in the body will exhibit this dielectric effect due to the change in permittivity of body tissue. However, once the electromagnetic wave leaves the body, the electromagnetic wave returns to its normal velocity and the miniaturization effect is lost.

The dielectric effect in general is usually not reported, or correctly identified, in the literature by those who study implantable devices since it is much more apparent with far-field links and at higher frequencies. Some recent works were either originally unaware of the effect, and thus required antenna modification to compensate, or have reported it as an effect present only in tissue [136], [140]. The most interesting function of the analysis of the dielectric effect is the reduction of the physical dimensions of the required antenna; this has been used to advantage in the intraocular antenna design.

6.4.4. Reflections

Electromagnetic waves, upon encountering a medium with different properties, are reflected at a ratio dependent on those material properties [145]. The previously defined intrinsic impedance η, defined in Equations (6.12) and (6.18), is used to formulate the reflection coefficient, Γ, as shown in Equation (6.20), where the subscript *1* denotes the first medium the electromagnetic wave is in and *2* denotes the second medium upon which the electromagnetic layer is about to enter.

$$\Gamma = \frac{\eta_2 - \eta_1}{\eta_2 + \eta_1} \tag{6.20}$$

When multiple layers are defined, such as in the human body where the response through many tissues varies, an impedance in terms of previous layers can be defined. Equation (6.21) follows the same nomenclature as Equation (6.20), but with the addition of subscript *3*, which is the third medium, as shown in Figure 6.4.

$$\eta_1 = \eta_{in} \frac{\eta_3 \cos\beta_2 l_2 + j\eta_2 \sin\beta_2 l_2}{\eta_2 \cos\beta_2 l_2 + j\eta_3 \sin\beta_2 l_2} \tag{6.21}$$

The discussion and theory presented in this section are highly relevant to implantable devices because the attenuation and reflection of an electromagnetic wave as it travels between multiple tissues can drastically affect transmission. Most of the reflection for implantable devices occurs between air and skin. Equation (6.22) shows the calculation of the reflection coefficient and skin. It is important to note that the reflection is frequency dependent, encapsulated in the permittivity values.

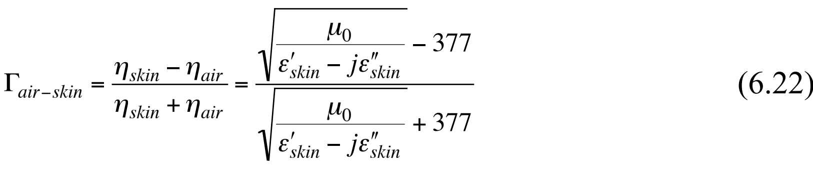

$$\Gamma_{air-skin} = \frac{\eta_{skin} - \eta_{air}}{\eta_{skin} + \eta_{air}} = \frac{\sqrt{\frac{\mu_0}{\varepsilon'_{skin} - j\varepsilon''_{skin}}} - 377}{\sqrt{\frac{\mu_0}{\varepsilon'_{skin} - j\varepsilon''_{skin}}} + 377} \qquad (6.22)$$

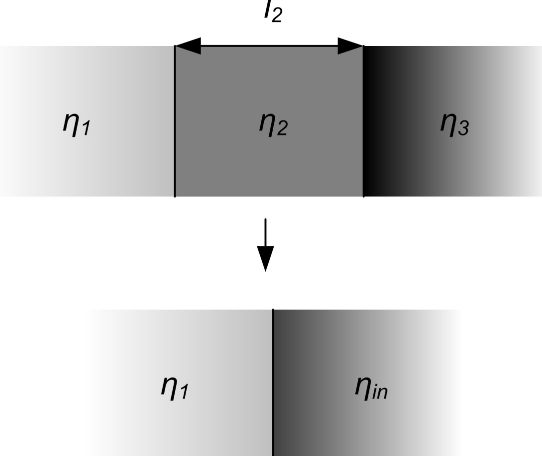

Figure 6.4. Simplifying reflection between multiple layers of medium with different electromagnetic properties

The large reflection at the air-skin interface introduces a unique solution to reduce unnecessary power consumption. In this application, the air-skin interface is eliminated. For this to work, the external receiver is placed directly on the skin through an impedance-matched ($\Gamma = 0$) layer, such as the closed eyelid. For this particular application, there is no need to radiate signals into air through the body at all times, conserving power for the implanted transmitter and avoiding this loss.

6.5. UWB Antenna Design

One of the biggest challenges for UWB communications is the antenna design. Typically, antennas are designed to operate at one specific frequency, which can be achieved by designing resonant antennas. However, for good UWB transmission, non-resonant antennas are often the best choice.

Based on a literature review, two types of antennas were studied in greater detail, the Archimedean spiral and the equiangular, or logarithmic, spiral. Non-resonant antennas must radiate at many frequencies, and spiral antennas achieve this through a constantly varying distance between the two arms as the angle of rotation is varied around a center axis. These types of directional antennas achieve circular polarization,

eliminating dependence on orientation. They are directional, however, radiating normal to the surface both out of the substrate and into the substrate. Antennas can also be made omni-directional, but require a wideband reflector in order to conserve power that radiates away from the receiver. The chosen antennas are also of a planar design and therefore simple to fabricate. No ground plane is required, since the antenna is constructed and operated in a differential mode.

One of the drawbacks of spiral antennas is their bidirectional radiation; typically absorbing cavities are placed on the backside of the antenna to attenuate this radiation. Another challenge for impulse-type UWB is the frequency-dependent phase center of the antenna causing pulse dispersion. In this particular application, detection of the signal is more important than pulse shape, so this potential problem may be ignored since an external highly sensitive receiver can be used. High-data rate applications must be concerned with pulse dispersion since it may make wireless communication more difficult, especially in the presence of multiple wireless links. The most critical parameter for UWB antenna design is the frequency-dependent delay, or phase shift, the antenna applies. This causes pulse distortion, which for certain types of receivers, could make it extremely difficult to ensure successful reception. Again, for the particular application described here, this is not important because the data rate is very low.

6.5.1. Specifications

Once the system parameters have been defined, the specifications of the antenna can be determined. In this case, the antenna must meet UWB requirements, must be small enough to fit on the target dimensions of 1.5 mm x 2 mm, and must integrate with the rest of the device without any unneeded complexity. There are also external regulations, such as those provided by the Federal Communications Commission (FCC), in terms of maximum allowed power and allotted frequency bands, but these can be controlled by the output circuitry. Compliance with the FCC limits is not presented here.

In general, with increasing frequency, the antenna maximum dimensions can be decreased as the wavelength is reduced. The tradeoff with this benefit is that the attenuation that occurs at these higher frequencies, as explained in the previous section, increases with increasing frequency. Furthermore, higher frequencies may result in more

challenging circuit design due to limitations in speed and efficiency, reducing the total power delivered to the antenna. Additional concerns include interference from other sources of radiation, such as devices that operate in the unlicensed bands such as cell phones, wireless routers, and microwave ovens.

Taking all these restrictions into account, the upper frequencies within the UWB limit as defined by the FCC, were chosen for operation. The maximum Industrial, Scientific, and Medical (ISM) frequency that falls within the UWB band defined by the FCC is 5.8 GHz, so that value serves as the lower limit to avoid interference from common devices. The upper limit is chosen as the maximum possible within the FCC specification, or 10.6 GHz. The minimum bandwidth defined by the FCC is 500 MHz. Therefore, the final frequency range of operation for this device was chosen to be between 7 to 10 GHz.

As stated previously, the maximum antenna dimension available for use is 2 mm. Selecting the minimum frequency of 7 GHz, the wavelength can be calculated simply using the speed of light in free space to determine what the wavelength should be, as shown in Equation (6.9), yielding a value of 43 mm. However, depending on the type of antenna, some fraction of the wavelength may only be necessary, such as in quarter-wavelength dipole antennas, which is 10.75 mm in this case. For comparison, another interesting Industrial, Scientific, and Medical (ISM) frequency band is 60 GHz; this yields a quarter wavelength of 1.25 mm in free space.

The value calculated for 7 GHz is of course much too large to fit within the eye. However, in the previous sections the dielectric effect was introduced demonstrating how antenna miniaturization works. Calculating the resulting antenna dimensions is simple once the complex permittivity of the medium of interest is known at the specified frequency. Using the general form of Equation (6.9) and Equation (6.16), a new wavelength can be calculated based on the complex permittivity of the medium, as shown in Equation (6.23).

$$\lambda = \frac{2\pi}{\beta} = \frac{1}{f\sqrt{\frac{\mu\varepsilon'}{2}}\left(\sqrt{1+\left(\frac{\varepsilon''}{\varepsilon'}\right)^2}+1\right)^{1/2}} \qquad (6.23)$$

In general, the lower frequency limit is the dimensional limiting factor, since it is the larger wavelength. Simulation results have verified that an antenna operating within the eye at frequencies as low as 7 GHz should fit within the maximum dimension of 2 mm. However, as the antenna approaches the edge of the substrate, the dielectric effect and characteristic impedances will change. In order to limit the dynamic impedance changes (through the frequency band of interest), the lower frequency has been raised further. The new frequency band is selected as 9 GHz to 10 GHz and easily fits within the required dimensions.

Many of the critical design parameters can be calculated by hand for the lower and upper frequency band, including wavelength, characteristic impedance, and attenuation. It is important to note that when calculating characteristic impedance, the electrical properties of the medium as well as the substrate need to be taken into account.

6.5.2. Material Properties

The material properties of both the substrate, which is typically a dielectric, and the conductor, which serves as the current-carrying medium, are also dependent on frequency. Metal conductors are often simply chosen based on their conductivity. In this regard, materials such as copper and silver are the best choices since their conductivities are the highest of all metals. However, there are other material properties that play an important role, such as the formation of oxides and the conductivity of such oxides. Surface oxides can cause conduction losses for high-frequency devices due to the skin effect, as described in Equation (6.24), where α and β were previously defined in Equation (6.16) and σ is the conductivity of the material [145]. Skin depth δ is the distance from the surface of the material towards the center where the bulk of the current flows, for each $e^{-2\alpha\delta} = e^{-1}$ [121].

$$\delta = \frac{1}{\sqrt{\pi f \mu \sigma}} = \frac{1}{\alpha} = \frac{1}{\beta} \tag{6.24}$$

In general, this effect suggests that as frequency increases, current travels closer to the surface of the conductor. This means all the electrons are traveling through the conductor in a smaller region, increasing effective resistance. This problem is worsened

if part of this region has become oxidized, since the conductance may drop dramatically. Materials such as gold do not readily oxidize and may actually be a better choice in this regard. Therefore, electroplated-copper followed by an electroplated or even evaporated thin gold layer may provide two levels of protection. First, gold does not oxidize and therefore will not succumb to reduced conductance. High-frequency signals will still conduct through the copper layer due to the difference in conductivities of the two materials. Second, gold is biocompatible whereas exposed copper has shown cytoxicity [152].

Typical substrates used for planar antennas are low-loss dielectrics, such as Rogers Duroid or ceramics such as Low Temperature Co-Fired Ceramic (LTCC). In this work, glass is used as a substitute for those materials since it is compatible with MEMS processing techniques such as batch-fabrication and anodic bonding to form pressure sensors. The dielectric properties of borosilicate glass, specifically chosen for its similarity to silicon in its coefficient of thermal expansion, are shown in Table 6.1.

Material	***Frequency***	***Loss Tangent***	***Permittivity***	***Thermal Expansion Coefficient***
Borosilicate Glass [34]	1 MHz	3.7×10^{-4}	4.6	3.25×10^{-6} K^{-1}
High-Resistivity Silicon [153]	6 GHz	5×10^{-3}	11.7	2.6 x 10-6 K^{-1}
LTCC [154]	10 GHz	1.4×10^{-2}	7.8	5.8 x 10-6 K^{-1}

Table 6.1. Substrate material properties at a temperature of 300 K.

For biological materials, such as the cornea or aqueous humor, the complex dielectric properties are heavily dependent on frequency. Two materials have been selected to demonstrate this phenomenon, saline and cornea. The saline values were calculated using the Cole-Cole model [155] and appear in Figure 6.5 and Figure 6.6. The cornea values were retrieved from a web database created from previously collected data [156] and are shown in Figure 6.7 and Figure 6.8. Further ocular data is also found in [157]; although it is for rabbit eyes, it is probably quite similar to human eyes.

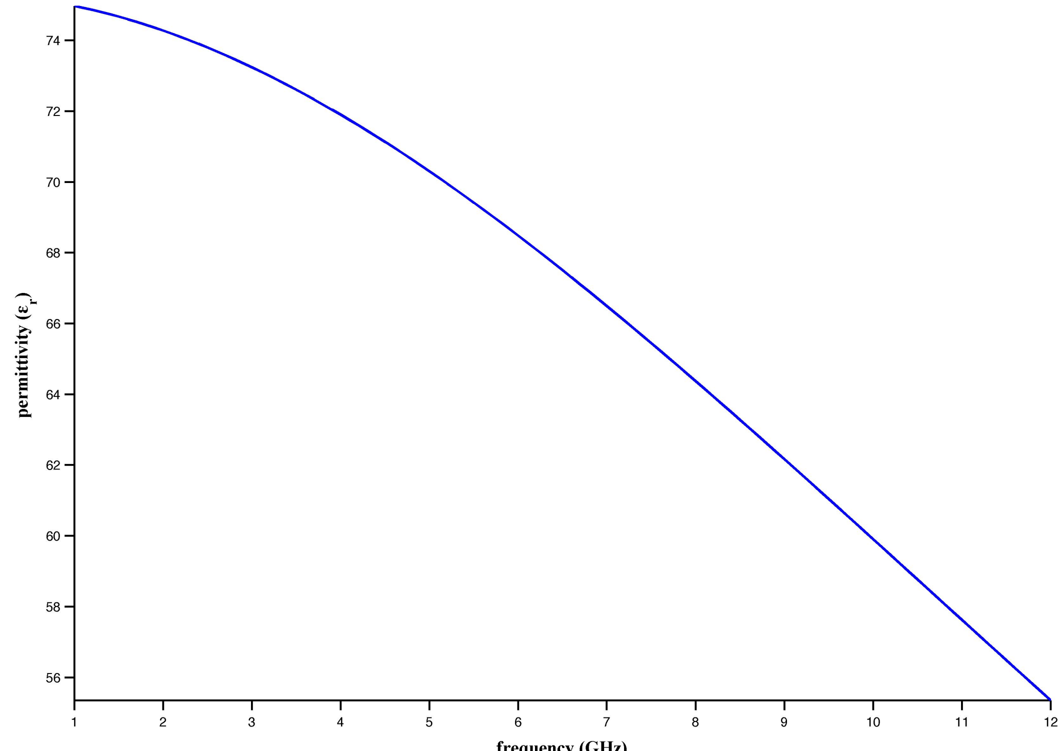

Figure 6.5. Permittivity of saline

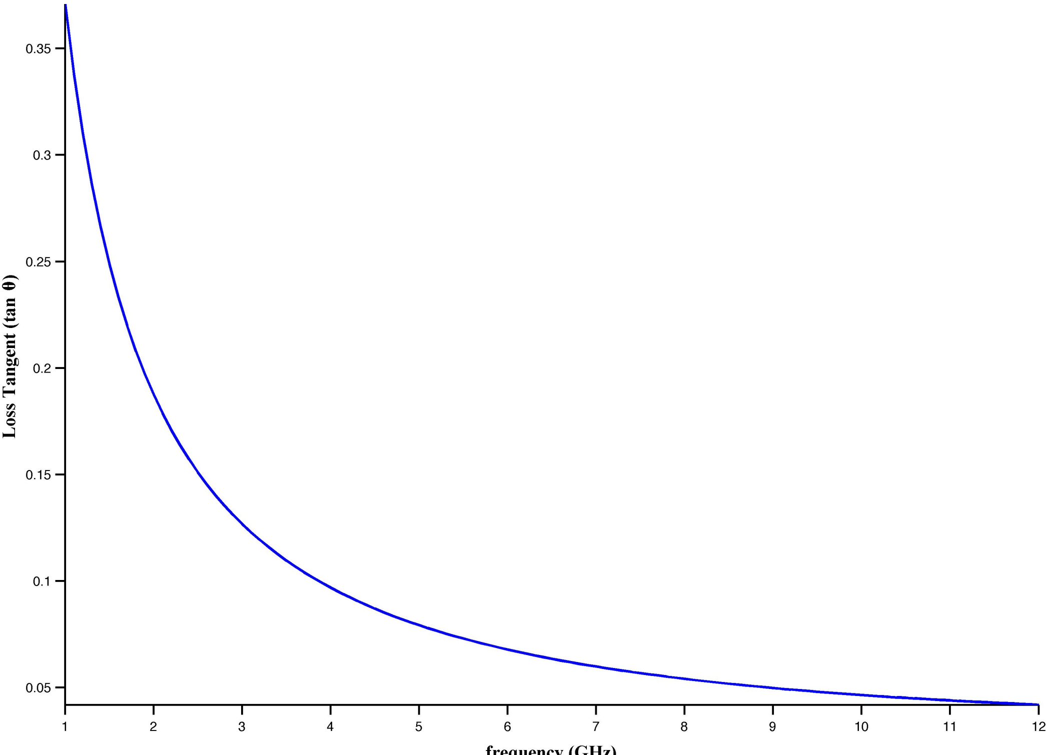

Figure 6.6. Loss tangent of saline

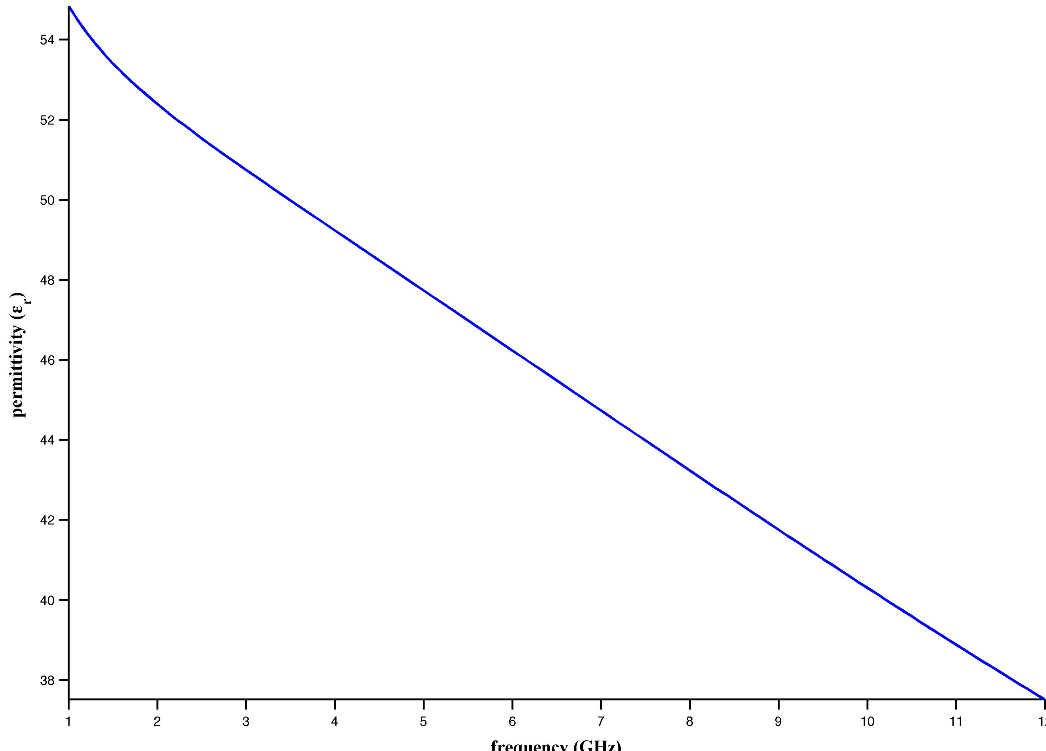

Figure 6.7. Permittivity of the cornea

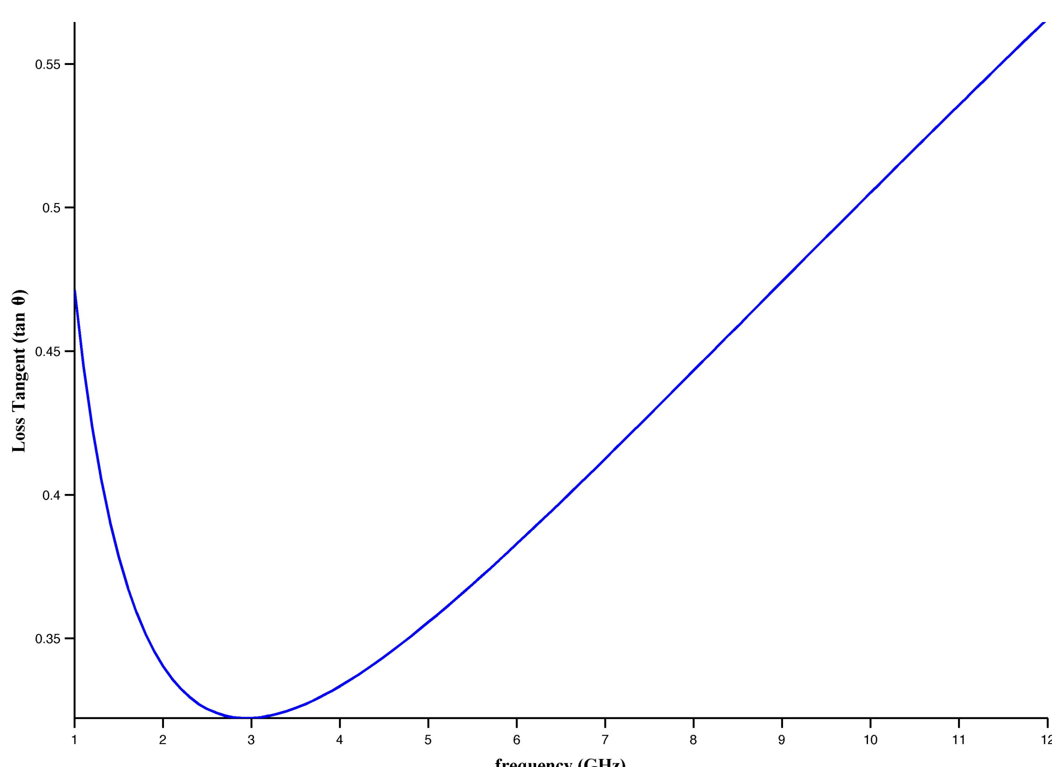

Figure 6.8. Loss tangent of the cornea

6.5.3. Archimedean Spiral

The Archimedean spiral is an antenna with a fixed wire width, fixed spacing between consecutive spirals, and a constant growth rate of the spiral [158]. The smallest radius, or start radius, of the spiral is determined by the highest frequency the antenna should operate at. However, since this dimension is smaller than the outer radius, it is often made several times smaller than it needs to be. The larger outer radius is defined by the lower frequency of the bandwidth of interest. Equation (6.25) is used to calculate the radii for the specific frequencies, and was determined based on the operation of the antenna. Equation (6.26) describes the spiral itself in polar coordinates, where ρ is the radial position and ϕ is the angle [158]. By setting r in Equation (6.25) to ρ, the limits required for adequate radiation at specific frequencies can be found. k is a constant that determines the starting point, while a is the growth-rate of the spiral and controls the spiral tightness.

$$\lambda = 2\pi r \tag{6.25}$$

$$\rho = a\phi + k \tag{6.26}$$

6.5.4. Equiangular Spiral

The equiangular spiral antenna is similar to the Archimedean except that the rate at which the antenna width increases as the angle ϕ rotates around the center axis varies. This means the wire width and spacing between arms are not fixed. Using polar coordinates, the equation that describes the radial position ρ, growth rate a, and outer radius r_0 is shown in Equation (6.27). One difference between the Archimedean spiral and the equiangular spiral is the termination used. Typically, a “straight-cut” is used at the end of the spiral, generating reflections that may cause interference and turns the antenna into a resonant-type antenna. While this effect did not strongly affect the performance of the Archimedean spiral antenna, it was much more apparent with the equiangular antenna during simulation studies. In order to reduce these reflections, a tapering effect was used after the termination of the antenna, behaving more like a real resistance and absorbing reflections from the end point of the spiral arms. This is readily apparent in the layout of the antennas, as shown in Figure 6.13.

$$\rho = r_0 e^{a\phi} \tag{6.27}$$

6.5.5. Simulation Results

Ansoft HFSS is the software tool used to calculate and determine scattering parameters (s-parameters). In the tool, two identical antennas are placed facing each other to determine the transmission efficiency while a single antenna can be used to calculate the reflection parameters (s_{11}). In both simulations, the antennas were placed on a glass substrate with two feedthroughs acting as the differential inputs. The antennas were also placed in the medium of interest, ranging from saline to cornea, skin, and so on, as captured in data provided by [156].

Simulation results for the antennas were used to determine transmission and reflection scattering parameters as shown in Figure 6.9. An optimization program was written in MATLAB, sweeping parameters of interest to find the optimal geometry by varying parameters such as line width and spacing between adjacent wires. Output data includes a SPICE circuit model that can be introduced as a block in the circuit design stage, generated by HFSS. The antenna itself is generated in MATLAB and imported into HFSS; a GDS file can be exported from HFSS and imported into a layout tool for mask design during fabrication.

Sample data for several different geometries over the 7 to 10 GHz frequency band are shown in Figure 6.11 and Figure 6.12 for Archimedean spiral antennas. The first plot, Figure 6.11, shows the reflection scattering parameters. Good antennas reflect less than 10 dB across the band of interest, indicating that at least 90% of the applied signal did not reflect back to the input. This does not guarantee radiation, however. Figure 6.10 is a screenshot of two antennas placed within a ‘bubble’ of saline to measure transmission scattering parameters (s_{12}) between two antennas placed 10 mm apart. The transducer power gain in Figure 6.12 plots how much power is transferred between the two antennas.

The important point to note in these plots is the roughly frequency-independent behavior across a large bandwidth of frequency. This is characteristic of non-resonant antennas, whereas a narrowband antenna will demonstrate a very low reflection at a single frequency. Secondly, the larger the bandwidth, the less constraint on the drive

circuitry. This means that the antenna should radiate as long as the drive circuitry generates a pulse that contains frequencies within the bandwidth of the antenna.

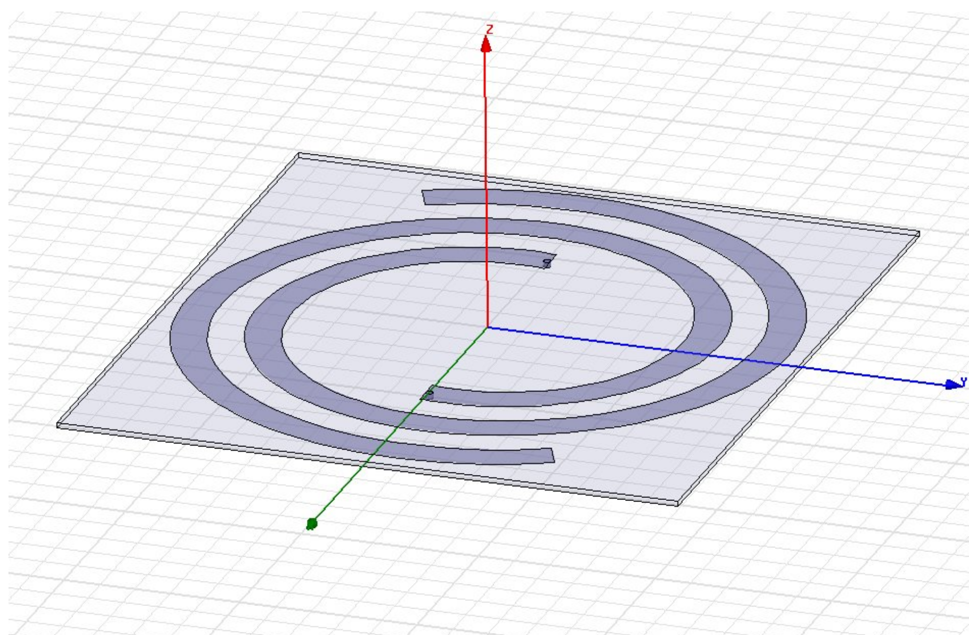

Figure 6.9. Screenshot of an Archimedean antenna in HFSS on thin glass substrate with copper feedthroughs.

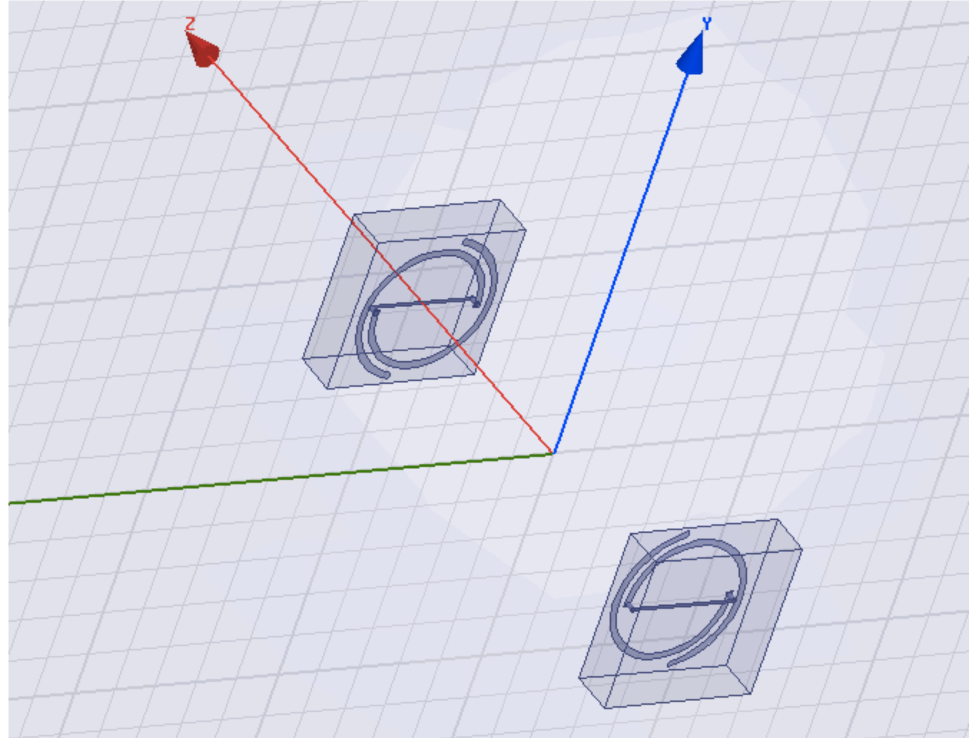

Figure 6.10. Screenshot from an HFSS simulation showing two identical antennas placed 10 mm apart used to determine transmission parameters (s12).

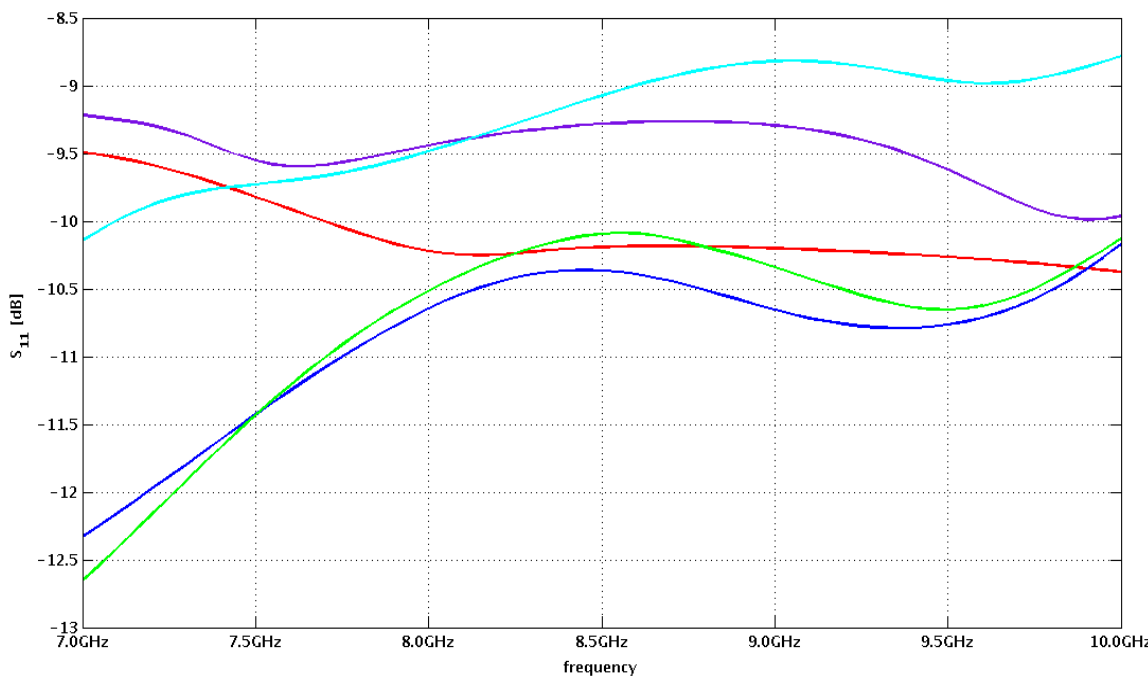

Figure 6.11. S11 reflection parameters for the Archimedean antenna in saline with variations in geometric parameters such as line width.

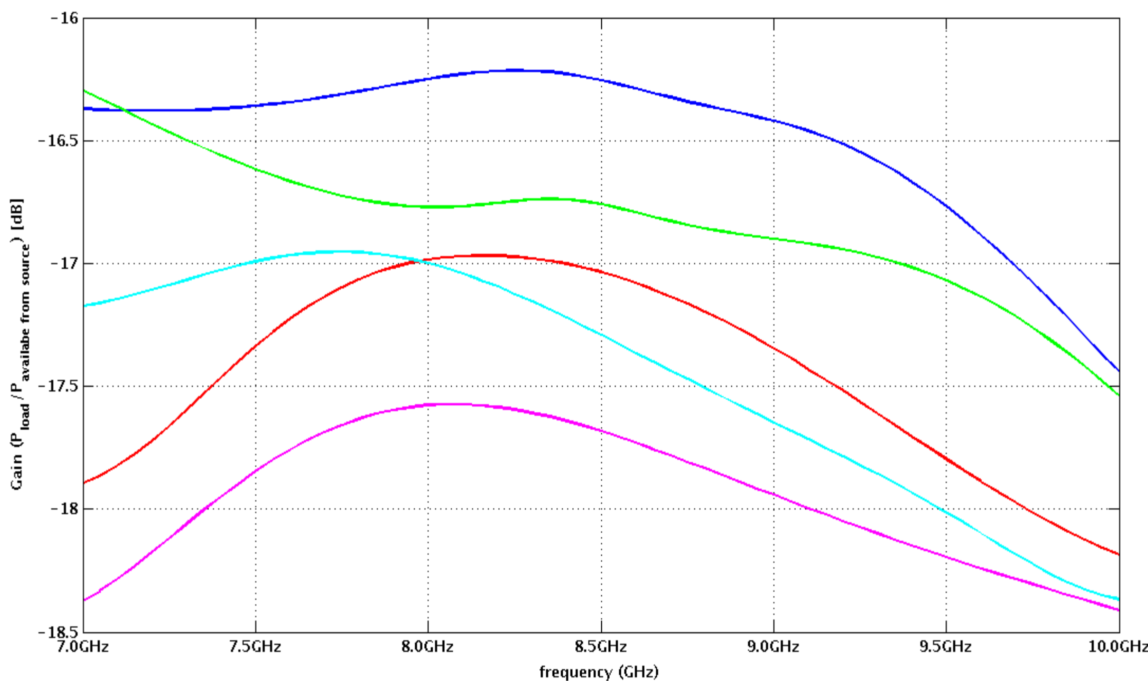

Figure 6.12. Transducer power gain between two Archimedean antennas in saline with variations in geometric parameters such as line width.

6.5.6. Fabrication

A few of the more optimal designs were imported to layout tools for fabrication. Figure 6.13 shows the layout of four different kinds of antennas, two equiangular and two

Archimedean spiral antennas. A redistribution layer provides metal connections between the ASIC, which is placed on the other side of the antenna, and the antenna itself using through-glass vias. The extra metal pads are used for routing between the microbattery and pressure sensors, located on the same side as the ASIC. The antennas are centered on the gray-colored glass substrate. The ASIC is shifted slightly to allow room for routing interconnects for the pressure sensor.

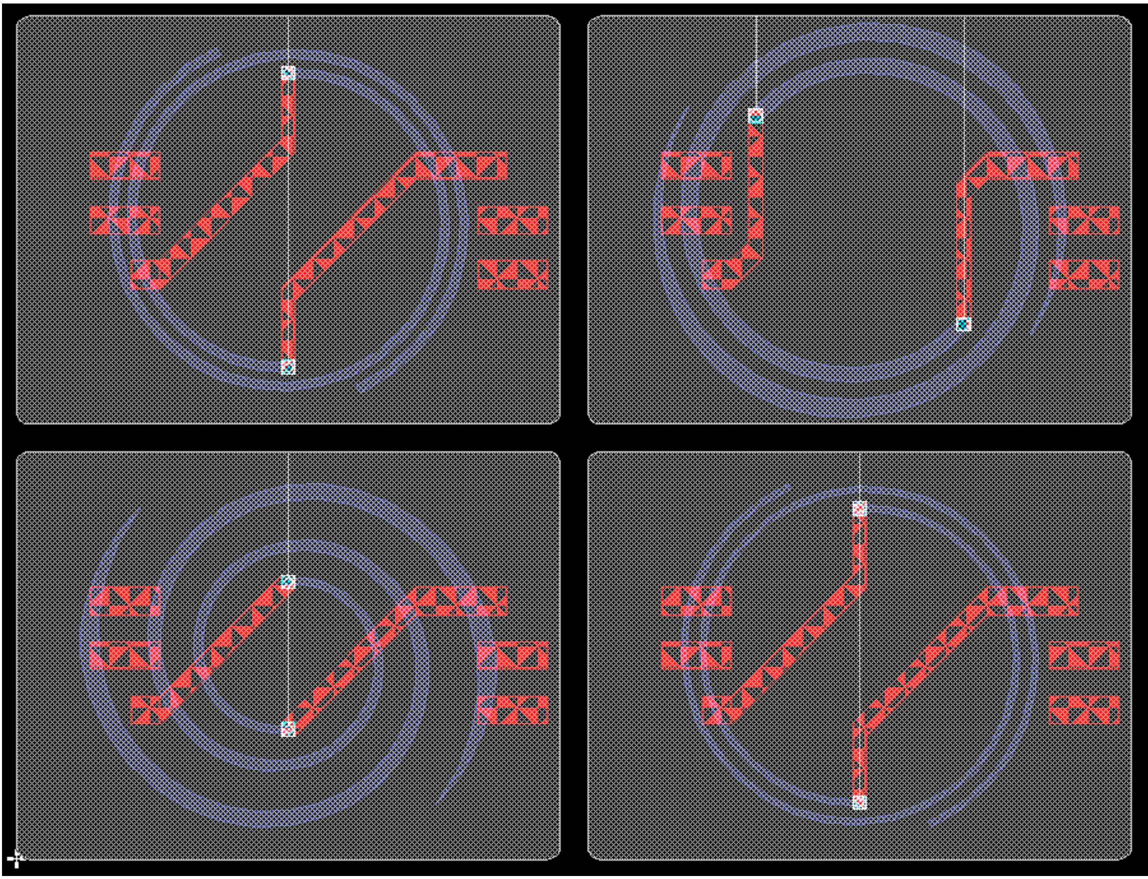

Figure 6.13. Layout of four different antennas on a glass substrate. The red metal lines provide a redistribution layer allowing the ASIC to connect to the antenna with vertical interconnects.

The fabrication process is shown in Figure 6.14. It is very similar to what has been shown previously for the pressure sensor and the microbattery designs, but differs in that the silicon feedthroughs are removed completely and instead replaced with high-conductivity electroplated copper feedthroughs. These glass-in-silicon wafers are constructed in the same manner as the other intraocular modules. Details of this fabrication process were described in Chapter 2.

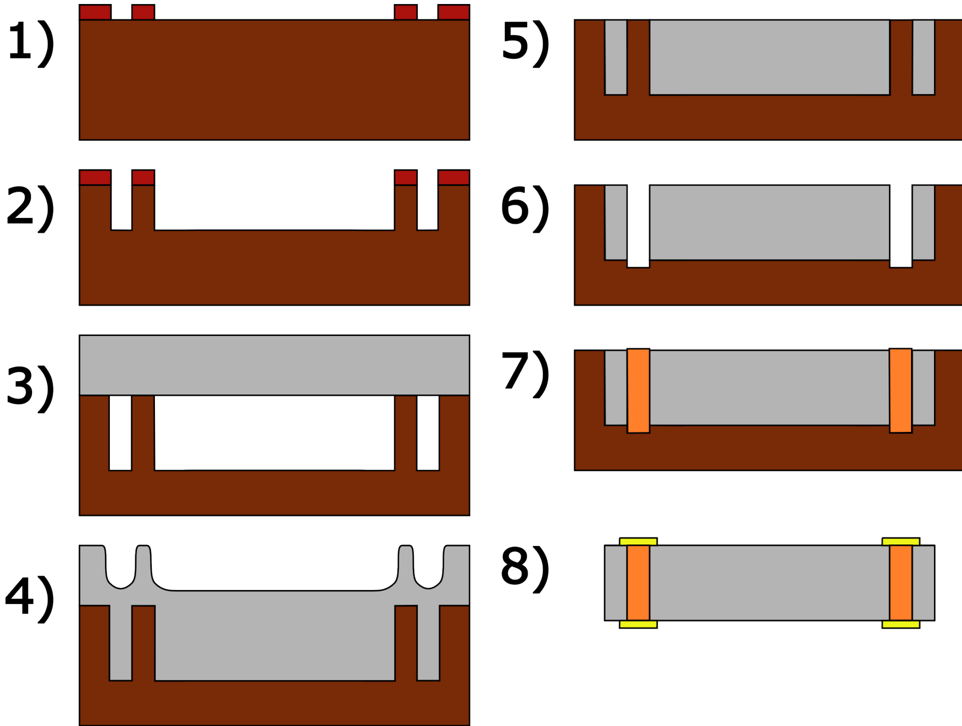

Figure 6.14. Process flow for the antenna module.

6.5.7. Antenna Testing

At this time the antenna has not been fabricated and only simulation data along with preliminary mask layouts are presented. Testing the antenna is extremely challenging due to the small size and the fact that the expected operating medium is not air. A simpler way to verify antenna functionality may be to measure impedance and scattering parameters (S_{11} and S_{12}) to verify simulation results.

For *in-vitro* testing a fixed electrical connection must be made to the antenna. This can be accomplished using micro-coaxial cables and soldered to the metal pads on the backside of the vias. However, this technique can result in interference due to the unterminated shield of the coaxial cables. Furthermore, the antenna has to be designed specifically for the measured properties of saline. This will confirm the accuracy of the simulation model without designing for the specific properties of saline; the losses may appear to be too high due to mismatches with the target medium.

A phantom recipe for the fluid in the eye, the aqueous humor, is available that closely mimics the electrical parameters of the eye [140]. However, these antennas were specifically designed for intraocular tissue and their respective lossy characteristics,

therefore should perform optimally in such an environment. *In-vivo* testing is the ideal method to verify functionality but will require the entire microsystem to be complete and fully functional. Further work will be required to get to that point.

6.6. Summary

The wireless module discussed in this chapter has been described at length in terms of the fundamental electromagnetics behind wireless communication in the body. It is suggested that the wireless link needs to be reanalyzed for microsystem sizes approaching a maximum physical dimension of 2 mm. Standard inductive links show low power transfer for coils 2 mm or less in dimension due to the comparatively large communication distances. Far-field links perform better, but bring along many design challenges ranging from high-frequency absorption, antenna scaling, reflections and so on. In order to take all of this into account, simulations using HFSS for Archimedean and equiangular type antennas were used to determine optimal designs. The advantages of these types of antennas are the circular polarization, compact size, good use of available surface area, and planar construction. Vertical feedthroughs made of copper provide electrical interconnect between the antenna and the driver chip. The antenna itself sits on a glass substrate, reducing coupling losses to the integrated circuit. A parylene overcoat protects the antenna from the body environment. Various antennas are proposed for fabrication using a slightly modified glass-in-silicon process that removes silicon feedthroughs and substitutes electroplated copper. Antenna testing will verify operation and also provide a circuit model of the antenna that can be used during circuit design of the output stage to minimize reflections and enhance antenna efficiency.

Overall, the work in this chapter has discussed the need for an alternative wireless communication technique when applied to a microsystem of such small dimensions that the efficiency of current preferred techniques, specifically inductive links, is reduced. The design of an ultrawideband antenna and communication method has been described and simulated, demonstrating feasibility in the approach. Remaining work should focus on further developing and fabricating the antenna to prepare for testing in saline. Future design work based upon verification of simulation results can then focus on measured qualities of the tissue and fluids within the eye, such as the aqueous humor.

CHAPTER 7

CONCLUSIONS AND SUGGESTIONS FOR FUTURE WORK

This thesis has presented an approach for developing an intraocular microsystem designed to take autonomous pressure readings from inside the eye. A system-level view has been used to evaluate the many tradeoffs of the system. Two important goals were identified directing numerous design choices. The first was to minimize the size of the implant, and the second was to reduce power consumption as much as possible. Smaller device size results in minimally-invasive surgery, resulting in quicker patient recovery, and eliminates any potential for impacting the patient's field of view. Size constraints also affect the second goal, limiting available energy storage. Power consumption for all microsystem components has been reduced as much as possible, introducing an ultra-low-power custom ASIC and a simplified wireless approach.

The preceding chapters first began by examining glaucoma and motivating the need for an implantable intraocular pressure sensor that also records data continuously. A unique, transparent package was then developed along with a dedicated fabrication process. An absolute pressure sensor based on the dissolved wafer process was fabricated and tested, showing good linearity by operating in the touch-mode. The capacitive pressure sensor is hermetically sealed using an anodic bond to a glass substrate with embedded vertical interconnects. The power subsystem was then discussed, with preliminary work showing the feasibility of fabricating a thin-film microbattery using standard MEMS cleanroom materials, silver and zinc. The electrolyte is a non-toxic saline solution. Additional power solutions are also presented, including solar power generation using on-chip solar cells made possible because of the transparent glass package. Next, a simple custom ASIC was designed that implements a finite-state machine triggered by an externally applied optical pulse, eliminating the need for a dedicated wakeup receiver circuit for initiating data transfer. The ideal ASIC for an intraocular application was discussed, incorporating features of both the ASIC designed

in this work as well as that of a collaborative work, the Phoenix microcontroller. Finally, the wireless subsystem was discussed, introducing an uncommon method of wireless data transmission that is particularly well suited to this application. Low data rates and stringent power constraints suggest that a pulse-based wireless transmission method is attractive here, but requires non-resonant antennas. Initial work on the design and simulation, including the antenna design, of such a system was reported.

Together, all these separate modules result in an intraocular microsystem that can perform autonomous pressure sensing, recharge an on-board battery using solar power, and wirelessly transfer data collected over a full day on-demand. All of this is achieved in a package size of 1.5 mm x 2 mm x 0.5 mm. Removal of the implant should be possible with sutureless implantation on the surface of the iris and recovery should be quick with minimal complications due to the minimally-invasive techniques that can be used. Batch-mode fabrication reduces costs for fabrication of the components, while microsystem assembly is done on an individual basis to ensure a fully-functional device. This all leads to a compact highly-integrated autonomous wireless implantable microsystem that can continuously track intraocular pressure.

7.1. Thesis Contributions

This thesis provides the following contributions:

1) Design and development of a highly-integrated, compact implantable microsystem compatible with minimally-invasive surgery and fast patient recovery.

2) Development of a new glass-in-silicon reflow process, resulting in robust yet thin wafers consisting of glass embedded in silicon.

3) Introduction of a glass packaging technique with embedded cavities and vertically-stacked individual modules.

4) Design of haptics to facilitate implantation onto the surface of the iris without requiring sutures and allowing simple removal of the implanted device as needed.

5) Design of a sensitive and linear capacitive pressure sensor operating in touch-mode.

6) Demonstration of hermetically-sealed vertical interconnects embedded in glass.

7) Development and testing of cleanroom-compatible electrode deposition for thin-film microbatteries, including RF-sputtered silver for deposition of silver oxide.

8) Development of a custom ASIC implemented in the TSMC 0.18 μm mixed-signal CMOS process that included a simple finite-state machine triggered by an external optical source.

9) Application of circuit implementations that reduce power consumption to picowatt levels and provide local power storage for high-instantaneous current draws.

10) Development of a process for electroplating metals through glass for the metal vias necessary for high-frequency signals.

11) Design and simulation of multiple non-resonant antennas that operate in the 7-10 GHz frequency bands and utilize pulse-based transmissions to reduce power consumption.

12) Design of a platform on which implantable sensors can be designed and built for various other applications.

7.2. SUGGESTIONS FOR FUTURE RESEARCH

The intraocular application provides a compelling target for implantable microsystems. The eye is one of the smallest organs in the body so if an implant can be made to fit within it, similar devices should be able to work in other applications, such as intracranial pressure monitoring. For implantable sensors the advantage is clear, but for environmental sensors, this packaging approach could also be of great benefit since it can protect sensitive electronics from a variety of hostile conditions. The potential of the work described in this thesis thus goes well beyond the intraocular application, and even beyond implantable devices. Several other developments, such as the protected electrical interconnects and the vertical stacking technique, can also be easily applied to other domains.

This thesis has attempted to look at all the necessary components for an intraocular pressure monitoring microsystem, but several areas still need to be explored before a complete implantable solution can be tested.

Specifically, the following recommendations are made for further research in implantable devices:

- Perform animal studies evaluating the ability of the haptics to adequately secure the microsystem to the iris in a living functional eye and redesign if necessary. Develop a surgical approach for implantation and explantation of device.

- Conduct long-term *in-vitro* studies to evaluate the ability of the package to protect embedded circuitry from moisture.

- Develop a redesigned custom ASIC combining features from the Phoenix microprocessor and the intraocular ASIC presented in this thesis. This chip should focus on minimizing active area and should include solar cells.

- Develop a power subsystem including optical power harvesting and voltage recharge circuitry for the on-board power source.

- Determine the ideal long-term power source and test its functionality, including charge cycle limitations. Evaluate commercial solutions as potential implantable batteries by conducting *in-vitro* studies.

- Test the ultrawideband transmitter circuitry and proposed antenna designs. Evaluate their performance compared to conventional inductive links and verify their functionality *in-vitro* and *in-vivo*.

- Conduct long-term *in-vivo* studies on fully-assembled intraocular microsystems and evaluate their performance compared with standard intraocular pressure measurement techniques.

- Develop devices capable of sensing medication levels in the eye, applied via eye drops, to verify their efficacy in controlling intraocular pressure when used with intraocular pressure sensing.

- Incorporate the intraocular pressure sensor with other intraocular devices, such as artificial corneas. Patients with artificial corneas are at much higher risk for developing glaucoma and would benefit from a single surgical procedure that not only replaces the cornea but also provides intraocular pressure measurements.

- Explore ways of gathering additional information in addition to intraocular pressure with the intraocular microsystem, e.g., blood sugar levels [159].

It has been stated in much of the literature and the media that the reason why implantable microsystems have not yet significantly benefitted humankind in a practical manner is the difficulty of making complicated and functional devices small enough [160]. The work in this thesis has taken a dramatic step towards the needed miniaturization.

BIBLIOGRAPHY

[1] H. A. Quigley and A. T. Broman, "The number of people with glaucoma worldwide in 2010 and 2020," *Br. J. Ophthalmol.,* vol. 90, pp. 262-267, Mar. 2006.

[2] K. C. Katuri, S. Asrani and M. K. Ramasubramanian, "Intraocular pressure monitoring sensors," *IEEE Sensors Journal,* vol. 8, pp. 9-16, 2008.

[3] A. J. Sit, "Continuous monitoring of intraocular pressure: rationale and progress toward a clinical device," *J. Glaucoma,* vol. 18, pp. 272-279, Apr-May. 2009.

[4] L. C. Titcomb, "Eye Disorders: Treatment of Glaucoma, part 2," *Pharmaceutical Journal,* vol. 263, pp. 526-530, 1999.

[5] E. Chihara, "Assessment of true intraocular pressure: the gap between theory and practical data," *Surv. Ophthalmol.,* vol. 53, pp. 203-218, May-Jun. 2008.

[6] S. Melamed, G. J. Ben Simon, M. Goldenfeld and G. Simon, "Efficacy and safety of gold micro shunt implantation to the supraciliary space in patients with glaucoma: a pilot study," *Arch. Ophthalmol.,* vol. 127, pp. 264-269, Mar. 2009.

[7] S. C. Sacca, M. Rolando, A. Marletta, A. Macri, P. Cerqueti and G. Ciurlo, "Fluctuations of intraocular pressure during the day in open-angle glaucoma, normal-tension glaucoma and normal subjects," *Ophthalmologica,* vol. 212, pp. 115-119, 1998.

[8] P. Henkind, M. Leitman and E. Weitzman, "The diurnal curve in man: new observations," *Invest. Ophthalmol.,* vol. 12, pp. 705-707, Sep. 1973.

[9] E. L. Price, L. S. Gray, L. Humphries, C. Zweig and N. F. Button, "Effect of exercise on intraocular pressure and pulsatile ocular blood flow in a young normal population," *Optom. Vis. Sci.,* vol. 80, pp. 460-466, Jun. 2003.

[10] S. Van de Veire, P. Germonpre, C. Renier, I. Stalmans and T. Zeyen, "Influences of atmospheric pressure and temperature on intraocular pressure," *Invest. Ophthalmol. Vis. Sci.,* vol. 49, pp. 5392-5396, Dec. 2008.

[11] Courtesy: National Eye Institute, National Institutes of Health.

[12] D. S. Morris, J. E. A. Somner, K. M. Scott, I. J. C. McCormick, P. Aspinall, B. Dhillon, "Corneal thickness at high altitude", *Cornea*, vol. 26, pp. 308-311, April 2007.

[13] S. Sacca, A. Marletta, A. Pascotto, S. Barabino, M. Rolando, R. Giannetti and G. Calabria, "Daily tonometric curves after cataract surgery," *Br. J. Ophthalmol.,* vol. 85, pp. 24-29, Jan. 2001.

[14] D.L. Van Horn and R. a Hyndiuk, "Endothelial Wound Repair in Primate Cornea," *Experimental Eye Research*, vol. 21, Aug. 1975, pp. 113-24.

[15] J. E. Somner, D. S. Morris, K. M. Scott, I. J. MacCormick, P. Aspinall and B. Dhillon, "What happens to intraocular pressure at high altitude?" *Invest. Ophthalmol. Vis. Sci.,* vol. 48, pp. 1622-1626, Apr. 2007.

[16] B. E. Klein, R. Klein and M. D. Knudtson, "Intraocular pressure and systemic blood pressure: longitudinal perspective: the Beaver Dam Eye Study," *Br. J. Ophthalmol.,* vol. 89, pp. 284-287, Mar. 2005.

[17] S. D. McLeod, S. K. West, H. A. Quigley and J. L. Fozard, "A longitudinal study of the relationship between intraocular and blood pressures," *Invest. Ophthalmol. Vis. Sci.,* vol. 31, pp. 2361-2366, Nov. 1990.

[18] D. M. Silver and R. A. Farrell, "Validity of pulsatile ocular blood flow measurements," *Surv. Ophthalmol.,* vol. 38 Suppl, pp. S72-80, May. 1994.

[19] E. M. Hoffmann, F. H. Grus and N. Pfeiffer, "Intraocular pressure and ocular pulse amplitude using dynamic contour tonometry and contact lens tonometry," *BMC Ophthalmol.,* vol. 4, pp. 4, Mar 23. 2004.

[20] C. C. Collins, "Miniature passive pressure transensor for implanting in the eye," *IEEE Transactions on Biomedical Engineering,* vol. BME-14, pp. 74-83, 04. 1967.

[21] M. Leonardi, P. Leuenberger, D. Bertrand, A. Bertsch and P. Renaud, "First steps toward noninvasive intraocular pressure monitoring with a sensing contact lens," *Invest. Ophthalmol. Vis. Sci.,* vol. 45, pp. 3113-3117, Sep. 2004.

[22] K. Mansouri and T. Shaarawy, *First clinical experience with the SENSIMED Triggerfish ® during 24-hour continuous IOP monitoring*, Lausanne, Switzerland: 2010.

[23] K. Stangel, S. Kolnsberg, D. Hammerschmidt, B. J. Hosticka, H. K. Trieu and W. Mokwa, "A programmable intraocular CMOS pressure sensor system implant," in *26th European Solid-State Circuits Conference,* 2001, pp. 1094-100.

[24] Po-Jui Chen, S. Saati, R. Varma, M. S. Humayun and Yu-Chong Tai, "Implantable flexible-coiled wireless intraocular pressure sensor," in *MEMS 2009,* 2009, pp. 244-7.

[25] U. Schnakenberg, P. Walter, G. Vom Bogel, C. Kruger, H. Ludtke-Handjery, H. A. Richter, W. Specht, P. Ruokonen and W. Mokwa, "Initial investigations on systems for measuring intraocular pressure," in *EUROSENSORS,* 2000, pp. 287-91.

[26] E.Y. Chow, S. Chakraborty, W.J. Chappell, and P.P. Irazoqui, “Mixed-signal integrated circuits for self-contained sub-cubic millimeter biomedical implants,” *2010 IEEE International Solid-State Circuits Conference - (ISSCC)*, IEEE, 2010, pp. 236-237.

[27] H. Wensink, J. W. Berenschot, H. V. Jansen and M. C. Elwenspoek, "High resolution powder blast micromachining," in *Proceedings IEEE Thirteenth Annual International Conference on Micro Electro Mechanical Systems,* 2000, pp. 769-74.

[28] T. Diepold and E. Obermeier, "Smoothing of ultrasonically drilled holes in borosilicate glass by wet chemical etching," in *Sixth European Workshop on Micromechanics (MME'95),* 1996, pp. 29-32.

[29] V. Fascio, R. Wuthrich, D. Viquerat and H. Langen, "3D microstructuring of glass using electrochemical discharge machining (ECDM)," in *Towards the New Century,* 1999, pp. 179-83.

[30] T. Abe, X. Li and M. Esashi, "Endpoint detectable plating through femtosecond laser drilled glass wafers for electrical interconnections," *Sensors and Actuators A (Physical),* vol. A108, pp. 234-8, 11/15. 2003.

[31] X. Li, T. Abe and M. Esashi, "Deep reactive ion etching of Pyrex glass using SF6 plasma", *Sensors and Actuators A (Physical),* vol. A87, pp. 139-45, 01/05. 2001.

[32] W. L. Perry, K. Waters, M. Barela and H. M. Anderson, "Oxide etch behavior in a high-density, low-pressure, inductively coupled C2F6 plasma: Etch rates, selectivity to photoresist, plasma parameters, and CFx radical densities," *Journal of Vacuum Science & Technology A (Vacuum, Surfaces, and Films),* vol. 19, pp. 2272-81, 2001.

[33] K. Kolari, "Deep plasma etching of glass with a silicon shadow mask", *Sensors & Actuators: A. Physical,* vol. 141, pp. 677-84, 02/15. 2008.

[34] SCHOTT North America. (2009, SCHOTT BOROFLOAT® 33. SCHOTT North America, Germany. Available: http://www.us.schott.com/borofloat/english/download/borofloat_33_e.pdf

[35] M.K. Ghantasala and D.K. Sood, “Novel method for electroplating on silicon without the need of a continuous-plating base film,” *Proceedings of SPIE*, SPIE, 1997, pp. 52-58.

[36] T. Fujita, S. Nakamichi, S. Ioku, K. Maenaka, and Y. Takayama, “Seedlayer-less gold electroplating on silicon surface for MEMS applications,” *Sensors and Actuators A: Physical*, vol. 135, Mar. 2007, pp. 50-57.

[37] P. Merz, H. J. Quenzer, H. Bernt, B. Wanger and M. Zoberbier, "A novel micromachining technology for structuring borosilicate glass substrates," in *IEEE International Solid-State Sensors and Actuators Conference,* 2003, pp. 258-61.

[38] Chiung-Wen Lin, Chia-Pao Hsu, Hsueh-An Yang, C. W. Wei and W. Fang, "Implementation of silicon-on-glass MEMS devices with embedded through-wafer silicon vias using the glass reflow process for wafer-level packaging and 3D chip integration," *J Micromech Microengineering,* vol. 18, pp. 025018-1, 02. 2008.

[39] E. J. Eklund and A. M. Shkel, "Glass blowing on a wafer level," *J Microelectromech Syst,* vol. 16, pp. 232-239, 2007.

[40] R. M. Haque, D. E. Serrano, X. Gao, A. N.-Shirazi, V. Keesara, F. Ayazi and K. D. Wise, “Hermetic Packaging of Resonators with Vertical Feedthroughs using a Glass-in-Silicon Reflow Process,” in *2011 16th International Solid-State Sensors, Actuators and Microsystems Conference*, 2011, pp. 2303-2306.

[41] R. Pal, M. Yang, R. Lin, B. N. Johnson, N. Srivastava, S. Z. Razzacki, K. J. Chomistek, D. C. Heldsinger, R. M. Haque, V. M. Ugaz, P. K. Thwar, Z. Chen, K. Alfano, M. B. Yim, M. Krishnan, A. O. Fuller, R. G. Larson, D. T. Burke, M. A. Burns, “An Integrated Microfluidic Device for Influenza and Other Genetic Analyses,” *Lab on a chip*, vol. 5, no. 10, pp. 1024-32, Oct. 2005.

[42] J.S. Mitchell, “Low Temperature Wafer Level Vacuum Packaging Using Au-Si Eutectic Bonding and Localized Heating”, *University of Michigan*, 2008.

[43] H. Gray, *Anatomy of the Human Body*. Philadelphia: Lea & Febiger, 1918.

[44] P. Chen, S. Saati, R. Varma, M. S. Humayun and Y. Tai, "Implantable flexible-coiled wireless intraocular pressure sensor," in *22nd IEEE International Conference on Micro Electro Mechanical Systems, MEMS 2009, January 25, 2009 - January 29,* 2009, pp. 244-247.

[45] Samaun, K. D. Wise and J. B. Angell, "An IC piezoresistive pressure sensor for biomedical instrumentation," *IEEE Transactions on Biomedical Engineering,* vol. BME-20, pp. 101-9, 03. 1973.

[46] Y. Zhang, S. Massoud-Ansari, G. Meng, W. Kim and N. Najafi, "An ultra-sensitive, high-vacuum absolute capacitive pressure sensor," in *14th IEEE International Conference on Micro Electro Mechanical Systems (MEMS 2001), January 21, 2001 - January 25,* 2001, pp. 166-169.

[47] A. V. Chavan, "An Integrated High Resolution Barometric Pressure Sensing System," *University of Michigan,* 2000.

[48] S. Yamamoto, O. Nakao, and H. Nishimura, “Touch mode capacitive pressure sensor for passive tire monitoring system,” *Sensors, 2002. Proceedings of IEEE*, IEEE, 2002, p. 1582–1586.

[49] H. Lv, Q. Guo, and G. Hu, “A touch mode capacitive pressure sensor with long linear range and high sensitivity,” *Nano/Micro Engineered and Molecular Systems, 2008. NEMS 2008. 3rd IEEE International Conference on*, IEEE, 2008, p. 796–800.

[50] Y. Zhang, “Non-Planar Diaphragm Structures for High-Performance Silicon Pressure Sensors,” *University of Michigan*, 1994.

[51] A. DeHennis and K. D. Wise, "A double-sided single-chip wireless pressure sensor," in *15th IEEE International Conference on Micro Electro Mechanical Systems MEMS 2002, January 20, 2002 - January 24,* 2002, pp. 252-255.

[52] A. D. DeHennis, "Remotely Powered Wireless Monitoring Systems," *University of Michigan,* 2004.

[53] Hin-Leung Chau and K. D. Wise, "An ultraminiature solid-state pressure sensor for a cardiovascular catheter," *IEEE Trans. Electron Devices,* vol. 35, pp. 2355-62, 12. 1988.

[54] M. Di Giovanni, *Flat and Corrugated Diaphragm Design Handbook.* New York: Marcel Dekker, Inc., 1982, pp. 404.

[55] H. Seidel, “Anisotropic Etching of Crystalline Silicon in Alkaline Solutions,” *Journal of The Electrochemical Society*, vol. 137, 1990, p. 3612.

[56] Y. Chuan and L. Chen, “The Compensation for Hysteresis of Silicon Piezoresistive Pressure Sensor,” *IEEE Sensors Journal*, 2011, pp. 1-6.

[57] R. Maboudian and C. Carraro, “Surface chemistry and tribology of MEMS.,” *Annual review of physical chemistry*, vol. 55, Jan. 2004, pp. 35-54.

[58] C.H. Mastrangelo, “Suppression of stiction in MEMS,” *Materials Research Society Symposium - Proceedings*, Mater. Res. Soc, 2000, pp. 105-116.

[59] C. Cabuz, E.I. Cabuz, T.R. Ohnstein, J. Neus, and R. Maboudian, “Factors enhancing the reliability of touch-mode electrostatic actuators,” *Sensors and Actuators A: Physical*, vol. 79, Feb. 2000, pp. 245-250.

[60] M. R. Houston, R. Maboudian, and R.T. Howe, *Ammonium Fluoride Anti-stiction Treatments For Polysilicon Microstructures*, IEEE, 1995.

[61] U. Srinivasan, M.R. Houston, R.T. Rowe, and R. Maboudian, *Self-assembled fluorocarbon films for enhanced stiction reduction*, IEEE, 1997.

[62] T. M. Mayer, J.W. Elam, S.M. George, P.G. Kotula, and R.S. Goeke, “Atomic-layer deposition of wear-resistant coatings for microelectromechanical devices,” *Applied Physics Letters*, vol. 82, 2003, p. 2883.

[63] T. Pedersen, G. Fragiacomo, O. Hansen and E. V. Thomsen, "Highly sensitive micromachined capacitive pressure sensor with reduced hysteresis and low parasitic capacitance," *Sens Actuators A Phys,* vol. 154, pp. 35-41, 2009.

[64] J.S. Mitchell, “Low Temperature Wafer Level Vacuum Packaging Using Au-Si Eutectic Bonding and Localized Heating”, *University of Michigan*, 2008.

[65] Cymbet Corporation. Product datasheet: EnerChip CBC050 thin film battery. Available: http://www.cymbet.com/pdfs/DS-72-01.pdf

[66] S. Y. Yoon, H. Nakahara, H. Tsukamoto, Q. Wang, K. Amine, Z. Zhang and R. West, "Miniature Size Hermetically Sealed Lithium Rechargeable Battery with Liquid Siloxane Electrolyte for Implantable Medical Applications," *Meet. Abstr. - Electrochem. Soc.,* vol. 503, pp. 121-121, 02/22. 2006.

[67] K. Amine, Q. Wang, D. R. Vissers, Z. Zhang, N. A. A. Rossi and R. West, "Novel silane compounds as electrolyte solvents for Li-ion batteries," *Electrochemistry Communications,* vol. 8, pp. 429-33, 03. 2006.

[68] J. Pan, Y. Sun, Z. Wang, P. Wan, X. Liu and M. Fan, "Nano silver oxide (AgO) as a super high charge/discharge rate cathode material for rechargeable alkaline batteries," *Journal of Materials Chemistry,* vol. 17, pp. 4820-5, 12/07. 2007.

[69] F. Chamran, Hong-Seok Min, B. Dunn and Chang-Jin Kim, "Zinc-air microbattery with electrode array of zinc microposts," in *2007 20th IEEE International Conference on Micro Electro Mechanical Systems - MEMS '07,* 2007, pp. 871-4.

[70] K. Gerasopoulos, M. McCarthy, E. Royston, J. N. Culver and R. Ghodssi, "Microbatteries with tobacco mosaic virus templated electrodes," in *21st IEEE International Conference on Micro*

Electro Mechanical Systems, MEMS 2008 Tucson, January 13, 2008 - January 17, 2008, pp. 960-963.

[71] A. Heller, "Potentially implantable miniature batteries," *Analytical and Bioanalytical Chemistry,* vol. 385, pp. 469-473, 2006.

[72] K. Marquardt, R. Hahn, T. Luger and H. Reichl, "Assembly and hermetic encapsulation of wafer level secondary batteries," in *19th IEEE International Conference on Micro Electro Mechanical Systems, January 22, 2006 - January 26,* 2006, pp. 954-957.

[73] Energizer Holdings Inc. Product datasheet: Energizer CR2032. Available: http://data.energizer.com/PDFs/cr2032.pdf

[74] J. Dlutowski, C. J. Biver, W. Wang, S. Knighton, J. Bumgarner, L. Langebrake, W. Moreno and A. Cardenas-Valencia, "The development of BCB-sealed galvanic cells. Case study: aluminum-platinum cells activated with sodium hypochlorite electrolyte solution," *J Micromech Microengineering,* vol. 17, pp. 1737-45, 08. 2007.

[75] F. Albano, Y. S. Lin, D. Blaauw, D. M. Sylvester, K. D. Wise and A. M. Sastry, "A fully integrated microbattery for an implantable microelectromechanical system," *J. Power Sources,* vol. 185, pp. 1524-32, 12/01. 2008.

[76] T. Ōsaka and M. Datta, *Energy Storage Systems for Electronics.* CRC, 2000,

[77] T. R. Crompton, *Battery Reference Book.* ,Second ed.London, UK: Butterworths, 1995, pp. 734.

[78] D. Linden, *Handbook of Batteries and Fuel Cells.* New York, NY, USA: McGraw-Hill, 1984, pp. 1045.

[79] B. L. Ki and L. Lin, "Electrolyte-based on-demand and disposable microbattery," *J Microelectromech Syst,* vol. 12, pp. 840-7, 12. 2003.

[80] Q. Li and N. J. Bjerrum, "Aluminum as anode for energy storage and conversion: a review," *J. Power Sources,* vol. 110, pp. 1-10, 7/20. 2002.

[81] B. M. L. Rao, S. A. Shah, J. Zakrzewski, R. P. Hamlen and W. Halliop, "Multimode battery," in *Proceedings of the Symposium on Autonomous Underwater Vehicle Technology - AUV '90, June 5, 1990 - June 6,* 1990, pp. 109-112.

[82] D. Buchel, C. Mihalcea, T. Fukaya, N. Atoda and J. Tominaga, "Investigations of sputtered silver oxide deposits for the super-RENS high density optical data storage application," in *Applications of Ferromagnetic and Optical Materials, Storage and Magnetoelectronics Symposium,* 2001, pp. 3-2.

[83] Xiao-Yong Gao, Song-You Wang, J. Li, Yu-Xiang Zheng, Rong-Jun Zhang, P. Zhou, Yue-Mei Yang and Liang-Yao Chen, "Study of structure and optical properties of silver oxide films by ellipsometry, XRD and XPS methods," in *3rd International Conference on Spectroscopic Ellipsometry,* 2004, pp. 438-42.

[84] Yung-Chiun Her, Yuh-Chang Lan, Wei-Chih Hsu and Song-Yeu Tsai, "The characteristics of reactively sputtered AgOx films prepared at different oxygen flow ratios and its effect on super-resolution near-field properties," *Japanese Journal of Applied Physics, Part 1 (Regular Papers, Short Notes & Review Papers),* vol. 43, pp. 267-72, 01. 2004.

[85] I. Nakamori, H. Nakamura, T. Hayano and S. Kagawa, "The Thermal Decomposition and Reduction of Silver(I) Oxide," *Bulletin of the Chemical Society of Japan,* vol. 47, pp. 1827-1832, 1974.

[86] G. Waterhouse, G. Bowmaker and J. Metson, "The Thermal Decomposition of Silver (I, III) Oxide: A Combined XRD, FT-IR and Raman Spectroscopic Study," *Phys. Chem. Chem. Phys.,* vol. 3, pp. 3838-3845, 2001.

[87] J. F. Pierson and C. Rousselot, "Stability of reactively sputtered silver oxide films," *Surf. Coat. Technol.,* vol. 200, pp. 276-9, 10/01. 2005.

[88] A. V. Kolobov, A. Rogalev, F. Wilhelm, N. Jaouen, T. Shima and J. Tominaga, "Thermal decomposition of a thin AgOx layer generating optical near-field," *Appl. Phys. Lett.,* vol. 84, pp. 1641-3, 03/08. 2004.

[89] New Jersey Department of Health, "Hazardous substance fact sheet: Potassium hydroxide," Trenton, NJ, October 1985,

[90] T. Lakhanisky, "Potassium hydroxide," UNEP Publications, Bern, Switzerland, Tech. Rep. SIDS Initial Assessment Report For SIAM 13, February 2002,

[91] S. Awad, S. P. Allison and D. N. Lobo, "The history of 0.9% saline," *Clinical Nutrition,* vol. 27, pp. 179-188, 4. 2008.

[92] H. Okamoto, "Au-Zn (Gold-Zinc)," *Journal of Phase Equilibria and Diffusion,* vol. 27, pp. 427, August 2006.

[93] J. C. Rivière and S. Myhra, *Handbook of Surface and Interface Analysis: Methods for Problem-Solving.* CRC PRESS, 1998,

[94] Anonymous "Model 617 programmable electrometer instruction manual," Keithley Instruments, Inc., Cleveland, Ohio, Tech. Rep. 617-901-01, Rev. G, 1984.

[95] Cymbet Corporation, "Rechargeable Thin Film Battery 12µAh, 3.8V," EnerChipTM CBC012 datasheet, 2009.

[96] G. Chen, H. Ghaed, R. Haque, M. Wieckowski, Y. Kim, G. Kim, D. Fick, D. Kim, M. Seok, K. D Wise, D. Blaauw, D. Sylvester, "A cubic-millimeter energy-autonomous wireless intraocular pressure monitor," *Solid-State Circuits Conference Digest of Technical Papers (ISSCC), 2011 IEEE International* , pp. 310-312, 20-24 Feb. 2011

[97] E.Y. Chow, S. Chakraborty, W.J. Chappell, and P.P. Irazoqui, "Mixed-signal integrated circuits for self-contained sub-cubic millimeter biomedical implants," *2010 IEEE International Solid-State Circuits Conference - (ISSCC)*, IEEE, 2010, pp. 236-237.

[98] P.-J. Chen, S. Saati, R. Varma, M.S. Humayun, and Y.-C. Tai, *Implantable Flexible-Coiled Wireless Intraocular Pressure Sensor*, California Institute of Technology, Pasadena, CA, United States: IEEE, 2009.

[99] D. Baderna, A. Cabrini, M. Pasotti, and G. Torelli, "Power Efficiency Evaluation in Dickson and Voltage Doubler Charge Pump Topologies", *Microelectronics Journal*, vol. 37, no. 10, pp. 1128-1135, Oct. 2006.

[100] M. Ferri, D. Pinna, E. Dallago, and P. Malcovati, "Integrated Micro-Solar Cell Structures for Harvesting Supplied Microsystems in 0.35-µm CMOS Technology," in *IEEE Sensors*, 2009, pp. 542-545.

[101] Y. Arima and M. Ehara, "On-Chip Solar Battery Structure for CMOS LSI" *IEICE Electronics Express*, vol. 3, no. 13, pp. 287-291, 2006.

[102] E. R. Fossum, "CMOS image sensors: electronic camera-on-a-chip," *IEEE Transactions on Electron Devices*, vol. 44, 1997, pp. 1689-1698.

[103] N. J. Guilar, T. J. Kleeburg, A. Chen, D. R. Yankelevich, and R. Amirtharajah, "Integrated Solar Energy Harvesting and Storage," *IEEE Transactions on Very Large Scale Integration (VLSI) Systems*, vol. 17, May. 2009, pp. 627-637.

[104] I. Nam and K. Lee, "High-Performance RF Mixer and Operational Amplifier BiCMOS Circuits using Parasitic Vertical Bipolar Transistor in CMOS TechnologyD" *IEEE Journal of Solid-State Circuits*, vol. 40, no. 2, pp. 392-402, Feb. 2005.

[105] H. I. Kwon, I. M. Kang, B.-G. Park, J. D. Lee, and S. S. Park, "The Analysis of Dark Signals in the CMOS APS Imagers From the Characterization of Test Structures," *IEEE Transactions on Electron Devices*, vol. 51, Feb. 2004, pp. 178-184.

[106] S.-W. Han, S.-J. Kim, and E. Yoon, “Low dark current CMOS image sensor pixel with photodiode structure enclosed by P-well,” *Electronics Letters*, vol. 42, 2006, pp. 102-106.

[107] H.-Y. Cheng and Y.-C. King, “An ultra-low dark current CMOS image sensor cell using n^+ ring reset,” *IEEE Electron Device Letters*, vol. 23, Sep. 2002, pp. 538-540.

[108] J. O. M. Miranda, “Electrostatic Vibration-to-Electric Energy Conversion,” Massachusetts Institute of Technology, 2003.

[109] S. Roundy, P.K. Wright, and J.M. Rabaey, *Energy Scavenging for Wireless Sensor Networks*, 2003.

[110] B. H. Stark, P.D. Mitcheson, P. Miao, T.C. Green, E.M. Yeatman, and A.S. Holmes, “Power processing issues for micro-power electrostatic generators,” *2004 IEEE 35th Annual Power Electronics Specialists Conference*, Dept. of Electr. & Electron. Eng., Imperial Coll. London, UK: IEEE, 2004, pp. 4156-4162.

[111] E. O. Torres and G.A. Rincon-Mora, “Electrostatic energy harvester and Li-Ion charger circuit for micro-scale applications,” *2006 49th Midwest Symposium on Circuits and Systems, MWSCAS’06*, 2006, pp. 65-69.

[112] R. Tashiro, N. Kabei, K. Katayama, E. Tsuboi, and K. Tsuchiya, “Development of an electrostatic generator for a cardiac pacemaker that harnesses the ventricular wall motion,” *Journal of Artificial Organs*, vol. 5, 2002, pp. 239-245.

[113] S. Nakamura, J. Umeda, and O. Nakada, “Response times of light-emitting diodes,” *IEEE Transactions on Electron Devices*, vol. 19, Aug. 1972, pp. 995-997.

[114] A.B. Brailovsky and V.V. Mitin, “Fast switching of light-emitting diodes,” *Solid-State Electronics*, vol. 44, Apr. 2000, pp. 713-718.

[115] S. Hanson, M. Seok, Yu-Shiang Lin, Y. F. Zhi, D. Kim, Y. Lee, N. Liu, D. Sylvester and D. Blaauw, "A low-voltage processor for sensing applications with picowatt standby mode," *IEEE J Solid State Circuits,* vol. 44, pp. 1145-55, 04. 2009.

[116] Yu-Shiang Lin, D. Sylvester and D. Blaauw, "A sub-pW timer using gate leakage for ultra low-power sub-hz monitoring systems," in *2007 IEEE 29th Custom Integrated Circuits Conference,* 2007, pp. 397-400.

[117] G. Chen, H. Ghaed, R. M. Haque, M. Wieckowski, Y. Kim, G. Kim, D. Fick, M. Seok, K. D. Wise, D. Blaauw, D. Sylvester, "A Cubic-Millimeter Energy-Autonomous Wireless Intraocular Pressure Monitor", *ISSCC Dig. Tech. Papers*, February 2011.

[118] B. Otis, J. M. Rabaey and SpringerLink (Online service), *Ultra-Low Power Wireless Technologies for Sensor Networks.* Boston, MA: Springer Science+Business Media, LLC, 2007,

[119] H. A. Wheeler, "The radiansphere around a small antenna," *Proceedings of the Institute of Radio Engineers,* vol. 47, pp. 1325-1331, 08. 1959.

[120] C. A. Balanis, *Antenna Theory. Analysis and Design.* London, UK: Harper & Row, 1982.

[121] D. M. Pozar, *Microwave Engineering.* ,3rd ed.Hoboken, NJ, USA: John Wiley & Sons, 2005,

[122] H. Zimmermann, "OSI reference model--The ISO model of architecture for open systems interconnection," *IEEE Trans. Commun.,* vol. 28, pp. 425, 1980.

[123] T. Melodia, M. C. Vuran and D. Pompili, "The state of the art in cross-layer design for wireless sensor networks," in *Revised Selected Papers,* 2006, pp. 78-92.

[124] W. Su and T. L. Lim, "Cross-layer design and optimization for wireless sensor networks," in *Seventh ACIS International Conference on Software Engineering, Artificial Intelligence, Networking, and Parallel/Distributed Computing,* 2006, pp. 7.

[125] C. T. Charles, "Wireless data links for biomedical implants: Current research and future directions," in *2007 IEEE Biomedical Circuits and Systems Conference, BIOCAS 2007,* 2008, pp. 13-16.

[126] J. A. Potkay, "Long term, implantable blood pressure monitoring systems," *Biomed. Microdevices,* vol. 10, pp. 379-392, 2008.

[127] A. D. DeHennis, "Remotely-powered wireless monitoring systems," University of Michigan, 2004.

[128] A. Kurs, A. Karalis, R. Moffatt, J. D. Joannopoulos, P. Fisher and M. Soljacic, "Wireless power transfer via strongly coupled magnetic resonances," *Science,* vol. 317, pp. 83-6, 07/06. 2007.

[129] S. O'Driscoll, A. Poon and T. H. Meng, "A mm-sized implantable power receiver with adaptive link compensation," in *2009 IEEE International Solid-State Circuits Conference (ISSCC 2009),* 2009, pp. 294-5.

[130] J. M. Rabaey, J. M. Carmena, B. Knight, D. Chen, M. Mark, R. S. Muller, S. Gambini and S. Venkatraman, "Microscopic wireless to power brain-machine interfaces (keynote address)," in 2008,

[131] K. Finkenzeller, *RFID Handbook: Radio-Frequency Identification Fundamentals and Applications.* Chichester: John Wiley, 1999, pp. xvii, 304 p.

[132] R. Giannetti, B. Tellini, S. L. Martinez and J. L. R. Marrero, "Intraocular pressure sensors: Analysis of a passive device approach," in *2003 Instrumentation and Measurement Technology Conference (IMTC 2003),* 2003, pp. 1547-50.

[133] Po-Jui Chen, S. Saati, R. Varma, M. S. Humayun and Yu-Chong Tai, "Implantable flexible-coiled wireless intraocular pressure sensor," in *MEMS 2009,* 2009, pp. 244-7.

[134] L. Rosengren, Y. Backlund, T. Sjostrom, B. Hok and B. Svedbergh, "A system for wireless intra-ocular pressure measurements using a silicon micromachined sensor," *J Micromech Microengineering,* vol. 2, pp. 202-4, 1992.

[135] Yu-Shiang Lin, D. Sylvester and D. Blaauw, "Alignment-independent chip-to-chip communication for sensor applications using passive capacitive signaling," *IEEE J Solid State Circuits,* vol. 44, pp. 1156-66, 04. 2009.

[136] E. Y. Chow, A. Kahn and P. P. Irazoqui, "High data-rate 6.7 GHz wireless ASIC transmitter for neural prostheses," in *29th Annual International Conference of the IEEE EMBS,* 2007, pp. 6580-3.

[137] A. M. Sodagar, K. D. Wise and K. Najafi, "A fully-integrated mixed-signal neural processing module for implantable multi-channel cortical recording," in *2006 IEEE Biomedical Circuits and Systems Conference - Healthcare Technology (BioCas),* 2006, pp. 37-40.

[138] K. Arshak, E. Jafer, G. Lyons, D. Morris and O. Korostynska, "A review of low-power wireless sensor microsystems for biomedical capsule diagnosis," *Microelectronics International,* vol. 21, pp. 8-19, 2004.

[139] G. Chen, H. Ghaed, R. M. Haque, M. Wieckowski, Y. Kim, G. Kim, D. Fick, M. Seok, K. D. Wise, D. Blaauw, D. Sylvester, "A Cubic-Millimeter Energy-Autonomous Wireless Intraocular Pressure Monitor", *ISSCC Dig. Tech. Papers*, February 2011.

[140] K. Gosalia, G. Lazzi and M. Humayun, "Investigation of a microwave data telemetry link for a retinal prosthesis," *IEEE Trans. Microwave Theory Tech.,* vol. 52, pp. 1925-33, 08. 2004.

[141] T. Buchegger, G. Ossberger, E. Hochmair, U. Folger, A. Reisenzahn and A. Springer, "An ultra low power transcutaneous impulse radio link for cochlea implants," in *Joint UWBST & IWUWBS 2004,* 2004, pp. 356-60.

[142] M. Chae, W. Liu, Z. Yang, T. Chen, J. Kim, M. Sivaprakasam and M. Yuce, "A 128-channel 6mW wireless neural recording IC with on-the-fly spike sorting and UWB tansmitter," in *2008*

IEEE International Solid State Circuits Conference, ISSCC, Febrary 3, 2008 - Febrary 7, 2008, pp. 146-147+135+603.

[143] M. Ghavami, L. B. Michael, R. Kohno, *Ultra-Wideband Signals and Systems in Communication Engineering*. Hoboken, NJ: John Wiley & Sons, Inc. 2004

[144] A. Salim, A. Baldi and B. Ziaie, "Inductive link modeling and design guidelines for optimum power transfer in implantable wireless microsystems," in *Proceedings of the 25th Annual International Conference of the IEEE Engineering in Medicine and Biology Society,* 2003, pp. 3368-71.

[145] W. H. Hayt and J. A. Buck, *Engineering Electromagnetics.* Boston: McGraw-Hill, 2001

[146] I.J. Bahl, P. Bhartia, and S.S. Stuchly, "Design of microstrip antennas covered with a dielectric layer," *IEEE Transactions on Antennas and Propagation*, vol. AP-30, 1982, pp. 314-318.

[147] D. C. Yates, A. S. Holmes and A. J. Burdett, "Optimal transmission frequency for ultralow-power short-range radio links," *IEEE Trans. Circuits Syst. I Fundam. Theor. Appl.,* vol. 51, pp. 1405-13, 07. 2004.

[148] P. H. Cole, "Coupling and quality factors in RFID," in *Design, Characterization, and Packaging for MEMS and Microelectronics II,* 2001, pp. 1-11.

[149] J. Kim, J. -. Plouchart, N. Zamdmer, N. Fong, Liang-Hung Lu, Y. Tan, K. A. Jenkins, M. Sherony, R. Groves, M. Kumar and A. Ray, "High-performance three-dimensional on-chip inductors in SOI CMOS technology for monolithic RF circuit applications," in *IEEE MTT-S International Microwave Symposium - IMS 2003,* 2003, pp. 77-80.

[150] M. Suster, W. H. Ko and D. J. Young, "An optically powered wireless telemetry module for high-temperature MEMS sensing and communication," *J Microelectromech Syst,* vol. 13, pp. 536-41, 06. 2004.

[151] T. H. Lee, *The Design of CMOS Radio-Frequency Integrated Circuits.* Cambridge, UK: Cambridge University Press, 2004, pp. xviii, 797 p.

[152] M. C. Cortizo and Lorenzo de Mele, Mónica Fernández, "Cytotoxicity of copper ions released from metal," *Biol. Trace Elem. Res.,* vol. 102, pp. 129-141, 2004.

[153] J. Krupka, J. Breeze, A. Centeno, N. Alford, T. Claussen and L. Jensen, "Measurements of permittivity, dielectric loss tangent, and resistivity of float-zone silicon at microwave frequencies," *IEEE Trans. Microwave Theory Tech.,* vol. 54, pp. 3995-4001, 11. 2006.

[154] DuPont. (2009, 11-2009). DuPont GreenTape: Low temperature co-fired ceramic system Available: http://www2.dupont.com/MCM/en_US/assets/downloads/prodinfo/GreenTape_Design_Layout_Guidelines.pdf

[155] K. Nortemann, J. Hilland and U. Kaatze, "Dielectric properties of aqueous NaCl solutions at microwave frequencies," *Journal of Physical Chemistry A,* vol. 101, pp. 6864-9, 1997.

[156] S. Gabriel, R. W. Lau and C. Gabriel, "The dielectric properties of biological tissues. II. Measurements in the frequency range 10 Hz to 20 GHz," *Phys. Med. Biol.,* vol. 41, pp. 2251-69, 11. 1996.

[157] C. Gabriel, R. J. Sheppard and E. H. Grant, "Dielectric properties of ocular tissues at 37° C," *Phys. Med. Biol.,* vol. 28, pp. 43-9, 01. 1983.

[158] R. Bawer and J. J. Wolfe, "The spiral antenna," *IRE International Convention Record,* vol. 8, pp. 84-95, 1960.

[159] W. F. March, K. Ochsner, and J. Horna, "Intraocular Lens Glucose Sensor", *Diabetes Technology & Therapeutics*, vol. 2, no. 1, pp. 27-30, Jan. 2000.

[160] J. T. Borenstein, "Medicine by micromachine," *IEEE Spectrum,* vol. 46, pp. 36-41, Nov. 2009.

[161] R. Tashiro, N. Kabei, K. Katayama, E. Tsuboi and K. Tsuchiya, "Development of an electrostatic generator for a cardiac pacemaker that harnesses the ventricular wall motion," *Journal of Artificial Organs,* vol. 5, pp. 0239-0245, 12/20. 2002.

[162] J. A. Hagerty, F. B. Helmbrecht, W. H. McCalpin, R. Zane and Z. B. Popovic, "Recycling ambient microwave energy with broad-band rectenna arrays," *IEEE Trans. Microwave Theory Tech.,* vol. 52, pp. 1014-24, 03. 2004.

[163] F. Kocer and M. P. Flynn, "An RF-powered, wireless CMOS temperature sensor," *IEEE Sensors Journal,* vol. 6, pp. 557-64, 06. 2006.

[164] H. Seki, T. Ono, Y. Kawai and M. Esashi, "Bonding of a Si microstructure using field-assisted glass melting," *J Micromech Microengineering,* vol. 18, 2008.